Electrochemical properties of self-assembled films of single-walled carbon nanotubes, monolayer-protected clusters of gold nanoparticles and iron (II) phthalocyanines at gold electrodes

by

Jeseelan Pillay

Dissertation submitted in fulfilment of the requirements for the degree

of

Doctor of Philosophy

University of Pretoria

Chemistry Department

November 2009

Supervisor: Dr. K. I. Ozoemena

DECLARATION

I declare that the dissertation, which I hereby submit for the degree of Doctor of Philosophy in the Faculty of Natural and Agricultural Sciences at the University of Pretoria, is my own work and has not previously been submitted by me for a degree at this or any other tertiary institution.

_____

JESEELAN PILLAY

s26518504

DEDICATION

To my dear friend and mentor Dr. Kenneth Ozoemena

"thank you for believing in me from Hons to PhD"

ACKNOWLEDGEMENTS

I would like to express my sincere gratitude to my inspirational supervisor Dr. Kenneth Ozoemena for his uncompromising guidance that has helped me to improve in all aspects of my life. For his encouragement when I failed to get any results for almost a year, for his compassion whenever I had difficulties in my personal life but most of all for his confidence in me. It has been an honour and privilege to work alongside the best electrochemist in South Africa who has inspired me to continue research in this field.

I would like to thank my dad and Nitasha for their encouragement and support during this challenging period. I would also like to express my gratitude to every person I have met during my journey from undergraduate to PhD. I am extremely grateful to all the PhD (Solomon, Adekunle, Dudu and Wendy) and MSc (Alfred, Nsovu and Joel) students in Dr. Ken's group (07-09) as well as Dr. Bolade for their continuous advice, constructive criticism and suggestions. I also sincerely appreciate all the Naomi Steenkamp's administrative assistance.

National Research Foundation (NRF) and Mintek (AuTEK Project) for their financial assistance. Finally, I wish to acknowledge several colleagues for constructive criticism as well as the concerns raised by referees of the published works from this dissertation.

ABSTRACT

Electrochemical properties of self-assembled films of single-walled carbon nanotubes, monolayer-protected clusters of gold nanoparticles and iron (II) phthalocyanines at gold electrodes

by

Jeseelan Pillay

Supervisor: Dr. K. I. Ozoemena

Submitted in fulfilment of the requirements for the degree Doctor of Philosophy, University of Pretoria, Department of Chemistry

This dissertation investigates the heterogeneous electron transfer dynamics and electrocatalytic behaviour of the following molecules immobilized on gold electrode: **(a)** 2-dimethylaminoethanethiol (DMAET), with and without integration with *poly*(*m*-aminobenzenesulfonic acid) functionalised single-walled carbon nanotubes (SWCNT-PABS); **(b)** SWCNT-PABS and iron (II) phthalocyanine nanoparticles (*nano*FePc); **(c)** Colloidal gold / Gold nanoparticles (AuNP) and *nano*FePc **(d)**; water-soluble iron (II) tetrasulfophtalocyanine (FeTSPc) and SWCNT-PABS, and **(e)** novel monolayer protected gold nanoparticles (MPCAuNPs) by means of either (i) layer-by-layer (LBL) self-assembly or (ii) self-assembled monolayer (SAM) fabrication strategy.

Atomic force microscopy and electrochemical studies (cyclic voltammetry, and electrochemical impedance spectroscopic) were used to monitor the substrate build-up, via strong electrostatic interaction. The surface pK_a of DMAET was estimated at 7.6, smaller than its solution pK_a of 10.8. It is also shown that SWCNT-PABS is irreversibly attached to the DMAET SAM. For layered films involving SWCNT-PABS and *nano*FePc (Au-DMAET- SWCNT-PABS-*nano*FePc)$_n$ (n=1-5 layers) as the number of bilayers increase, the electron transfer kinetics of the $[Fe(CN)_6]^{3-/4}$ redox probe decreases. On the contrary, LBL assembly involving AuNP and *nano*FePc (Au-DMAET-AuNP-*nano*FePc)$_n$ (n=1-4 layers) shows an increase followed by a decrease in electron transfer kinetics subsequent to the adsorption of *nano*FePc and AuNP layers, respectively. For SAMs involving FeTSPc and SWCNT-PABS, the mixed hybrid (Au-DMAET-SWCNT-PABS/FeTSPc) exhibited fastest charge transport compared to other electrodes. For the novel MPCAuNPs, the protecting or stabilizing ligands investigated were the (1-sulfanylundec-11-yl) tetraethylene glycol (PEG-OH) and the (1-sulfanylundec-11-yl) polyethylene glycolic acid (PEG-COOH). Three different mass percent ratios (PEG-COOH : PEG-OH), viz. 1:99 (MPCAuNP-COOH$_{1\%}$), 50:50 (MPCAuNP-COOH$_{50\%}$) and 99:1 (MPCAuNP-COOH$_{99\%}$) were used to protect the gold nanoparticles. The impact of these different ratios on the electron transfer dynamics in

organic and aqueous media was explored. The average electron transfer rate constants (k_{et} / s^{-1}) in organic medium decreased as the concentration of the surface-exposed –COOH group in the protecting monolayer ligand increased: MPCAuNP-$COOH_{1\%}$ (~ 10 s^{-1}) > MPCAuNP-$COOH_{50\%}$ (~ 9 s^{-1}) > MPCAuNP-$COOH_{99\%}$ (~ 1 s^{-1}). In aqueous medium, the trend is reversed. This behaviour has been interpreted in terms of the hydrophobicity (quasi-solid nature) and hydrophilicity (quasi-liquid nature) of the terminal –OH and –COOH head groups, respectively. The ionization constants of the terminal groups (i.e., surface pK_a) was estimated as ~ 8.2 for the MPCAuNP-$COOH_{1\%}$, while both MPCAuNP-$COOH_{50\%}$ and MPCAuNP-$COOH_{99\%}$ showed two pK_a values of about 5.0 and ~ 8.0, further confirming the hydrophilicity / hydrophobicity of these surface functional groups.

Hydrogen peroxide (H_2O_2), epinephrine (EP) and ascorbic acid (AA) were used as model analytes to examine electrocatalytic ability of these nanostructured assemblies. The electrochemical reduction of H_2O_2 at a constant concentration was amplified upon increasing bilayer formation of SWCNT-PABS and *nano*FePc, while SWCNT-PABS/FeTSPc showed the best response towards the detection of epinephrine. MPCAuNP-$COOH_{99\%}$ showed an excellent suppression of the voltammetric response of the AA and an enhanced electrocatalytic activity towards the detection of EP compared to the other MPCAuNPs.

Table of Contents Page

LIST OF ABBREVIATIONS

AA	=	Ascorbic acid
AFM	=	Atomic Force Microscopy
Ag|AgCl	=	Silver|silver Chloride Reference Electrode
CA	=	Chronoamperometry
CE	=	Counter Electrode
CME	=	Chemically Modified Electrode
CNT	=	Carbon Nanotube
CPE	=	Constant Phase Angle Element
CV	=	Cyclic Voltammetry / Cyclic Voltammetric
CVD	=	Chemical Vapour Decomposition
DMAET	=	Dimethylaminoethanethiol
DMF	=	*N*,*N*-Dimethylformamide
EDX	=	Energy-Dispersive X-Ray
EIS	=	Electrochemical Impedance Spectroscopy
EP	=	Epinephrine
FeTSPc	=	Iron (II) Tetrasulphonated Phthalocyanine
GCE	=	Glassy Carbon Electrode
H_2O_2	=	Hydrogen peroxide
IHP	=	Inner Helmholtz Plane
IR	=	Infra-Red
IUPAC	=	International Union of Pure and Applied

$K_3Fe(CN)_6$	=	Potassium hexacyanoferrate(III)
$K_4Fe(CN)_6$	=	Potassium hexacyanoferrate(II)
KCl	=	Potassium Chloride
LBL	=	Layer-by-layer
LoD	=	Limit of Detection
LSV	=	Linear Sweep Voltammetry
MES	=	Sodium 2-Mercaptoethanesulphonate
MPc	=	Metallophthalocyanine
MPCAuNPs	=	Monolayer-Protected Clusters of Gold
MPCs	=	Monolayer-protected Clusters
MTAPc	=	Metallotetraamino-phthalocyanine
MWCNT	=	Multi-Walled Carbon Nanotube
NaCl	=	Sodium Chloride
*nano*FePc	=	nano Iron (II) Phthalocyanine nanoparticles
OHP	=	Outer Helmholtz Planes
PBS	=	Phosphate Buffer Solutions
Pc	=	Phthalocyanine
PEG	=	Polyethylene Glycol
R_{ct}	=	Charge Transfer Resistance
RDE	=	Rotating Disc Electrode
RE	=	Reference Electrode

R_s	=	Solution Resistance
SAM	=	Self-Assembled Monolayer
SEM	=	Scanning Electron Microscopy
SWCNT	=	Single-Walled Carbon Nanotube
SWCNT-PABS	=	Single-Walled Carbon Nanotubes poly (*m*- aminobenzene sulfonic acid)
SWV	=	Square Wave Voltammetry
$TBABF_4$	=	Tetrabutylammonium Tetrafluoroborate
TEM	=	Transmission Electron Microscopy
UV-vis	=	Ultraviolet-visible
WE	=	Working Electrode
Z_w	=	Warburg Impedance

LIST OF FIGURES

LIST OF SCHEMES

LIST OF TABLES

CHAPTER ONE

INTRODUCTION

1 INTRODUCTION

1.1 General Overview

Advances in nanomaterials are helping to develop electrochemical sensors with increased sensitivity that can be extensively applied to a wide variety of analytical problems including clinical, medicinal, drug discovery, food and environmental areas. Electrochemical methods have proven to be more cost effective, simple, user friendly, portable, and faster than other analytical methods. Therefore, there is a need to design and develop high-speed and high-performance electrochemical sensors that can hold an outstanding ability among analytical devices available for environmental applications. However, the success of electrochemical sensing device is determined by (i) the electrode, (iii) the construction technique (which determines its stability or shelf life and reliability) and (ii) the electrocatalyst. Over the past decade, carbon nanotubes and phthalocyanine complexes have received considerable attention because of their unique physico-chemical and electronic properties. However, their smart integration in electrochemical sensing is hugely under-explored. It is also anticipated that the interaction of phthalocyanine complexes with monolayer-protected clusters of gold nanoparticles will provide a combination that

will revolutionize their applications as electrocatalysts in electrochemical sensors.

This project describes the electron transport and electrocatalytic behaviour of single-walled carbon nanotubes (SWCNTs), monolayer-protected clusters of gold nanoparticles (MPCAuNPs) independently and phthalocyanine complexes immobilized on a thiol based gold substrate towards the detection of epinephrine and hydrogen peroxide.

Aim of Dissertation:

i. To characterize redox-active phthalocyanine complexes integrated with (i) Single-walled carbon nanotube and (ii) MPCAuNPs spectroscopic, microscopic and electrochemical techniques.
ii. To modify bare gold electrode with self assembled mono and multi-layers of SWCNT, MPCAuNPs and MPc complexes, and establish their electrochemical properties.
iii. To investigate the electrocatalytic ability of modified electrodes towards the detection of epinephrine and hydrogen peroxide.

This introductory section provides a general overview of electrochemistry, electrochemical techniques, electrode modification processes, carbon nanotubes, phthalocyanine complexes, monolayer-

protected clusters of gold nanoparticles, relevant analytes such as epinephrine and hydrogen peroxide as well as microscopic techniques. In chapter two the procedure adopted for the experiment is provided. Chapter three discusses the results obtained.

1.2 Electrochemistry : An Overview

1.2.1 Basic Concepts

Electrochemistry may simply be defined as the study of chemical reactions used to produce electric power or, alternatively, the use of electricity to effect chemical processes or systems [1,2]. Hence, electrochemistry can be seen as the relationship between electricity and chemistry, namely the measurements of electric quantities, such as current, potential, and charge, and their relationship to chemical parameters. These chemical reactions involving the transfer of electrons to and from a molecule or ion are often referred to as redox (reduction/oxidation) reactions. The use of electrochemistry for analytical purposes has found a wide range of applications in industrial quality control, metallurgy, geology, pharmacy, medicinal chemistry, biomedical analysis and environmental monitoring [2].

Unlike many chemical measurements, which involve homogenous bulk solutions, the fundamental electrochemical reactions are heterogeneous in nature as they take place at interfaces, usually electrode-solution boundaries. The electrode creates a phase boundary that differentiates otherwise identical solute molecules; those at a distance from the electrode, and those close enough to the surface of the electrode to participate in the electron transfer process [1,2]. This

section takes a closer look at some of the electroanalytical techniques and electrode processes employed in this dissertation.

1.2.1.1 Electrochemical Equilibrium: Introduction

The system represented in Equation 1.1, used to describe the electrochemical equilibrium process, reaches a state of equilibrium when an inert metal (usually platinum electrode) is added to a solution containing potassium hexacyanoferrate(II), $K_4Fe(CN)_6$, and potassium hexacyanoferrate(III), $K_3Fe(CN)_6$ dissolved in water.

$$Fe(CN)_6^{3-}(aq) + e^- \rightleftharpoons Fe(CN)_6^{4-}(aq) \qquad 1.1$$

When the state of equilibrium is reached the rate at which $Fe(CN)_6^{4-}$ gives up electrons to the electrode is exactly balanced by the rate at which electrons are released by the electrode to the $Fe(CN)_6^{3-}$ anions. The $Fe(CN)_6^{3-}$ and $Fe(CN)_6^{4-}$ anions are said to be reduced and oxidised respectively. The reaction involves the transfer of charged particles (electrons). Therefore, if the reaction lies to the right or left when equilibrium is reached a charge separation develops at the solution - electrode interface. Accordingly, an electrode potential is established at the metal electrode relative to the solution. Chemical processes, such as this example which establish electrode potentials,

are referred to as potential determining equilibria [3]. Other examples where an electrochemical process is capable of forming a potential on the electrode in an aqueous medium include: (i) the hydrogen electrode, (ii) the silver|silver chloride electrode and (iii) the calomel electrode.

1.2.1.2 Electrochemical Equilibrium: Electron Transfer at the Electrode – Solution Interface

The electrode – solution interface also known as "electric double layer" is illustrated in Figure 1.1 It is the currently accepted representation [3] that was derived from the Helmholtz and Guoy-Chapman models which show the interface as a single capacitor and as a Boltzman distribution of ions respectively.

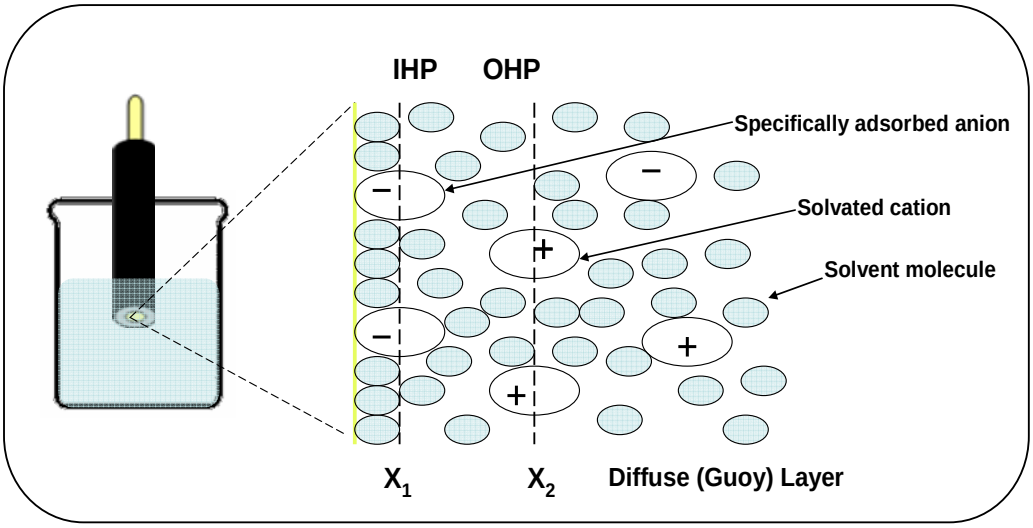

Figure 1.1: Model of the electrode – solution double layer region [3].

Introduction.....

The electrical double layer comprises of inner layer, outer layer and the diffuse or Guoy layer. The inner layer, also referred to as, the Inner Helmholtz Plane (IHP) is area closest to the electrode surface where adsorbed ions and solvent molecules are found. The outer layer, the Outer Helmholtz Planes (OHP) is the imaginary plane passing through the solvated cations. The solvated cations undergo nonspecfic adsorption and are pulled towards the electrode surface by long range coulombic forces. Technically, the Inner and Outer Helmholtz Planes do not exist, nor can they be measured. However, the distance can be explained using the solvent molecules as well as the radius of the ions, where, the distance from the electrode surface to the IHP (X_1) is equivalent to the radius of the cation and the distance to the OHP is approximately two solvent molecules and the radius of the ion. These two layers are strongly held by the electrode and they remain at the surface even if the electrode is removed from solution. The outer most layer which extends from the OHP to the bulk is known as the diffuse or Guoy layer. The three dimensional region of scattered ions is as a result of the balance between the disorder caused by random thermal motion and the order due to electrostatic attractive and repulsive forces from the electrode surface. The presence of the electrode cannot be felt by the ion beyond this region.

1.2.1.3 Classification of Electrochemical Techniques

The flowchart represented in Figure 1.2 illustrates the classes and sub–divisions of electrochemical techniques.

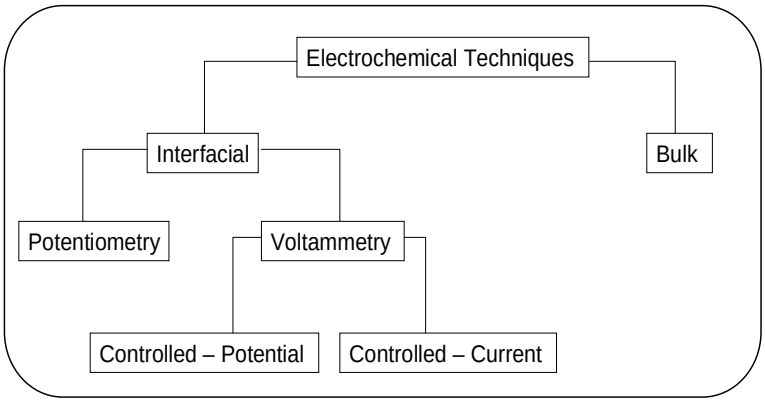

Figure 1.2: Flowchart representing Electrochemical Techniques

Bulk techniques are based on the phenomena that occur in the solution whereas interfacial techniques are based on the events occurring at the electrode–solution interface. Interfacial is sub–divided into potentiometric and voltammetric methods. Voltammetric techniques may be further divided into controlled–potential and controlled–current methods. Frequently used techniques such as voltammetry and chronoamperometry are an example of controlled–potential. It involves controlling the potential while measuring the current. The advantages of this technique include high sensitivity and selectivity towards electroactive species, portable and low cost instrumentation.

1.2.1.4 Faradaic and Non-Faradaic Processes

The current response obtained in controlled–potential experiments is as a result of the analyte species that is oxidized or reduced at the electrode–solution interface. This current response is deduced from the transfer of electrons during the redox process of the target analyte as shown in Equation 1.2:

$$Ox + ne^- \rightleftharpoons Red \qquad 1.2$$

where Ox and Red represent the oxidised and reduced forms of the analyte, respectively, while n is the number of electrons transferred. The current that arises from the oxidation or reduction of the analyte species is called the Faradaic current. For a thermodynamically controlled reversible process the applied potential (E) of the electrode is given by the well known Nernst equation, Equation 1.3:

$$E = E^\circ + \frac{2.303RT}{nF}\log\frac{C_{ox}}{C_{red}} \qquad 1.3$$

where E^o = standard potential of the redox couple; R = universal gas constant; T = temperature (K); n = number of electrons transferred; F = Faraday's constant; C_{ox} = Concentration of the oxidized species; C_{red} = Concentration of the reduced species.

Non Faradaic currents are a result of those processes that do not involve the transfer of electrons across the electrode–solution interface and they stem from the electrical capacitance present at the interface. The capacitance (C) of the electrical double layer can be calculated using Equation 1.4.

$$C = \frac{q}{E} \qquad 1.4$$

where q and E represent charge and potential respectively.

1.2.1.5 The Electrochemical Cell

All current-measuring (voltammetric / amperometric) techniques make use of a three-electrode electrochemical cell (Fig. 1.3) [4-6].

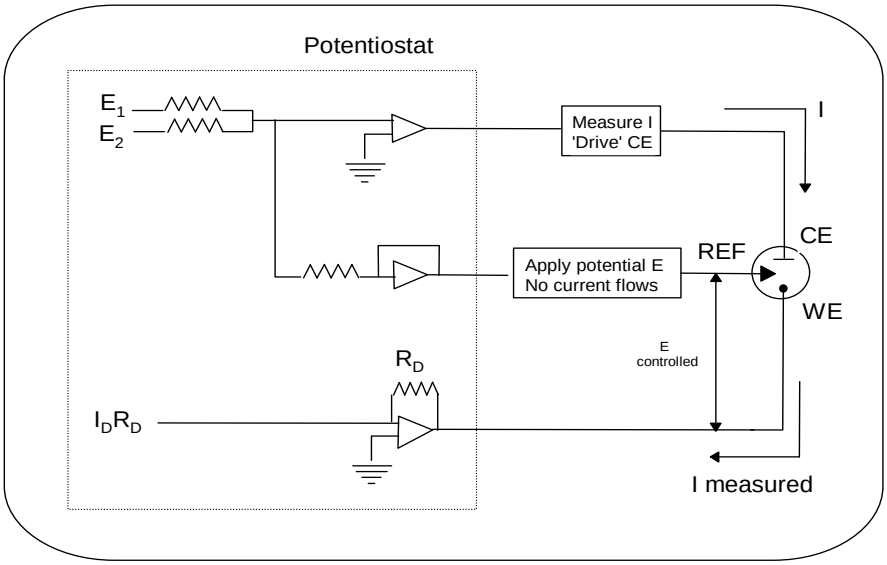

Figure 1.3: Graphical representation of a conventional three-electrode cell [5].

The surface of the working electrode, W.E., is the platform of the electrochemical reaction being studied. R.E. is the reference electrode, while the counter electrode, C.E., completes the electric circuit. The best reference electrode is one whose potential does not shift from equilibrium (i.e. non polarisable). In order to minimize the potential shift, a reference electrode with very large surface area is often used [1]. Potentiostats based on operational amplifiers are often used in the complete elimination of reference electrode polarisation. As shown in Figure 1.1 the potentiostat maintains the potential difference, ΔE, between the R.E. and W.E. and supplies the current, i, needed for affecting the changes occurring at W. E.

There are numerous reference electrodes employed in electroanalytical experiments, but the most common being the silver|silver chloride (Ag|AgCl, sat'd KCl) electrode. It is a piece of silver wire anodized with silver chloride which is immersed in potassium chloride or sodium chloride solution and encased in a glass tube. The electrode is protected from the bulk of the solution by a non-selective salt-bridge [7]. Platinum rods, wire, loops, gauze or foil are consistently used as counter electrodes. Commonly used working electrodes include mercury, carbon and inert materials such as platinum or gold.

1.2.1.6 Mass Transport Processes

The fundamental movement of charged or neutral species in an electrochemical cell to the electrode surface is facilitated by three processes namely: diffusion, migration or convection [2,3] as illustrated in Figure 1.4.

Diffusion is mass transport resulting from the spontaneous movement of analyte species from regions of high concentrations to lower ones, with the aim of minimizing concentration differences. A concentration gradient develops if an electrochemical reaction depletes (or produces) some species at the electrode surface. To minimize the concentration difference an electroactive species will diffuse from the bulk solution to the electrode surface (or from the electrode surface into the bulk solution.

Migration refers to movement of a charged particle in a potential field. In most voltammetric experiments, migration is undesirable but can be eliminated by the addition of a large excess of supporting electrolyte. Inert anions and cations (i.e., electrochemically inert – not oxidized or reduced) that are formed from dissociation of the supporting electrolyte now function as the migration current carriers and also increase the conductivity of the solution [1].

Finally ***convection*** is a mass transport achieved by some form of external mechanical energy acting on the solution or the electrode

such as stirring the solution, solution flow or rotation and/or vibration of the electrode.

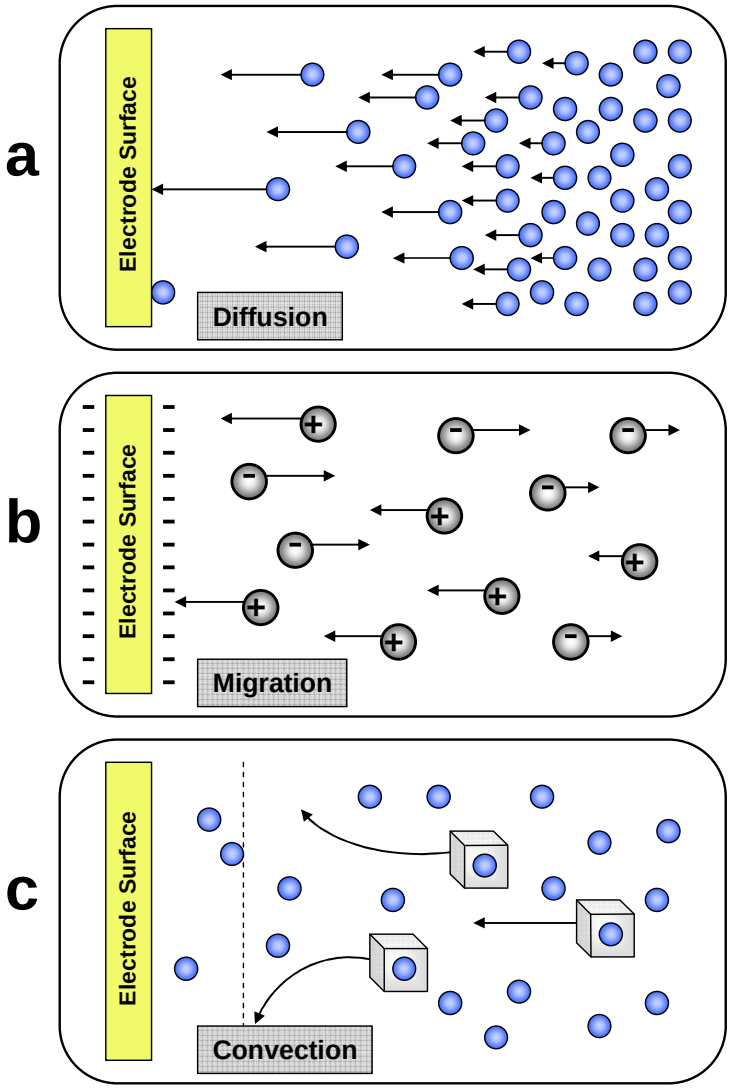

Figure 1.4: Schematic representation of the three mass transport modes viz. (a) Diffusion, (b) Migration and (c) Convection [2].

1.2.2 Voltammetry

Voltammetry is a branch of electroanalytical techniques and it is often used in industrial processes to obtain information about the analyte species by varying the potential and measuring the current.

1.2.2.1 Types of Voltammetry

1.2.2.1.1 Cyclic Voltammetry

Cyclic voltammetry (CV) depicted in Figure 1.5 is the most extensively used electrochemical technique and is used to study electrochemical reactions as well as to provide information on the reversibility and kinetics of such reactions [5,8]. During a cyclic voltammetry experiment, the potential of an electrode is scanned linearly from an initial potential to a final potential and then back to the initial potential. The potential at which the peak current occurs is known as the peak potential (E_p) where the redox species has been depleted at the electrode surface and the current is diffusion limited. The magnitude of the Faradaic current (I_{pa} - anodic peak current) or (I_{pc} - cathodic peak current), gives an indication of the rate at which electrons are being transferred between the redox species and the electrode. Cyclic voltammetric processes could be reversible, quasi-reversible and irreversible.

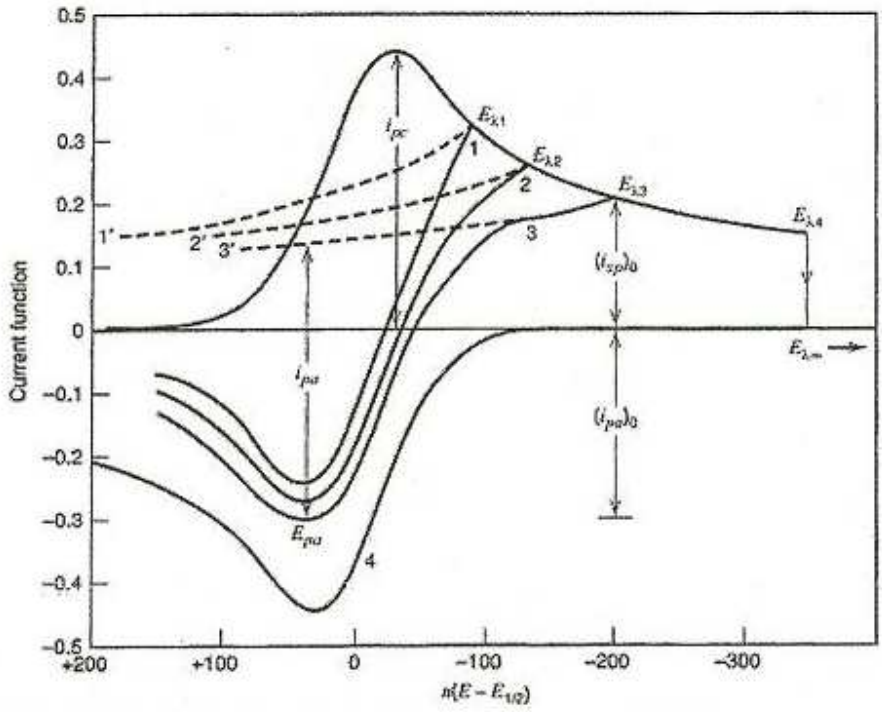

Figure 1.5: Typical cyclic voltammogram for a reversible process [3].

Reversible Process

A reversible process is one in which the electron transfer process is rapid, and the electroactive oxidised (or reduced) species in the forward scan is in equilibrium with the electroactive reduced (oxidised) species in the reverse scan (Eq. 1.5).

$$Red \rightleftharpoons Ox + ne^- \qquad 1.5$$

Figure 1.5 shows a typical CV for a reversible process. The electroactive species are stable and so the magnitudes of I_{pc} and I_{pa}

are equal and proportional to the concentrations of the active species. ΔE_p (E_{pa} – E_{pc}) should be independent of the scan rate (ν) but in practice ΔE_p increases slightly with increasing ν, this is due to the solution resistance (R_S) between the reference and working electrodes [9,10]. Theoretically, the potential difference between the oxidation and reduction peaks is 59 mV for one-electron reversible redox reactions. However, in practice, ΔE_p is sometimes found in the 60-100 mV range.

Reversibility is a direct and straight forward means of probing the stability of an electroactive species. An unstable species reacts as it is formed and hence produces no current wave in the reverse scan whereas a stable species remains in the vicinity of the electrodes surface and produces a current wave of opposite polarity to the forward scan. Larger differences or asymmetric reduction and oxidation peaks are an indication of irreversible reactions. Irreversibility is a result of slow exchange between the redox species and the working electrode [5]. At 25°C, the peak current is given by the Randles-Ševčík equation [2,3]:

$$i_p = \left(2.69\times10^5\right)n^{3/2}AC\left(D\nu\right)^{1/2} \qquad 1.6$$

where, i_p = peak current (A); n = number of electrons transferred; A = electrode area (cm^2); C = concentration (mol cm^{-3}); D = diffusion coefficient (cm^2 s^{-1}) and ν = scan rate (V s^{-1}). These parameters make CV most suitable for characterization and mechanistic studies of redox reactions at electrodes.

A linear plot of i_p vs. $\nu^{1/2}$ indicates that the currents are controlledby planar diffusion to the electrode surface [9]. The ratio of anodic to cathodic currents i_{pa} / i_{pc} is equal for a totally reversible process and deviation from this is indicative of a chemical reaction involving either one or both of the redox species. The potential where the current is half of its limiting value is known as the half-wave potential $E_{1/2}$ (also called formal potential or equilibrium potential, E°′) which is the average of the two peak potentials, represented by Equation 1.7.

$$E_{1/2}(orE^{\circ'}) = \frac{E_{pa} + E_{pc}}{2} \qquad 1.7$$

where E_{pa} and E_{pc} are the anodic and cathodic peak potentials, respectively. The separation between two peak potentials, ΔE_p for a

reversible couple is given by Equation 1.8 and can be used to obtain the number of electrons transferred.

$$\Delta E = E_{pa} - E_{pc} = 2.303\frac{RT}{nF} \qquad 1.8$$

ΔE_p is independent of the scan rate, and at 25 °C Equation 1.8 can be simplified to Equation 1.9:

$$\Delta E_p = 2.303\frac{RT}{nF} = \frac{0.059V}{n} \qquad 1.9$$

At appropriate conditions (i.e. at 25 °C, first cycle voltammogram) the standard rate constant (*k*) for the heterogeneous electron transfer process can be estimated [1,11].

Irreversible Process

For an irreversible process, only forward oxidation (reduction) peak is observed but at times with a weak reverse reduction (oxidation) peak as a result of slow electron exchange or slow chemical reactions at the electrode surface [7]. The peak current, i_p for irreversible process is given by Equation 1.10:

$$i_p = \left(2.99\times10^5\right)n[(1-\alpha)n]^{1/2} Ac(D\nu)^{1/2} \qquad 1.10$$

where α is the coefficient of electron transfer, the rest of the symbols are defined above in Equation 1.3. For a totally irreversible system, ΔE_p is calculated from Equation 1.11:

$$\Delta E_p = E^{o'} - \frac{RT}{\alpha nF}\left[0.78 - \ln\frac{k}{D^{1/2}}\ln\left(\frac{\alpha nF}{RT}\right)^{1/2}\right] \qquad 1.11$$

where all symbols are defined above. At 25 °C, E_p and $E_{1/2}$ differ by $0.048/\alpha n$.

Quasi-Reversible Process

Unlike the reversible process in which the current is purely mass-transport controlled, currents due to quasi-reversible process are controlled by a mixture of mass transport and charge transfer kinetics [2,12]. The process occurs when the relative rate of electron transfer with respect to that of mass transport is insufficient to maintain Nernst equilibrium at the electrode surface. For quasi-reversible process, i_p increases with $\nu^{1/2}$ but not in a linear relationship and $\Delta E_p > 0.059/n$ [3]. The slight differences in three cyclic voltammetric processes are summarized in Table 1.1.

Table 1.1: The diagnostic criteria for reversible, irreversible and quasi-reversible cyclic voltammetric processes [3,7,12]

Parameter	**Cyclic Voltammetry Process**		
	Reversible	*Irreversible*	*Quasi-reversible*
E_p	Independent of ν	Shifts cathodically by $30/\alpha n$ mV for a 10-fold increase in V	Shifts with ν
$E_{pc} - E_{pa}$	~ 59/n mV at 25°C and independent of ν	_	May approach 60/n mV at low ν but increases as ν increases
$I_p / \nu^{1/2}$	Constant	Constant	Virtually independent of ν
I_{pa} / i_{pc}	Equals 1 and independent of ν	No current on the reverse side	Equals 1 only for $\alpha = 0.5$

1.2.2.1.2 Square Wave Voltammetry

In square wave polarographs the base-current can be suppressed by using alternating voltage of square-wave shape, where the base-current decays more rapidly than the Faradaic current after the application of a voltage-pulse to the electrode. Therefore, a measurement of the current a short time before each new pulse leads to elimination of the base-current from the recorded polarogram. This principle was first used in the square-wave polarograph of Barker and Jenkins [13]. Janet G. Osteryoung used this concept to develop the differential electrochemical technique, Square Wave Voltammetry (SWV) [14]. It depends on excitation functions that overlay the features of a large amplitude square wave modulation and a single staircase waveform [15]. Throughout any given square wave cycle, the current is sampled at the end of the forward and reverse scans and the difference between the forward (i_f) and reverse current (i_r), are plotted against the average potential of each waveform cycle. In this technique, the peak potential occurs at the $E_{1/2}$ of the redox couple because the current function is symmetrical around the half-wave potential [15]. The scan rate of a square wave voltammetry experiment is given by the Equation 1.12:

$$\nu = f.\Delta E_s \qquad 1.12$$

where f is the square wave frequency (Hz) and ΔE_s is the potential step size. Major advantages of this powerful electrochemical technique include its capacity to use of faster scan rates compared to conventional differential pulse voltammetry, its ability to reject capacitive charging currents and its fantastic sensitivity.

1.2.2.1.3 Chronoamperometry

Chronoamperometry (CA) is an electrochemical technique that is a simple short-lived amperometric method where the current is recorded as a function of time as a result of the potential being stepped. This uncomplicated potential step wave form (Fig. 1.6) monitors the current response following the working electrode potential being stepped from an initial potential at which the oxidized (reduced) species is stable in solution, to the first step potential where a redox reaction occurs forming the reduced (oxidized) species and it is held at this value for the duration of the first step time in a single potential experiment. In a double potential step experiment, the potential is stepped twice. First for the period mentioned above and thereafter that stepped to a second step potential where it is held for the duration of the second step time.

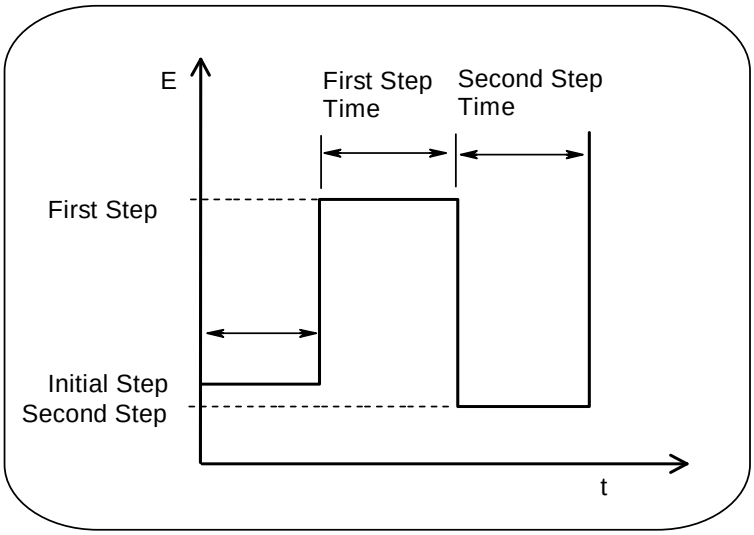

Figure 1.6: Simple potential wave form depicting chronoamperometry.

The analysis of chronoamperometry (CA) data is based on the Cottrell equation, 1.13 [16-18]. A plot of i versus $t^{-1/2}$ is often referred to as the Cottrell plot which defines the current-time dependence for linear diffusion control and can be used to calculate the diffusion coefficient (D) resulting from the slope of the plot.

$$i = nFACD^{1/2}\pi^{-1/2}t^{-1/2} \qquad 1.13$$

where n = number of electrons transferred /molecule; F = Faraday's constant (96 485 C mol^{-1}); A = electrode area (cm^2); D = diffusion coefficient (cm^2 s^{-1}); C = concentration (mol cm^{-3}) and t = time (s)At intermediate times of chronoamperometric measurements the catalytic

rate constant (k) can be determination using the established Equation 1.14 [3, 16-18]:

$$\frac{I_{cat}}{I_L} = \pi^{1/2}\left(kC_o t\right)^{1/2} \qquad 1.14$$

where I_{cat} and I_L are the currents of the electrode in the presence and absence of the analytes, respectively; k and t are the catalytic rate constant (M^{-1} s^{-1}) and time elapsed (s), respectively; and C_o is the bulk concentration of analytes. The catalytic rate constant can be determined from the slope of the plot of I_{cat} / I_L vs. $t^{1/2}$.

1.2.2.1.4 Rotating Disk Electrode

A rotating disk electrode (RDE) is a hydrodynamic working electrode that is used in a three electrode system [3]. This technique is usually employed in electrochemical studies when investigating redox related mechanistic reactions. The conductive disk or working electrode is made of glassy carbon or a noble metal which is embedded in an inert non-conductive polymer or resin. In this technique the working electrode, controlled by the attached electric motor, actually rotates, and in so doing provides an influx of the analyte species at the electrode surface. The disk's rotation is often described in terms of angular velocity. As it turns it pulls the solution closest to its surface (hydrodynamic boundary layer) with, creating a

whirlpool effect thus the solution from the centre of the electrode is displaced as a result of centrifugal force. Solution from the bulk now flows up, perpendicular to the electrode, to replace the boundary solution. The sum result is a laminar flow across and towards the electrode surface. The rate of the rotating disk controls the solution flow which in turn controls the steady-state current. This method is different to unstirred techniques where the steady-state current is controlled by diffusion. In this work I used linear sweep voltammetry at various rotation speeds to investigate the electron transfer behaviour.

The analysis of RDE data is based on the Equation 1.15: A plot of limiting current (I_L) vs. $\omega^{1/2}$ which is often referred to as the Koutecky-Levich plot and can be used to calculate the catalytic rate constant, k_{ch}, resulting from the slope of the plot.

$$\frac{1}{i_{\lim}} = \frac{1}{i_k} + \frac{1}{i_{lev}} = \frac{1}{(nFAk_{ch}\Gamma C)} + \frac{1}{(0.620nFAcD^{2/3}\gamma^{-1/6}\omega^{1/2})} \qquad 1.15$$

where i_{lim}, i_k, i_{lev} are the measured current, kinetic and diffusion-limited currents, respectively, n is the number of electrons transferred which is 2 for epinephrine electrooxidation, k_{ch} is the catalytic rate constant ($mol^{-1}\ cm^3\ s^{-1}$) obtained from the intercepts of the regression lines, F is

the Faraday constant (96 485 C mol^{-1}), A is the electrode surface area which is 0.1963 cm^2, ω is the rotating speed (rps), Γ (mol cm^{-2}) is the redox active species (DMAET-SWCNT-PABS) concentration on electrode surface, C is the bulk concentration of analyte (mol cm^{-3}), D is the diffusion coefficient (cm s^{-1}) of epinephrine and γ is the kinematic viscosity of the solution.

1.2.2.1.5 Linear Sweep Voltammetry

Linear sweep voltammetry (LSV) is a voltammetric method that measures the current at the working electrode while the potential between the working and a reference electrode is linearly swept in time. A measure of the current signal is denoted by a peak or trough that is formed at the potential where the species begins to be oxidized or reduced. Linear sweep voltammetry is a general term applied to any voltammetric method in which the potential applied to the working electrode is varied linearly in time. These methods would include polarography, cyclic voltammetry, and rotating disk voltammetry. LSV is similar to CV except that the potential range is scanned starting at the initial potential and ending at the final potential whereas in CV the direction of the potential scan is reversed at the end of the forward scan, and the potential range is scanned again in the reverse direction. In the case of CV the potential changes as a linear function of time and

the rate of change of potential with time is referred to as the scan rate.

1.2.2.2 Electrocatalysis Using Voltammetry

Electrocatalysis using voltammetric techniques is characterized by current enhancement and/or a potential shift to lower values in the case of CV and SWV. Scheme 1.1 shows the basic mechanisms through which electrocatalytic reactions operate at electrodes modified with a catalyst (such as SWCNT-PABS, MPCAuNP or MPc as studied in this project).

The catalyst is first oxidized, which then interacts with the analyte leading to the formation of the oxidized analyte and regeneration of the catalyst [19,20]. Electrocatalysis amplifies the detection signal of an analyte resulting in faster electrode reactions at a lower potential in comparison to the bare (unmodified) electrode. Lowering of detection potentials minimizes interferences from co-existing electroactive species. Chemically modifying the electrodes improves their electrocatalytic current necessary for sensitive detection of target analytes using cyclic voltammetry, square wave voltammetry or chronoamperometry.

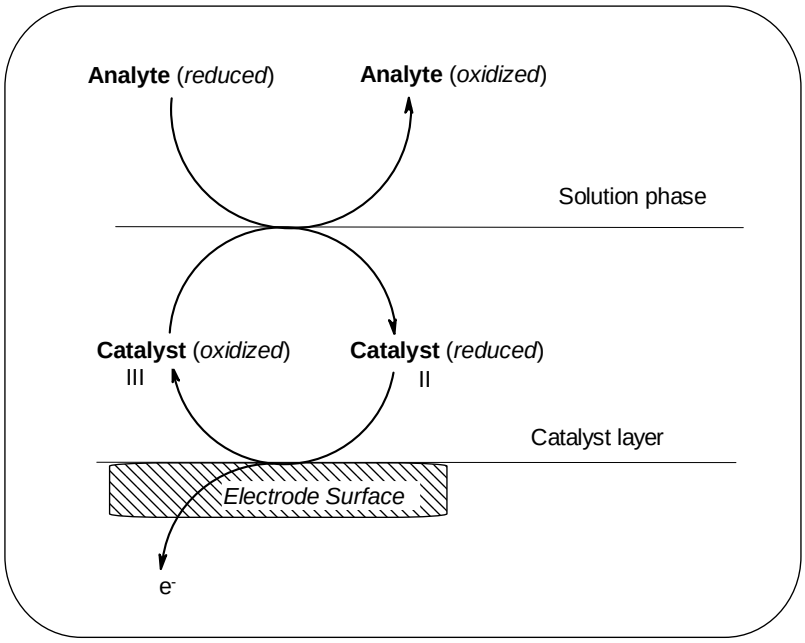

Scheme 1.1: Generalized schematic representation of electrocatalysis at an electrode modified with a catalyst.

1.2.3 Electrochemical Impedance Spectroscopy

Electrochemical Impedance Spectroscopy (EIS) is a very versatile electrochemical tool used to investigate the electrochemical properties of systems and their interfaces with conductive electrodes [21]. It is an effective technique for interrogating the kinetics at interfaces and distinguishing between the various mechanisms that govern charge transfer [21-23]. EIS can be used in various applications, however, this work focuses on its ability to characterize thin film formation and hence determine its electron transport properties.

Basics of impedance spectroscopy

The principle of impedance stems from the alternating current theory that defines the response to an alternating current or voltage as a function of frequency [21]. Impedance is the opposition to the flow of alternating current in a complex electrical system and is measured by applying a sinusoidal potential, V (t), of small amplitude to an electrochemical cell and measuring resultant sinusoidal current, I (t), through the cell [21,24]. The applied sinusoidal potential and resulting sinusoidal current are represented as a function of time. These measurements are done over a suitable frequency range and the results can be related to the physical and chemical properties of the material [21,25]. The relationship is shown in Equation 1.16:

$$Z = \frac{V(t)}{I(t)} \qquad 1.16$$

where V (t) is the sinusoidal applied voltage at time t, $V(t) = V_o \sin \omega t$ where V_o is the maximum potential amplitude, ω is the radial frequency (in rad s^{-1}) and can be related to frequency f (Hz) as $\omega = 2\pi f$. However, the current response is only sinusoidal if the voltage amplitude is small relative to 59 mV, and centered at the OCP. At the same frequency as the applied sinusoidal potential the current

response I(t) is also sinusoidal but with a shift in phase, $I(t) = I_o \sin(\omega t + \theta)$, where I_o is the maximum current applied and θ represents the phase shift by which the voltage lags the current [3,21] as depicted in Figure 1.7 (a). The impedance is a vector quantity with magnitude and direction. The magnitude of impedance is Z (V / I) and the direction is represented as a phase angle, θ as shown in Figure 1.7 (b). Impedance can be represented by Equation 1.17:

$$Z = Z' + jZ'' = Z_{real} + jZ_{imaginary} \qquad 1.17$$

where Z' and Z'' are the real and imaginary parts of the impedance, respectively and j is a complex number [24].

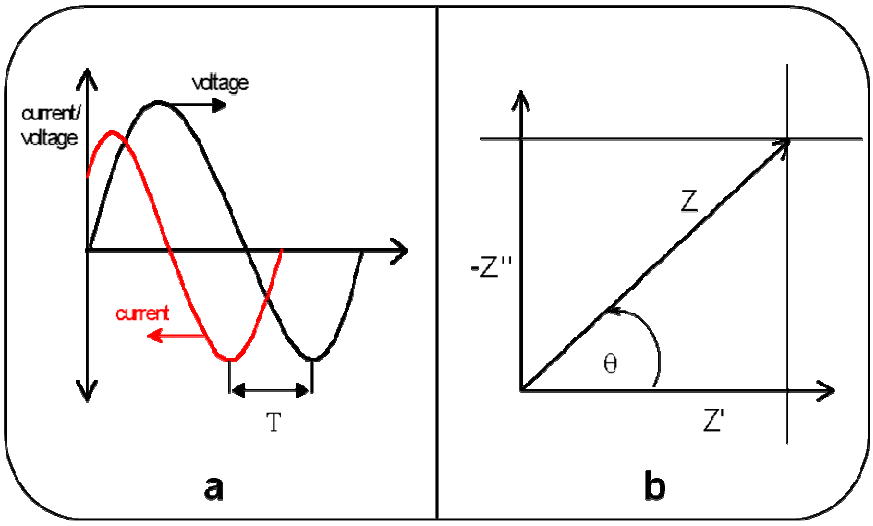

Figure 1.7: (a) Applied sinusoidal voltage and resulting sinusoidal current response. (b) Vector representation of real Z' and imaginary Z'' parts of impedance (Z) [21,24].

Data representation of EIS

Impedance data can be analysed using equivalent circuits i.e. circuits that "fit" the impedance data with the least possible error percentage. The impedance data were fitted to an equivalent circuit using the FRA software package for complex non-linear least squares calculations based on the EQUIVCRT programme. Within the circuit, simple electric elements such as resistors and capacitors, measuring resistance and capacitance respectively, are connected to model the electrochemical process [21,24]. The resistance in the circuit is an indication of the electrical conductivity of the electrolyte and the constant phase element (CPE) results from the charge which is in excess at the electrode-electrolyte interface. Ideal Randles equivalent circuit involves double layer (C_{dl}) as shown in Figure 1.8 (a), while modified Randles circuit uses CPE as illustrated in Figure 1.8 (b). CPE is for real, practical situations. CPE may occur as a result of several factors [21], including (i) the nature of the electrode (e.g., roughness and polycrystallinity), (ii) distribution of the relaxation times due to heterogeneities existing at the electrode/electrolyte interface, (iii) porosity and (iv) dynamic disorder associated with diffusion. The impedance of CPE is given as [21]:

$$Z_{CPE} = \frac{1}{[Q(j\omega)^n]} \qquad 1.18$$

where Q is the frequency-independent constant relating to the surface electroactive properties, ω is the radial frequency, the exponent n arises from the slope of the bode plot; log Z vs. log f (and has values $-1 \leq n \leq 1$). If n = 0, the CPE behaves as a pure resistor; n = 1, CPE behaves as a pure capacitor, n = −1 CPE behaves as an inductor; while n = 0.5 corresponds to Warburg impedance (Z_w) which is associated with the domain of mass transport control arising from the diffusion of ions to and from the electrode|solution interface.

The Randles equivalent circuit may be employed to "fit" the electrochemical impedance data depending on the nature of the impedance data. There are numerous circuits that can be assembled in order to provide the most accurate "fit". An indication of the correct circuit that may be used to fit the data is given by the graphical representation of the impedance data referred to as the Nyquist plot. The Nyquist plot ($Z_{imaginary}$ vs. Z_{real}) shown in Figure 1.9 a displays a characteristic semi-circle at high frequencies and a straight line at low frequencies, corresponding to kinetic and diffusion processes, respectively, where The described spectra is generally fitted using the Randles equivalent circuit of mixed kinetic and diffusion control, where the resistance of the electrolyte and electrode contacts, R_S is connected in series to the parallel combination of charge-transfer resistance R_{CT} (domain of kinetic control) and CPE. The resistance to

charge-transfer is proportionally related to the diameter of the semi-circle of the nyquist plot. In some systems the reaction rate might be controlled by transport phenomenon and this effect needs to be taken into consideration, the measured impedance can be explained by the component that depends on the conditions of the transport or diffusion of ions to the electrode interface from the bulk of the electrolyte [21,24]. This component is known as the Warburg impedance (Z_W) (domain of mass transport control) and is connected in series to the charge transfer resistance. In this work, the Randles equivalent circuit was predominantly used to fit the electrochemical data.

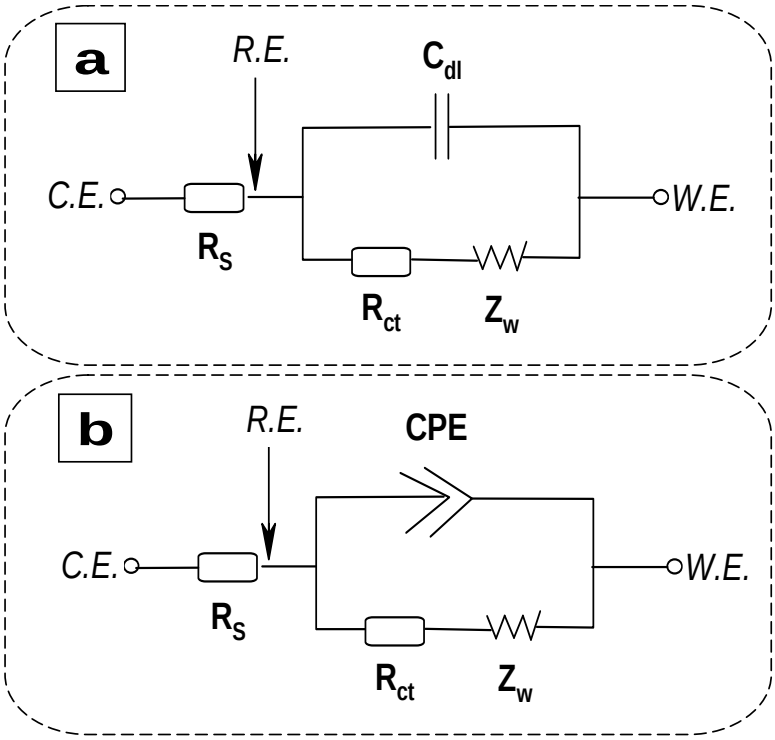

Figure 1.8: Modified Randles equivalent circuit representing the electrochemical system in (a) Ideal situation and (b) Real, practical situation.

Impedance data can also be graphically represented by bode plots shown in Figure 1.9 (b) [21,25]. From the plot of phase angle (θ) vs. logarithm of the frequency (log. f), the peak height represented the capacitive nature of the electrode surface and the relaxation process of the electrode|solution interface is indicated by the phase angle and frequency values respectively. A phase angle of 90° implies the material on the electrode surface displays pure capacitance, whereas a value of less than 90° indicates a more pseudo-capacitive behaviour [24]. As mentioned above, the capacitive nature of the electrode surface is also attained from the value of the slope from the plot of the log. |Z| vs. log f (Fig. 1.9 b).

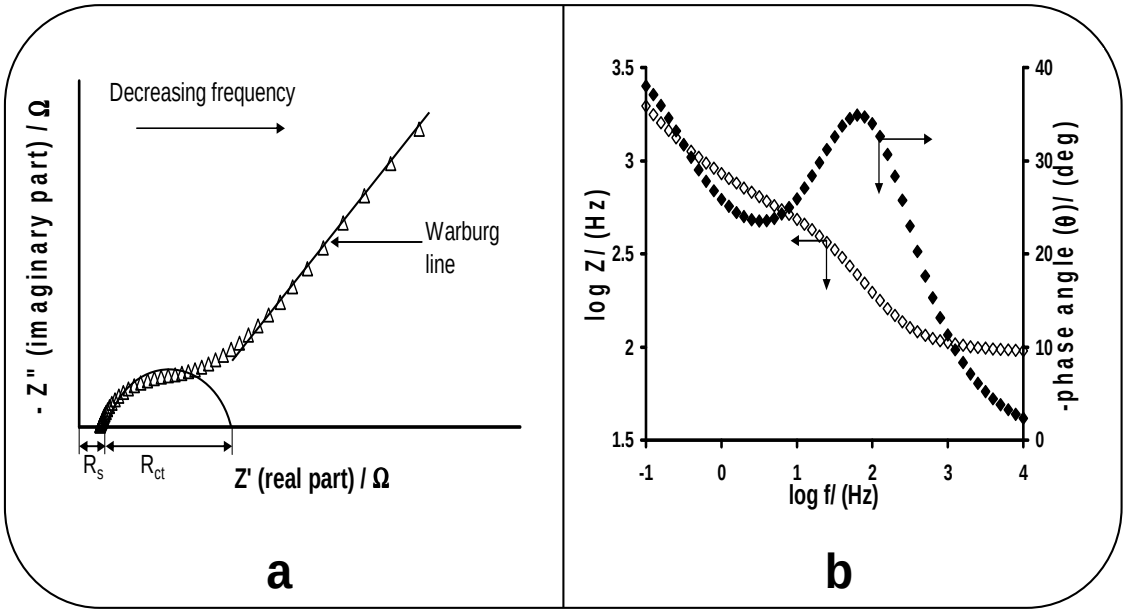

Figure 1.9: Nyquist plot (a) and Corresponding bode plot (b) for the randles equivalent circuit.

Electrochemical impedance spectroscopy offers several advantages over other techniques, these include: (i) the capacity of the system to remain at equilibrium due to the use of low amplitude-sinusoidal voltage (~ 5 mV), (ii) the ability to obtain accurate, reproducible measurements, (iii) the capability of this technique to adapt to various applications, (iv) characterize interfacial properties in the absence of redox reactions and (v) rapid acquisition of data such as ohmic resistance, capacitance, film conductivity, as well as charge or electron transfer at the electrode-film interface.

An electrode-film interface is a result of the electrode modification with electron transfer mediators such as carbon nanotubes or redox active nanomaterials in order to overcome the sluggish electron transfer behaviour at the bare electrode. The following section describes a few regularly used electrode modification techniques.

1.3 Modified Electrodes

According to International Union of Pure and Applied Chemistry (IUPAC) [26], a chemically modified electrode (CME) can be defined as "an electrode made of a conducting or semi-conducting material that is coated with a film of a chemical modifier and that by means of Faradaic (charge transfer) reactions or interfacial potential differences (no net charge transfer) exhibits chemical, electrochemical, and/or optical properties of a film." In other words, if a specific material is attached to the surface of an electrode then that material imparts on the electrode some chemical, electrochemical or desirable properties not available at the unmodified electrode [27-29]. However, the material first needs to be immobilized onto the surface of the electrode.

1.3.1 General Methods of Modifying Electrode Surfaces

There are numerous techniques that may be used to modify electrode surfaces. A few are listed below.

Covalent Bonding

This method employs a linking agent (e.g. an organosilane) to covalently attach one of several monomolecular layers of the chemical modifier to the electrode surface [30-31].

Drop-dry Coating (or solvent evaporation)

A few drops of the polymer, modifier or catalyst solution are dropped onto the electrode surface and left to stand to allow the solvent to dry out [32].

Dip-dry Coating

The electrode is immersed in a solution of the polymer, modifier or catalyst for a period sufficient for spontaneous film formation to occur by adsorption. The electrode is then removed from solution and the solvent is allowed to dry out [33].

Composite

The composite electrode is prepared by a simple impregnation of the bulk electrode material with a chemical modifier such as an MPc catalyst. A good example is the popular carbon paste electrode [34].

Spin-Coating (or spin-casting)

This method involves evaporating a drop of polymer, modifier or catalyst solution from an electrode surface by using centrifugal force at high-speed rotations. For example, oxide xerogel film electrodes prepared by spin-coating a viscous gel on an indium tin oxide substrate [35].

Electrodeposition

In this method, the electrode surface is immersed in a concentrated solution (~10^{-3} mol L^{-1}) of the polymer, modifier or catalyst followed by repetitive voltammetric scans. The first and second scans are similar, subsequent scans decrease with the peak current. For example, electrochemical deposition of poly(*o*-toluidine) on activated carbon fabric [36].

Electropolymerization

In this technique the electrode is immersed in a polymer, modifier or catalyst solution and layers of the electropolymerized material builds on the electrode surface. Generally, the peak current increases with each voltammetric scan such that there is a noticeable difference between the first and final scans indicating the presence of the polymerized material. For example, electropolymerization of aniline on polyaniline modified platinum electrodes [37].

Langmuir-Blodgett Technique

This technique involves transferring the ordered monolayer or multilayer film formed at the air/water interface onto the electrode surface [38].

Chemisorption

In this method, the chemical film is strongly and ideally irreversibly adsorbed (chemisorbed) onto the electrode surface [30]. Electrode modification using self assembled monolayer falls into this category.

1.3.2 Self-Assembly

Smart immobilisation of ultrathin solid films of nanomaterials on solid surface has continued to attract major research interests because of the potential to open up a wide range of diverse novel technological and engineering applications. In this regard, immobilisation of materials on electrode surfaces, using the conventional self-assembly strategy [39] to form molecular monolayers and its related layer-by-layer self-assembly [40] to form molecular multi-layers have continued to receive considerable attention. Self-assembly method is advantageous because of its simplicity and control of the order of materials build-up which might allow synergic relationship between the materials towards specific purposes.

1.3.2.1 Self-Assembled Monolayer-Modified Electrodes

The self-assembled monolayer (SAM) may be described as the ordered arrangement of spontaneously adsorbed molecules (such as

thiol species) from solution directly onto the surface of an appropriate substrate (such as gold) resulting in the formation of an ultrathin film [1,41]. In 1946, four decades after Langmuir [42] introduced the concept of monolayers, Zisman [43] demonstrated the self-assembly of alkylamine monolayers onto a platinum substrate. Since then a number of adsorbate/substrate SAM forming combinations have been found that are able to form SAMs e.g., alkyltrichlorosilanes on glass [44] and fatty acids on metal oxides [45]. In 1983, Allara and Nuzzo [46] showed the adsorption of sulphur-containing compounds onto gold surfaces. However, it was only after the numerous articles published in 1987 and 1988 that there was an influx of thiol based SAM research [47-50]. Since then the fabrication of ultrathin, well-ordered self-assembled monolayer films of thiol-derived organic molecules on gold substrates have been a major research interest due to the potential ability of such ultrathin films to be used as scaffolds in a plethora of nanotechnological applications and fundamental studies including the immobilization of biomolecules (e.g., proteins, DNA) and redox-active functional materials for catalysis and sensing. For example, several potential applications of carbon nanotubes mean that some of their future applications in catalysis, sensing and electronics will require their integration on solid substrates as ultrathin nano-scaled molecular films.

Sulphur containing compounds (eg. thiols) have a high affinity for gold and are used in the self assembly formation of the base monolayer on gold surfaces. Cysteamine is one such example which also allows for the covalent attachment of other species. In 1997, Caruso *et al.* [51] introduced a 2-dimethylaminoethanethiol (DMAET) SAM as a platform for integrating DNA on gold surfaces. Since then, no work has been reported on this important SAM. This motivated me to use this innovative SAM as a potential base monolayer for forming multilayer films. However, successful future applications of DMAET SAM is dependent on thorough understanding of the state of the amino head group from which further surface functionality can be derived. Therefore, in this work, I have used cyclic voltammetry and electrochemical impedance spectroscopy to probe the behaviour of the $-NH^{+}(CH_3)_2$ head group of DMAET SAM in solutions containing outer-sphere redox probe ($K_4Fe(CN)_6$ / $K_3Fe(CN)_6$), different electrolytes and epinephrine.

From an electrochemistry point of view, the chemisorption of thiolates on gold depicted in Figure 1.10 is regarded [1] as the most important class of SAMs. The nature and the formation of the bond between gold surface and the thiol has been a subject of much interest [1,52-55] but it is often recognised that the gold-thiolate bond results from cleavage of the S-H bond. Gold substrates are preferred in thiol

SAMs because of the strong interaction between gold and sulphur that allows the formation of monolayers in the presence of many other functional groups [54]. Generally, the central feature of all SAMs is the strong interaction between the functional group of the adsorbate and the bare substrate as well as the van der Waals interactions among the adsorbed molecules [1].

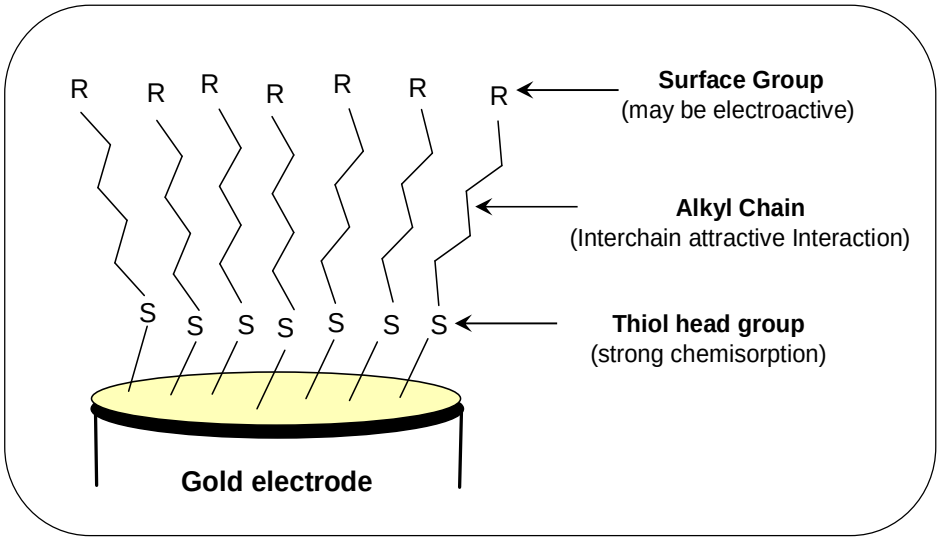

Figure 1.10: Representation of a thiolate on gold SAM.

The self-assembling technique offers several advantages over other film formation techniques which include:

(a) Spontaneous adsorption onto the electrode surface resulting in the formation of a thermodynamically equilibrated final film structure.

(b) The SAM film does not readily undergoing desorption as a result of the sulphur-gold bond.

(c) The adsorbate does not have to be compatible with water like in the case of the Langmuir-Blodgett technique.

(d) The cost effectiveness of the fabrication process because it does not require expensive equipment.

(e) The orientation of the film (lying flat or standing perpendicular to the substrate) can be controlled, for example the formation of mixed monolayer.

Additional molecular material may be added onto the primary monolayer by means of the layer-by-layer technique.

1.3.2.2 Layer-by-layer Self Assembly

One of the elegant means of forming ultrathin films on solid substrates is the self-assembly used in forming molecular monolayers, and the layer-by-layer (LBL) self-assembly for forming molecular multi-layers. LBL has recently been elegantly reviewed by Zhang *et al.* [56]. LBL, first discovered in 1966 by Iler [57] and re-discovered in 1991 by Decher and Hong [58,59] may simply be described as controlled coordination or stepwise self-assembly strategy based on the alternating adsorption of materials containing complementary charged or functional groups to form integrated, well-organized arrays of ultrathin superstructure films on solid surfaces [56] that are often less than 1 μm [60,61], on solid surfaces. This strategy could provide a

powerful bottom-up approach for the construction of nano-scaled 3D architectures with various properties. Indeed, the simplicity and versatility of this technique makes it admirable for producing high quality and consistent films.

After the introduction of the LBL technique based on physical adsorption driven by ionic attraction, other LBL methods emerged. Some of which were based on hydrogen bonds, step-by-step reactions, sol–gel processes, molecular recognition, charge-transfer, stepwise stereocomplex assembly and electrochemistry [56]. This work concentrates on the LBL method that uses electrostatic interaction as the main driving force. The basic principle in the assembly is "charge reversal", where oppositely charged material referred to as bilayers are successively adsorbed. Each bilayer is approximately 1-100 nm thick [62] and can be tailored by adjusting the pH [63], counter ion [64], ionic strength [65], chemistry [66], molecular weight [67] and temperature [68]. The original construction of these multilayer films involved the use of polyelectrolytes, and thereafter extended to conjugated polymers [69-71], nanomaterials [72,73], dye and drug crystals [74], organic latex particles [75], inorganic particles [76], protein [77], biological cells [78], DNA [79], antigen-antibody pairs [80], CNTs [81] metallophthalocyanines [82] and monolayer-protected-clusters of gold

[83]. This LBL technique produces high quality and consistent films that have a few advantages over other multilayer fabrication processes.

(a) The fabrication of multilayers is a simple method that does not require the use of complicated instruments.

(b) The deposition times and material used during the process are user controlled.

(c) The prospect of adjusting the layer thickness at the nanometer scale results in improved control of the mechanical properties.

(d) Increased versatility of applications subsequent to the development of LBL methods based on intermolecular interactions other than electrostatic.

Furthermore, the LBL assembly does not require only planar substrates as demonstrated by the step-wise build up on a spherical template [84]. However, it does require a surface with the lowest possible roughness since roughness leads to an assembly with poor uniformity and far less stability to electrochemical cycling [85] which inevitably has an adverse affect on the applications.

This relatively new technique already has applications [86] in a few areas which include drug and gene delivery, fuel cells, electrical conductors, photo-detection, biosensing and electrochemical sensing devices. However, this dissertation concentrates on the fabrication of electrochemical sensors via electrostatic interaction using either the

self assembly or layer-by-layer assembly processes to incorporate carbon nanotubes, monolayer-protected clusters of gold nanoparticles and MPc complexes.

Given the plethora of potential technological applications of CNTs and MPc complexes and their hybrids, an emerging area of research is on the smart integration of CNTs with MPc complexes for enhancing electrocatalysis and sensing. Reports on the CNT-MPc nanohybrids or thin films have shown these nanohybrids to be more efficient in improving electrochemical responses compared to the bare electrode or the individual CNT or MPc species [87-91]. To improve the physico-chemical properties of MPc complexes for potential nanotechnological applications, continued investigation on their nanostructures are essential. Although there are reports on the self-assembled monolayers (SAMs) of electroactive MPc complexes [92-95] and their CNT hybrids [20], there are limited studies on the use of LBL for electroactive MPc complexes. Indeed, the few reports on LBL involving MPc complexes have been those of Oliveira and co-workers [96-99] who only reported the LBL multilayer films of polyelectrolyte cations with the popular and commercially-available, water-soluble tetrasulphonated MPc complexes using ITO based electrode.

Transition metal tetrasulfophthalocyanine complexes, notably iron (II) tetrasulfophthalocyanine (FeTSPc), are highly water-soluble

species and well recognized for their high catalytic activity in homogeneous electrocatalysis. The ease with which they are washed away from electrodes during electrochemical studies has long been a major setback and has limited their fundamental studies and potential applications for heterogeneous electrocatalysis in aqueous environment. To date, all available reports on the surface-confinement of water-soluble metallotetrasulfophthalocyanine (MTSPc, where M = central metal ion) complexes involved indium tin oxide (ITO)-coated glass electrodes and LBL strategy using polycationic and/or highly-branched polymeric complexes such as polyamidoamine (PAMAM) dendrimers [97], poly(diaallyldimethylammonium chloride) (PDDA) incorporating poly(2-(methacryloxy)ethyl)trimethylammonium chloride (PCM), poly(3,4-ethylenedioxythiophene) (PEDOT) and poly(4-styrenesulfonate) (PSS) [100], chitosan [98] and PAMAM [99]. Bedioui and co-workers [87] reported the use of drop-casting to immobilize slurry of nickel (II) tetrasulfophthalocyanine (NiTSPc) and SWCNTs onto a glassy carbon electrode (GCE). The most common feature of the LBL strategies includes the use of a cocktail of relatively expensive reagents and the confinement of the MTSPc inside the thick multi-layered polymeric films. The main problems usually associated with physical anchorage (i.e., drop-casting method) of such films onto a GCE surface are poor stability as well as the difficulty in controlling the

amount of film or thickness deposited. These problems have the tendency to compromise on the application of the films. Therefore, it is without doubt very crucial to continue the search for other means of immobilizing them onto electrode surfaces as thin stable solid films without compromising on their electrocatalytic activity towards the detection of analytes in aqueous conditions. More importantly, integrating such water-soluble redox-active MPc complexes with CNTs (as electron transfer mediators) could provide an interesting synergistic means of further enhancing the electron transfer dynamics of MPc complexes.

In this study, using positively-charged 2-dimethylaminoethanethiol monolayer as the base co-ordinating species I show for the first time, the integration of: (i) nanostructed iron (II) phthalocyanine with (a) SWCNT-*poly* (m-amino benzene sulfonic acid); (b) monolayer-protected clusters of gold nanoparticles and (ii) sulfonic acid functionalized iron (II) phthalocyanine with SWCNT-*poly* (m-amino benzene sulfonic acid), singly or mixed immobilization onto gold electrode via. electrostatic interaction either by the conventional self-assembly or the related layer-by-layer assembly strategy. The electron transfer dynamics of such electrodes were interrogated as well as their catalytic properties towards the detection of epinephrine and hydrogen peroxide as analytical probes.

The following three sections further summarize the structure, properties and applications of carbon nanotubes, phthalocyanines and monolayer-protected clusters of gold nanoparticles.

1.3.3 Carbon Nanotube Modified Electrodes

Historical Perspective

The frequently used phrase *"since the discovery of carbon nanotube by Iijima in 1991…"* is a common misconception. A recent editorial by Monthioux and Kuznetsov [101], show that the first Transmission electron microscopy (TEM) images of hollow carbon filaments with a nano-sized diameter were published in 1952 by two Russian scientists, Radushkevich and Lukyanovich [102]. The images of the nano-sized carbon filaments were regarded to be of multi-walled tubular nature but, unfortunately due to the cold war, Russian scientific publications were not easily accessible. Therefore, it is argued that may be they should be credited with the discovery of "carbon nanotubes". However, it is worth mentioning, the concept of forming carbon filaments (through thermal decomposition of gaseous hydrocarbon) was envisaged as early as 1889 [103]. In fact, Iijima's "rediscovery" [104] was at the back of a couple of "carbon nanotube" related reports [102,105]. In 1978, Wiles and Abrahamson [105] grew fine fibres as small as 4 nm in diameter (viz. nanotubes) on graphite and carbon anodes. Nevertheless, Iijima's rediscovery created tremendous impact in the scientific world, probably because it was published in a top-ranked journal that was available to all scientists or perhaps the scientific community was finally ready to accept the concept of *"nano"*

in the 1990s. He reported needle-like tubes (fullerene related structures which consist of graphite cylinders closed at either end) while investigating material deposited on the cathode during the arc-evaporation synthesis (Fig. 1.11a) of fullerenes. It was later shown that by varying the conditions of the arc discharge method nanotubes could be produced in bulk quantity [106, 107]. In 1993, Iijima and Ichihashi [108] were unquestionably the first to discover single-walled carbon nanotube. Later that year Yacaman *et al*. [109] used a new technique known as chemical vapour decomposition (CVD) to report the catalytic growth of CNT (Fig. 1.11c) and in 1996 Smalley and co-workers [110] reported the synthesis of bundles of aligned SWCNT by use of the laser-ablation technique (Fig. 1.11b).

From the discoveries made, CNTs are commonly categorised as either SWCNTs or MWCNTs. However, today it is possible to have double walled CNTs [112]. SWCNT shown in Figure 1.12 (a) is essentially formed by rolling a single graphite sheet into a seamless tube capped at each end by half-spherical fullerene structures [113]. They have a diameter of approximately 1-2 nm and a tube length that can be thousands of times more.

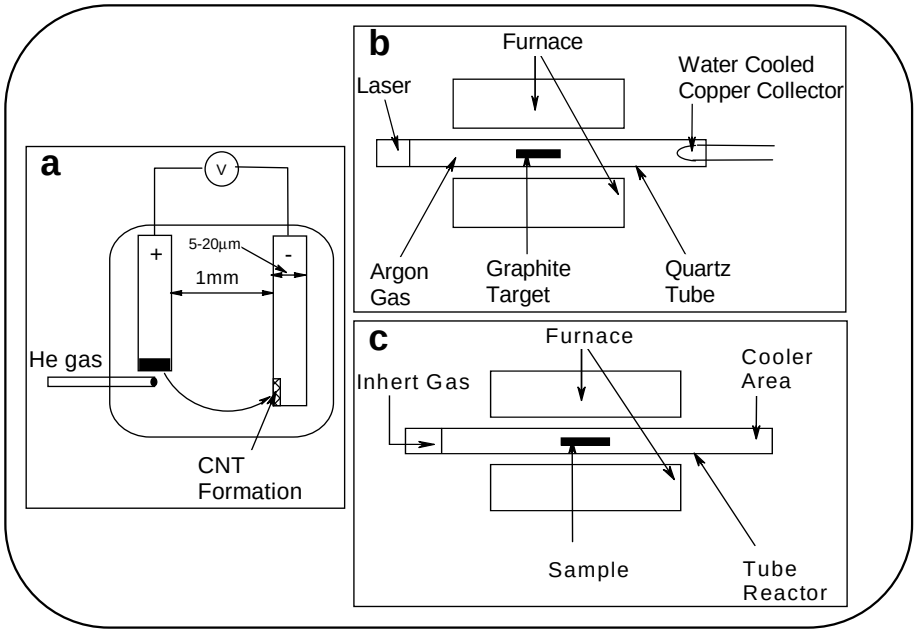

Figure 1.11: Experimental arrangement for synthesizing carbon nanotubes via. (a) Arc-discharge (b) Laser-evaporation (c) Catalytic growth by decomposition of hydrocarbon gas [111].

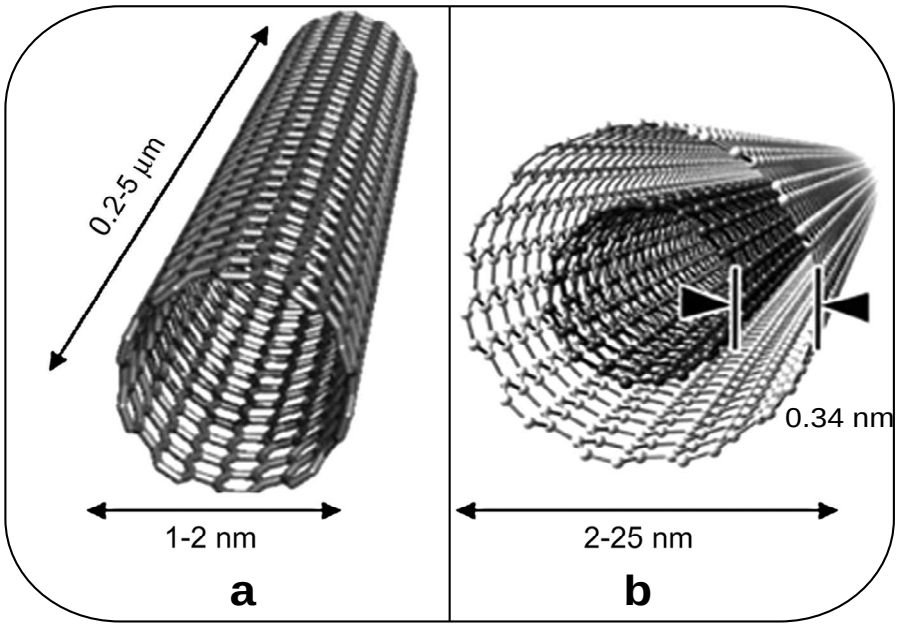

Figure 1.12: Illustration of (a) Single-walled carbon nanotube and (b) Multi-walled carbon nanotube [114(a)].

MWCNT represented in Figure 1.12 (b) comprises of numerous concentric cylinders fitted one inside the other. The number of tubes range from 2-50 graphite cylindrical sheets, with the tubes separated by a distance of 0.34 nm and the innermost tube having a diameter of approximately 1-2 nm [104].

The work described in this dissertation is based on SWCNTs which has received considerable attention for nearly two decades and continued to be investigated as viable electrochemical materials because of their unique properties [111,114-125]. SWCNTs have certain special features over the MWCNTs including smaller size, larger specific area, stronger adsorptive properties and inter-tube attraction [111]. In addition, its characteristic curve-shaped surface enables bonding of supramolecular complexes via non-covalent or hydrophobic interactions [126]. However, in the synthesis process, unlike MWCNTs, SWCNTs requires the use of catalysts [111].

Structure

Carbon nanotubes consist of sp^2 carbon units and the arrangement of the carbon-atom hexagons are in a helical fashion with respect to the needle axis [104]. The three most common structures of carbon nanotubes represented in Figure 1.13 are the (a) armchair, (b) zig-zag and (c) chiral forms. While carbon nanotubes are not actually formed

by rolling graphite sheet (graphene) into a tube, the concept can be used to explain the different structures by considering the manner in which graphene might be rolled into tubes. The above mentioned structures can be described by the manner in which the graphene is rolled about the T vector represented in Figure 1.14. Formation of the armchair structure occurs when the graphene is rolled about the T vector parallel to C-C bonds of the carbon hexagons while the zigzag and chiral structures are as a result of the T vector having different orientations except parallel to the C-C bonds [110,111]. This implies that chirality of the tubes is dependent on the direction in which the graphene is rolled in respect to the T vector. The manner in which the graphene is rolled also determines if the CNT is metallic, semi-metallic or semi-conducting [127,128].

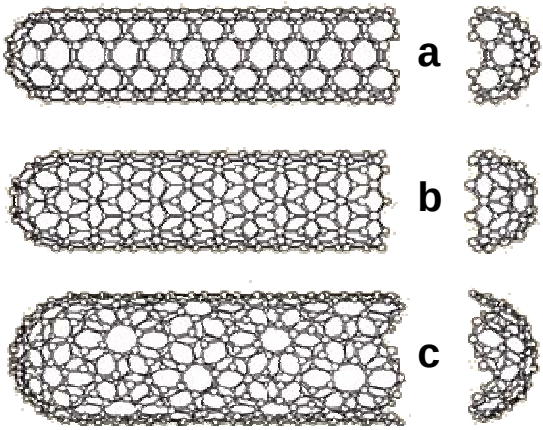

Figure 1.13: Illustration of possible carbon nanotubes structures: (a) Armchair (b), Zigzag and (c) Chiral forms [111].

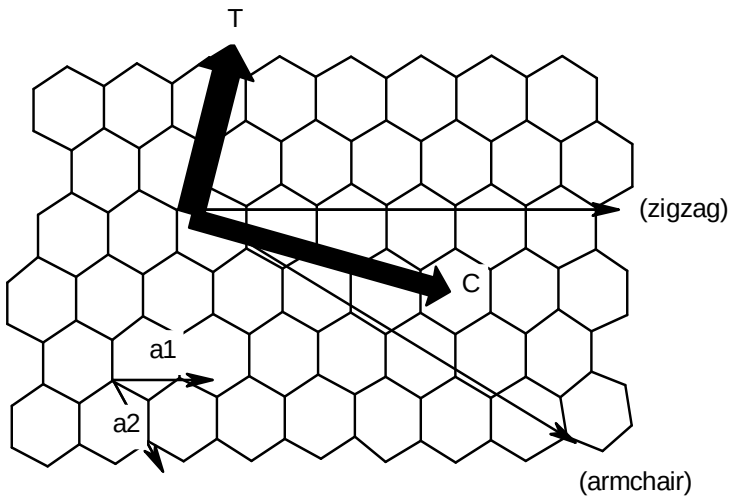

Figure 1.14: Representation of the helical arrangement of an unrolled graphite sheet that can be used to explain carbon tube structures [107]. a_1 and a_2 are the basis vectors of the graphene sheet while C is the circumferential vector.

Pristine CNT can exist as any of these forms. However, functionalization of CNTs is usually required for attachment of CNT to other materials or devices in order to maximise its full potential in various applications. Ever since Smalley's laser-oven functionalization technique [110], there have been numerous reports underlining functionalized CNT modification [129-134]. Functionalization is important to improve solubility [134], especially for potential applications in biology and material science and also to permit the unique properties of carbon nanotubes to be coupled to those of other materials [135]. Carboxylic group [129], fluorine [130], amino [131], alkyl groups [132] and sulfonic groups [133] are a few examples of some of the groups that can

be functionalized on carbon nanotubes. In this work, I used SWCNT-*poly* (m-amino benzene sulfonic acid) (SWCNT-PABS).

Properties

Carbon nanotubes has been one of the most extensively studied materials since its "re-discovery" in 1991 owing predominantly to their plethora of properties. One of their most admirable properties due to their limited atomic defects [114(b)] is their ability to demonstrate tremendous mechanical strength [115,116]. In fact, the tensile strength (a measure of the amount of stress required to pull a material apart) of carbon nanotube is approximately 45 billion pascals, which is roughly 20 times more than the tensile strength of steel [111]. Other unique properties of carbon nanotubes include elasticity [116], high thermal conductivity [117(a)], electronic and vibrational properties [117(b)], field emission [118], electrochemical properties [119], optical [120], magnetic [121], photophysical properties [122], morphological and rheological properties [123], pseudocapactive properties [124], ion storage [125] and a high surface area [110] to mention but a few. These properties are often applied to find new applications for carbon nanotubes.

Applications

Since Iijima's rediscovery in 1991, there has been a substantial increase in reports involving CNT investigations (Fig. 1.15) which include over one thousand review articles. A steady increase at an average of ~20% increase per annum means the number CNT publications will exceed 11000 by 2010. The unusual properties of carbon nanotubes have made it possible to frequently find new applications in different fields.

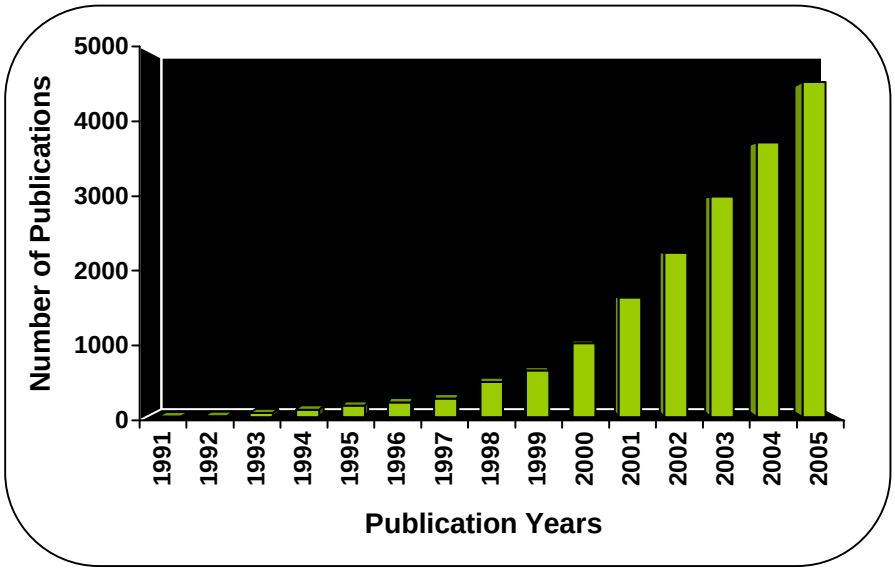

Figure 1.15: 3-D histogram depicting the number of publications concerning carbon nanotubes from 1991-2005 [136].

Some of the applications of carbon nanotubes include their use in the development of artificial muscles [137], as a substitute for the graphite anode in lithium ion batteries [138], as catalyst support in proton-exchange membrane, hydrogen/oxygen and methanol fuel cells

[139-142], battery technology [143], superconductors [144], supercapacitors [145], hydrogen energy storage [146], field-effect transistors [147], catalyst support [148], electronic devices [149], nanotweezers [150] electrochemical energy device [151], ultra high-strength engineering fibers [152], and quantum wires [153], drug and gene delivery systems [154-157], acoustic actuators (speakers) [158], tips for scanning probe microscopy [159], logic circuits in computers [160], chemical sensors [161-163] etc. However, the emphasis here is on the fabrication of electrochemical sensors using carbon nanotubes.

Electrochemical sensors represent a subclass of chemical sensors in which the electrode used meets the size, cost and power requirements. The ability of CNT based electrodes to function as electrocatalysts permit them to operate as electrochemical sensors [164]. In 1996, Britto and co-workers [119] were the first to show that the important neurotransmitter, dopamine could be electrocatalytically oxidised using multi-walled carbon nanotubes modified onto glassy carbon electrodes. A few years later, they used MWCNT microelectrodes in the study of electrocatalytic reduction of dissolved oxygen [165]. In 1997, Davis *et al*. [166] immobilized cytochrome C and azurin proteins on nanotubes to demonstrate the ability of carbon nanotube modified electrodes to act as biosensing devices. In 2001, Li and co-workers [167] catalysed the electrochemical reaction of

dopamine, epinephrine and ascorbic acid using carboxyl terminated single-walled carbon nanotubes cast on glassy carbon electrode. The electrocatalytic ability of carbon nanotubes membranes [168], carbon nanotube paste electrodes [169] and carbon nanotubes modified platinum [170] and gold electrodes [171,172] have also been investigated. Other analytes that have been investigated using carbon nanotube based sensors include 3,4-dihydroxy phenylacetic acid [173], nitric oxide [174], NADH [175], serotonin [176], carbohydrates [177], tinidazole [178], DNA [179], homocysteine [180], insulin [181], TNT [182], nucleic acids [183], glucose [184], pesticides [185] and hydrogen peroxide [186]. The performances of these electrodes were found to be superior to other carbon electrodes in terms of promoting electron-transfer and improving reversibility. Nowadays the ability to modify carbon nanotubes with a functional group of interest and use it for the electrochemical detection of any known or unknown analyte is restricted only by the imagination of the electrochemist.

An emerging area of research is on the smart integration of CNTs with metallophthalocyanine (MPc) complexes (to be discussed in the following section) for enhancing electrocatalysis and sensing. Several reports have shown CNT-MPc nanohybrids to be more efficient in improving electrochemical responses compared to the bare electrode or the individual CNT or MPc species [87-95,187-200]. The surprisingly few

reports on LBL assembled MPc-CNT films has prompted me to further investigate the electron transport and electrocatalytic behaviour of these self-assembled thin film hybrids.

1.3.4 Metallophthalocyanine Modified Electrodes

Historical Perspective

The first observation of a "phthalocyanine" complex was in 1907 when two German scientists reported the appearance of an unknown blue by-product [201]. Two decades later, researchers from Switzerland tried to convert *o*-dibromobenzene into phthalonitrile but instead synthesized copper phthalocyanine, copper naphthalocyanine and copper octamethylphthalocyanine [202]. In 1928 the "real discovery" of phthalocyanine accidentally occurred during the preparation of phthalimide at the Grangemouth plant of the Scottish Dyes Ltd, which later became part of the Imperial Chemical industries [203]. History has it that during the preparation of phthalimide, a glass lined vessel cracked thereby exposing the reaction to the outer steel casing resulting in the formation of traces of a dark blue impurity in the phthalimide. At the Imperial College, Linstead [204] analyzed these impurities and found it to be iron "phthalocyanine" (FePc), the structure of which was confirmed by Robertson [205,206] using X-Ray diffraction techniques. Linstead named the compound phthalocyanine (*phthalo* from its precursor, 'phthalic acid', and *cyanine* from the greek work 'blue').

Structure and Synthesis

Metallophthalocyanine (MPc) is a planar, 18 π-electron macrocyclic aromatic compound, consisting of four isoindole subunits linked together by aza nitrogen atoms [206,207]. These beautiful bright blue to green coloured materials are biological mimics of the naturally occurring metalloporphyrins but they have extended conjugation due to the benzene rings, hence, improved chemical and thermal stability. The central cavity of its structure (Fig. 1.16a) can enclose any one of 70 metal cations [203] ranging from groups I and II to the lanthanide and actinides [207,208]. Phthalocyanine molecules can also incorporate ring substituents as shown in Figure 1.16 (b). Many of the phthalocyanine properties, example solubility, can be varied by changing the central metal ions and ring substituents [207]. Metallophthalocyanine synthesis is aimed at introducing a metal ion into the central cavity. The synthesis of metallophthalocyanine requires the use of precursors such as phthalic anhydride, diiminoisoindline, phthalonitrile and o-cyanobenzamide [207,209].

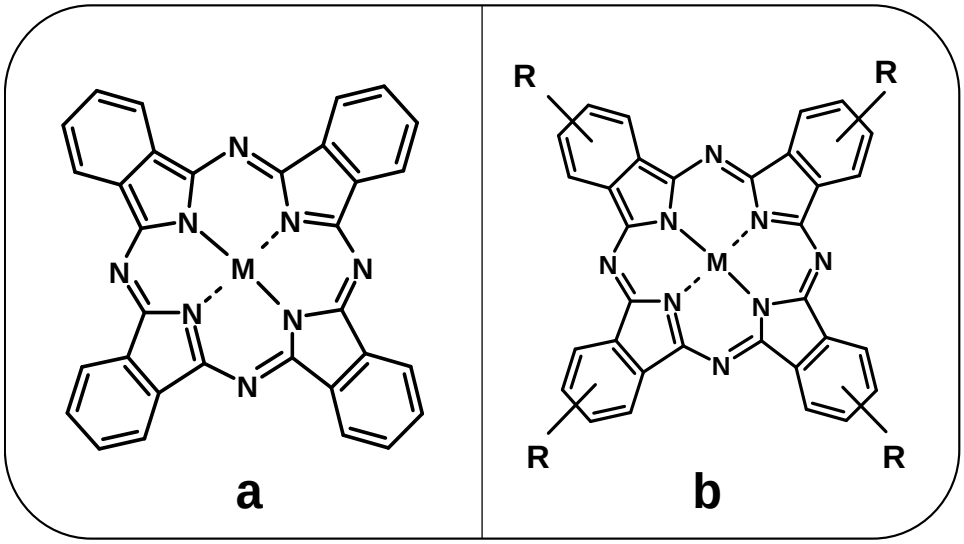

Figure 1.16: The geometric structure of (a) Metallophthalocyanine (b) Metallo-tetraaminophthalocyanine (MTAPc) complex, where M = transition metals (Example: Co, Ni or Fe) and R = (Example: SO_3^{2-}, NH_2, COOH).

Through the years, metallophthalocyanines have established themselves as versatile organometallic complexes with a wide range of excellent properties [210] such as fastness to light, structural, remarkable chemical stability, electronic, optical and beautiful bright blue to green colours etc. However, these properties are size-dependent and can be varied by adjusting the particle size. It is well documented that nanoscopic materials have fundamentally different properties compared to their bulk counterparts [211,212]. The preparation of nanophthalocyanine was first reported in 1991 by two independent groups viz. Saito *et al*. and Enokida *et al*. [213,214]. A few years later nanophthalocyanine was further investigated by Wang *et*

al. [215] using nanoscopic oxovanadium phthalocyanine. They noticed an improvement in photoconductivity and attributed this to the presence of the huge surface area of nanoscopic oxovanadium nanophthalocyanine.

In this study, the electrocatalytic ability of nano iron (II) phthalocyanine (*nano*FePc) and iron (II) tetrasulphonated phthalocyanines (FeTSPc) will be further investigated. It is anticipated that the emergence of new properties for nanoscopic material will enhance the applications of the macroscopic form.

Applications

Phthalocyanines and related complexes have been one of the most researched areas in science over the last century but their renaissance over the last two decades has lead to an exponentially increasing number of publications (Fig. 1.17), especially in the context of emerging nanoscience and nanotechnology. In the last 20 years, number of publications increased at an average of ~20% /5 year period, meaning that if the same growth persists, then by 2010 it could be predicted to be ~10500 publications. As mentioned earlier, phthalocyanines have a wide range of properties and have been used in the past mainly as dyes for jeans and clothing, inks in ballpoint pens and paints for plastic and metal surfaces.

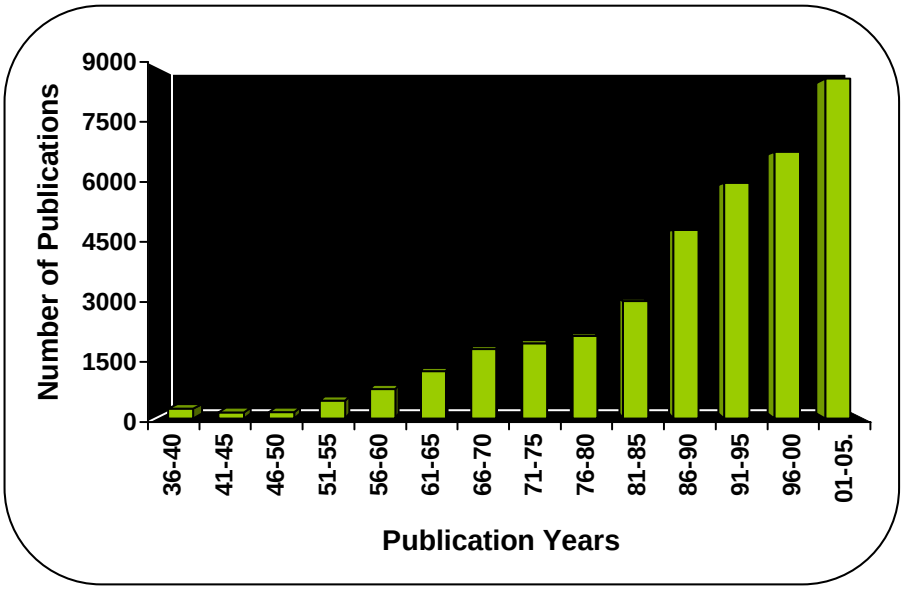

Figure 1.17: 3-D histogram depicting the number of publications concerning phthalocyanines from 1936-2005 [216].

Nowadays they are the molecules of targets for numerous scientific and technological applications in various fields such as catalysis [217-220], sensors [221-223], photodynamic therapy [224-228], ink jet printing [229], electrophotography [229,230], photocopying and laser printing [229,231], electrochromic display devices [232-234], optical computer re-writable discs and information storage systems [235-237], liquid crystal display devices [238], photovoltaic cells [239,240], fuel cells [241], molecular electronics [242], semi-conductor devices [243-245], and electrochemical sensors [187-200]. A recent review by de la Torre *et al*. [216] discusses several reasons for their involvement in some of the above listed applications but the focus remains on the fabrication of

electrochemical sensors using nano iron (II) phthalocyanine and iron (II) tetrasulphonated phthalocyanines.

MPc complexes have the ability to retain their molecular structure and stability upon addition or removal of electrons [246] which enables them to exhibit electrocatalytic activity towards redox reactions. Thus they have established themselves as excellent electrocatalysts for several organic and inorganic analytes [247-251] and have recently been reviewed by Ozoemena and Nyokong [252]. In contrast there has been limited work relating to the electrocatalytic ability of nanostructured MPc complexes [253,254] which is surprising given their potential to enhance the electrochemical response. However, I believe that the electrochemical response can be further enhanced by integrating nanostructured MPc complexes with other redox active material such as SWCNTs and monolayer-protected clusters of gold nanoparticles. Indeed, previous studies [89, 90] have shown it has been shown MPC-CNT hybrids exhibit excellent electrocatalysis and sensing. However, there is no work yet on MPC-MPCAuNP.

1.3.5 Monolayer-Protected Clusters of Gold Nanoparticles Electrodes

Historical Perspective

Solid gold was first extracted in the 5th millennium B.C. in Bulgaria; whereas soluble gold is believed to have been in existence from the 5th or 4th century B.C. when it was used to make ruby glass and for colouring ceramics. The procedure for making gold ruby glass also known as "Purple of Cassius" [255] was described by Andreus Cassius in 1685. Its beautiful colour was often suspected to be a gold tin compound that may have been formed as a result of the starting material used in the preparation process [256]. However, in 1857, Faraday reported the formation of a deep red gold solution when he used white phosphorous to reduce an aqueous solution of chloroaurate ($AuCl_4^-$) and attributed the colour of ruby glass to the minute size of the gold particles [257]. This discovery reiterated a statement made by Kunchel in 1676 [258], where he claimed "gold must be present in such a degree of communition that it is not visible to the human eye". A few years after Faraday's discovery, in 1861, the term colloid [259] was derived to describe dispersion of one substance in another and as a result gold in solution. Colloidal gold, gold colloid or soluble gold was also referred to as gold nanoparticles or nano gold after Norio Taniguchi [260] coined the term nanoparticle in 1974. The term was

used to describe any kind of particle that has at least one dimension in the range of 1 - 100 nm. More than a century after Faraday's initial discovery, Murray and Chen [261] showed it was possible to attach alkanethiols to "gold nanoparticles". A few years later, gold nanoparticles surrounded by a thiol monolayer were termed monolayer-protected gold cluster molecules [262] also known as monolayer-protected clusters of gold nanoparticles (MPCAuNP).

Structure and Synthesis

Gold colloids are routinely prepared by chemical reduction of a suitable gold precursor such as $AuCl_4^-$ ions and there are several reducing agents that can be used to achieve nanoparticles from this precursor. As mentioned earlier, Michael Faraday first used white phosphorous to reduce an aqueous solution of $AuCl_4^-$. Since then there have been several routes using different reducing agents to prepare nanosized gold colloids. However, only two preparation techniques have become well established. One of the most widely used methods is the innovative two-phase Brust-Schiffrin method [263], where aqueous sodium borohydride is used to reduce $AuCl_4^-$ in toluene in the presence of stabilizing thiols. Thiolate ligands are attached to provide superior stability. The strong interaction between the sulphur of the thiolate ligands and the gold facilitates the formation of a protective shell

around the particle which is responsible for this stability.The other reliable method is the older Turkevich synthesis [264], where gold salt is boiled together with citrate to get 10-15 nm water-soluble particles.

MPCAuNP used in this work was supplied by Mintek (South Africa) and synthesised by treating citrate-stabilised gold with a mixture of carboxyl and hydroxyl polyethylene glycol (PEG) ligands. Scheme 1.2 shows a cartoon representation of the reaction. To my knowledge, this dissertation reports the first time (i) their self assembled nano-thin films and (ii) their electrochemical integration to investigate their heterogeneous electron transport behaviour as well as their electrocatalytic ability.

The most widely investigated family of ligands are thiolates (RS^-, R = organic moiety), frequently derived from organic thiols and disulfides. The strong interaction between the sulphur of the thiolate ligands and the gold surface facilitates the formation of a protective shell around the particle which (i) improves the stability by preventing uncontrolled aggregation of the particles and (ii) furnishes the nanoparticle with additional functionality, such as electronic, optical, thermal, catalytic, sensor, biomolecular recognition or transport properties [265,266] for potential applications in the fields of physics, chemistry, biology, medicine, and material science [267].

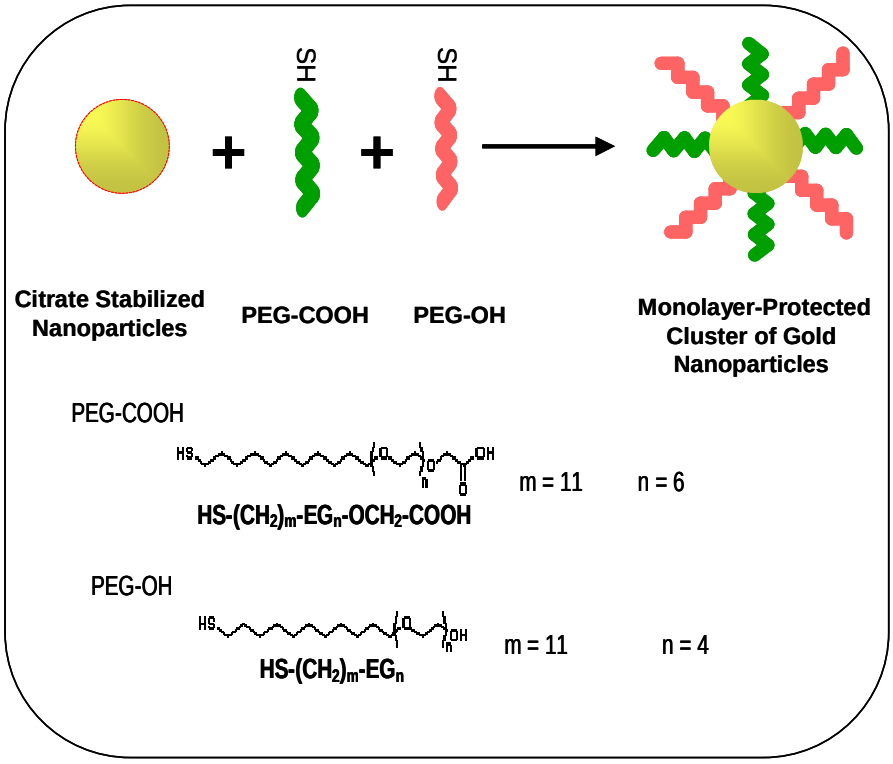

Scheme 1.2: Reaction scheme illustrating the one-step stabilization and functionalization of gold nanoparticles with carboxyl and hydroxyl PEG ligands.

Applications

The significant amount of work carried out in the field on monolayer-protected clusters of gold nanoparticles have already found a wide range of applications in nonlinear optical devices, electrophoresis, optoelectronic devices, fluorescence, catalysis, biochemistry, drug delivery and sensors [268-270]. However, in this study I investigated the electron transport properties and electrocatalytic behaviour of SAM modified electrochemical sensors, where this time

MPC of gold nanoparticles were used as the modifier in this fabrication process. MPCAuNP have been used for nanotechnology applications since the development of the Au_{55} cluster by Schmid *et al*. in 1981 [271]. In 1996, the Brust-Schiffrin group [272] studied 1,9 nonanethiol ($HS(CH_2)_9SH$) derivatized gold nanoparticles towards $[Fe(CN)_6]^{4-/3-}$. The layer-by-layer assembly of gold clusters and nonanethiol promoted and impeded the electrode's ability, respectively. Consequently, there was an increase in the rate of electron transfer when gold clusters were used as the outer layers and a decrease following nonanethiol assembly. However, it was work done by Murray's group in 1998 that led to an influx of investigations describing the electron transport behaviour of MPCAuNPs. They used gold clusters modified with anthraquinone to demonstrate the enhancement of 1,1 –dinitrocyclo-haxane reduction [273,274] and described MPCAuNP as multivalent redox species that can store charge. A year later, Zhong *et al*. [275] showed that rate of electron transfer between gold nanoparticles immobilized on dithiol gold substrates depend on (i) the arrangement of the nanoparticles and (ii) the distance between the underlying electrode and the gold nanoparticles. Musick *et al*. [276] investigated the impact of numerous layers of gold clusters modified onto dithiol electrodes. When less than seven layers were used, the wave shaped voltammogram indicated

that the electrode functioned as independent microelectrodes in a blocking film, while the peak shaped voltammograms observed for more than seven layers indicated a planar diffusion controlled process of the solution probe to the electrode. Hu *et al*. [277] also reported the presence of peak shaped voltammograms when he investigated the behaviour of gold clusters immobilized on cysteamine assembled gold surface towards the $[Fe(CN)_6]^{4-/3-}$ redox probe. In 2000, Chen [278] reported the electron transfer behaviour using CV and impedance measurements of a dithiolate MPCAuNP monolayer assembled directly onto the gold surface. Hicks *et al*. [279] also used electrochemical impedance spectroscopy to investigate the electron transport properties of a mixed monolayer (hexanethiolate/ mercaptoundecanoic (MUA)) MPCAuNP attached to MUA-functionalized gold electrode. Bharathi *et al.* [280] incorporated gold nanoparticles in to a silicate network to promote the rate of electron transfer. Maye *et al*. [281] assembled decanthiolate protected gold clusters on 1,9-nonanedithiol and 11-mercaptoundecanoic acid substrates to demonstrate the amplification of methanol oxidation. In contrast, Yang and Zhang [282] found no improvement in the electronic communication between the solution species: $Fe(CN)_6^{3-}$ or $Ru(NH_3)_6^{3+}$ and the underlying gold electrode surface subsequent to the attachment of gold nanoparticles to 1,6-hexanedithiol and 1,9- nonanedithiol modified electrodes. In

2004, Toyota *et al*. [283] studied the charging-discharging aspects of gold nanoparticles immobilized on amine-terminated siloxane on an Indium tin oxide electrode. In 2007, Jensen *et al*. [284] showed that gold nanoparticles can act as efficient redox relay for cytochrome c assembled at gold electrodes. Recently enhanced electron transport properties of MPCAuNP modified electrodes were investigated using scanning electron microscopy [285] and temperature [286] techniques. Therefore, nowadays it is well known that electrodes decorated with MPCAuNP mostly improve the electron transport behaviour.

Typical sizes of MPCAuNPs range from 1 to 40 nm depending on the preparation technique. Considering most preparation techniques produce MPCAuNPs that are insoluble in water, it should perhaps not be surprising that there are limited reports on the electron transfer properties and electrochemical biomolecular recognition properties of MPCAuNPs in aqueous media [287]. Thus, for electro-bioanalytical applications, it is essential to develop MPCAuNP systems that are stable, water soluble and capable of molecular recognition in aqueous media.

This work reports for the first time the surface electrochemistry of these stable, yet chemically versatile water-soluble MPCAuNPs self-assembled on polycrystalline electrode disk in terms of their (i) heterogeneous electron transfer dynamics in aqueous and non-

aqueous media, (ii) surface ionization properties, and (iii) voltammetric recognition properties towards epinephrine and ascorbic acid. These new MPCAuNPs were prepared by varying the ratio of its two different stabilizing ligands, (1-sulfanylundec-11-yl) polyethylene glycolic acid (herein abbreviated as PEG-COOH) and (1-sulfanylundec-11-yl) tetraethylene glycol (abbreviated as PEG-OH). The extent to which these ratios of protecting ligands influence heterogeneous electron transport and surface pK_a is crucial for the potential applications of such platforms in many areas such as molecular electronics as well as chemical and biological sensing. Here, it is clearly shown that mixtures of different stabilizing ligands have distinct impacts on their electron transfer dynamics in aqueous and non-aqueous media as well as their electrochemical recognition properties towards biologically relevant analytes, epinephrine and ascorbic acid. The importance of catecholamine neurotransmitters (e.g., epinephrine) in the body has been well documented [288-289]. However, the most common challenge in the electroanalytical detection of epinephrine in body fluids is the interference by ascorbic acid; the oxidation peaks of epinephrine and ascorbic acid are very close at physiological pH environment which often results in their voltammetric peaks overlapping thereby inhibiting the detection of epinephrine.

1.4 Species Investigated as Probe Analytes

1.4.1 Epinephrine

In 1886, William Bates reported the discovery of a substance produced by the adrenal gland in the New York Medical Journal. The substance better known as epinephrine (Fig. 1.18) was first isolated in 1895 by Napoleon Cybulski.

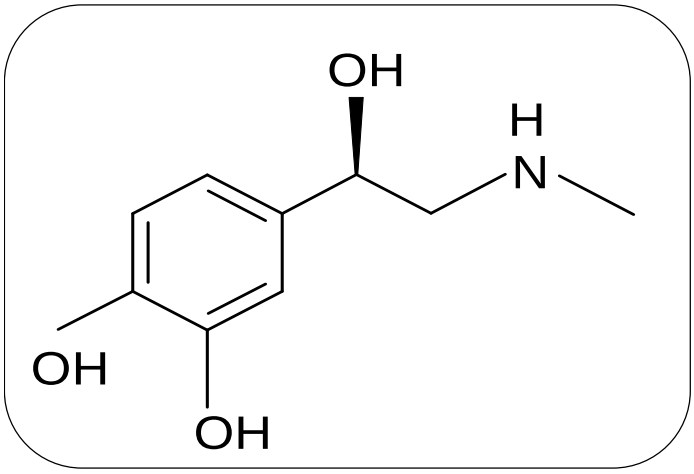

Figure 1.18: Structure of Epinephrine.

It is a catecholamine neurotransmitter commonly referred to as adrenalin or "fight or flight" hormone, derived from the amino acids phenylalanine and tyrosine and released from the adrenal gland in emergency situations. It is an important component of the mammalian central nervous system that exists as large organic cations in the body fluid and the nervous tissue, where it controls the nervous system in the performance of a series of biological reactions and nervous

chemical processes [290]. This means the concentration of EP affects processes such as heart rate, blood pressure, contraction of smooth muscles, glycogenolysis in liver and muscle, lipolysis in adipose tissue etc. [291]. Therefore, the detection and analysis of EP is of significant importance for improved pharmacological research and a better understanding of the effects of the nervous system. The determination of epinephrine has been reported with the use of chromatographic methods [292,293], capillary electrophoresis [294,295], spectroscopic methods [296,297], chemiluminescence [298,299], flow injection analysis [300,301] and various electrochemical methods [302-309].

However, the major challenge in epinephrine analysis is the elimination of interferences from ascorbic acid; the oxidation peaks of epinephrine and ascorbic acid are very close which often results in their peaks overlapping. The pK_a values of the hydroxyl groups of epinephrine are 8.7, 9.9 and 12.0, respectively [310,311], while the pK_a of the amino H of epinephrine is reported to be 9.9 [312]. This implies that at the physiological pH epinephrine remains neutral whereas ascorbic acid with pK_a values of 4.17 and 11.5 exists primarily as a monohydrogen ascorbate anion. Wang *et al.* [313] used negatively charged nafion isomer to repel the ascorbic acid but their electrode showed low sensitivity.

However, EP detection with high selectivity and sensitivity remains a major challenge in electroanalytical research [314,315] since EP exists together with ascorbic acid in the biological environment, and AA is oxidized at a similar potential to EP thus resulting in an overlapping voltammetric response. This problem may be resolved by either separating the electrochemical response of EP and AA [315] or eliminating the AA interference altogether [314].

1.4.2 Hydrogen Peroxide

The choice of this analyte stems from the knowledge that FePc is a natural mimic of the iron-containing proteins such as the horseradish peroxidase (HRP) and cytochrome C (cyt C) known for their redox-mediating role in the detection of H_2O_2. Given the high cost, temperature and stability constraints of these biomolecules for use in the detection of hydrogen peroxide (H_2O_2), it is reasonable that a much cheaper, highly stable (chemically and thermally) and easily available nanostructured FePc species could be an admirable alternative redox-mediator.

It is a pale blue liquid which appears colourless in dilute solutions and its strong oxidising properties make it a powerful bleaching agent. It was first isolated in 1818 by Louis Jacques Thénard upon reacting barium peroxide with nitric acid [316]. This process was used until the

middle of the 20th century. Nowadays, this molecule is known to be the by product of several biological and enzyme-catalysed reactions (oxidases) and since it is difficult to obtain an accurate measure of biological material present in the body, H_2O_2 is often measured as an indirect indication of the starting material. A common example is the detection of glucose:

$$\text{Glucose} + O_2 \xrightarrow{\text{Glucose oxidase}} \text{Gluconic acid} + H_2O_2 \qquad 1.16$$

In the oxidation of glucose to gluconic acid in the presence of glucose oxidase, the amount of glucose is indirectly detected using the direct detection of the by-product, H_2O_2. Therefore, the need for a high selectivity and extremely sensitive H_2O_2 sensor in food industry, environmental waste and medical diagnosis is of significant importance.

1.5 Microscopic and Spectroscopic Techniques

1.5.1 Scanning Electron Microscopy

Scanning electron microscopy (SEM) is a surface technique employed by the scanning electron microscope to image the surface of samples by scanning it with a high-energy beam of electrons in a raster scan manner. There is an interaction between these electrons and the atoms of the sample, resulting in signals that contain information about the sample's surface topography and composition [317]. In 1935, Max Knoll obtained the first SEM image of silicon steel showing electron channeling contrast [318]. In 1937, Manfred von Ardenne further investigated the beam specimen interactions and the physical principles of the SEM [319,320]. The operation of the SEM is as follows: At the top of a SEM column an electron gun generates a beam of electrons which are attracted through the anode, condensed (condenser lens) and focused (objective lens) as a fine point onto the sample. These electrons are collected by a secondary detector or a backscatter detector. The secondary electron detector produces a clear and focused topographical image of the sample whereas the backscatter electron detector reflects an elemental composition of the sample and is used for energy dispersive X-ray analysis [317,321].

1.5.2 Energy Dispersive X-Ray

Energy dispersive X-ray also referred to as an electron spectroscopy for chemical analysis, is an electron spectroscopic method used to determine the elemental and chemical composition of materials on metal surfaces [322]. The presence of the desired elements in the film can be confirmed using the EDX spectra and evaluating the atomic composition [323]. EDX is based on the photoelectron effect [322] where the surface is irradiated with photons. When incoming primary electrons bombard target material electrons an X-ray photon, characteristic of its own atom (element) is released [324]. Thus measuring the energy lost as a result of secondary electrons being displaced from the primary beam, the corresponding element to that energy loss may be determined.

An atom has a conventional sequence of electrons known as 'electron shells' arranged around its nuclei as a result of electrical charge differences between them. The shells are, also conventionally, labeled K, L, M, N, O, P, and Q from innermost to outermost. Primary electrons strike the atom (Fig. 1.19 a), and knock electrons out of their shell. As a result the atom is excited to higher energy state and relaxes after the 'knocked out' electrons are replaced with outer shell electrons. Therefore, there is a difference in energy states where the excess energy can be released in the form of an X-

ray, which carries this energy difference, and has a wavelength that is characteristic of the atomic species from which it came. This same process can occur with the L and M electrons and as a result leads to a large number of generated X-rays of differing wavelengths and hence a number of possible lines of X-rays available for analysis [322-323]. A spectrum (Fig. 1.13 b) is an accumulation of an index of X-rays collected from a particular spot on the sample surface each X-ray generated from an element are characteristic of that particular element and can thus be used to identify elements that are truly present under the electron probe [322].

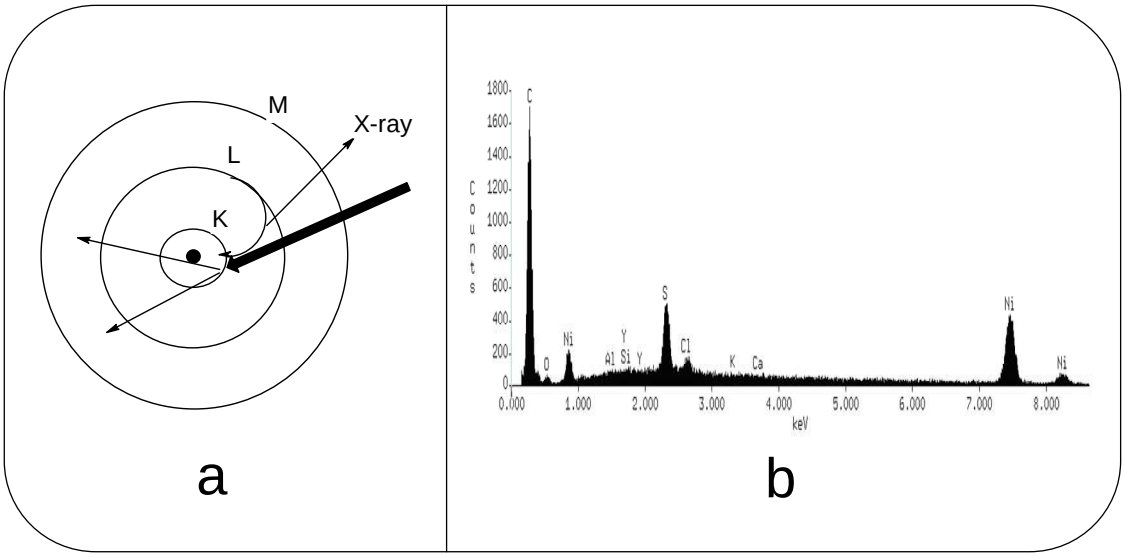

Figure 1.19: Simple representation of the first three shells showing, (a) the formation of energy dispersive X-ray resulting in (b) a unique spectrum.

1.5.3 Atomic Force Microscopy

Atomic force microscopy is a surface characterization technique that uses a sharp probe to scan across a sample detecting interactions between the silicon tip and the conductive or insulating sample resulting in nanoscale resolutions. The acronym AFM also refers to atomic force microscope which is the instrument used for the above mentioned technique. The first AFM was developed by Binnig, Quate and Gerber in 1986 [325]. Atomic force microscopy can be sub-divided into contact mode, acoustic AC mode and magnetic AC mode. Acoustic AC mode was exclusively used during this project because the samples used are not magnetic and unlike contact mode it does not drag across the sample. It essentially monitors the amplitude of a vibrating cantilever, by bouncing a laser beam off it and onto a detector, as it raster scans across the sample using a piezoelectric scanner. The fixed end of the cantilever is moved up and down in the Z direction by the piezoelectric scanner as it raster scans across the surface in the X and Y direction with the aid of a feedback mechanism employed to adjust the "tip-to-sample distance" in order to maintain constant amplitude and hence constant force derivative. The Z position of the tip at each data point in the X-Y plane produces the topographic image of the surface. Most of the surface characterizations in this project make use of the AFM because unlike the SEM which provides a two-dimensional

image of the sample, it provides a true three-dimensional surface profile. In addition the AFM functions perfectly in air or liquid environments and the samples viewed by AFM do not require special treatments like carbon coating whereas the SEM requires an expensive vacuum chamber for proper operation.

1.5.4 Transmission Electron Microscopy

Transmission Electron Microscopy (TEM) is a technique operated at a high resolution where the electron is transmitted through the sample owing to the interest in internal detail thus revealing the morphology (size, shape and arrangement of the particles), the crystallographic information (the atom arrangement) and the compositional information (the elemental composition) of the material examined [326-327]. The operation of a TEM is similar to that of a slide projector; however, it shines a beam of electrons, instead of light, generated from an electron gun. This stream of electrons is focused by a coherent beam that is restricted by a condenser aperture. The beam striking the sample transmits portions of the sample which are focused by the objective lens into an image that is projected onto a screen. There are dark and light areas of the image representing the more densely packed section which allowed fewer electrons to

pass through and the less densely packed section which allowed more electrons to pass through, respectively [326-327].

Reference:

1. A. E. Kaifer, M. Gómez-Kaifer, *Supramolecular Electrochemistry*, Wiley-VCH, New York, 1999.
2. J. Wang, *Analytical Electrochemistry*, VCH Publishers Inc., New York, 1994.
3. A.J. Bard, L.R. Faulkner, *Electrochemical Methods: Fundamentals and Applications, 2nd ed.*, John Wiley & Sons, Hoboken, NJ, 2001.
4. J.J.T. Maloy in: P.T. Kissinger and W.R. Heineman (Eds.), *Laboratory Techniques in Electroanalytical Chemistry*, Marcel Dekker Inc., New York, 1996.
5. R.G. Compton, C.E. Banks, *Understanding Voltammetry*, World Scientific Publishing Co., Singapore, 2007.
6. V.J. Puglisi, A.J. Bard, J. *Electrocem. Soc*. 119 (1972) 833.
7. F.M. Hawkridge in: P.T. Kissinger and W.R. Heineman (Eds.), *Laboratory Techniques in Electroanalytical Chemistry 2nd ed.*, Marcel Dekker Inc., New York, 1996.
8. D.B. Hibbert, *Introduction to Electrochemistry*, Macmillan, London, 1993.
9. J. E. B. Randles, *Trans. Faraday Soc*. 44 (1948) 327.

10. P.A. Christenson, A. Hamnet, *Techniques and Mechanisms in Electrochemistry*, *1st ed.*, Blackie Academic and Professional, London, 1994.

11. R. S. Niccholson, *Anal. Chem*. 37 (1965) 1351.

12. E. R. Brown, R. F. Large in: A. Weissberger and B. Rossiter (Eds.), *Physical Methods of Chemistry. Electrochemical Methods Vol.1-Part IIA*, Wiley-Interscience, New York, 1971.

13. G. C. Barker, I. L. Jenkins, *Analyst* 77 (1952) 685.

14. J.G. Osteryoung, *Acc. Chem. Res*. 26 (1993) 77.

15. J. Wang, D.B.Luo, P.A.M. Farias, J.S. Mahmoud, *Anal. Chem.* 57 (1985) 158.

16. M.H. Pournaghi-Azar, R. Sabzi, *J. Electroanal. Chem*. 543 (2003) 115.

17. P. Santhosh, K.M. Manesh, K.-P. Lee, A.I. Gopalan, *Electroanalysis* 18 (2006) 894.

18. K.M. Manesh, P. Santhosh, A.I. Gopalan, K.-P. Lee, *Electroanalysis* 18 (2006) 1564.

19. B. Agboola, T. Nyokong, *Talanta* 72 (2007) 691.

20. K. I. Ozoemena, T. Nyokong, D. Nkosi, I. Chambrier, M. J. Cook, *Electrochim. Acta* 52 (2007) 4132.

21. J.R. Macdonald, W.B. Johnson in: E. Barsoukov, J.R. Macdonald (Eds.), *Impedance Spectroscopy, 2nd ed.*, John Wiley and Sons Inc., NJ, 2005.

22. K.A. Joshi, M. Prouza, M. Kum, J. Wang, J. Tang, R. Haddon, W. Chen, A. Mulchandani, *Anal. Chem.* 78 (2006) 331.

23. O.V. Shulga, C. Palmer, *Anal. Bioanal. Chem*. 385 (2006) 1116.

24. S. Krause in: A.J. Bard, M. Stratmann, P.R. Ulwin (Eds.), *Instrumentation and Electroanalytical Chemistry Vol.3*, Wiley-GmbH & Co., 2003.

25. M.A.C. Brett, A.M. O. Brett, *Electrochemical Principles, Methods and Applications*, Oxford University Press, New York, 1993.

26. IUPAC Recommendation, *Pure and Appl. Chem*. 69 (1997) 1317.

27. R. F. Lane, A. T. Hubbard, *J. Phys. Chem*. 77 (1973) 1401.

28. C. M. Elliot, R. W. Murray, *Anal. Chem*. 48 (1976) 1247.

29. C.R. Martin, C.A. Foss Jr. in: P.T. Kissinger and W.R. Heineman (Eds.), *Laboratory Techniques in Electroanalytical Chemistry 2nd ed.*, Marcel Dekker Inc., New York, 1996.

30. L. Netzer, J. Sagiv, *J. Am. Chem. Soc.* 105 (1983) 674.

31. B.F. Watkins, J.R. Behling, E. Kariv, L.L. Miller, *J. Am. Chem. Soc*. 97 (1975) 3549.

32. N. Diab, J. Oni, W. Schuhmann, *Bioelectrochemistry* 66 (2005) 105.

33. C. Deng, M. Li, Q. Xie, M. Liu, Y. Tan, X. Xu, S. Yao, *Anal. Chim. Acta* 557 (2006) 85.

34. Z. Chen, Y. Zhou, *Surface & Coatings Technology* 201 (2006) 2419.

35. S. Pyun, J-S. Bae, *J. Power Sources* 68 (1997) 669.

36. C. Sivakumar, J-N. Nian, H. Teng, *J.Power Sources* 144 (2005) 295.

37. E. Mun˜oz, M. A. Heras, A. I. Colina, V. Ruiz, J. Lo´pez-Palacios, *Electrochim. Acta* 52 (2007) 4778.

38. K. B. Blodgett, *J.Amer. Chem. Soc.* 56 (1934) 495.

39. A. J. Bard, *J. Chem. Ed*. 60 (1983) 303.

40. J.J. Gooding, D.B. Hibbert, *TrAC* 18 (1999) 52.

41. H. O. Finklea in Encyclopedia Chemistry, A. J. Bard and I. Rubinstein, Eds., Marcel Dekker: New York, 1996, Vol.19, pp109-335.

42. I. Langmuir, *J. Am. Chem. Soc.* 39 (1917) 1848.

43. W.C. Bigelow, D.L. Pickett, W.A. Zisman, *J. Colloid interface Sci.* 1 (1946) 513.

44. J. Sagiv, *J. Am. Chem. Soc.* 102 (1980) 92.

45. D.L. Allara, R.G. Nuzzo, *Langmuir* 1 (1985) 45.

46. R.G. Nuzzo, D.L. Allara, *J. Am. Chem. Soc.* 105 (1983) 4481.

47. R.G. Nuzzo, F.A. Fusco, D.L. Allara, *J. Am. Chem. Soc.* 109 (1987) 2358.

48. H.O. Finklea, S. Avery, M. Lynch, T. Furtsch, *Langmuir* 219 (1987) 365.

49. E. Sabatani, I. Rubinstein, *J. Phys. Chem.* 91 (1987) 6663.

50. L. Strong, G.M. Whitesides, *Langmuir* 4 (1988) 546.

51. F. Caruso, E. Rodda, D.N. Furlong, V. Haring, *Sens. Actuators B* 41 (1997) 189.

52. C-J. Zhong, R.C. Brush, J, Anderegg, M.D. Porter, *Langmuir* 15 (1999) 518.

53. K. Nishiyama, S-I., Tahara, Y. Uchida, S. Tanoue, I. Tangiguchi, *J. Electroanal. Chem.* 478 (1999) 83.

54. C.D. Bain, E.B. Troughton, Y-T. Tao, J. Eval, G.M. Whitesides, R.G. Nuzzo, *J. Am. Chem. Soc.* 111 (1989) 321.

55. R.L. Garell, J.E. Chadwick, D.L. Severance, N.A. McDonald, D.C. Myles, *J. Am. Chem. Soc.* 117 (1995) 11563.

56. X. Zhang, H. Chen, H. Zhang, *Chem. Commun.* (2007) 1395.

57. R.K. Iler, *J. Colloid Interface Sci.* 21 (1966) 569.

58. G. Decher, J.D. Hong, *Makromol. Chem. Macromol. Symp.* 46 (1991) 321.

59. G. Decher, J.D. Hong, *Ber. Bunsen-Ges. Phys. Chem.* 95 (1991) 1430.

60. Y. Lvov, G. Decher, H. Mohwald, *Langmuir* 9 (1993) 481.

61. G. Decher, Y. Lvov, J. Schmitt, *Thin Solid Films* 244 (1994) 772.

62. J. C. Jan, M.D. Walton, E.P. McConnell, W.S. Jang, Y.S. Kim, J.C. Grunlan, *Carbon* 44 (2006) 1974.

63. S.S. Shiratori, M.F. Rubner, *Macromolecules* 33 (2000) 4213.

64. H.N Zhang, J. Ruhe, *Macromolecules* 36 (2003) 6593.

65. R. A. McAloney, M. Sinyor, V. Dudnik, M.C. Goh, *Langmuir* 17 (2001) 6655.

66. O. Mermut, C.J. Barrett, *J. Phys. Chem. B* 107 (2003) 2525.

67. Z. J. Sui, D. Salloum, J.B. Schlenoff, *Langmuir* 19 (2003) 2491.

68. H.L. Tan, M.J. McMurdo, G.Q. Pan, P.G. Van Patten, *Langmuir* 19 (2003) 9311.

69. A.C. Fou, O. Onitsuka, M. Ferreira, M.F. Rubner, B.R. Hsieh, *J. Appl. Phys.* 79 (1996) 7501.

70. W.B. Stockton, M.F. Rubner, *Macromolecules* 30 (1997) 2715.

71. M. Raposo, R.S. Pontes, L.H.C. Mattoso, O.N. Oliveira Jr., *Macromolecules* 30 (1997) 6095.

72. S.W. Keller, H.N. Kim, T.E. Mallouk, *J. Am. Chem. Soc.* 116 (1994) 8817.

73. D.E. Cliffel, F.P. Zamborini, R.W. Murray, *Langmuir* 16 (2000) 9699.

74. F. Caruso, W.J. Yang, D. Trau, R. Renneberg, *Langmuir* 16 (2000) 8932.

75. E. Donath, G.B. Sukhorukov, F. Caruso, S.A. Davis, H. Mohwald, *Angew. Chem. Int. Ed.* 37 (1998) 2202.

76. B.G. De Geest, R.E. Vandenbroucke, A.M. Guenther, *Adv. Mater.* 18 (2006) 1005.

77. F. Caruso, D. Trau, H. Mohwald, R. Renneberg, *Langmuir* 16 (2000) 1485.

78. W. Shan, H. Liu, J. Shi, L. Yang, N. Hu, *Biophysical Chem.* 134 (2008) 101.

79. Y. Lvov, G. Decher, G. Sukhorukov, *Macromolecules* 26 (1993) 5396.

80. V. Zucolotto, K.R.P. Daghastanli, C.O. Hayasaka, A. Riul, P. Ciancaglini, O.N. Oliveira Jr., *Anal. Chem.* 79 (2007) 2163.

81. M. Olek, J. Ostrander, S. Jurga, H. Mohwald, N. Kotov, K. Kempa, M. Giersig, *Nano Lett.* 4 (2004) 1889.

82. V. Zucolotto, M. Ferreira, M.R. Cordeiro, C.J.L. Constantino, D.T. Balogh, A.R. Zanatta, W.C. Moreira, O.N. Oliveira Jr. *J. Phys.Chem. B* 107 (2003) 3733.

83. A.C. Templeton, W.P. Wuelfing, R.W. Murray, *Acc. Chem. Res.* 33 (2000) 27.

84. F. Caruso, R. A. Caruso, H. Mohwald, *Science* 282 (1998) 1111.

85. D. Losic, J. G. Shapter, J. J. Gooding, *Langmuir* 17 (2001) 3307.

86. P. Podsiadlo, B.S. Shim, N.A. Kotov, *Coordination Chem. Rev.* 253 (2009) 2835.

87. J. F. Silva, S. Griveau, C. Richard, J.H. Zagal, F. Bedioui, *Electrochem. Commun*. 9 (2007) 1629.

88. J.H. Zagal, S. Griveau, K.I. Ozoemena, T. Nyokong, F. Bedioui, *Nanosci. Nanotechnol.* 9 (2009) 2201.

89. J. Pillay, K. I. Ozoemena, *Electrochem. Commun*. 7 (2007) 1816.

90. J. Pillay, K.I. Ozoemena, *Electrochim. Acta 52 (2007) 3630.*

91. J. Pillay, K.I. Ozoemena, *Chem. Phys. Lett*. 441 (2007) 72.

92. K.I. Ozoemena, P. Westbroek, T. Nyokong, *Electrochem. Commun.* 3 (2001) 529.

93. K.I. Ozoemena, T. Nyokong, *Electrochim. Acta* 47 (2002) 4035.

94. B.O. Agboola, K.I. Ozoemena, *Phys.Chem.Chem.Phys.* 10 (2008) 2399.

95. K.I. Ozoemena, T. Nyokong, P. Westbroek, *Electroanalysis* 15 (2003) 1762.

96. V. Zucolotto, M. Ferreira, M.R. Cordeiro, C.J.L. Constantino, W.C. Moreira, O.N. Oliveira Jr., *Synth. Met.* 137 (2003) 945.

97. J.R. Siqueira Jr., L.H.S. Gasparotto, O.N. Oliveira Jr., V. Zucolotto, *J. Phys. Chem. C.* 112 (2008) 9050.

98. J.R. Siqueira Jr., L.H.S. Gasparotto, F.N. Crespilho, A.J.F. Carvalho, V. Zucolotto, O.N. Oliveira Jr., *J. Phys. Chem. B* 110 (2006) 22690.

99. J.R. Siqueira Jr., F.N. Crespilho, V. Zucolotto, O.N. Oliveira Jr., *Electrochem. Commun.* 9 (2007) 2676.

100. H. Benten, N. Kudo, H. Ohkita, S. Ito, *Thin Solid Films* 517 (2009) 2016.

101. M. Monthioux, V. L. Kuznetsov, *Carbon* 44 (2006) 1621.

102. L.V. Radushkevich, V.M Lukyanovich, *Zurn Fisic Chim.* 26 (1952) 88.

103. Hughes T.V, Chambers C.R. *US Patent 405480*, 1889.

104. S. Iijima, *Nature* 354 (1991) 56.

105. P.G. Wiles, J. Abrahamson, *Carbon* 16 (1978) 341.

106. T. W. Ebbesen, P.M. Ajayan, *Nature* 358 (1992) 220.

107. Y. Ando, S. IiJima, *Jpn. J. Appl. Phys.* 37 (1993) L107.

108. S. Ijima, T. Ichihashi, *Nature* 363 (1993) 603.

109. M. J. Yacaman, M. M. Yoshida, L. Rendon, J. G. Santiesteban, *Appl. Phys. Lett.* 62 (1993) 202.

110. A. Thess, R. Lee, P. Nikolaev, H. Dai, P. Petit, J. Robert, C. Xu, Y. H. Lee, S. G. Kim, A. G. Rinzler, D. T. Colbert, G. E. Scuseria, D. Tomane´k, J.E. Fischer, R.E. Smalley, *Science* 273 (1996) 483.

111. C.P. Poole Jr., F.J. Owens, *Introduction to Nanotechnology*, John Wiley and Sons Inc., Hoboken, New Jersey, 2003.

112. S.C. Lyu, T.J. Lee, C.W. Yang, J.C. Lee, *Chem. Comm.* 12 (2003) 1404.

113. C. E. Banks, R. G. Compton, *Analyst* 131 (2006) 15.

114. [a] The Nanotube site: http://nanotube.msu.edu:05/02/07. [b] J. Despres, E. Daguerre, K. Lafdi, *Carbon* 33 (1995) 87.

115. S. Iijima, C. Brabec, A. Maiti, J. Bernholc, *J. Chem. Phys.* 104 (1996) 2089.

116. B.I. Yakobson, C. J. Brabec, J. Bernholc, *Phys. Rev. Lett.* 76 (1996) 2511.

117. [a] J. Hone, M. Whitney, A. Zettle, *Synth. Met.* 103 (1999) 2498. [b] M. Burghard, *Surface Science Reports* 58 (2005) 1.

118. A.G. Rinzler, J.H. Hafner, P. Nikolaev, L. Lou, S.G. Kim, D. Tomanec, P. Nordlander, D.T. Colbert, R.E. Smalley, *Science* 269 (1995) 1550.

119. P. J. Britto, K. S. V. Santhanam, P. M. Ajayan, *Bioelectronics and Bioenergetics* 41 (1996) 121.

120. J.W.G. Wilder, L.C. Venema, A.G. Rinzler, R.E. Smalley, C. Dekker, *Nature* 391 (1998) 59.

121. T. Mühl, D. Elefant, A. Graff, R. Kozhuharova, A. Leonhardt, I. Mönch, M. Ritschel, P. Simon, S. Groudeva-Zotova, C.M. Schneider, *J. of Appl. Phys.* 93 (2003) 7894.

122. F. Cordella, M. Nardi, E. Menna, C. Hébert, M.A. Loi, *Carbon* 47 (2009) 1264.

123. V.N. Popov, *Materials Science and Engineering R* 43 (2004) 61.

124. C.Y Chen, T.C Chien, Y.C Chan, C.K. Lin, S.C. Wang, *Diamond and Related Materials* 18 (2009) 482.

125. S. Kawasaki, Y. Iwai, M. Hirose, *Carbon* 47 (2009) 1081.

126. J. Kong, N. R. Franklin, C. Zhou, M. G. Chapline, S. Peng, K. Cho, H. Dai, *Science* 287 (2000) 622.

127. R.A Jishi, M.S. Dresselhaus, G. Dresselhaus, *Matter and Materials Physics* 47 (1993) 16671.

128. M.S. Strano, C.A. Dyke, M.L. Usrey, P.W. Barone, M.J. Allen, H. Shan, C. Kittrell, R.H. Hauge, J.M. Tour, R.E. Smalley, *Science* 301 (2003) 1519.

129. C.N.R. Rao, A. Govindaraj, B.C. Satishkumar, *Chem. Commun.* 13 (1996) 1525.

130. E.T. Mickelson, I.W. Chiang , J.L. Ziammerman, P.J. Boul, J. Lozano , J. Liu, R.E. Smalley , R.H. Hauge , J.L. Margrave, *J. Phys. Chem. B*. 103 (1999) 4318.

131. J. Zhu, J.D. Kim, H.Q. Peng, J.L. Margrave, V.N. Khabashesku, E.V. Barrera, *Nano Lett.* 3 (2003) 1107.

132. P.J. Boul, J.Liu, E.T. Mickelson, C.B. Huffman, L.M. Ericson, I.W. Chiang, K.A. Smith, D.T. Colbert, R.H. Hauge, J.L. Margrave, R.E. Smalley, *Chem. Phys. Lett.* 310 (1999) 367.

133. B. Zhao, H. Hu, R.C. Haddon, *Adv. Funct. Mater.* 14 (2004) 71.

134. J. Chen, M.A. Hamon, H. Hu, Y. Chen, A.M. Rao, P.C. Eklund, R.C. Haddon, *Science* 282 (1998) 95.

135. R.H. Baughman, C. Cui, A.A. Zakhidov, Z. Iqbal, J.N. Barisci, G.M. Spinks, G.G. Wallace, A. Mazzoldi, D. De Rossi, A.G. Rinzler, O. Jaschinski, S. Roth, M. Kertesz, *Science* 284 (1999) 1340.

136. G.G. Wildgoose, C.E. Banks, H.C. Leventis, R.G. Compton, *Microchim Acta* 152 (2006)187.

137. G. Che, B.B. Lakshmi, E.R. Fisher, C.R. Martin, *Nature* 393 (2000) 346.

138. T. Matsumoto, T. Komatsu, H. Nakano, K. Arai, Y. Nagashima, E. Yoo, T. Yamazaki, M. Kijima, H. Shimizu, Y. Takasawa, J. Nakamura, *Catal. Today* 90 (2004) 277.

139. Z. Liu, X. Lin, J.Y. Lee,W. Zhang, M. Han, L.M. Gan, *Langmuir* 18 (2002) 4054.

140. W. Li, C. Liang, J. Qiu, W. Zhou, H. Han, Z. Wei, G. Sun, Q. Xin, *Carbon* 40 (2002) 787.

141. T. Matsumoto, T. Komatsu, K. Arai, T. Yamazaki, M. Kijima, H. Shimizu, Y. Takasawa, J. Nakamura, *Chem. Commun.* 7 (2004) 840.

142. N. Jha, A.L.M. Reddy, M.M. Shaijumon, N. Rajalakshmi, S. Ramaprabhu, *International Journal of Hydrogen Energy* 33 (2008) 427.

143. battery

144. Z. K. Tang, L. Zhang, N. Wang, X.X. Zhang, G.H. Wen, G.D. Li, J.N. Wang, C.T. Chan, P. Sheng, *Science* 292 (2001) 2462.

145. V. Gupta, N. Miura, *Electrochim. Acta* 52 (2006) 1721.

146. A.C. Dillon, K.M. Jones, T. A. Bekkedahl, C.H. King, D.S . Bethune, M.J . Heben, *Nature* 386 (1997) 377.

147. S.J . Tans, R.M. Verschueren, C. Dekker, *Nature* 393 (1998) 49.

148. J. M.Planeix, N.Coustel, B. Coq, V.Brotons, P.S. Kumbhar, R. Dutartre, P.Geneste, P.Bernier, P. M. Ajayan, *J. Am. Chem. Soc.* 116 (1994) 7935.

149. S.Saito, *Science* 278 (1997) 77.

150. P.Kim, C.M. Lieber, *Science* 286 (1999) 2148.

151. K.H. An, W.S. Kim, Y.S. Park, J.-M. Moon, D.J. Bae, S.C. Lim, Y.S. Lee, Y.H. Lee, *Adv. Funct. Mater.* 11 (2001) 387.

152. M.S. Dresselhaus, *Nature* 358 (1992) 195.

153. S.J. Tan, M.H. Devoret, H. Dai, A. Thess, R.E. Smalley, L.J. Geerligs, C. Dekker, *Nature* 386 (1997) 474.

154. A. Bianco, K. Kostarelos, C.D. Partidos, M. Prato, *Chem. Commun.* 5 (2005) 571.

155. K. Kostarelos, L. Lacerda, C.D. Partidos, M. Prato, A. Bianco, *J. Drug Deliv. Sci. Technol.* 15 (2005) 41.

156. N.W.S. Kam, Z. Liu, H. Dai, *J. Am. Chem. Soc.* 127 (2005) 12492.

157. A. Bianco, K. Kostarelos, M. Prato, *Curr. Opin. Chem. Biol.* 9 (2005) 674.

158. X. Yu, R. Rajamani, K.A. Stelson, T. Cui, *Sensors and Actuators* 132 (2006) 626.

159. Y. Shingaya, T. Nakayama, M. Aono, *Physica B* 323 (2002) 153.

160. Ph. Avouris, R. Martel, V. Derycke, J. Appenzeller, *Physica B* 323 (2002) 6.

161. J.Kong, N.R. Franklin, C. Zhou, M.G. Chapline, S. Peng, K. Cho, H. Dai, *Science* 287 (2000) 622.

162. J. Kong, M.G. Chapline, H.Dai, *Adv. Mater.* 13 (2001) 1384.

163. P.G. Collins, K. Bradley, M. Ishigami, A. Zettl, *Science* 287 (2000) 1801.

164. A. Qureshi, W.P. Kang, J.L. Davidson, Y. Gurbuz, *Diamond and Related Materials* (2008) doi:10.1016/j.diamond.2009.09.008.

165. P.J. Britto, K.S.V. Santhanam, A. Rubio, J.A. Alonso, P.M. Ajayan, *Adv. Mater.* 11 (1999) 154.

166. J. J. Davis, R.J. Coles, H. A.O. Hill, *J. Electroanal. Chem*. 440 (1997) 279.

167. H. Luo, Z. Shi, N. Li, Z. Gu, Q. Zhuang, *Anal. Chem.* 73 (2001) 915.

168. G. Che, B.B. Lakshmi, E.R. Fisher, C.R. Martin, *Nature* 393 (1998) 346.

169. F. Valentini, A. Amine, S. Orlanducci, M. Letiziu, G. Palleschi, *Anal. Chem.* 75 (2003) 5413.

170. Z. Di- Zhao, W.De Zhang, H. Chen, Q. M. Luo, *Talanta* 58 (2002) 529.

171. J.J. Gooding, R. Wibowo, J. Liu, W. Yang, D. Losic, S. Orbons, F.J. Mearns, J.G. Shapter, D.B. Hibbert, *J. Am. Chem. Soc.* 125 (2003) 9006.

172. J. Wang, M. Li, Z. Shi, N. Li, Z. Gu, *Microchim. J.* 73 (2002) 325.

173. J. Wang, M. Li, Z. Shi, N. Li, Z. Gu, *Electrochim. Acta* 47 (2001) 651.

174. F.H. Wu, G.C. Zhao, X.W. Wei, *Electrochem. Commun.* 4 (2002) 690.

175. M. Musameh, J. Wang, A. Merkoci, Y. Lin, *Electrochem. Commun.* 4 (2002) 743.

176. K. Wu, J. Fei, S. Hu, *Anal. Biochem.* 318 (2003) 100.

177. K.B. Malea, S. Hrapovica, Y. Liua, D. Wang, J.H.T. Luong, *Anal. Chim. Acta* 516 (2004) 35.

178. C. Yang, *Anal. Sci.* 20 (2004) 821.

179. G-Q Zhang, X-G Zhang, Y-G Wang, *Carbon* 42 (2004) 3097.

180. N.S. Lawrence, R.P. Deo, J. Wang, *Talanta* 63 (2004) 443.

181. J. Wang, M. Musameh, *Anal. Chimica Acta* 511 (2004) 33.

182. J. Wang, S.B. Hocevar, B. Ogorevc, *Electrochem. Commun*. 6 (2004) 176.

183. M.L. Pedano, G.A. Rivas, *Electrochem. Commun*. 6 (2004) 10.

184. J-S Yea, Y. Wen, W.D. Zhang, L.M. Gan, G-Q Xu, F-S Sheu, *Electrochem. Commun*. 6 (2004) 66.

185. R.P. Deo, J. Wang, I. Block, A. Mulchandani, K.A. Joshi, M. Trojanowicz, F. Scholz, W. Chen, Y. Lin, *Anal. Chim. Acta* 530 (2005) 185.

186. N.S. Lawrence, R.P. Deo, J. Wang, *Electroanalysis* 17 (2005) 65.

187. D. Nkosi, K.I. Ozoemena, *J. Electroanal. Chem.* 621 (2008) 304.

188. F.C. Moraesa, L.H. Mascaroa, S.A.S. Machadob, C.M.A. Brett, *Talanta* 79 (2009) 1406.

189. V. Selvaraj, M. Alagar, K. S. Kumar, *Appl. Catal. B: Environ.* 75 (2007) 129.

190. A. Salimi, C.E. Banks, R.G. Compton, *Analyst* 129 (2004) 225.

191. D.A. Geraldo, C.A. Togo, J. Limson, T. Nyokong, *Electrochim. Acta*, 53 (2008) 8051.

192. T. Mugadza, T. Nyokong, *Electrochim. Acta* 54 (2009) 6347.

193. K.I. Ozoemena, J. Pillay, T. Nyokong, *Electrochem. Commun.* 8 (2006) 1391.

194. M.P. Siswana, K.I. Ozoemena, T. Nyokong, *Electrochim. Acta* 52 (2006) 114.

195. D. Nkosi, K.I. Ozoemena, *Electrochim. Acta* 53 (2008) 2782.

196. B. O. Agboola, S.L. Vilakazi, K. I. Ozoemena *J. Solid State Electrochem.* 13 (2009) 1367.

197. A.S. Adekunle, K.I. Ozoemena, *Electrochim. Acta* 53 (2008) 5774.

198. A.S. Adekunle, K.I. Ozoemena, *J. Solid State Electrochem.* 12 (2008) 1325.

199. A.S. Adekunle, J. Pillay, K. I. Ozoemena, *Electroanalysis* 20 (2008) 2587.

200. K. I. Ozoemena, D. Nkosi, J. Pillay, *Electrochim. Acta* 53 (2008) 2844.

201. A. Braun, J. Tcherniac, *Berichte der Deutschen Chemischen Gesellschaft* 40 (1907) 2709.

202. H. de Diesbach, E. von der Weid, *Helevtica Chimica Act* 10 (1927) 886.

203. P.Gregory, *J. Porphyrins Phthalocyanines* 3 (1999) 468.

204. R.P. Linstead, *J. Chem. Soc.* (1934) 1016.

205. J.M. Roberston, *J. Chem. Soc.* (1935) 615.

206. J.M. Roberston, *J. Chem. Soc.* (1936) 1195.

207. *Phthalocyanines: Properties and Applications,* C.C. Leznoff and A.B.P.Lever, Eds., VCH Publishers, New York, Vols. 1-4, 1989, 1993, 1993, 1996.

208. E.Ough, T. Nyokong, K.A.M. Creber, M.J. Stillman, *Inorg. Chem.* 27 (1988) 2725.

209. R.B. Linstead, A.R. Lowe, *J. Chem. Soc.* (1934) 1022.

210. J.H. Zagal, *Coord. Chem. Rev.* 119 (1992) 89.

211. C.B. Murray, D.J. Norris, M.G. Bawendi, *J. Am. Chem. Soc.* 115 (1993) 8706.

212. B.O. Dabbousi, M.G. Bawendi, O. Onitsuka, M.F. Rubner, *Appl. Phys. Lett.* 66 (1995) 1316.

213. T. Enokida, R. Hirohashi, S. Mizukami, *J. Imaging Sci.* 35 (1991) 235.

214. T. Saito, T. Kawanishi, A. Kakuta, *Jpn. J. Appl. Phys. A* 30 (1991) L1182.

215. Y. Wang, K. Deng, L. Gui, Y. Tang, J. Zhou, L. Cai, J. Qiu, D. Ren and Y. Wang, *J. Colloid Interface Sci.* 213 (1999) 270.

216. G. de la Torre, C.G. Claessens, T. Torres, *Chem. Commun.* (2007) 2000.

217. R.K. Sen, J. Zagal, E. Yerger, *Inorg. Chem*. 16 (1977) 3379.

218. J. Limson, T. Nyokong, *Electroanalysis* 9 (1997) 255.

219. K. Hanabusa, H. Sharai in: A.P.B. Lever and C.C. Leznoff (Eds.), *Phthalocyanines: Properties and Applications*, VHC Publishers, New York, 1993, Vol.2.

220. H. Kasuga in: A.P.B. Leverand C.C. Leznoff (Eds.), *Phthalocyanine: Properties and Applications,* VCH Publishers, New York, 1996, Vol.4.

221. M. Thamae, T. Nyokong, *J. Electroanal. Chem*. 470 (1999) 126.

222. K. Morishige, S. Tomoyasu, G. Iwano, *Langmuir* 13 (1997) 5184.

223. A.W. Snow, W.R. Barger in: A.P.B. Lever and C.C. Leznoff (Eds.), *Phthalocyanines: Properties and Applications*, VCH Publishers, New York, 1989, Vol.1.

224. E. Ben-Hur, I. Rosenthal, *Int. J. Radiat. Biol*. 47 (1985) 145.

225. E. Ben-Hur, I. Rosenthal, *J. Photochem. Photobiol*. 42 (1985) 129.

226. I. Rosenthal, E. Ben-Hur in: A.P.B. Lever and C.C. Leznoff *Phthalocyanine: Properties and Applications,* VCH Publishers, New York, 1989, Vol.1.

227. D. Phillips, *Pure Appl. Chem*. 67 (1995) 117.

228. I.J. MacDonald, T. Dougherty, *J. Porphyrins Phthalocyanines* 5 (2001) 105.

229. P. Gregory, *J. Porphyrins Phthalocyanines* 3 (1999) 468.

230. P. Gregory in: *High Technology Applications of Organic Colorants*, Plenum Press, New York, 1991.

231. N.B. McKeown, *Chem. Ind*. (1999) 92.

232. G.C.S. Collins, D.J. Schiffrin, *J. Electroanal. Chem*. 139 (1982) 335.

233. M.M. Nicholson in: A.P.B.Lever and C.C. Leznoff (Eds.), *Phthalocyanine: Properties and Applications*, VCH Publishers, New York, 1993. Vol. 3.

234. N. Toshina, T. Tominaga, *Bull. Chem. Soc. Jpn.* 69 (1996) 2111.

235. J.E. Kuder, *J. Imaging Sci*. 32 (1988) 51.

236. R. Ao, L. Kummert, D. Haarer, *Adv. Mater*. 5 (1995) 495.

237. S. Nalwa, J.A. Shirk in: A.P.B. Lever and C.C. Leznoff (Eds.), *Phthalocyanine: Properties and Applications,* VCH Publishers, New York, 1993, Vol. 4.

238. D.K.P. Ng, Y-O Yeung, W.K. Chan, S-C Yu, *Tet. Lett*. 38 (1997) 6701.

239. D. Worhle, D. Meissener, *Adv. Mater*. 3 (1991) 129.

240. D. Worhle, L. Kreienhoop, D. Schlettwein in: A.P.B. Lever and C.C. Leznoff (Eds.), *Phthalocyanine: Properties and Applications*, VCH Publishers, New York, 1996, Vol.4.

241. A.B.P. Lever, M.R. Hempstead, C.C. Leznoff, W. Lui, M. Melnik, W.A. Nevin, P. Seymour, *Pure Appl. Chem*. 58 (1986) 1467.

242. B. Simic-Glavaski in: A.P.B. Lever and C.C. Leznoff (Eds.), *Phthalocyanine: Properties and Applications*, VCH Publishers, New York, 1993, Vol.3.

243. J. Simon, J.J. Andre, *Mol. Semicond.*, Springer, Berlin, 1985.

244. J. Simon, T. Toupance in: D.N. Reinhoudt (Ed.), *Comprehensive Supramolecular Chemistry Vol.10*, Pergamon, London, 1996.

245. M. Iwamoto, *J. Mater. Chem*. 10 (2000) 99.

246. P. Vasuvedan, N. Poughat, A.K. Shuklat, *Appl. Organomet. Chem*. (1996) 591.

247. M. Thamae, T. Nyokong, *J. Electroanal. Chem*. 470 (1999) 126.

248. E. Ben-Hur, I. Rosenthal, *Int. J. Radiat. Biol*. 47 (1985) 145.

249. D. Phillips, *Pure Appl. Chem*. 67 (1995) 117.

250. Y. Lu, R.G. Reddy, *Electrochim. Acta* 52 (2007) 2562.

251. N. Martz, C. Roth, H. Fueb, *J. Appl. Electrochem*. 35 (2005) 85.

252. K.I. Ozoemena, T. Nyokong, in: C. A Grimes, E.C. Dickey, M.V. Pishko, (Eds.), *Encyclopedia of Sensors Vol.3, Chapter E, pp.157 – 200*, American Scientific Publishers, California, 2006.

253. M. Siswana, K.I. Ozoemena, T. Nyokong, *Talanta* 69 (2006) 1136.

254. S.A. Mamuru, K.I. Ozoemena, *Mat. Chem. Phys.* 114 (2009) 113.

255. G. Savage, *Glass and Glassware*; Octopus Books: London, 1975.

256. G. Lussac, *Annalen der Physik* 101(1832) 629.

257. M. Faraday, *Philos. Trans.* 147 (1857) 145.

258. J. Kunckels, *Nuetliche Observationes oder Anmerkungen von Auro und Argento Potabili*; Schutzens: Hamburg, 1676.

259. T. Graham, *Philos. Trans. R. Soc*. 151 (1861) 183.

260. N. Taniguchi, "*On the Basic Concept of 'Nano-Technology'*," Proc. Intl. Conf. Prod. Eng. Tokyo, Part II, Japan Society of Precision Engineering, 1974

261. S. Chen, R.W. Murray, *Langmuir* 15 (1999) 682.

262. A.C. Templeton, M.J. Hostetler, C.T. Kraft, R.W. Murray, *J. Am. Chem. Soc.* 120 (1998) 1906.

263. M. Brust, M. Walker, D. Bethell, D. J. Schiffrin, R. Whyman, *J. Chem. Soc. Chem. Commun.* 7 (1994) 801.

264. B. V. Enustun, J. Turkevich, *J. Am. Chem. Soc.* 85 (1963) 3317.

265. C.-C. You, A. Chompoosor, V.M. Rotello, *Nanotoday* 2 (2007) 34.

266. A. Verma, V.M. Rotello, *Chem. Commun.* 3 (2005) 303.

267. M.H. Rashid, R.R. Bhattacharjee, A. Kotal, T.K. Mandal, *Langmuir* 22 (2006) 7141.

268. L. N. Lewis, *Chem. Rev.* 93 (1993) 2693.

269. S. Guo, E. Wang, *Anal. Chim. Acta* 598 (2007) 181.

270. M-C. Daniel, D. Astruc, *Chem. Rev.* 104 (2004) 293.

271. G. Schmid, R. Pfeil, R. Boese, F. Bandermann, S. Meyers, G.H.M. Calis, W.A. Vandervelden, *Chem. Ber.* 114 (1981) 3634.

272. D. Bethell, M. Brust, D.J. Schiffrin, C. Kiely, *J. Electroanal. Chem.* 409 (1996) 137.

273. R.S. Ingram, R.W. Murray, *Langmuir* 14 (1998) 4115.

274. J.J. Pietron, R.W. Murray, *J. Phys. Chem. B* 103 (1999) 4440.

275. C.J. Zhong, W.X. Zheng, F.L. Leibowitz, *Electrochem. Commun.* 1 (1999) 72.

276. M.D. Musick, D.J. Pena, S.L. Botsko, T.M. McEvoy, J.N. Richardson, M.J. Natan, *Langmuir* 15 (1999) 844.

277. X.Y. Hu, Y. Xiao, H.Y. Chen, *J. Electroanal. Chem.* 466 (1999) 26.

278. S. Chen, *J. Phys. Chem. B* 104 (2000) 663.

279. J.F. Hicks, F.P. Zamborini, R.W. Murray, *J. Phys. Chem. B* 106 (2002) 7751.

280. S. Bharathi, M. Nogami, S. Ikeda, *Langmuir* 17 (2001) 1.

281. M.M. Maye, J. Luo, Y. Lin, M.H. Engelhard, M. Hepel, C.-J Zhang, *Langmuir* 19 (2003) 125.

282. M. Yang, Z. Zhang, *Electrochim. Acta* 49 (2004) 5089.

283. A. Toyota, N. Nakashima, T. Sagara, *J. Electroanal. Chem.* 565 (2004) 335.

284. P.S. Jensen, Q. Chi, F.B. Grumsen, J.M. Abad, A. Horsewell, D.J. Schiffrin, J. Ulstrup, *J. Phys. Chem. C* 111 (2007) 6124.

285. P. Ahonen, V. Ruiz, K. Kontturi, P. Liljeroth, B. M. Quinn, *J. Phys. Chem. C* 112 (2008) 2724.

286. A. S. Nair, K. Kimura, *Langmuir* 25 (2009) 1750.

287. T. R. Tshikhudo, D. Demuru, Z. Wang, M. Brust, A. Secchi, A. Arduini and A. Pochini, *Angew. Chem. Int. Ed.* 44 (2005) 2.

288. P. Hern´andez, I. S´anchez, F. Pat´on, L. Hern´andez, *Talanta* 46 (1998) 985.

289. J. O. Schenk, E. Milker, R. N. Adam, *J. Chem. Educ.* 60 (1983) 311.

290. Q.M. Xue, *Physiological and Pathological Chemistry of Nervous System*, Science Press, Beijing, 1978.

291. D. Voet, J.G. Voet, *Biochemistry 3rd ed.*, John Wiley & Sons, Hoboken, 2004, pp.659 and 664–666.

292. O. Gyllenhaal, L. Johansson, J. Vessman, *J. Chromatography A* 190 (1980) 347.

293. H.G. Lovelady, L.L. Foster, *J. Chromatography A* 108 (1975) 43.

294. L.Y. Zhang, S.F. Qv, Z.L. Wang, J.K Cheng, *J. Chromatogr. B* 792 (2003) 381.

295. S.L. Wei, G.Q. Song, J.M. Li, *J. Chromatogr. A* 166 (2005) 1098.

296. M.H. Sorouraddin, J.L. Manzoori, E. Kargarzadeh, *J. Pharm. Biomed.* 18 (1998) 877.

297. M. Zhu, X.M. Huang, J. Li, *Anal. Chim. Acta* 357 (1997) 261.

298. Y.Y. Su, J. Wang, G.N. Chen, *Talanta* 65 (2005) 531.

299. J. Michalowski, P. Halaburda, *Talanta* 55 (2001) 1165.

300. E.M. Garrido, J.L. Lima, D.M. Cristina, *J. Pharm. Biomed.* 15 (1997) 845.

301. J.X. Du, L.H. Shen, J.R. Lu, *Anal. Chim. Acta* 489 (2003) 183.

302. Z. Yang, G. Hu, X. Chen, J. Zhao, G. Zhao, *Colloids Surf. B: Biointerf.* 54 (2007) 230.

303. H.S. Wang, D-Q. Huang, R-M. Liu, *J. Electroanal. Chem.* 570 (2004) 83.

304. J. Gong, X. Lin, *Electrochim. Acta* 49 (2004) 4351.

305. W. Ren, H.Q. Luo, N.B. Li, *Biosens. Bioelectron.* 21 (2006) 1086.

306. N.B. Li, W. Ren, H.Q. Luo, *Anal. Chim. Acta* 378 (1999) 151.

307. M. Marazuela, L. Agui, A. Gonzalez-Cortes, P. Yanez-Sedeno, J.M. Pingarro, *Electroanalysis* 11 (1999) 1333.

308. F. Valentini, G. Palleschi, E. Lopez Morales, S. Orlanducci, E. Tamburri, M. L. Terranova, *Electroanalysis* 19 (2007) 859

309. Z. Guo, S. Dong, *Electroanalysis* 17 (2005) 607.

310. S.L. Jewett, S. Eggling, L. Geller, *J. Inorg. Biochem* 66 (1997) 165.

311. C.E. Sanger-van de Griend, A.G. Ek, M.E. Widahl-Nasman, E.K.M.J. Andersson, *Pharm. Biomed. Anal.* 41 (2006) 77.

312. E.L. Ciolkowski, K.M. Maness, P.S. Cahlil, R.M. Wightman, *Anal. Chem.* 66 (1994) 3611.

313. J. Wang, P. Tuzhi, T. Golden, *Anal. Chim. Acta* 194 (1987) 129.

314. J. Ni, H. Ju, H. Chen, D. Leech, *Anal. Chim. Acta* 378 (1999) 151.

315. H. Zhang, X. Zhou, R. Hui, N. Li, D. Liu, *Talanta* 56 (2002) 1081.

316. L.J. Thenard, *Annales de chimie et de physique* 8 (1818) 308.

317. C.A. Gervasi, P.E. Alvarez, M.V. Fiori Bimbi, M.E. Folquer, *J. Electroanal. Chem.* 601 (2007) 194.

318. M. Knoll, *Zeitschrift für technische Physik* 16 (1935) 467.

319. M. von Ardenne, *Zeitschrift für Physik* 108 (1938) 553.

320. M von Ardenne, *Zeitschrift für technische Physik* 19 (1938) 407.

321. P.E. Alvarez, S.B. Ribotta, M.E. Folquer, C.A. Gervasi, J.R. Vilche, *Corros. Sci*. 44 (2002) 49.

322. J. B. Hudson, *Surface Science: An Introduction*, John Wiley & Sons, New York, 1998.

323. M.H. Kibel, in: D. J. O'Connor, B.A. Sexton, R. St. C. Smart, (Eds.), *Surface Analysis Methods in Material Science*, Springer-Verlag, Berlin Heidelberg, Germany, 1993.

324. X. Jiang, T. Wang, *Applied Surface Science* 252 (2006) 8029.

325. G. Binnig, C.F. Quate, C. Gerber, *Phys. Rev. Lett.* 56 (1986) 930.

326. E. Le Bourhis, G. Patriarche, *Micron* 38 (2007) 377.

327. C.S. Pande, S. Smith, L.E. Richards, in: G.W. Bailey (Ed.), *Proceedings of 43rd Annual Meeting of Electron Microscopy Society of America*, San Francisco Press Inc., San Francisco, CA, 1985.

CHAPTER TWO

EXPERIMENTAL

2 EXPERIMENTAL

2.1 Materials and Reagents

Single-walled carbon nanotube-*poly* (m-amino benzene sulfonic acid) (SWCNT-PABS, Figure 2.1a), Epinephrine, 2-Dimethylaminoethanethiol hydrochloride ($HS(CH_2)_2N^+H(CH_3)_2Cl^-$ DMAET), Hexadecyltrimethylammonium bromide (CTAB) and N, N-Dimethylformamide (DMF) obtained from Sigma-Aldrich; DMF was distilled and dried before use. 5 nm Colloidal Gold (AuNP) of 0.01% $HAuCl_4$ concentration was purchased from Sigma. Monolayer-protected clusters of gold nanoparticles (MPCAuNP) were supplied by Mintek. Sodium 2-mercaptoethanesulphonate (MES) was obtained from Merck. Iron (II) tetrasulfophtalocyanine (FeTSPc - Figure 2.1b) was synthesised following the well established Weber and Busch strategy [1] and the nanostructured iron (II) phthalocyanine (*nano*FePc), was synthesized as described by Siswana *et al*. [2]. The main principle of the synthesis as depicted in Scheme 2.1 is simply the breaking of the intramolecular forces and protecting the species in CTAB environments. Tetrabutylammonium tetrafluroborate ($TBABF_4$) was Ultra pure water of resistivity 18.2 MΩ.cm was obtained from a Milli-Q Water System (Millipore Corp., Bedford, MA, USA) and was used throughout for the preparation of solutions. Phosphate buffer solutions

(PBS, pH 7.4) were prepared with appropriate amounts of K_2HPO_4 and KH_2PO_4. Potassium hexacyanoferrate (II) was obtained from B. Jones Ltd., SA, potassium hexacyanoferric (III) was purchased from Bio-Zone Chemicals, SA. All electrochemical experiments were performed with nitrogen-saturated phosphate buffer. All other reagents were of analytical grades and were used as received from the suppliers without further purification.

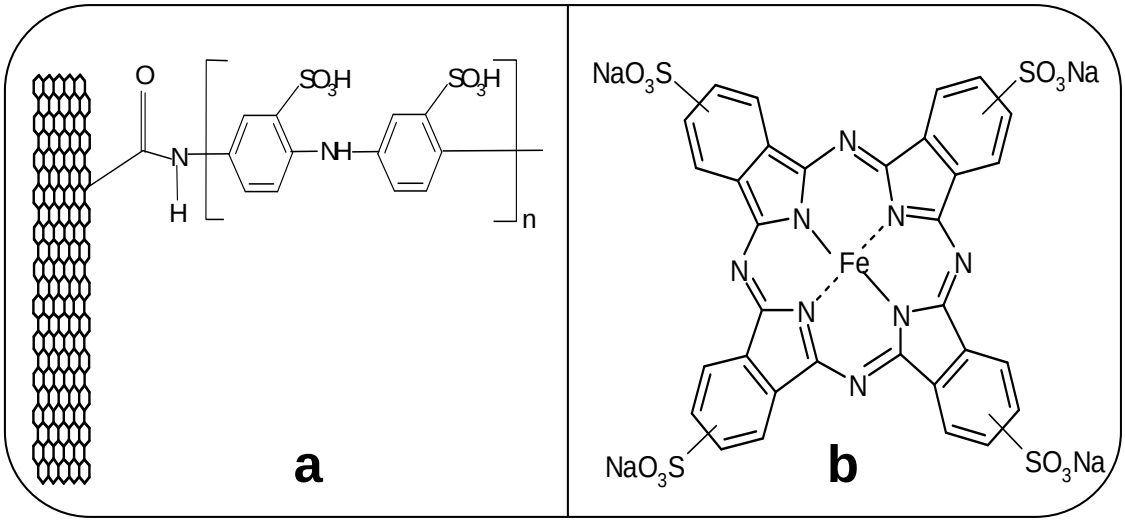

Figure 2.1: Molecular structure of (a) Single-walled carbon nanotube-*poly* (m-amino benzene sulfonic acid) and (b) Iron (II) tetrasulfophtalocyanine.

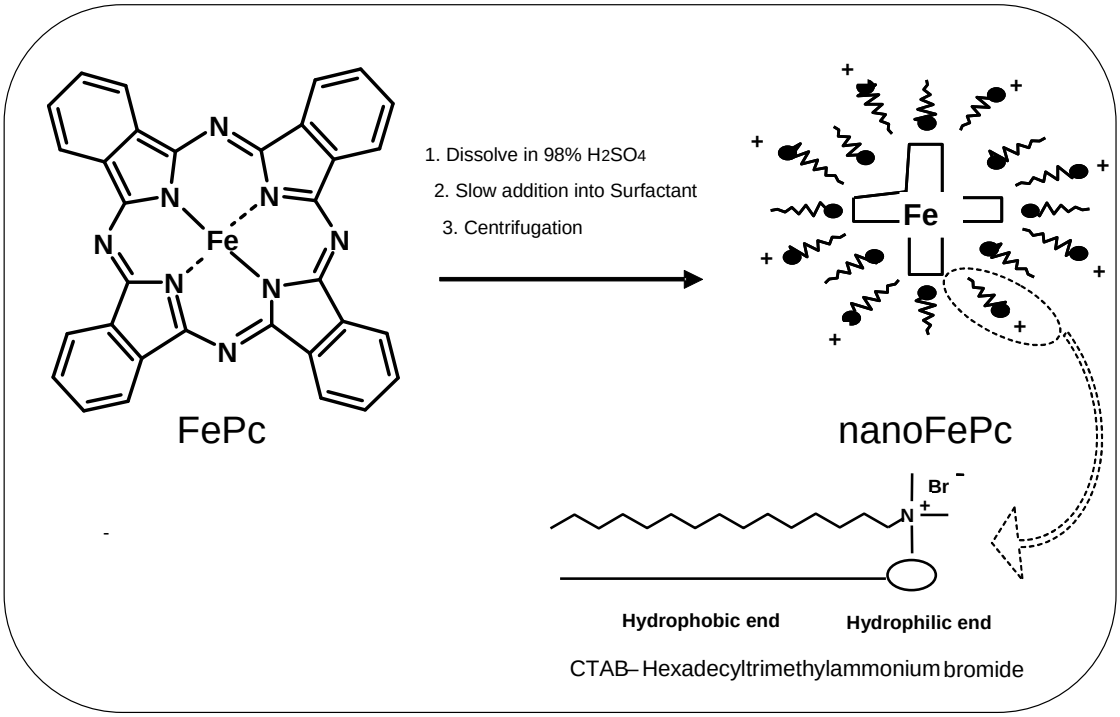

Scheme 2.1: Cartoon representation showing the synthesis of nanostructured Iron (II) phthalocyanine from Iron (II) phthalocyanine complex.

2.2 Apparatus and Procedure

All electrochemical experiments were carried out using an Autolab Potentiostat PGSTAT 302 (Eco Chemie, Utrecht, Netherlands) driven by the GPES and FRA softwares version 4.9). Electrochemical impedance spectroscopy measurements were performed using a 5 mV rms sinusoidal modulation in a solution of 1 mM of $K_4Fe(CN)_6$ and 1mM $K_3Fe(CN)_6$ (1:1) mixture containing 0.1 M KCl, and at the $E_{1/2}$ of the $[Fe(CN)_6]^{3-/4-}$ (0.124V vs. Ag|AgCl, sat'd KCl). The FRA software allowed the automatic fitting of the raw EIS data to equivalent circuit

models using a *complex non-linear least squares* (CNLS) method based on the EQUIVCRT programme [3], with *Krammers-Kronig rule check*. Gold electrode (BAS, r = 0.08 cm) was used as the working electrode. Ag|AgCl, sat'd KCl and platinum electrodes were used as pseudo-reference and counter electrodes, respectively. All solutions were de-aerated by bubbling pure nitrogen (Afrox) prior to each electrochemical experiment. All experiments were performed at 25±1°C. All pH measurements were performed using Labotec Orion bench top pH meter model 420A. Solutions were sonicated using a 220V UMC 5th Integral Systems sonicator. Transmission electron microscopy (TEM) studies of the particles were carried out at an accelerating voltage of 197 kV using a Philips CM200 microscope equipped with a LaB_6 source at Mintek Advanced Materials Division. Field emission scanning electron microscopy (FESEM) images were obtained using JEOL JSM 5800 LV (Japan) while the energy dispersive x-ray spectra were obtained from NORAN VANTAGE (USA) at the Microscopy and Microanalysis Laboratory of the University of Pretoria. All the AFM images were obtained using Eco-Chemie SPR gold disks and the AFM experiments were performed using a AFM 5100 System (Agilent Technologies, USA) using a AC contact mode AFM scanner interfaced with a PicoScan controller (scan range 1.25 µm in x–y and 2.322 µm in z). Silicon type PPP-NCH-20 (Nanosensors®) of thickness

4.0±1.0 µm, length 125±10 µm, width 30±7.5 µm, spring constants 10 – 130 N m^{-1}, resonant frequencies of 204 – 497 kHz and tip height of 10-15 µm were used. All images (256 samples/line × 256 lines) were taken in air at room temperature and at scan rates 0.9–1.0 lines s^{-1}.

2.3 Electrode Modification and Pre-treatment

Prior to the experiments, the Polycrystalline gold electrode (BAS) was first cleaned using slurries of aluminum oxide nano-powder (Sigma-Aldrich), mirror finished on a Buehler felt pad and then subjected to ultrasonic vibration in ethanol to remove residual alumina nano-powder at the surface. The gold electrodes were then treated with 'Piranha' solution {1:3 (v/v) 30% H_2O_2 and concentrated H_2SO_4} for about 2 min, this step is necessary in order to remove organic contaminants and was followed by thorough rinsing with distilled water and ethanol. The gold electrode was finally cleaned electrochemically by carrying out CV experiments in 0.5 M H_2SO_4 and scanning the potential between −0.5 and 1.5 V (versus Ag|AgCl, sat'd KCl) at a scan rate of 0.05 V s^{-1} until a reproducible CV scan was obtained. The electrode was again rinsed with absolute ethanol and immediately placed into a nitrogen-saturated absolute ethanol solution of 4.5 mM DMAET for 18 h in the dark to form the base monolayer (Au-DMAET).

The pK_a of DMAET is ~ 10.8 and expected to be positively charged [4]. The newly formed Au-DMAET electrode was rinsed in copious amount of distilled deionised water and ethanol for 2 min to remove weakly adsorbed DMAET molecules. Thereafter, SWCNT-PABS, FeTSPc, SWCNT-PABS/FeTSPc and MPCAuNP were assembled on the base monolayer as follows: to complete their respective self assembly processes.

2.3.1 SWCNT-PABS and AuNP Based Electrodes

The formation of SWCNT-PABS on the Au-DMAET was assembled by dipping the Au-DMAET electrode in a dispersion of SWCNT-PABS (1 mg SWCNT-PABS / 1 ml PBS, pH 7.4) for 3.5 h. The electrode containing SWCNT-PABS is herein referred to as Au-DMAET-SWCNT-PABS. Thereafter, Au-DMAET-SWCNT-PABS was immersed in a dispersion of *nano*FePc (1 mg *nano*FePc / 1 ml PBS, pH 7.4) for 3.5 h. The electrode containing a single layer of SWCNT-PABS and *nano*FePc is herein referred to as Au-DMAET-(SWCNT-PABS-*nano*FePc)$_1$. Layer-by-layer assembly involves the alternating adsorption of SWCNT-PABS and *nano*FePc affording the formation of a multilayer system where each consecutive adsorption of SWCNT-PABS and *nano*FePc is referred to as a bilayer. The multilayered electrode formed by layer-by-layer assembly is herein referred to Au-DMAET-(SWCNT-PABS-*nano*FePc)$_n$,

where n = 1 – 5 bilayers. Au-DMAET-(AuNP-*nano*FePc)$_n$, was fabricated using the above mentioned process where 1 ml AuNP was used instead of 1 mg ml^{-1} SWCNT-PABS.

2.3.2 FeTSPc Based Electrodes

For the FeTSPc based electrodes the freshly prepared bare gold electrode was immersed in a 5 mM DMAET ethanol solution for a period of 36 h. The subsequent FeTSPc assembly on Au-DMAET was formed by immersing the Au-DMAET in 10 ml aqueous solution of 4 mg FeTSPc for 6 h to obtain the electrode herein abbreviated as Au-DMAET-FeTSPc. Also, Au-DMAET was deposited for 6 h into a resultant mixture of an equal volume of SWCNT-PABS solution and FeTSPc solution to obtain the electrode herein abbreviated as Au-DMAET-SWCNT-PABS/FeTSPc. The resultant mixture of the SWCNT-PABS solution and FeTSPc solution was sonicated for 2 h.

2.3.3 MPCAuNP Based Electrodes

Citrate-stabilized gold nanoparticles of 14 nm diameter were prepared using the well known Turkevich-Frens procedure [5,6]. Briefly, an aqueous solution of sodium citrate (10 ml, 17 mM) was added to a boiling solution of $HAuCl_4$ (180 ml, 0.3 mM), and heated under reflux for 30 min. The reaction mixture was allowed to cool to room

temperature, and then continuously stirred for ~ 24 h, and finally filtered using a 0.45 µm Millipore filter paper before use. (1-sulfanylundec-11-yl) tetraethylene glycol (PEG-OH) and (1-sulfanylundec-11-yl) polyethylene glycolic acid (PEG-COOH) were purchased (Prochimia, Poland) or prepared using the established procedure [7,8]. For example, the 50:50 (PEG-COOH/PEG-OH) was prepared as follows. The ethanolic solutions of PEG-OH (1 mg, 0.5 mL) and PEG-COOH (1 mg, 0.5 mL) were mixed and added simultaneously under stirring into the citrate-stabilised gold nanoparticles (20 ml, 2 nM). The reaction mixture was stirred for 3 h and filtered using a 0.45 µm Millipore filter paper. The filtered particles were purified by repeated centrifugation and redispersion in distilled deionized water. This solution is abbreviated as MPCAuNP-$COOH_{50\%}$. Three different % mass ratios of PEG-COOH to PEG-OH (1:99, 50:50 and 99:1) were used. The same procedure was used for the preparation of the other ratios. The ratio of 1:99 (PEG-COOH : PEG-OH) is abbreviated as MPCAuNP-COOH1%, while that of 99:1 (PEG-COOH : PEG-OH) is abbreviated as MPCAuNP-$COOH_{99\%}$. The final concentration of each solution mixture was 1.5 nM (12.5 ml), obtained by using a molar absorption coefficient of 4.2 x 10^8 M^{-1} cm^{-1} (at 526 nm) based on gold nanoparticles of 15±1.2 nm diameter [9].

All the modified electrodes were then thoroughly rinsed with water and dried gently in a weak flowing nitrogen gas. The modified electrodes were stored in nitrogen-saturated phosphate buffer pH 7.4 at room temperature.

The real surface area of the bare gold electrode was determined using the Randles-Ševčík equation (Eq. 1.6) for reversible electrochemistry:

$$i_p = \left(2.69\times10^5\right)n^{3/2}AC\left(D\nu\right)^{1/2}$$

where n is the number of electrons involved (n = 1 in the $[Fe(CN)_6]^{3-/4-}$ redox system), A is the geometric area of the electrode (0.020 cm^2), D is the diffusion coefficient of the $[Fe(CN)_6]^{3-/4-}$ = 7.6×10^{-6} cm^2 s^{-1} [10], while C = 1.0×10^{-6} mol cm^{-3} is the bulk concentration of the $[Fe(CN)_6]^{3-/4-}$. From the slope of the plot of the anodic peak current (I_{pa}) versus the scan rate, the experimentally determined surface area (A) was found to be 0.0289 cm^2 giving a surface roughness factor of 1.44 (ratio of real to geometrical surface area).

Reference:

1. J.H. Weber, D.H. Busch, *Inorg. Chem.* 4 (1965) 472.
2. M. Siswana, K.I. Ozoemena, T. Nyokong, *Talanta* 69 (2006) 1136.
3. B.A. Boukamp, *Solid State Ionics* 20 (1986) 31.
4. F. Caruso, E. Rodda, D. N. Furlong, V. Haring, *Sens. Actuators B* 41 (1997)189.
5. J. Turkevich, P. C. Stevenson, J. Hillier, *Discuss. Faraday Soc.* 11 (1951) 55.
6. G. Frens, *Nature Phys. Sci.* 241 (1973) 20.
7. C. Pale-Grosdemange, E. S. Simon, K. L. Prime, G. M. Whitesides, *J. Am. Chem. Soc.* 113 (1991) 12.
8. T. R. Tshikhudo, D. Demuru, Z. Wang, M. Brust, A. Secchi, A. Arduini, A. Pochini, *Angew. Chem. Int. Ed.* 44 (2005) 2.
9. L. M. Demers, C. A. Mirkin, R. C. Mucic, R. A. Reynolds, R. L. Letsinger, R. Elghanian, G. Viswanadham, *Anal. Chem.* 72 (2000) 5535.
10. R.G. Compton, C.E. Banks, *Understanding Voltammetry*, World Scientific Publishing Co., Singapore, 2007.

CHAPTER THREE

RESULTS AND DISCUSSION*

* The following publications resulted from part of the research work presented in this dissertation and they are not referenced further. Other publications (Appendix A) not directly related to this thesis topic were not reported here but, were cited where necessary.

1. J. Pillay, B. O. Agboola, K. I. Ozoemena, Layer-by-layer self-assembled nanostructured phthalocyaninatoiron(II) / SWCNT-*poly*(*m*-aminobenzenesulfonic acid) hybrid system on gold surface: Electron transfer dynamics and amplification of H_2O_2 response", *Electrochem. Commun.* 11 (2009) 1292.
2. J. Pillay, K.I. Ozoemena, Electrochemistry of 2-dimethylaminoethanethiol SAM on gold electrode: Interaction with SWCNT-poly(*m*-aminobenzene sulphonic acid), electric field-induced protonation-deprotonation, and surface pKa", *Electrochim. Acta* 54 (2009) 5053.
3. J. Pillay, K.I. Ozoemena, T.R. Tshikhudo, "Monolayer-Protected Gold Nanoparticles: Impacts of Stabilizing Ligands on the Heterogeneous Electron Transfer Dynamics and Voltammetric Detection", Submitted to *Langmuir* (2010) DOI: 10.1021/la904463g.
4. B.O. Agboola, J. Pillay, K. Makgopa, K.I. Ozoemena, "Cyclic voltammetric and impedimetric properties of mixed self-assembled nanothin films of water-soluble SWCNT-*poly*(*m*-aminobenzene sulfonic acid) and iron (II) tetra-sulphophthalocyanine at gold electrode", Submitted to *Thin Solid Films*.
5. J. Pillay, K.I. Ozoemena, "Electron transport and voltammetric detection properties of gold nanoparticle-nanosized iron (II) phthalocyanine bilayer films", In preparation.

3 RESULTS AND DISCUSSION

3.1 2-Dimethylaminoethanethiol Self Assembled Monolayer

3.1.1 Electrode Fabrication and AFM Characterization

Scheme 3.1 represents the self-assembly fabrication from bare-Au to Au-DMAET-SWCNT-PABS. The build-up and formation of the films on gold plates were confirmed using AFM technique. Figure 3.1 shows the comparative AFM images of the (a) bare-Au (b) Au-DMAET and (c) Au-DMAET-SWCNT-PABS. There was no significant difference between the thickness of the bare-Au and Au-DMAET, which is expected for this short-chained alkanethiol SAM as other workers [1] also, did not observe any difference between bare-Au and on modification with long-chained SAM of 11-amino-1-undecanethiol. AFM features for the immobilisation of SWCNT-PABS on Au-DMAET show there is clear evidence of flat lying tubes on the surface of the DMAET molecules expected for a side walled functionalised CNTs using the negatively charged sulfonic group to form electrostatic attraction with the positively charged amino of DMAET (Fig. 3.1c).

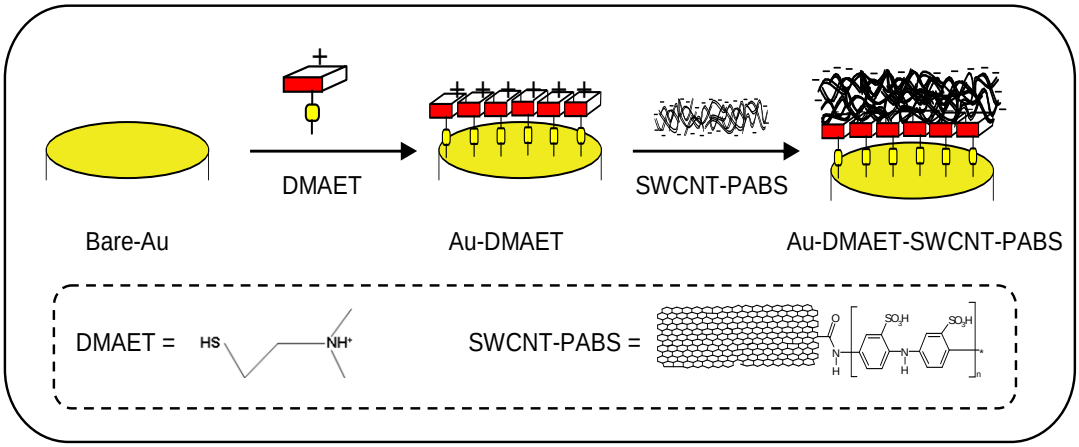

Scheme 3.1: Cartoon showing the schematic representation of the SAM formation of DMAET and DMAET–SWCNT-PABS.

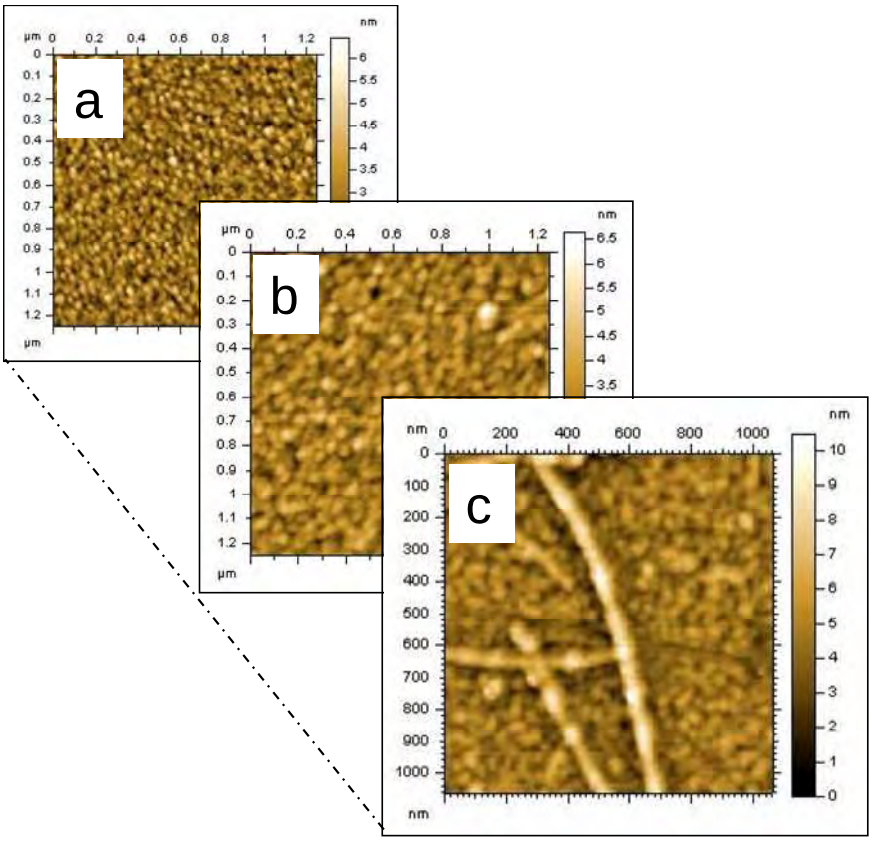

Figure 3.1: Topographic AFM images of (a) bare-Au (b) Au-DMAET and (c) Au-DMAET–SWCNT-PABS.

Furthermore, there is a continuous increase in maximum height (from a–c) as shown by the data in Figure 3.1. Also, the root mean square (R_q) of the roughness profile follows the same trend where, bare-Au (0.81 nm) < Au-DMAET (1.06 nm) < Au-SWCNT-PABS (1.95 nm). These facts provide evidence for the formation of the base monolayer and the subsequent attachment of SWCNT-PABS onto the electrode surface.

3.1.2 Protonation / Deprotonation Effect or Cyclic Voltammetric Behaviour in Various Electrolytes

Figure 3.2 compares the CV profiles of the three electrodes in PBS (pH 7.4). The reversible voltammogram for the Au-DMAET SAM is similar to those observed by White and co-workers for mercaptoundecanoic acid (MUA) SAMs on Ag(III) [2], Burgess and co-workers for MUA on polycrystalline gold [3] and 4-mercaptobenzoic acid (4-MBA) SAMs on polycrystalline gold electrode [4], which I associated with the electric field induced prototonation/deprotonation of the –COOH head groups rather than a Faradaic process.

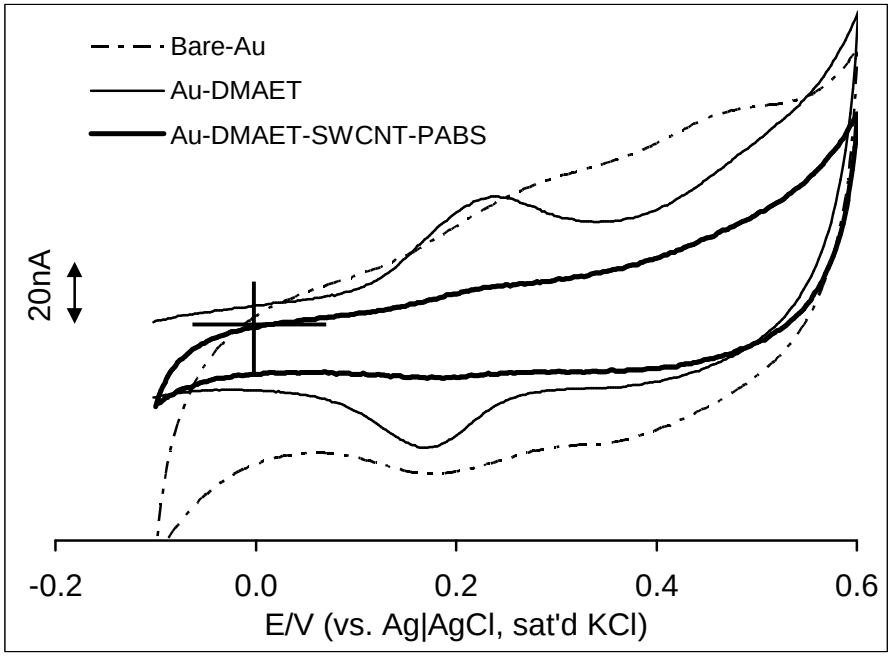

Figure 3.2: Typical cyclic voltammetric evolutions of the bare-Au, Au-DMAET and Au-DMAET–SWCNT-PABS electrodes in PBS pH 7.4.

I believe that the same process is what is being observed in this case, i.e., electric field driven prototonation/deprotonation of the $-N(H)^{+}(CH_3)_2$ head group of the DMAET (Eq. 3.1):

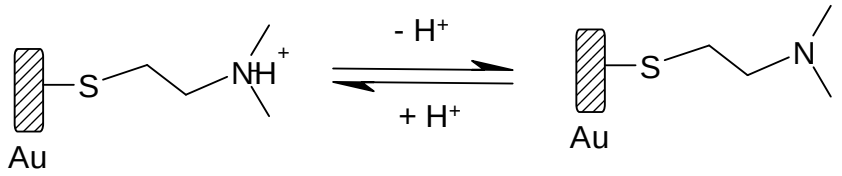

3.1

Figure 3.2 clearly suggests that the integration of the SWCNT-PABS via electrostatic interaction leads to suppression of the

protonation/deprotonation process. To test this hypothesis, I conducted a series of experiments in different unbuffered electrolytes (50 mM K_2SO_4, KCl, NaF, K_2SO_4 and $KClO_4$) with a view to establishing the impact of cations and anions on the evolution of this DMAET reversible voltammogram. As exemplified in Figure 3.3, unlike the NaF and KCl that showed the same reversible process as the PBS, the K_2SO_4 and $KClO_4$ (not shown) suppressed the Au-DMAET voltammogram. Repetitive scanning in any of the electrolyte showed stable voltammograms (exemplified in Figure 3.4 with NaF). It may be inferred from the CVs that (i) the appearance of the reversible peaks in chloride and non-chloride solutions (PBS and NaF) rules out this possibility adsorption/desorption of chloride ions being responsible for the peaks; (ii) cations do not have any impact contrary to the report of Rosentahl and Burgess on 4-MBA [4], and (iii) anions have impact but possibly depend on the size of anion; SO_4^{2-} and ClO_4^- are approximately of the same size and larger than Cl^- that did not show any impact. Unlike the SWCNT-PABS, the original Au-DMAET voltammogram can be regenerated when re-immersed in KCl solution (Fig. 3.3), meaning that SWCNT-PABS is irreversibly adsorbed onto the DMAET while the anions are weakly adsorbed. The CV of the SAM of Sodium 2-mercaptoethanesulphonate (same structure as DMAET, differing only in the head group) was also examined and no peaks

were observed in the PBS (Fig. 3.3 inset), which confirms that the reversible peaks in DMAET SAM arise from its amino head group.

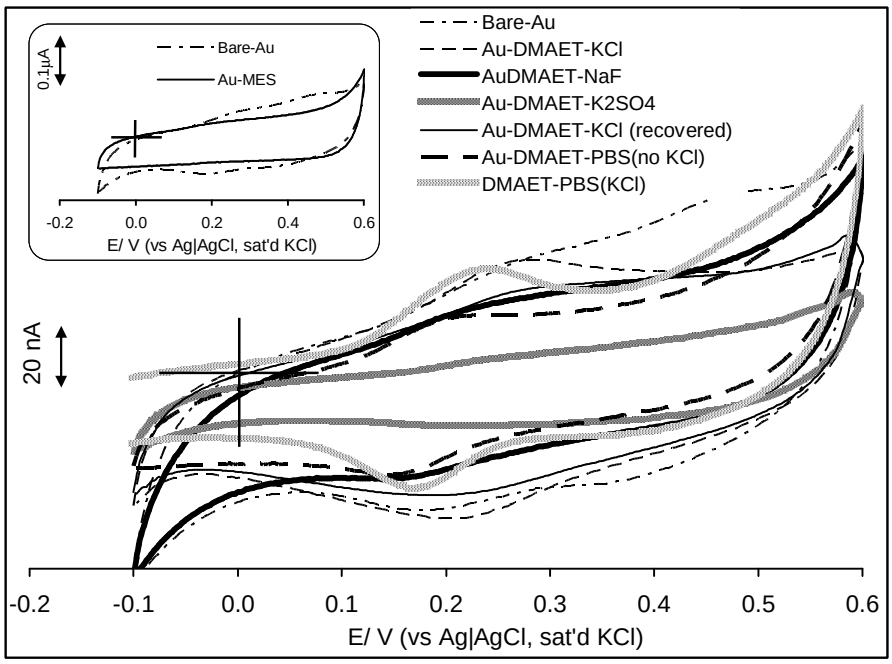

Figure 3.3: Typical cyclic voltammetric evolutions of Au-DMAET in 50 mM PBS (pH7.4), NaF, KCl and K_2SO_4; Inset shows the CV of the Sodium 2-mercaptoethanesulphonate SAM in 50 mM PBS (pH7.4).

Furthermore, the behaviour of the observed peak was also studied in PBS at different pH values. Figure 3.5 shows that the position of the peak potentials shifted as a function of the electrolyte's pH with a slope of *ca.* – 51 mV dec^{-1}.

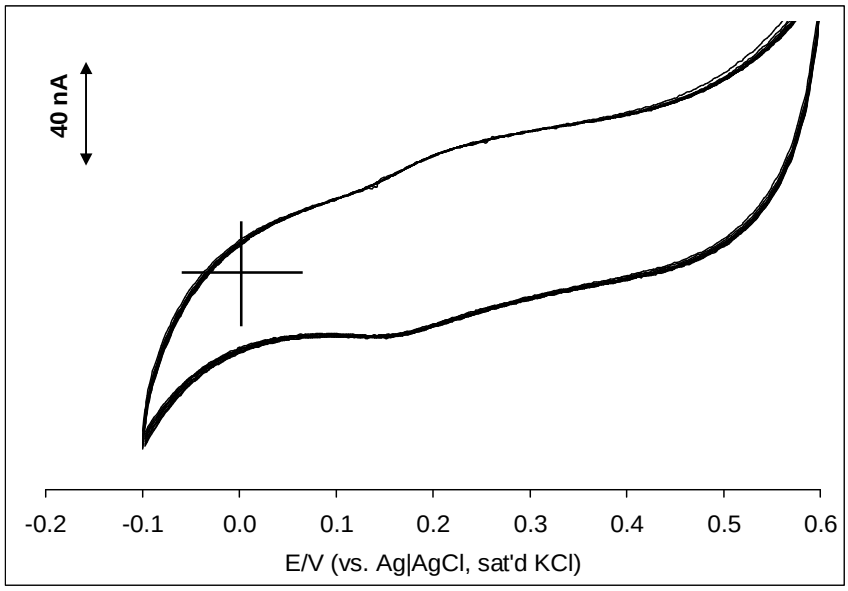

Figure 3.4: Cyclic voltammetric evolutions depicting the repetitive cycling of Au-DMAET in 50 mM NaF.

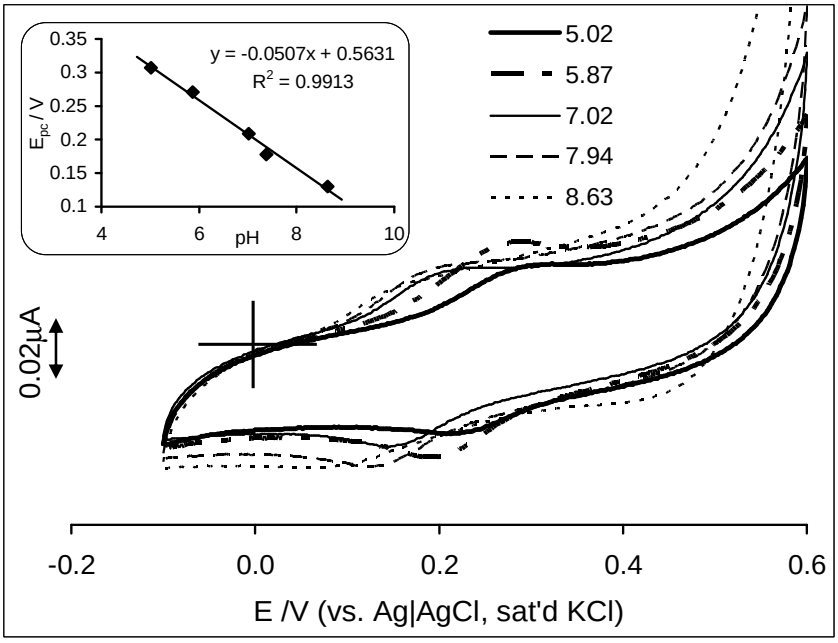

Figure 3.5: Typical cyclic voltammetric evolutions of Au-DMAET in phosphate buffer solutions at different pH levels.

3.1.3 Surface Coverage

Next, cyclic voltammetric reductive desorption experiment in 0.5 M KOH between 0 and –1.2 V (vs. Ag|AgCl sat'd KCl) were conducted. Equation 3.2 represents the chemistry of such irreversible desorption of the DMAET SAM:

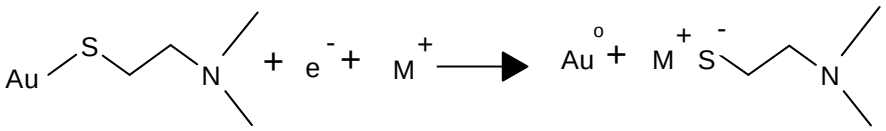

3.2

where, M+ represents the cation from the electrolyte [6]. The same equation holds for the DMAET-SWCNT-PABS. Figure 3.6 shows the sharp desorption peaks at -0.72 V and -0.68 V for DMAET and DMAET-SWCNT-PABS, respectively.

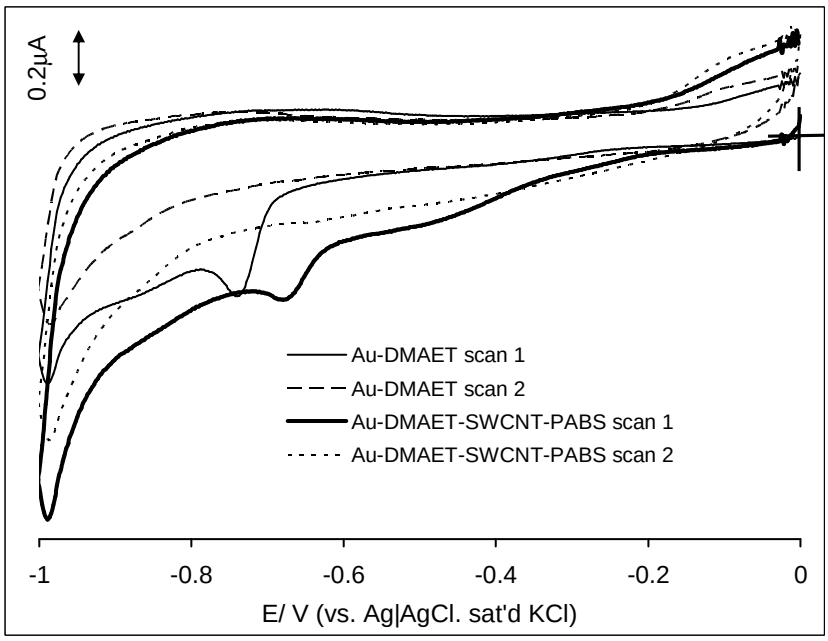

Figure 3.6: Cyclic Voltammetric reductive desorption of DMAET and DMAET-SWCNT-PABS in 0.5 M KOH.

From the area (i.e., charge, Q / C) under the respective reductive peaks, the surface concentrations (Γ_{SAM} /mol cm^{-2}) of the DMAET and DMAET-SWCNT-PABS were estimated from Equation 3.3:

$$\Gamma^{SAM} = \frac{\quad}{\quad} \qquad 3.3$$

where n represents number of electrons transferred (equals 1), F is the Faraday constant and A is the experimentally determined area of the gold electrode. The Γ_{SAM} was approximately 0.53 nmol cm^{-2} for DMAET and 0.58 nmol cm^{-2} for DMAET-SWCNT-PABS. This similar surface coverage for both SAMs suggests that the observed electrochemistry was due to SWCNT-PABS attached onto the surface of the DMAET molecules.

3.1.4 Electron Transfer Dynamics: Estimation of Surface pK_a of DMAET

The charge transfer resistance (R_{ct}/Ω) values, extracted from the impedance spectra using the Randles equivalent circuit shown in Figure 1.5 to fit the data, decreased as Au-DMAET (112 Ω) < Au-DMAET-SWCNT-PABS (115 Ω) < bare-Au (730 Ω). The slightly faster electron transfer recorded at the Au-DMAET compared to the Au-

DMAET-SWCNT-PABS is attributed to the strong electrostatic attraction between the positively charged DMAET and the negatively charged $[Fe(CN)_6]^{3-/4-}$ species.

The pK_a of the surface-confined species is the value of the pH in contact with monolayer when half of the functional groups are ionized [7-9]. Figure 3.7 represents typical impedance spectral profiles of Au-DMAET in PBS solutions of $[Fe(CN)_6]^{3-/4-}$. Increase in solution pH from ~4.5 to 9.0 clearly depicts changes in electron transport, signified by increasing R_{ct} values shown in Figure 3.8. At low pH (< pH 7.0), the $-N(H)^+(CH_3)_2$ head group is mostly protonated (reverse reaction of Equation 3.2 favoured) thereby enhancing electrostatic attraction between the Au-DMAET and the negatively charged $[Fe(CN)_6]^{3-/4-}$ redox probe. However, increase in solution of pH>7.0 leads to an increase in R_{ct} caused by deprotonation process (forward reaction of Equation 3.2 favoured) resulting in electrostatic repulsion between the DMAET head group and the redox probe. From the mid-points of the R_{ct} vs. pH plots (Fig. 3.8), the surface pK_a of the DMAET was estimated as ~7.6, which is about 3 pK_a units lower than its solution pK_a of 10.8 [10].

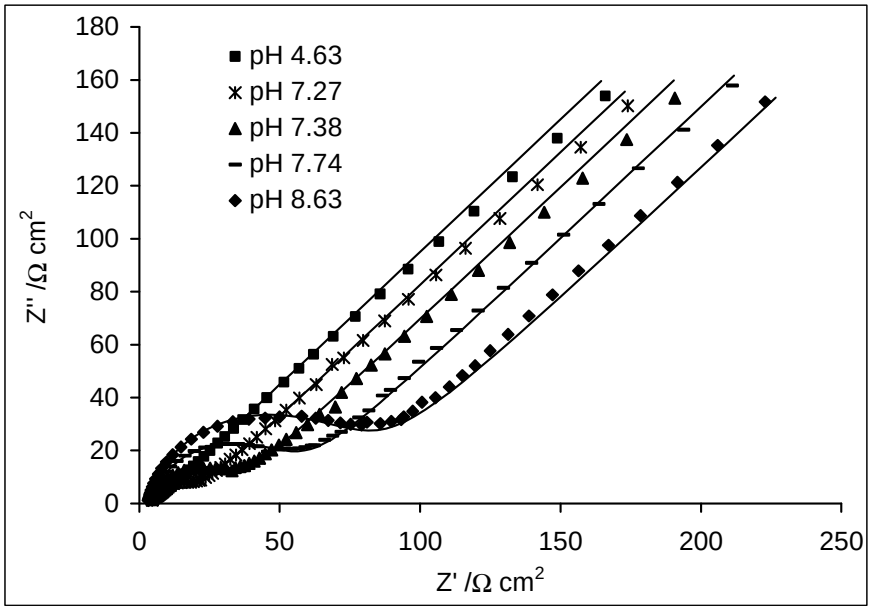

Figure 3.7: Examples of the impedimetric responses of Au-DMAET at different pH values of $[Fe(CN)_6]^{3-}$/ $[Fe(CN)_6]^{/4-}$ solutions.

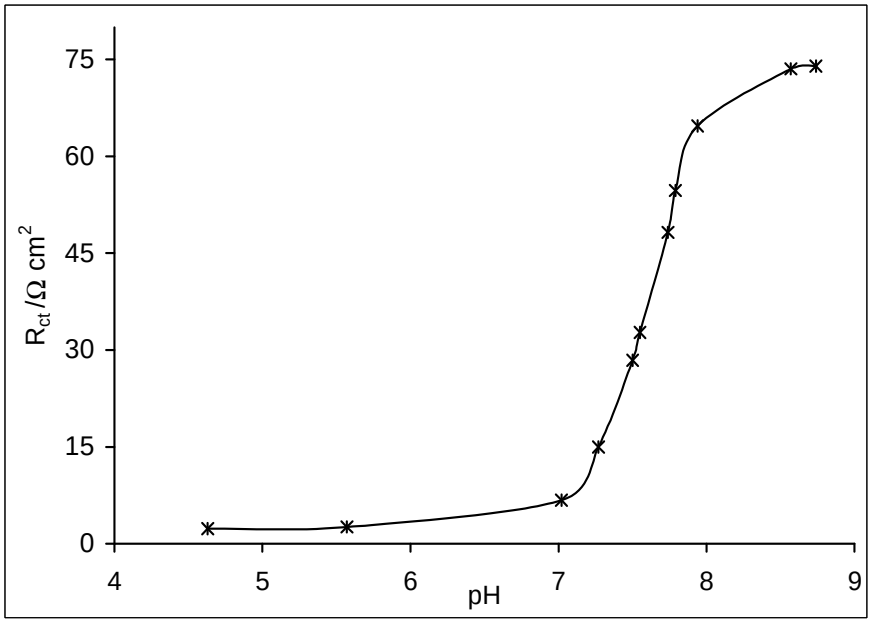

Figure 3.8: Plot of Charge Transfer Resistance (R_{ct}) from the impedimetric responses of Au-DMAET vs. pH in $[Fe(CN)_6]^{3-}$/ $[Fe(CN)_6]^{/4-}$ solutions.

The reason for this large shift of pK_a, as opposed to the usual order of < 1 pK_a is not understood at this time. However, the results are similar to the observation of Saby *et al.* [11] who reported a shift of the pK_a of benzoic acid from a value of 4.2 in solution to a value of 2.8 when covalently attached onto a glassy carbon electrode, which they speculated to be due to some specific interfacial effect between the carbon surface and the carboxylate functionalities or the phenyl ring of the layer. On the other hand, Abinam *et al.* [12] who also observed such large shifts in benzoic acid proved this to be due to some thermodynamic effects. Also, interestingly, Abinam *et al.* [13] observed a large shift in the pK_a of "Jeffamine" from a value of 9.7 in solution to a value of 7.1 when covalently attached onto a carbon substrate and attributed that to entropic contribution arising from the ordering/disordering of solvent molecules at the carbon-water interface. Therefore, these results may be connected with some specific interfacial effect between the DMAET and the gold surface or thermodynamic effects playing some interesting role.

3.2 Single Walled Carbon Nanotubes and Nanosized Iron (II) Phthalocyanine modified Gold Electrodes

3.2.1 LBL Self-Assembly

Figure 3.9 shows the FESEM images of (a) Iron (II) phthalocyanine microcrystals and (b) Iron (II) phthalocyanine nanoparticles (*nano*FePc) clearly confirming the successful nanostructuring of the bulk (crystallite form) FePc molecules to their amorphous, nanoparticles protected by CTAB particles. The EDX profile of *nano*FePc depicted in Figure 3.9 (c) confirms the presence of iron and the sulphur peak at 2.4 eV could have arisen from the synthesis.

The multilayer build-up depicted in Scheme 3.2, involving *nano*FePc and SWCNT-PABS follows the well known LBL technique, where steps (ii) and (iii) are repeated four times for this assembly. To my knowledge, this is the first time this type of molecular building involving both SWCNT-PABS and FePc complex is described.

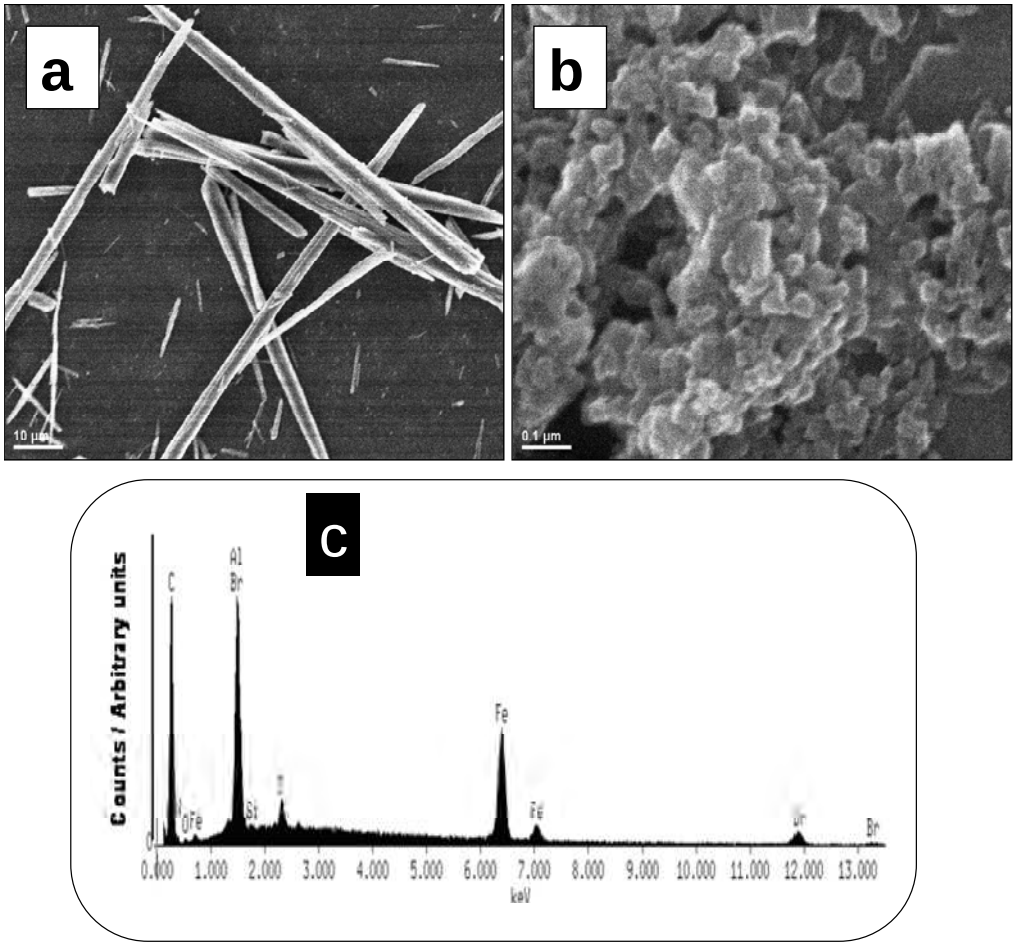

Figure 3.9: Scanning electron microscopy images of (a) Iron (II) phthalocyanine microcrystals and (b) Iron (II) phthalocyanine nanoparticles. (c) EDX profile of Iron (II) phthalocyanine nanoparticles.

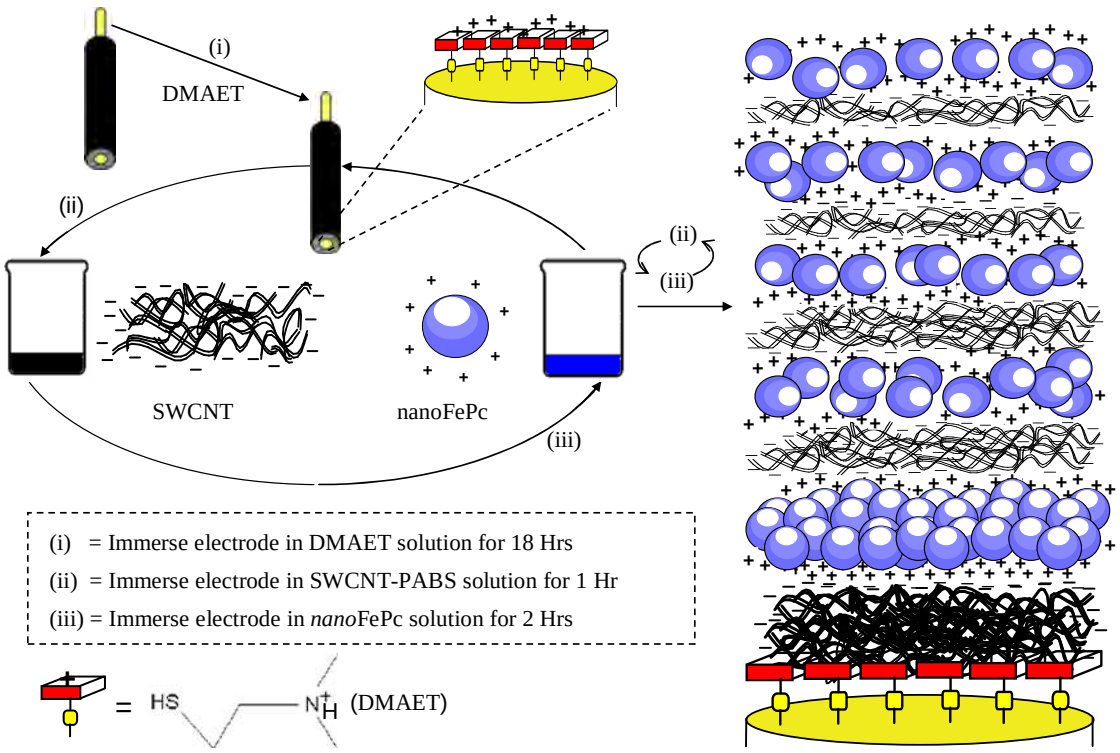

Scheme 3.2: Schematic representation depicting the layer-by-layer assembly of *nano*FePc and SWCNT-PABS on gold surface. The fabrication conditions are as stated in the experimental section. Note that this representation is merely a cartoon, so not drawn to scale.

3.2.2 Characterization

3.2.2.1 Atomic Force Microscopy

The AFM images of the bare-Au, Au-DMAET and Au-DMAET-SWCNT-PABS are shown and discussed in section 3.1.1. Figure 3.10 shows typical 3-D AFM images of (a) Au-DMAET-SWCNT-PABS and (b) Au-DMAET-(SWCNT-PABS-*nano*FePc)$_1$, (c) Au-DMAET-(SWCNT-PABS-*nano*FePc)$_3$ and (d) Au-DMAET-(SWCNT-PABS-*nano*FePc)$_5$.

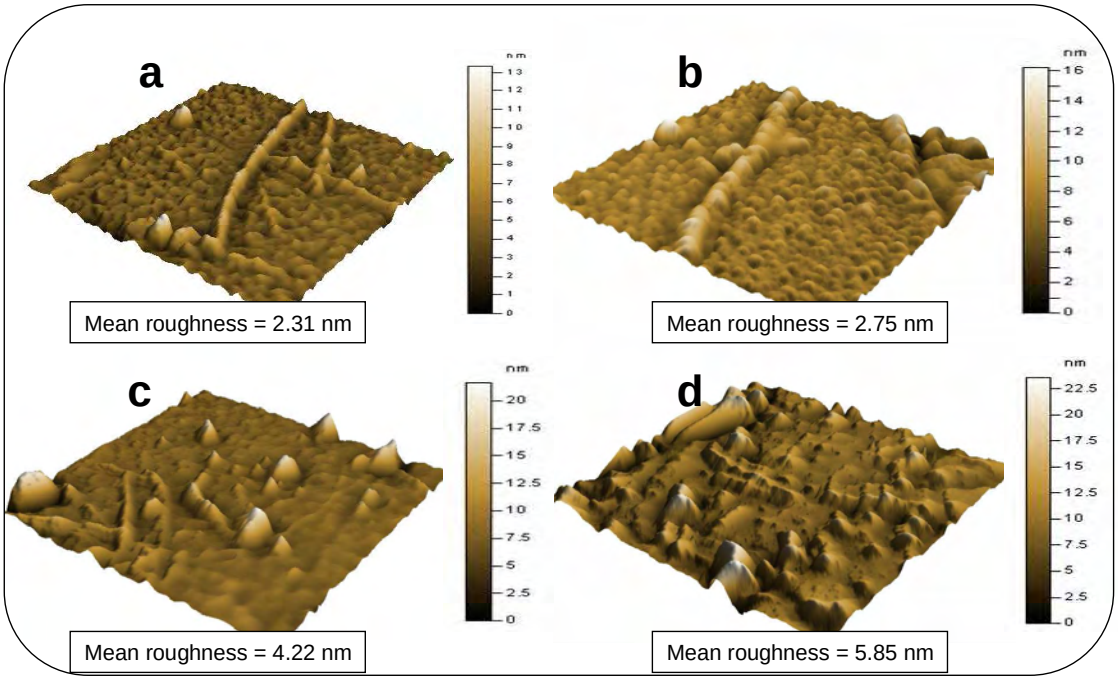

Figure 3.10: 3-D AFM images of (a) Au-DMAET-SWCNT-PABS and (b) Au-DMAET-(SWCNT-PABS-*nano*FePc)$_1$, (c) Au-DMAET-(SWCNT-PABS-*nano* FePc)$_3$ and (d) Au-DMAET-(SWCNT-PABS-*nano*FePc)$_5$.

As can be seen from the data in Figure 3.10, there is a continuous increase (from a–d) in the root mean square deviation (R_q) and maximum height (R_z) of the roughness profiles, indicating the formation of the various modifiers on gold plate. The electrostatic attraction between the negatively charged SWCNT-PABS and the positively charged *nano*FePc particles resulted in an aggregation of *nano*FePc particles forming clusters in the path of the tubes (Fig. 3.10b). Other important observations here include that the first SWCNT-PABS layer on the electrode (i.e, DMAET-SWCNT-PABS) is

much thicker than subsequent SWCNT-PABS layers (*nano*FePc-SWCNT-PABS), suggesting that the interaction between the base monolayer (DMAET) and SWCNT-PABS is stronger than that between SWCNT-PABS and *nano*FePc. Previous investigations have shown that MPC and related complexes strongly adsorb on CNT-modified electrodes [14]. In addition, *nano*FePc is thicker on the first bilayer compared to the subsequent bilayers, possibly due to the strong electrostatic interactions between DMAET and SWCNT-PABS. The AFM images (exemplified in Figure 3.10) show growth and formation of SWCNT-PABS-*nano*FePc films' root mean square (rms) increasing proportionally with increasing bilayers (Fig. 3.11).

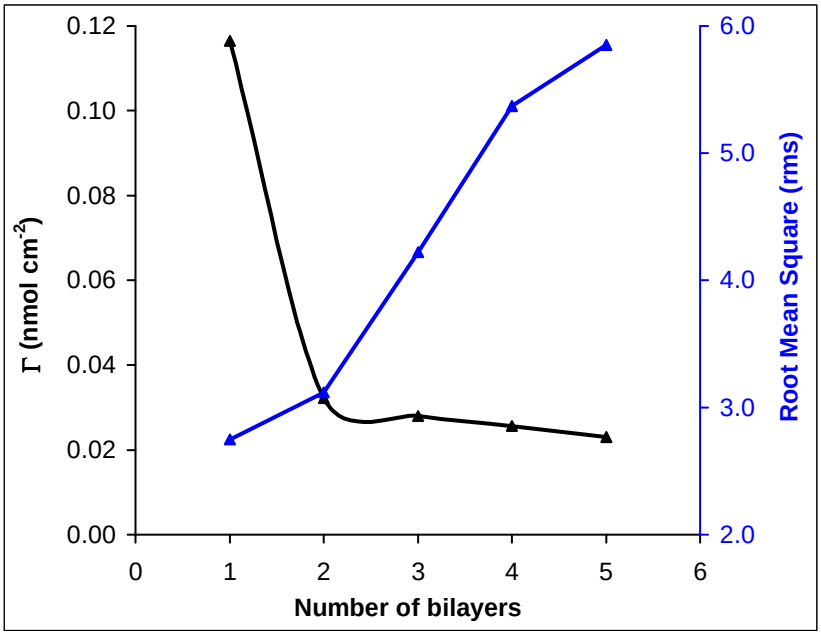

Figure 3.11: Plot of surface coverage (Γ) and Root Mean Square (rms) of *nano*FePc vs. bilayers.

3.2.2.2 Surface Coverage

Cyclic voltammetric evolutions of the bilayers in PBS (Fig. 3.12) showed clear quasi-reversible redox couple centered at $E_{1/2}$ ≈ 0.22 V (vs. Ag|AgCl, sat'd KCl) which, based on redox-active FePc thin fims reports, is attributable to the Fe^{III}/Fe^{II} redox couple [15]. Both Au-DMAET and Au-DMAET-SWCNT-PABS exhibited similar quasi-reversible processes as for the bilayers (not shown) but these couples are very weak with current responses much smaller (~ in the nA range) than the *nano*FePc (in the μA), supporting the assumption that the redox process is due to *nano*FePc. As the bilayer increases, the charges (anodic and cathodic) decreased.

The surface coverage (Γ_{MPc} /mol cm^{-2}) for each of the SWCNT-PABS-*nano*FePc bilayers was obtained by integrating the anodic charges (Q) and employing the formula given in Equation 3.3. From the plot of surface coverage vs. the number of bilayers (Fig. 3.11), the first layer (120 pmol cm^{-2}) was higher than the subsequent (2 – 5) bilayers (*ca.* 30 pmol cm^{-2}), implying that the first *nano*FePc layer mainly assumed standing/vertical orientation while the subsequent *nano*FePc layers lie flat on the underlying SWCNT-PABS layers (as depicted in the multi-layer cartoon, scheme 3.2). The highest coverage seen on the first bilayer suggests presence of more *nano*FePc than subsequent layers, corroborating the AFM topographic evolutions.

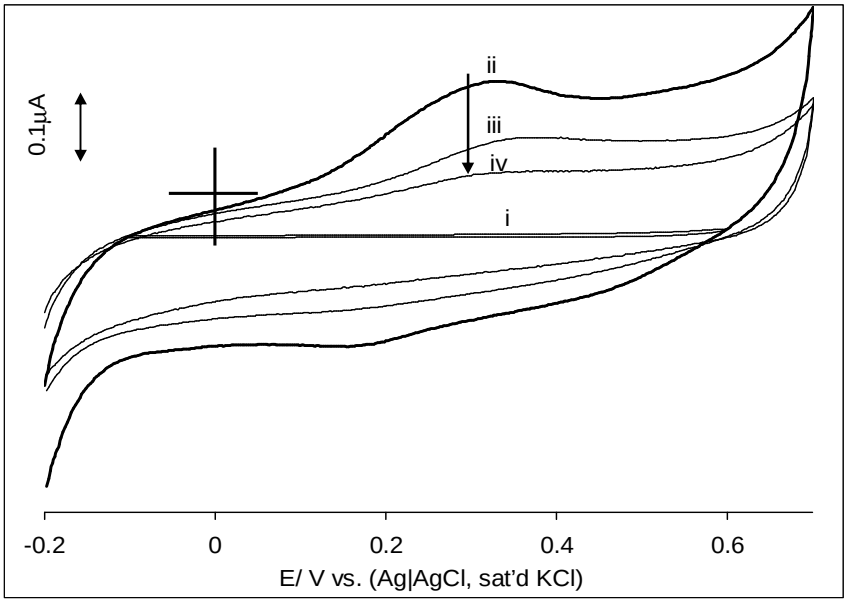

Figure 3.12: Typical CV profiles of (i) bare-Au, (ii) 1st, (iii) 3rd and (iv) 5th bilayers at a scan rate of 30 mV s^{-1} in PBS (pH 7.4). Current response decreases from (ii) to (iv), indicated by the direction of the arrow as the number of bilayers increase.

3.2.2.3 Cyclic Voltammetry

Figure 3.13 illustrates the CV evolutions of the electrodes in the same electrolyte conditions (5 mM $[Fe(CN)_6]^{4-}$ / $[Fe(CN)_6]^{3-}$). The experiment was aimed at answering the question as to what extent do the modifying species permit the electron transfer of the $[Fe(CN)_6]^{4-}$ / $[Fe(CN)_6]^{3-}$ to the underlying gold electrode. The CV responses of the electrodes (including the *nano*FePc-SWCNT-PABS (not shown) as the outer most layer) were essentially the same in terms of (i) the anodic (I_{pa}) and cathodic (I_{pc}) peak current heights, (ii) the peak-to-peak

separation potential ($\Delta E_p \approx 70$ mV vs. Ag|AgCl, sat'd KCl), and (iii) the equilibrium potential ($E_{1/2} \approx 0.25$ V vs. Ag|AgCl, sat'd KCl).

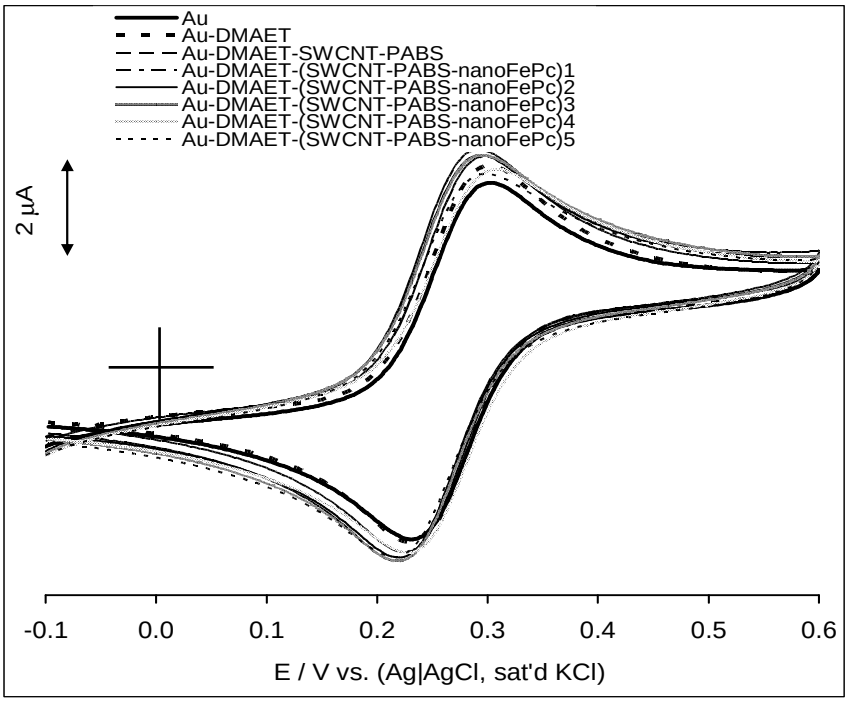

Figure 3.13: Typical CV profiles of the bare-Au, Au-DMAET, Au-DMAET-SWCNT-PABS and Au-DMAET-(SWCNT-PABS-*nano*FePc)$_{1\text{-}5}$ assemblies in 0.1 M KCl containing equimolar mixture of $[Fe(CN)_6]^{3-}$/ $[Fe(CN)_6]^{/4-}$ solutions at a scan rate of 25 mV s^{-1}.

3.2.2.4 Electrochemical Impedance Spectroscopy

Impedance spectroscopy provides a better description of the electrochemical system compared to cyclic voltammetry [16] and was therefore employed to follow the charge transfer kinetics occurring at these electrodes. The nyquist plots shown in Figure 3.14 for the bare-Au, Au-DMAET, Au-DMAET-SWCNT-PABS and subsequent bilayers

satisfactorily fitted (in terms of low percent errors obtained after several iterations, Table 3.1) the modified Randles equivalent circuit (Fig. 1.8a).

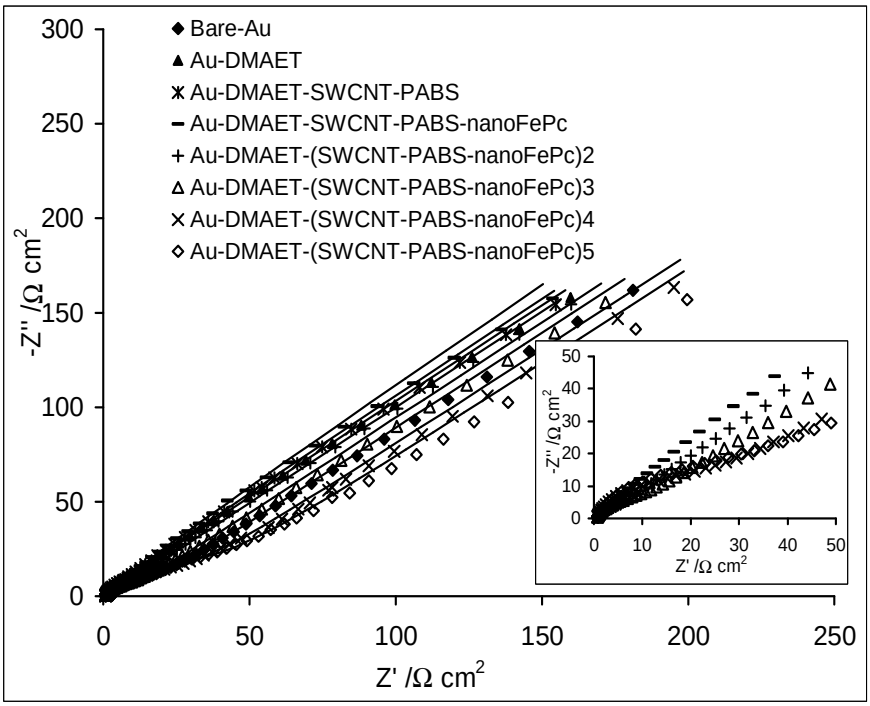

Figure 3.14: Nyquist plots resulting from the bare-Au, Au-DMAET, Au-DMAET-SWCNTPABS and Au-DMAET-(SWCNT-PABS-*nano*FePc)$_{1-5}$ assemblies in 0.1 M KCl containing equimolar mixture of $[Fe(CN)_6]^{3-}$/ $[Fe(CN)_6]^{/4-}$ solutions. Inset shows the high frequency area of the bilayers only.

This equivalent circuit comprised the mixed kinetic and diffusion-controlled processes with R_s as the resistance of the electrolyte and electrode, R_{ct} as the charge-transfer resistance (domain of kinetic control) and Z_w as the Warburg impedance (domain of mass transport

control) resulting from the linear diffusion of redox probe ions from the bulk electrolyte. It is also likely that mass transport is limited by diffusion within and inside the layered structure. Given the inherent roughness of the bare and modified gold surfaces (as also seen from the AFM images), the constant phase angle element, in which the double layer capacitance is replaced by CPE in the Randles' model was used to describe impedimetric data. CPE is ascribed to the energetic non-homogeneity arising from the surface roughness of the electrode. The impedance (Z_{CPE}) is a power-law dependent interfacial capacity given as shown in Equation 1.18:

$$Z_{CPE} = Q(j\omega)^{-n}$$

As previously mentioned n is an exponent (n≤1 for a physically reasonable situation) equals unity for the case of ideal capacitor. It is important to note that the n values lie approximately between 0.7 and 0.8 suggesting pseudocapacitive behavior. The Z_w values, which correspond to the diffusion process of the oxidized and reduced species of the $[Fe(CN)_6]^{3-/4-}$ couple, are approximately of the same magnitude for all the electrodes. Ideally, R_s and Z_w should not be affected by modification of the electrode surface [17].

From data in Table 3.1, the Au-DMAET gave the fastest electron transfer, which may be explained as the consequence of the strong

electrostatic attraction between the positively charged DMAET and the negatively charged $[Fe(CN)_6]^{3-/4-}$ species. In general, the result indicates that charge transfer processes between the $[Fe(CN)_6]^{3-/4-}$ and the underlying gold surface are easier on the initial bilayers than the subsequent bilayers. This may be due to the build-up of the negatively charged SWCNT-PABS leading to more repulsive interaction between the SWCNT-PABS and $[Fe(CN)_6]^{3-/4-}$ species. The modified electrode exhibited stable electrochemistry as each of the voltammograms recorded did not change after several repetitive cycling. After the fifth bilayer, there was no significant change.

The comparative Bode plots of -Phase angle vs. log f is shown in Figure 3.15 (a) showing well-defined symmetrical peaks at different maxima for the different electrodes, corresponding to the different relaxation processes of the electrode|solution interfaces. In all cases, the phase angles were less than 90°, confirming the pseudo-capacitive nature of the electrodes. The bare-Au gave a maximum value of ~41° at 316 Hz corresponding to the relaxation process of the Au|solution interface. Upon modification with the DMAET, this relaxation process is depressed. However when modified with the SWCNT-PABS and the first bilayer, the relaxations shifts to ~ 50° range and at lower frequencies (0.1- 10000 Hz range). Interestingly, from the 2nd to subsequent bilayers, the peaks shift to 43.6° to 60.3° at

approximately the same frequency (1 kHz). These data clearly confirm that the $[Fe(CN)_6]^{3-/4-}$ redox reactions now take place at the surface of the modifying films rather than directly on the bare-Au surface. The log |*Z*| vs. log f type bode plot represented in Figure 3.15 (b) was also studied.

Table 3.1: Summary of the electrochemical impedance spectroscopic evolutions of the electrodes (*n* = 5), percentage errors from fitting the raw EIS data are shown in bracket.

Electrode	**Electrochemical impedance spectral parameters**				
	R_s (Ω cm^2)	**CPE (μF cm^{-2})**	**n**	**R_{CT} (Ω cm^2)**	**10^6 Z_w (Ω cm^2)**
bare-Au	2.66 (0.6)	19.18 (4.7)	0.84 (0.7)	14.68 (2.1)	2.12 (0.3)
Au-DMAET	0.79 (2.1)	18.45 (4.7)	0.85 (0.7)	2.25 (6.6)	2.21 (0.4)
Au-DMAET-SWCNT	0.61 (2.6)	28.7 (11.3)	0.67 (1.5)	2.31 (8.5)	2.17 (1.2)
Au-DMAET-(SWCNT-*nano*FePc)$_1$	0.63 (1.1)	29.01 (4.9)	0.69 (0.7)	2.45 (5.1)	2.03 (1.0)
Au-DMAET-(SWCNT-*nano*FePc)$_2$	0.69 (2.4)	20.96 (11.8)	0.85 (2.5)	3.54 (11.1)	2.28 (0.8)
Au-DMAET-(SWCNT-*nano*FePc)$_3$	0.60 (2.5)	15.21 (6.2)	0.82 (1.1)	10.57 (3.6)	2.15 (0.5)
Au-DMAET-(SWCNT-*nano*FePc)$_4$	0.58 (5.2)	12.58 (8.4)	0.82 (1.3)	25.68 (4.1)	2.01 (1.4)
Au-DMAET-(SWCNT-*nano*FePc)$_5$	0.52 (4.4)	9.89 (6.0)	0.80 (0.9)	34.30 (2.9)	2.07 (1.21)

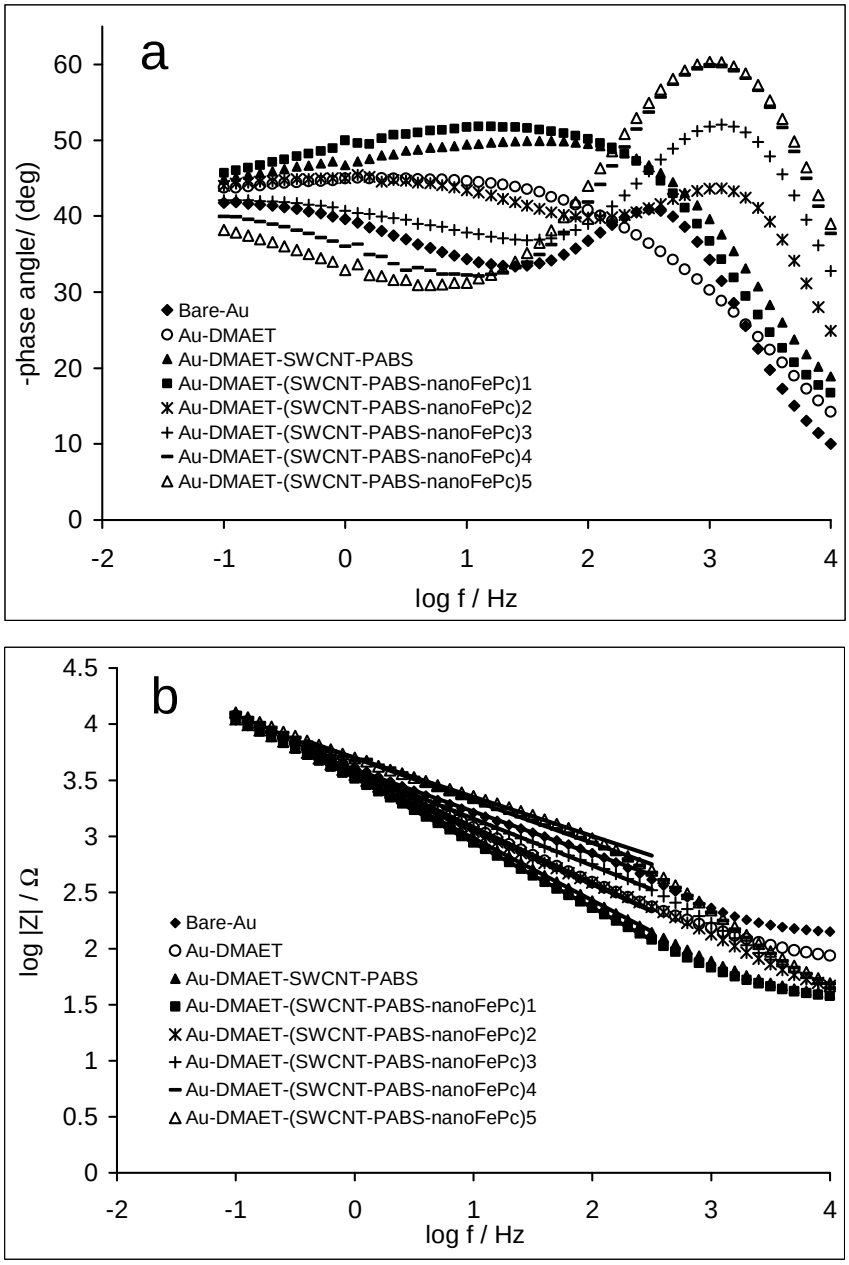

Figure 3.15: Bode plots of (a) -phase angle vs. log f and (b) log |Z| vs. log f for the bare-Au, Au-DMAET, Au-DMAET-SWCNT-PABS, Au-DMAET-(SWCNT-PABS-*nano*FePc)$_{1\text{-}5}$ bilayer assemblies in 0.1 M KCl containing equimolar mixture of $[Fe(CN)_6]^{3-}$/ $[Fe(CN)_6]^{4-}$ solutions.

From Figure 3.15 (b) the following slope values: -48 (r^2=0.999), -0.50 (r^2=0.999), -0.55 (r^2=0.999), -0.58 (r^2=0.999), -0.48 (r^2=0.999), -0.42 (r^2=0.999), -0.48 (r^2=0.998) and -0.45 (r^2=0.995) were obtained for bare-Au, Au-DMAET, Au-DMAET-SWCNT-PABS, 1st, 2nd, 3rd, 4th and 5th bilayers respectively. These slopes correspond to Warburg impedances and confirm that the SAMs studied in the work are redox-active and are not true capacitors as the estimated slopes are far from the ideal minus one value expected for true capacitors and usually observed for electro-inactive SAMs of alkanethiols.

3.2.3 Amplification of H_2O_2 Electrochemical Response

The possibility of using the electrode as a potential sensor for H_2O_2 in physiological pH conditions (pH 7.4) was also investigated. Figure 3.16 compares the reduction current responses of 1 mM H_2O_2 in PBS (pH 7.4) at increasing bilayers (*nano*FePc being the exposed layer, Figure 3.16a) and (SWCNT-PABS as the exposed layer, Figure 3.16b). The results show that unlike the *nano*FePc layers (Fig. 3.16a), when SWCNT-PABS forms the exposed layer of the electrode (Fig. 3.16b); there is no significant improvement in the response of H_2O_2 at a constant concentration. The results suggest that while *nano*FePc acts as the electrocatalyst, the SWCNT-PABS simply acts as the electron conducting nanowires for the reaction. This electrochemical

amplification of the current response of H_2O_2 by *nano*FePc multilayer is remarkable as it promises to provide a viable platform for the development of biosensors. From the current responses of the Au-DMAET-(SWCNT-PABS-*nano*FePc)$_5$ to changes in the concentrations of H_2O_2, the limit of detection and sensitivity was calculated to be 5.5×10^{-4} M and 0.87 m AM^{-1}, respectively. The modified electrode was stable and repeatedly used for the detection of H_2O_2 without significant deterioration of current signals.

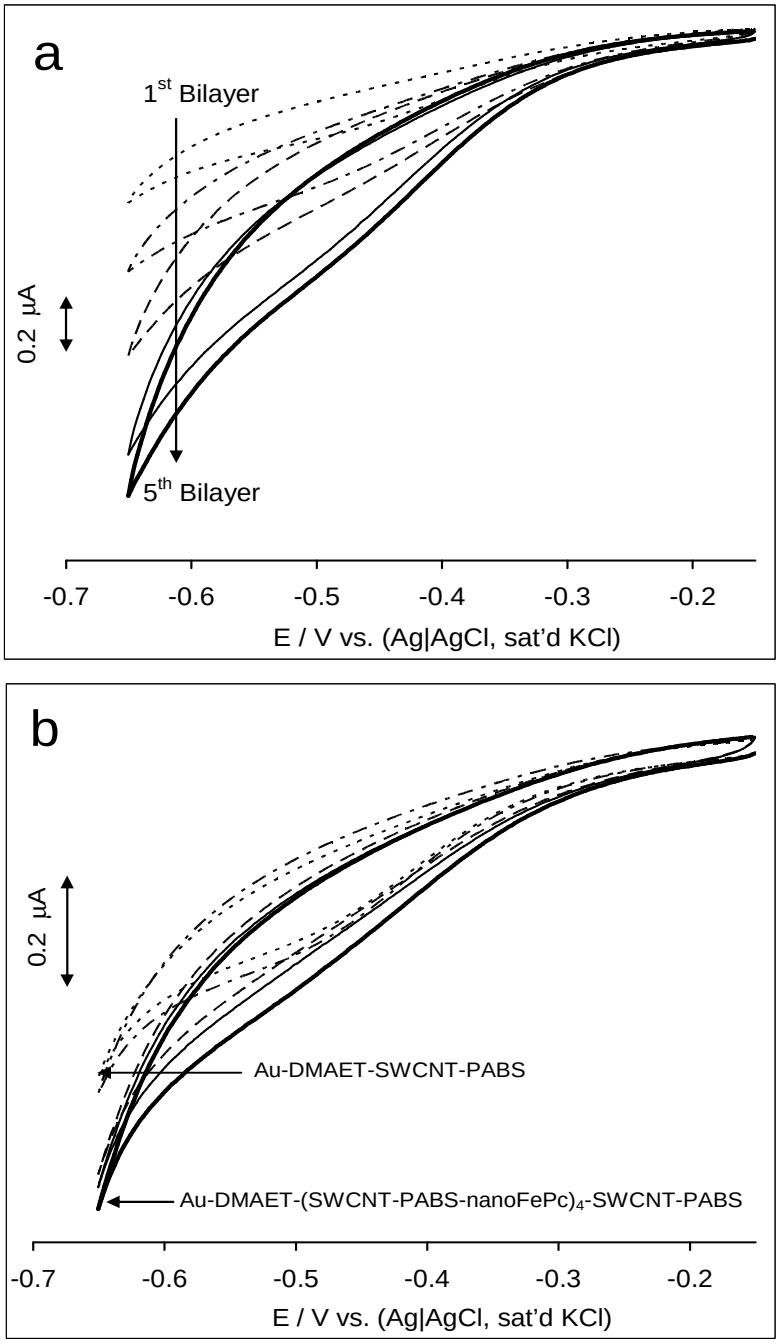

Figure 3.16: Typical CV profiles showing the impact of increasing (a) bilayer (*nano*FePc being the exposed layer) and (b) SWCNT-PABS layers (SWCNT-PABS as the exposed layer) on the current response of 1 mM H_2O_2 in PBS (pH 7.4). Scan rate: 25 mV s^{-1}.

3.2.3.1 Chronoamperometric Analysis

Based on the CV results described above, chronoamperometric technique was employed for the analysis of H_2O_2 (-300 mV) using the multilayer film electrode Au-DMAET-(SWCNT-*nano*FePc)$_5$ in pH 7.4 PBS. Figure 3.17 shows the chronoamperogram that was obtained for a series of H_2O_2 concentrations (0.032-0.268) mM.

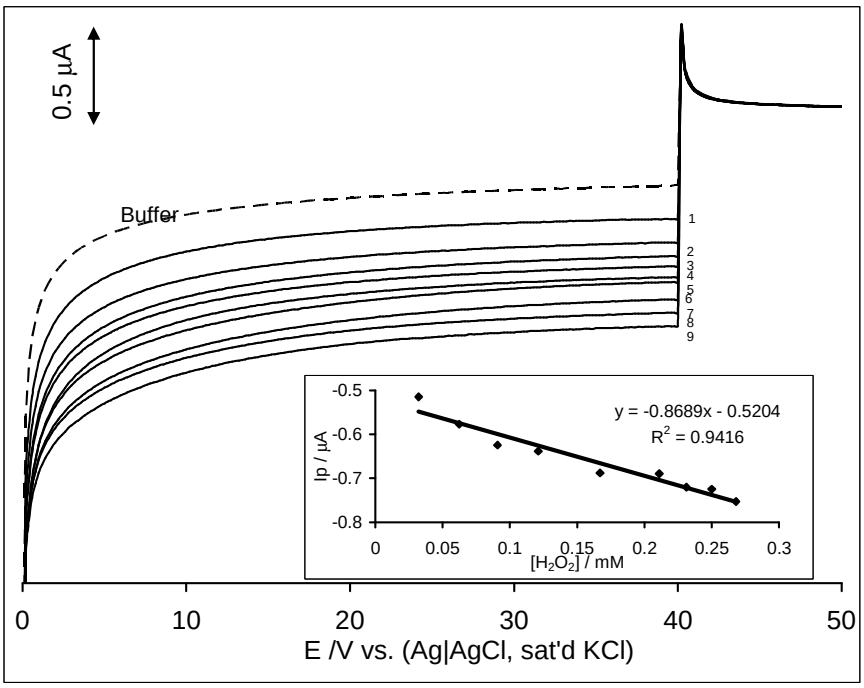

Figure 3.17: Chronoamperometric profile analysis of H_2O_2 in pH 7.4 PBS at a Au-DMAET-(SWCNT-*nano*FePc)$_5$ for a potential step of -300mV vs. Ag|AgCl. The numbers 1-9 correspond to 0.032, 0.062, 0.091, 0.121, 0.167, 0.211, 0.231, 0.250 and 0.268 mM H_2O_2 respectively.

From the current responses of the Au-DMAET-(SWCNT-*nano*FePc)$_5$ and the changes in the H_2O_2 concentration, the limit of detection (LoD

= 3.3s/m) [18], where s is the standard deviation of the intercept and the sensitivity, m, which is the slope of the plot of linear peak current vs. the concentration of H_2O_2,(inset Figure 3.17). The calculated values for the LoD and sensitivity are 5.50 x 10^{-4} M and -0.869 m AM^{-1} respectively. All data were obtained with the same electrode, rinsing the electrode prior to immersing it in a new concentration. Au-DMAET-(SWCNT-*nano*FePc)$_5$ was used in determining the catalytic rate constants and diffusion coefficients of H_2O_2 at constant concentration (at 10 μM in pH 7.4 PBS) poised at -0.3 V using the established Equation [19]:

$$\frac{I_{cat}}{I_d} = \gamma^{1/2}[\pi^{1/2} erf(\gamma^{1/2}) + \frac{\exp^{(-\gamma)}}{\gamma^{1/2}}] \qquad 3.4$$

where, $\gamma = kCt$ is the argument of the error function and in cases where $\gamma > 1.5$, erf($\gamma^{1/2}$) is almost equal to unity and the Equation 3.4 can be reduced to the following Equation 1.14:

$$\frac{I_{cat}}{I_L} = \pi^{1/2}(kC_o t)^{1/2}$$

where the symbols retain their usual meaning. At intermediate times (0– 2 s) of the chronoamperometric measurements the catalytic currents (I_{cat}) were dominated by the rate of the electrocatalyzed reduction of H_2O_2, therefore Equation 1.14 was used to calculate the

rate constant for the chemical reaction between H_2O_2 and the redox sites of surface immobilized $(SWCNT\text{-}nanoFePc)_5$. The plots of I_{cat}/I_L vs. $t^{1/2}$ (Fig. 3.18a) at different H_2O_2 concentrations for Au-DMAET-$(SWCNT\text{-}PABS\text{-}nanoFePc)_5$ were linear. The catalytic rate constant, k, calculated from the plot of slopes^2 vs. H_2O_2 concentration (Fig. 3.18b) is 12.15 $M^{-1}\ s^{-1}$.

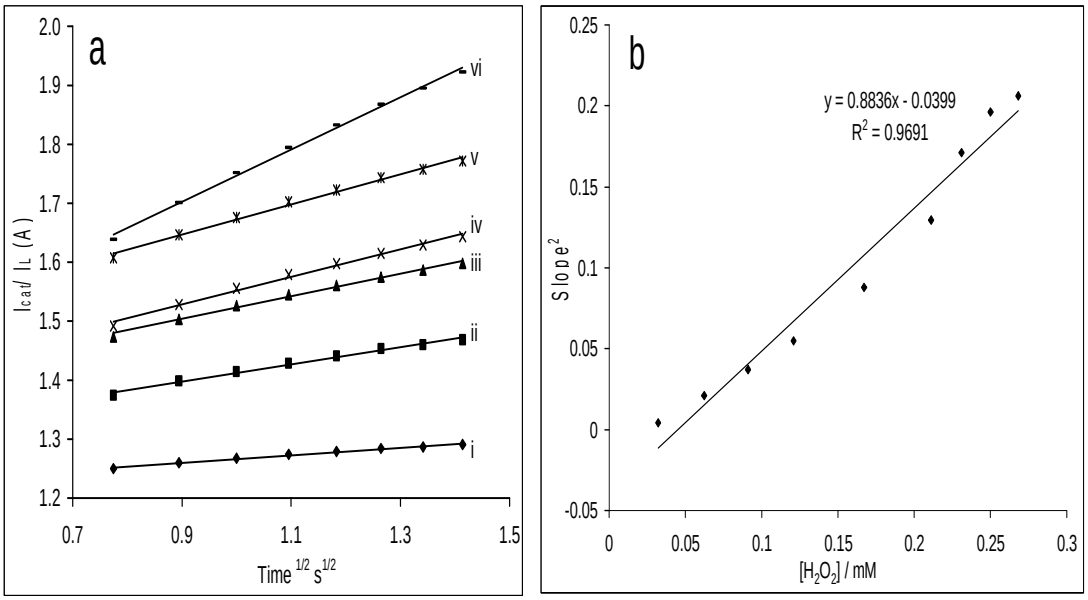

Figure 3.18: Plots of (a) I_{cat}/I_L vs. $t^{1/2}$ and (b) Slopes^2 vs. $[H_2O_2]$. The roman numerals (i) to (vi) correspond to 32.3, 62.5, 90.9, 121, 167 and 250 μM, respectively. Concentration values were selected for clarity.

Also, from the chronoamperometric data, the diffusion coefficient, D, was determined using the Cottrell equation represented in Equation 1.13:

$$I = nFAD^{1/2}C\pi^{-1/2}t^{-1/2}$$

where the symbols retain their usual meaning. The plots of I_{cat} vs. time$^{-1/2}$ (Fig. 3.19a) at different H_2O_2 concentrations for Au-DMAET-(SWCNT-PABS-nanoFePc)$_5$ were linear, and from the subsequent plot of the respective slopes vs. H_2O_2 concentration (Fig. 3.19b), the diffusion coefficient was calculated to be 12.80 x 10 cm^2 s^{-1}. The values vary from one electrode to another; various D values have been reported in literature [20, 21]. Yang et al. [20] reported a value of 2.0x10^{-9} cm^2 s^{-1} for epinephrine at GCE-cys-nanoAu while Wang et al. [21] reported a value of 7.4 x 10^{-5} cm^2 s^{-1} at nano-Au-mixed dithiothreitol/dodecanethiol gold electrode.

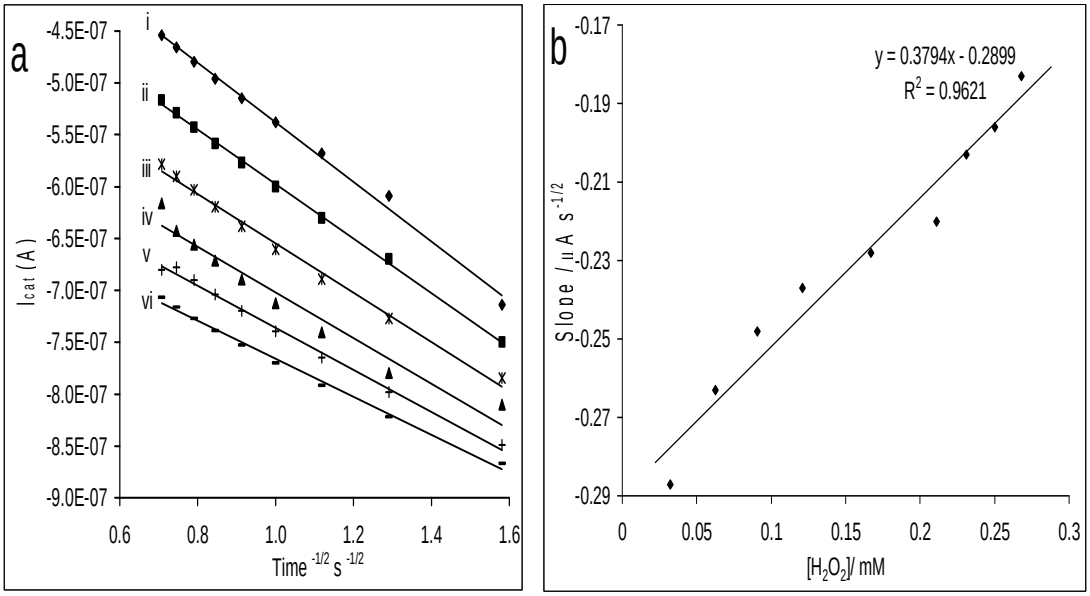

Figure 3.19: Plots of (a) I_{cat} vs. $t^{-1/2}$ and (b) Slopes vs. [H_2O_2]. The roman numerals (i) to (vi) correspond to 32.3, 62.5, 121, 211, 231 and 268 μM, respectively. Concentration values were selected for clarity.

3.2.4 Comparative Electrocatalytic Responses at Electrodes towards Epinephrine

The layer-by-layer assembly depicted in Figure 3.20 involving SWCNT-PABS and *nano*FePc showed an increase in bilayer formation results in a decrease in epinephrine current response. Figure 3.21 compares the cyclic voltammetric evolutions of 10 μM EP at bare-Au, Au-DMAET, Au-DMAET-SWCNT-PABS and Au-DMAET-SWCNT-PABS-*nano*FePc in phosphate buffer solution. The cyclic voltammetric evolutions obtained in buffer solution alone have been dealt with and discussed in section 3.1.2.

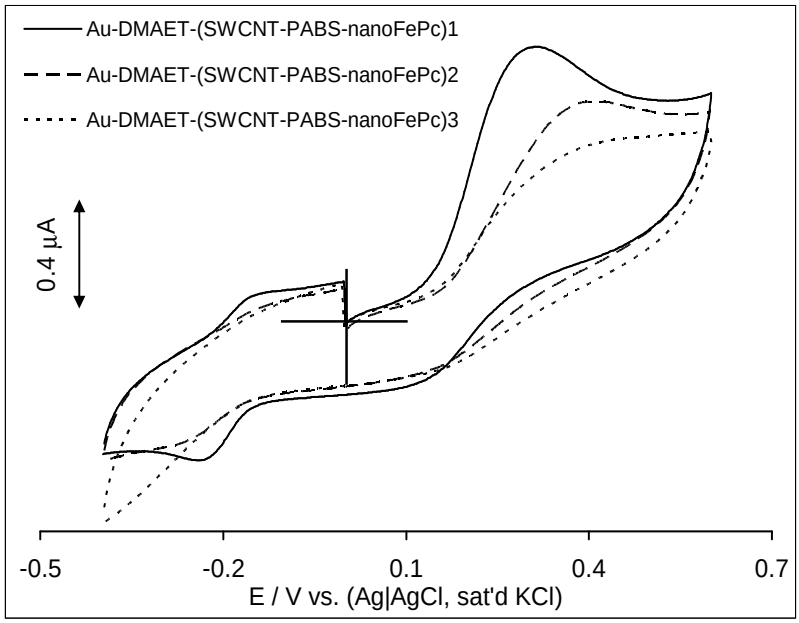

Figure 3.20: Cyclic voltammetric profiles of Au-DMAET-(SWCNT-PABS-*nano*FePc)$_{1-3}$ assemblies in 10 μM epinephrine in PBS (pH 7.4). Scan rate: 25 mV s^{-1}.

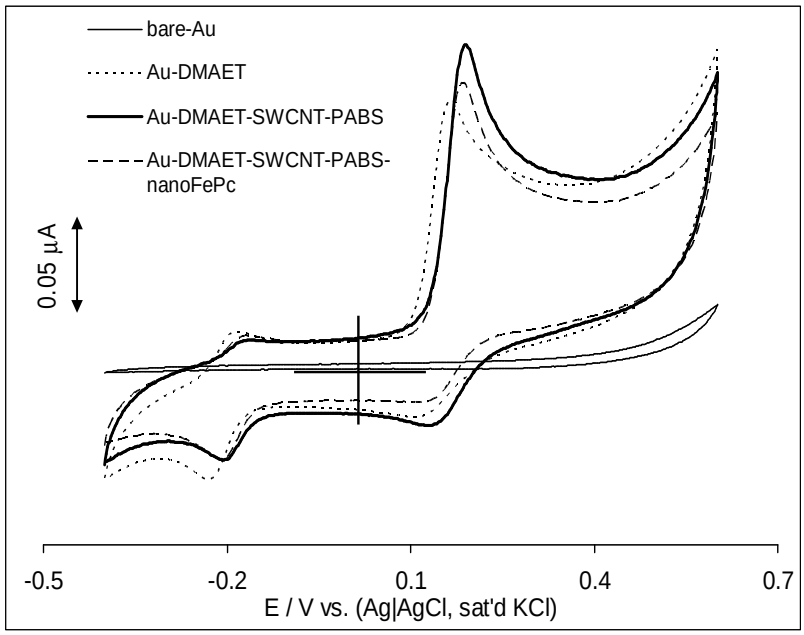

Figure 3.21: Cyclic voltammetric evolutions in the presence of 10 µM epinephrine in PBS (pH 7.4) at bare-Au, Au-DMAET, Au-DMAET-SWCNT-PABS and Au-DMAET-SWCNT-PABS-*nano*FePc. Scan rate: 25 mV s^{-1}.

The observed CV evolutions are characteristic of epinephrine redox process [22-23] involving an irreversible anodic peak at the anodic potential window (corresponding to the oxidation of epinephrine to epinephrinequinone), and at the reduction window, a pseudo-reversible couple corresponding to processes due to epinephrinequinone/ leucoadrenochrome and leucoadrenochrome/ adrenochrome. It can be seen from the comparative CV profiles in Figure 3.21 that Au-DMAET-SWCNT-PABS shows greater catalytic response towards the detection of 10 µM epinephrine compared to Au-

DMAET-SWCNT-PABS-*nano*FePc, Au-DMAET and bare-Au. However, it has been documented that Au-cys-SWCNT and Au-cys-SWCNT-CoTAPc show similar catalytic response in terms of current response towards the detection of epinephrine [24]. Therefore, the effect of electrode passivation was investigated.

3.2.4.1 Passivation Studies

Electrode passivation occurs when the surface of the electrode becomes 'blocked' by the species in solution. This implies that the electrodes may demonstrate a similar current response after a few scan as apposed to only after the initial scans. The extent of passivation for the electrodes in relation to each other can be measured from the plot of epinephrine peak current, I_p vs. number of scans shown in Figure 3.22. The percentage decrease in the peak current, I_p after the first scan for Au-DMAET is ~35% greater than the percentage decrease in the current after the first scan of Au-DMAET-SWCNT-PABS and Au-DMAET-(SWCNT-PABS-*nano*FePc)$_1$. After the second scan it can be seen that Au-DMAET-SWCNT-PABS is very stable whereas Au-DMAET-(SWCNT-PABS-*nano*FePc)$_1$ and Au-DMAET continue to show further decrease in peak current response upon subsequent scans. These results prove that Au-DMAET-SWCNT-PABS is

the best electrode and will therefore be used for the remaining electroanalytical studies in this section.

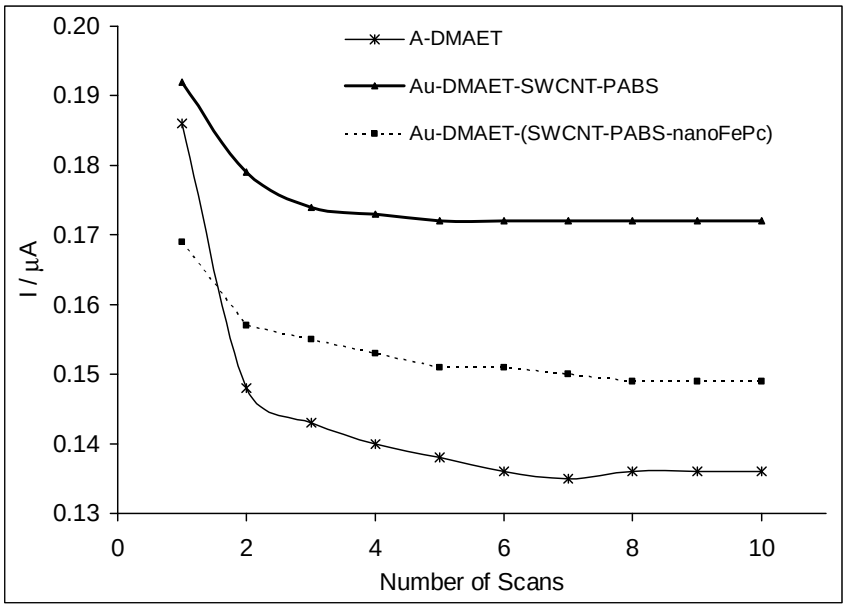

Figure 3.22: Plot of EP peak current (I_p) versus number of CV scans.

3.2.4.2 Rotating Disc Electrode Studies

Figure 3.23 shows the RDE data obtained at different rotating speeds (ω) for 10^{-5} M epinephrine electro-oxidation in phosphate buffer pH 7.4 using Au-DMAET-SWCNT-PABS. Figure 3.23 inset (a) shows the plot of limiting current (I_L) vs. $\omega^{1/2}$ (Koutecky-Levich plot) and (b) Tafel slope for the oxidation of epinephrine.

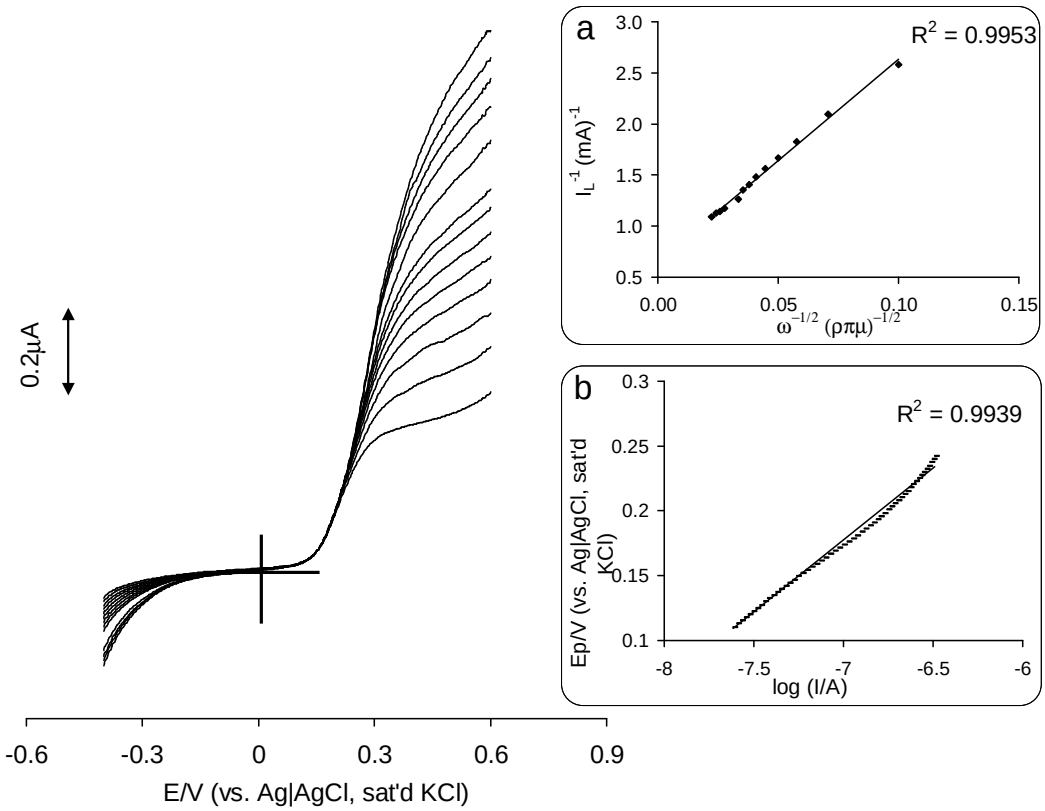

Figure 3.23: RDE voltammograms obtained at different rotating speed (ω) for 10^{-5} M epinephrine electro-oxidation in phosphate buffer pH 7.4 using Au-DMAET-SWCNT-PABS. Inset (a) shows the plot of I_L^{-1} versus $\omega^{-1/2}$ and (b) shows the Tafel slope for the oxidation of epinephrine from the RDE experiment. Scan rate = 50 mV s^{-1}.

The Koutecky-Levich plot was found to be linear with positive intercept; this indicates that the electrode reactions are controlled by both kinetics at the electrode surface and the mass transport of epinephrine species at the electrode surfaces. Using Equation 1.15 above the k_{ch} value obtained from the intercepts of the regression lines

was found to be $2.2x10^7$ $mol^{-1}cm^3s^{-1}$, a value much higher than that reported in literature [25]

Inset (b) in Figure 3.23 shows the plot of the Ep vs. the log of the kinetic current and the Tafel slope which represents the slope of this plot was approximately 70 mV dec^{-1} at all the potentials. Tafel slope value close to 60 mV dec^{-1} suggest a catalyst fast redox process as the first step followed by a non-redox (chemical step) rate-determining step (rds) such as analyte binding with the catalyst or possible deprotonation of the analyte [26,27] as a possible mechanism. The involvement of a chemical step in the rds is in agreement with the Koutecky-Levich plot which was found to be linear with positive intercept. The rate determining chemical step could be due to possible pi-pi interaction between SWCNT-PABS and EP molecule since CNTs are known for their ability to interact with organic aromatic compounds through pi-pi interaction and possibly also by hydrophobic interaction [28].

3.2.4.3 Chronoamperometric Analysis

Double potential step chronoamperometric experiments were recorded at the Au-DMAET, Au-DMAET-SWCNT-PABS and Au-DMAET-(SWCNT-PABS-*nano*FePc) by polarizing the potentials to 0.18 V and 0.0 V. Figure 3.24 shows well resolved double-step

chronoamperometric evolutions obtained at the Au-DMAET-SWCNT-PABS electrode in the absence (buffer alone) and presence of consecutive addition of 1 ml of 1 μM epinephrine in phosphate buffer.

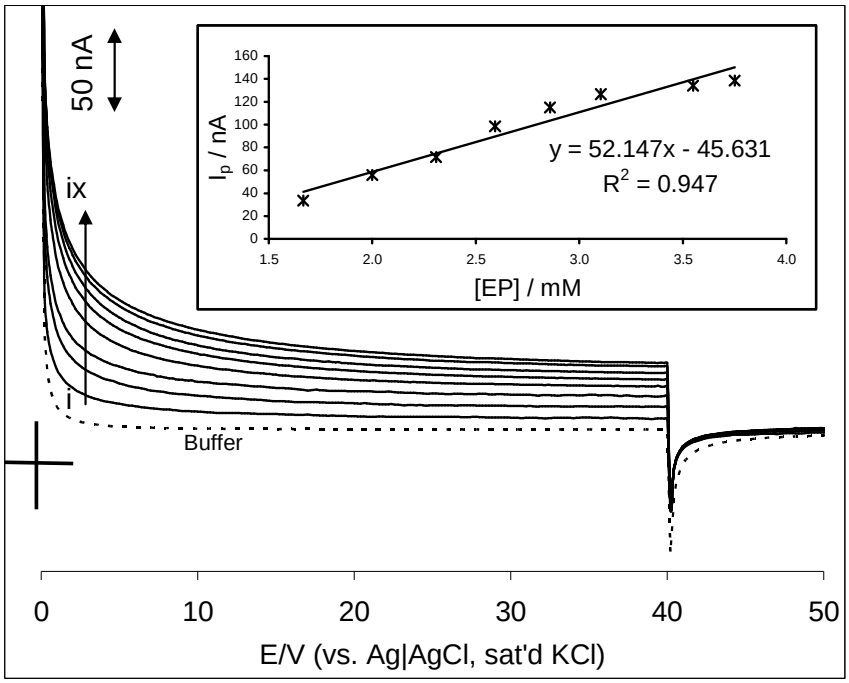

Figure 3.24: Typical double potential step chronoamperometric transients at Au-DMAET-SWCNT-PABS in PBS solution (pH 7.4) following addition of epinephrine. (i) to (ix) correspond to, 1.67, 2.00, 2.31, 2.59, 2.86, 3.10, 3.55, 3.75 μM, respectively. Inset shows the plot of chronoamperometric current at t = 1.6 s vs. [EP].

As previously shown the LoD and sensitivity were calculated from the linear relationship between transient catalytic current (measured at 1.6 s) and epinephrine concentrations. The LoD and sensitivity at Au-DMAET-SWCNT-PABS were calculated to be 3.35 x 10^{-7} M and 66.9 m AM^{-1} respectively. In order to investigate the real sample analysis

potential of the DMAET-SWCNT-PABS, the same experiment was carried out using a screen printed gold electrode (SPAuE); SPAuE is good for once off detection and ideal for real sample analysis. The LoD (4.52×10^{-7} M) value obtained is similar (within experimental error) to that obtained for Au-DMAET-SWCNT-PABS. When compared to presently available literature reports [29-37] on Au based electrodes towards the electrocatalytic detection of epinephrine (Table 3.2) it is observed that these results show comparable sensitivity and lower detection limits in some cases. Equations 1.13 and 1.14 were used as previously to calculate the diffusion coefficient (1.52×10^{-10} cm^2 s^{-1}) and catalytic rate constant (1.11×10^{7} M^{-1} s^{-1}) of epinephrine at constant concentration (at 10 μM in pH 7.4 PBS) poised at +180 mV versus Ag|AgCl. However, for this analyte n = 2 in the Cottrell equation (Eq. 1.13) as expected for the oxidation of epinephrine to epinephrinequinone [21,22,37].

Table 3.2: Comparative analytical data for the detection of epinephrine using electrochemical techniques.

Electrode[1]	**Analytical Parameter**				
	Electrolyte	**LCR**	**Sensitivity**	**LoD**	**Ref**
Au-DMAET-SWCNT-PABS	0.1 M PBS pH 7.4	3.3×10^{-8} – 1.4×10^{-7} M	66.9 m AM^{-1}	3.35×10^{-7} M	This work
SPAE-DMAET-SWCNT-PABS	0.1 M PBS pH 7.4	$4.22 – 3.57 \times 10^{-8}$ M	6.57 m AM^{-1}	4.52×10^{-7} M	This work
Au-DMAET-SWCNT-PABS/ FeTSPc	0.1 M PBS pH 7.4	$0.143 – 0.388 \times 10^{-6}$ M	2.45 m AM^{-1}	24×10^{-9} M	This work
Au-Cys-SWCNT	PBS, pH 7.0	Up to 130 μM	9.4×10^{-3} A M^{-1}	6×10^{-6} M	24
Au-DTT/DDT-*nano* Au	PBS, pH7.0	10^{-7} – 10^{-6} M, (10^{-5} – 2×10^{-4} M)	0.3261 μA μM^{-1}, (0.0233 μA μM^{-1})	60×10^{-9} M	22
Nano Au-ITO	0.1 M PBS pH 7.4	5×10^{-6} – 2×10^{-3} M	1.3199 μA mM^{-1}	1.8×10^{-6} M	29
Au-Cys-FeOCPc	PBS, pH 7.4	300 – 425 nM	0.53 m AM^{-1}	0.138×10^{-7} M	30

Au-Mascorbic Acid	PBS, pH 7.2	10^{-7} – 10^{-6} M, (10^{-5} – $2x10^{-4}$ M)		0.50 x 10^{-7}M	31
Au-Pen	PBS, pH 7.0	$5x10^{-7}$ – 10^{-6} M, (10^{-5} –$2x10^{-6}$ M)	0.0517 µA $µM^{-1}$, (0.0233 µA $µM^{-1}$)	0.1 x 10^{-6} M	32
Au-DMSA/PCA	PBS, pH 7.7	$5x10^{-6}$ – $8x10^{-4}$ M	0.00534 µA $µM^{-1}$	0.39 x 10^{-6} M (0.25 x 10^{-6} M)	33
Au-3MPA	PBS, pH 6.8	$2x10^{-7}$ – 10^{-6} M, ($1x10^{-6}$ – $5x10^{-4}$ M)	-	1.0 x 10^{-7} M	34
Au-LCys-FcAl	PBS, pH 7.4	$1.7x10^{-7}$ – 10^{-4} M	0.9202 µA $µM^{-1}$	0.18 x 10^{-7} M	35
Au-TA SBB	pH 4.4	10^{-7} – 10^{-5} M, (10^{-5} – $6x10^{-4}$ M)	0.083 A M^{-1}, (0.012 A M^{-1})	10 x 10^{-9} M	36

1. DTT/DDT: dithiothreitol/dodecanethiol, FeOCPc: iron octacarboxy phthalocyanine, SWCNT-CoTAPc: single-walled carbon nanotubes-cobalt(II)tetra-aminophthalocyanine, Mascorbic Acid: mercaptoacetic acid, Pen: penicillamine, DMSA/PCA: meso-2,3-dimercaptosuccinic acid/penicillamine, 3 MPA: 3-mercaptopropionic acid, LCys-FcAl: Lcysteine/aminylferrocene, TA: triazole. The values in parentheses were obtained at higher concentration ranges.

3.3 Colloidal Gold and Nanosized Iron (II) Phthalocyanine modified Gold Electrodes

Following the interesting LBL results seen in the previous section using *nano*FePc and SWCNT, I was curious to test the impact of the integration of *nano*FePc and colloidal gold (AuNP).

3.3.1 Layer-by-layer Self Assembly Process

The layer-by-layer assembly involving colloidal gold and *nano*FePc follows the similar fabrication process shown in Scheme 3.2. However, the SWCNT-PABS is obviously replaced by AuNP and four bilayers are used instead of five.

3.3.2 Atomic Force Microscopy

Figure 3.25 shows the topographic AFM images of (a) Au-DMAET and (b) Au-DMAET-AuNP, (c) Au-DMAET-(AuNP-*nano*FePc) and (d) Au-DMAET-(AuNP-*nano*FePc)$_4$. The AFM feature of the Au-DMAET has previously been discussed and added to Figure 3.25 merely for comparative reasons. Subsequent to the deposition of *nano*FePc onto the surface of the AuNP there is an increase in the topographic height as well as the mean roughness profile, indicating the change in surface morphology. Also, the base monolayer seen in Figure 3.25 (a) and (b) becomes less visible in Figure 3.25 (c) indicating a complete coverage

of *nano*FePc onto AuNP. Consequently in Figure 3.25 (d) the base monolayer can no longer be seen and the Au-DMAET-(AuNP-*nano*FePc)$_4$ the AFM feature can be described as a bunch of globular particles clumped together. The substantial growth in Figure 3.25 (d) is further confirmed by the dramatic increase in the root mean square deviation and maximum height of the roughness profiles. The grooves in some of the panels may indicate surfaces whose morphology was modified by the lateral movement of the tip.

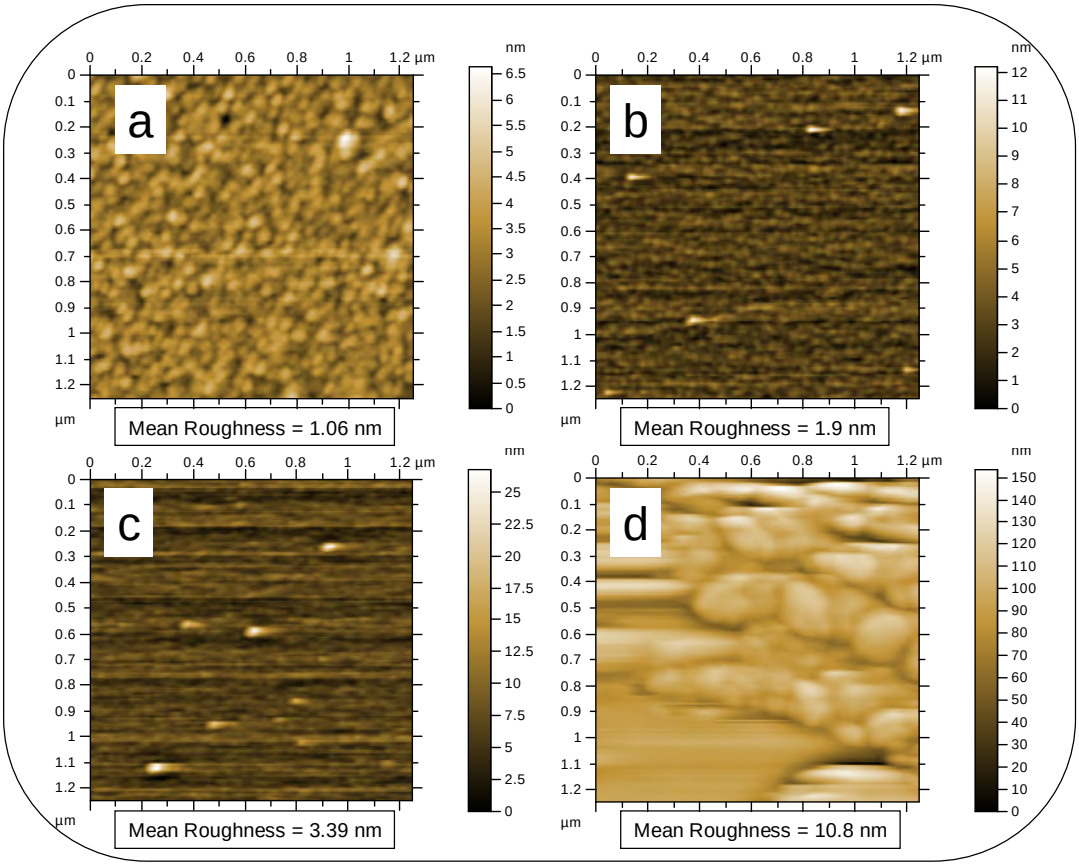

Figure 3.25: Topographic AFM images of (a) Au-DMAET and (b) Au-DMAET-AuNP, (c) Au-DMAET-(AuNP-*nano*FePc) and (d) Au-DMAET-(AuNP-*nano*FePc)$_4$.

3.3.3 Cyclic Voltammetry

Figure 3.26 shows the CV profiles of the (AuNP-*nano*FePc) individual bilayer assemblies in 0.1 M KCl containing equimolar mixture of $[Fe(CN)_6]^{3-}$/ $[Fe(CN)_6]^{/4-}$ solutions. The CV profiles of the layer-by-layer build up illustrated in Figure 3.26 shows the electrode's ability to impede and promote electron transport in $[Fe(CN)_6]^{4-/-3}$ solution. The electron transport ability of the electrode was impeded or blocked following the attachment of AuNP to *nano*FePc. This is not surprising considering gold nanoparticle films can behave as conducting or insulating material depending on the size and mutual distance of the metal cores. [38a] However, phthalocyanines are well known for their excellent electrocatalytic abilities [14,15] and this can be seen from the CVs in Figure 3.26 (b –d) where the electrodes electron transport ability is increased subsequent to the attachment of *nano*FePc onto AuNP at each bilayer.

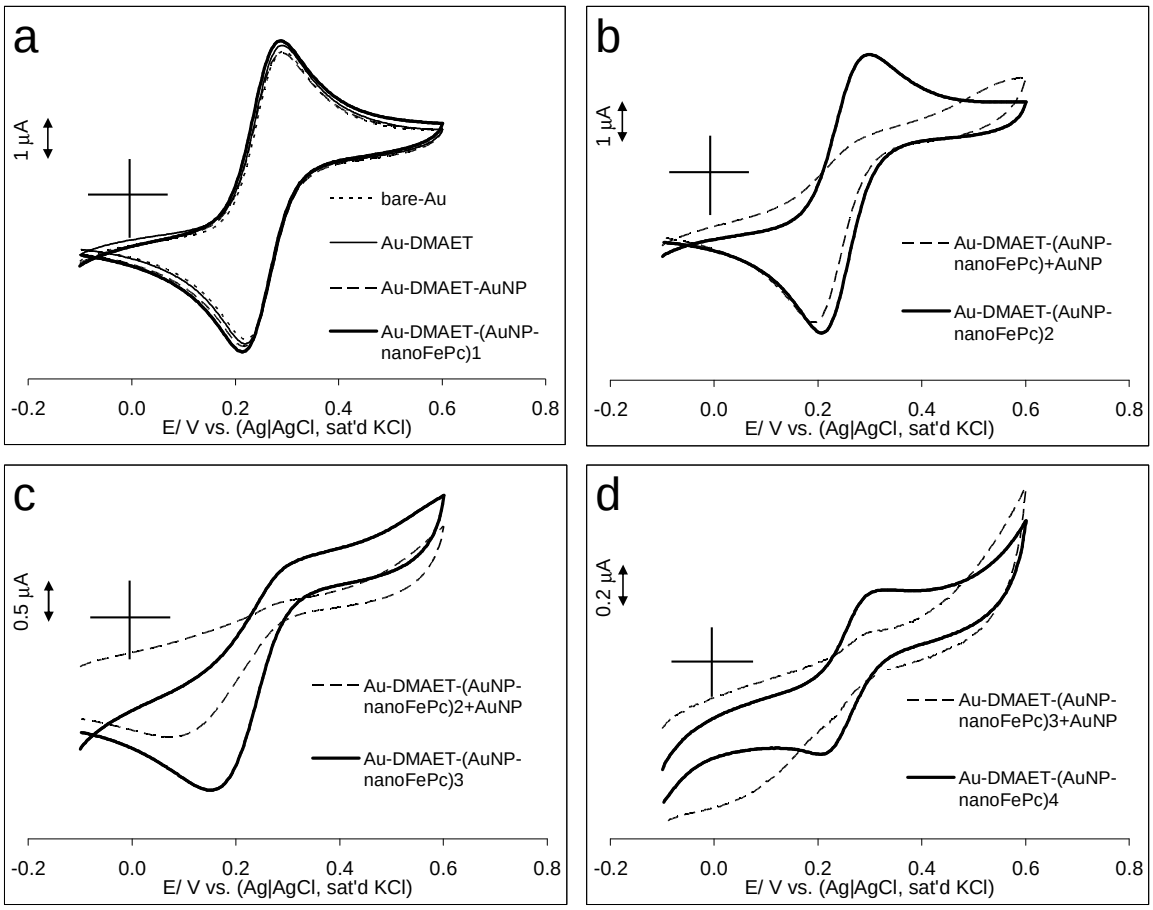

Figure 3.26: Typical CV profiles of (a) bare-Au, Au-DMAET, Au-DMAET-AuNP and Au-DMAET-(AuNP-*nano*FePc)$_1$, (b) 2nd Bilayer, (c) 3rd Bilayer and (d) 4th Bilayer assemblies in 0.1 M KCl containing equimolar mixture of $[Fe(CN)_6]^{3-}$/ $[Fe(CN)_6]^{4-}$ solutions at a scan rate of 25 mV s^{-1}.

The AuNP acts as an insulator that slows down the electron transfer rate between the electrode and the AuNP. Contrastingly, Bethell *et al.* [38b] showed that the thiol layer restricts the electrodes ability while the gold clusters deposited onto the thiol layers promotes the electrode. Although the *nano*FePc promoted the electrode, the

current was not restored to the previous current response. Also, the peak-to-peak separation potential (ΔE_p) increases from the first to fourth bilayer. Therefore, the rate of electron transport is the fastest at the first bilayer since it decreases with increasing (ΔE_p). The blocking of the electrode by the AuNP can be attributed to the repulsive interaction between the negative charges of the AuNP and negative redox probe. The nanoFePc is positively charged and therefore attracts the negatively charged $[Fe(CN)_6]^{-4/-3}$, thus promoting the electrode, resulting in an increased current response compared to the AuNP. It should be noted that this was not observed in the previous section involving negatively charged SWCNT-PABS and positively charged *nano*FePc possibly because the SWCNT acts as nanowires and readily accommodate the electrons movement along the tube.

3.3.4 Electrochemical Impedance Spectroscopy

The nyquist plots shown in Figure 3.27 for the bare-Au, Au-DMAET, Au-DMAET-AuNP, Au-DMAET-(AuNP-*nano*FePc)$_1$, Au-DMAET-(AuNP-*nano*FePc)$_1$+ AuNP and Au-DMAET-(AuNP-*nano*FePc)$_2$ satisfactorily fitted (in terms of low percent errors obtained after several iterations) the modified Randles equivalent circuit (Fig. 1.8a). The charge transfer resistance was only measured up until the 3rd bilayer since additional bilayers resulted in scattered points. The

nyquist plot of the 3rd bilayer was omitted in Figure 3.27 for clarity. However, the R_{ct} values for all the bilayers were included in the bar graph illustrated in Figure 3.28. The charge transfer resistance values showed the same trend for the rate of electron transport as the ΔE_p values showed in cyclic voltammetry; where the attachment of AuNP increases the resistance to flow of electrons while the attachment of *nano*FePc reduces the resistance.

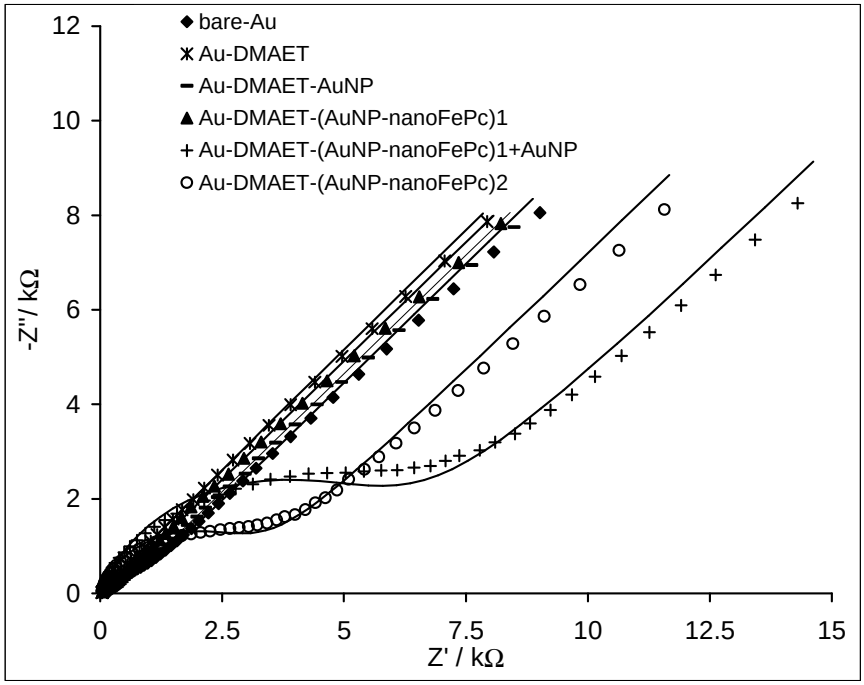

Figure 3.27: Nyquist plots for the bare-Au, Au-DMAET, Au-DMAET-AuNP, Au-DMAET-(AuNP-*nano*FePc)$_1$, Au-DMAET-(AuNP-*nano*FePc)$_1$+AuNP and Au-DMAET-(AuNP-*nano*FePc)$_2$. Successive bilayers were omitted for clarity.

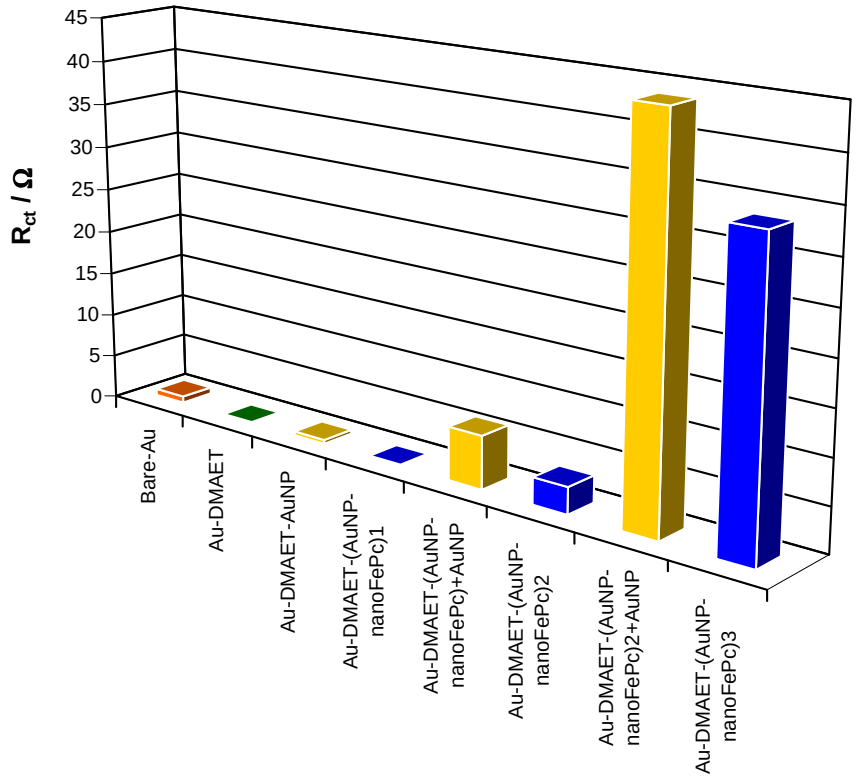

Figure 3.28: 3-D Bar graph representing the R_{ct} values of the bare-Au, Au-DMAET, Au-DMAET-AuNP and the underlying bilayers.

3.3.5 Electrochemical Response towards H_2O_2

The electrode was further tested at each bilayer to determine its ability as a potential sensor towards H_2O_2 detection in physiological pH conditions (pH 7.4). Figure 3.29 compares the reduction current responses of 1 mM H_2O_2 in PBS (pH 7.4) at increasing bilayers (*nano*FePc being the exposed layer). From CV profiles in Figure 3.29 it can be seen that the current response decrease upon increasing bilayers. A similar trend is observed when AuNP is represented as the outer most layer (*nano*FePc-AuNP). Therefore, Au-DMAET-(AuNP-

*nano*FePc)$_1$ is the best electrode in terms of current response for the detection of H_2O_2.

In general, increasing number of bilayers decrease electron transport and voltammetric response of H_2O_2.

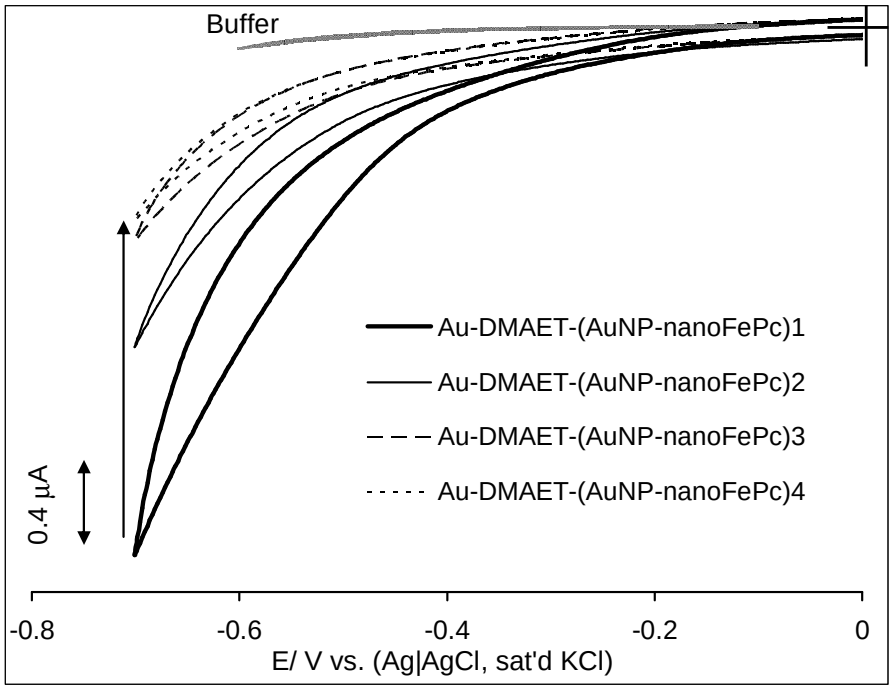

Figure 3.29: Typical CV profiles showing the impact of increasing (a) bilayers (*nano*FePc being the exposed layer) on the current response of 1 mM H_2O_2 in PBS (pH 7.4). Scan rate: 25 mV s^{-1}.

3.4 Single Walled Carbon Nanotubes and Iron (II) Tetrasulphophthalocyanine Modified Gold Electrodes

Following the use of positively charged phthalocyanine, I was now curious to learn the impact if any, of negatively charged phthalocyanine in particular the water-soluble iron (II) tetrasulfophtalocyanine (FeTSPc). However, due to the similar charges of SWCNT-PABS and FeTSPc, I formed a hybrid mixture (SWCNT/FeTSPc) of the two. As a result of their individual competitiveness for the positively charged base monolayer I had to ensure complete coverage of the base gold electrode. Therefore, longer deposition times (~36 h) and slightly higher concentration (5 mM) of DMAET were employed.

3.4.1 Electrode Self Assembly Process

Scheme 3.3 represents the self-assembly fabrication of the various electrodes via strong electrostatic interaction between the positively-charged DMAET and the negatively-charged FeTSPc and SWCNT-PABS species.

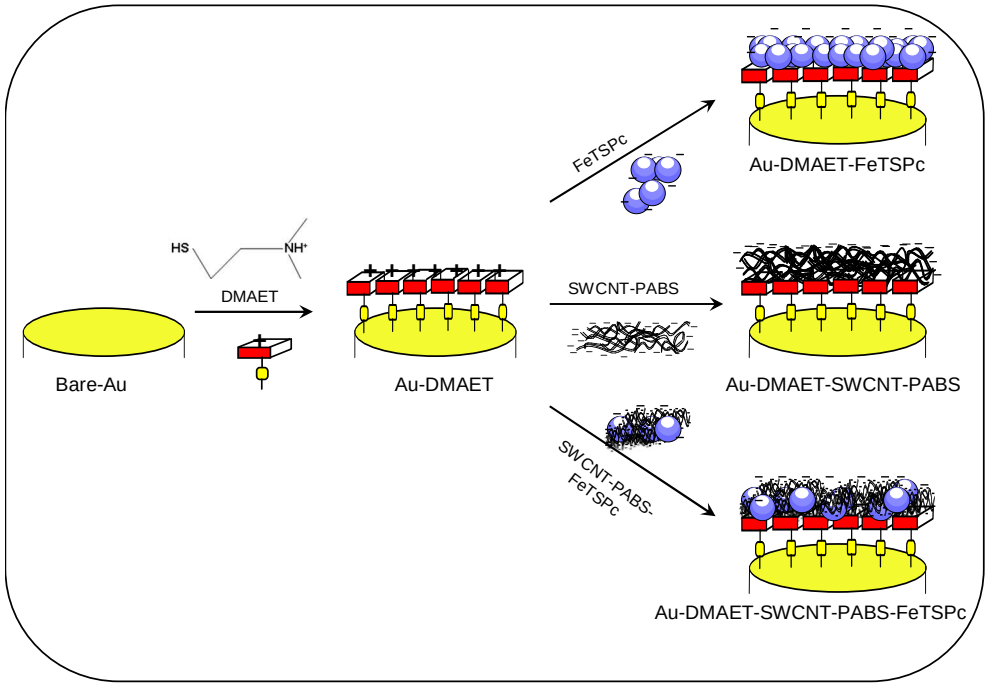

Scheme 3.3: Schematic representation showing the fabrication route for Au-DMAET-FeTSPc, Au-DMAET-SWCNT-PABS and Au-DMAET-SWCNT-PABS/FeTSPc.

3.4.2 Characterization

3.4.2.1 Atomic Force Microscopy

The build-up and formation of the films on gold plates were confirmed using AFM. The AFM images of bare-Au, Au-DMAET and Au-DMAET-SWCNT-PABS have been identified earlier as previously stated. However, since 5 mM DMAET was used in this experiment, Figure 3.30 represents the topographic AFM images of (a) Au-DMAET, (b) Au-DMAET-FeTSPc, (c) Au-DMAET-SWCNT-PABS, (d) Au-DMAET-SWCNT-PABS/FeTSPc. The Au-DMAET depicted in Figure 3.25 (a) shows increased roughness and height profiles than the Au-DMAET discussed

above. This could be as a result of the higher depostion times and increased concentrations of DMAET used.

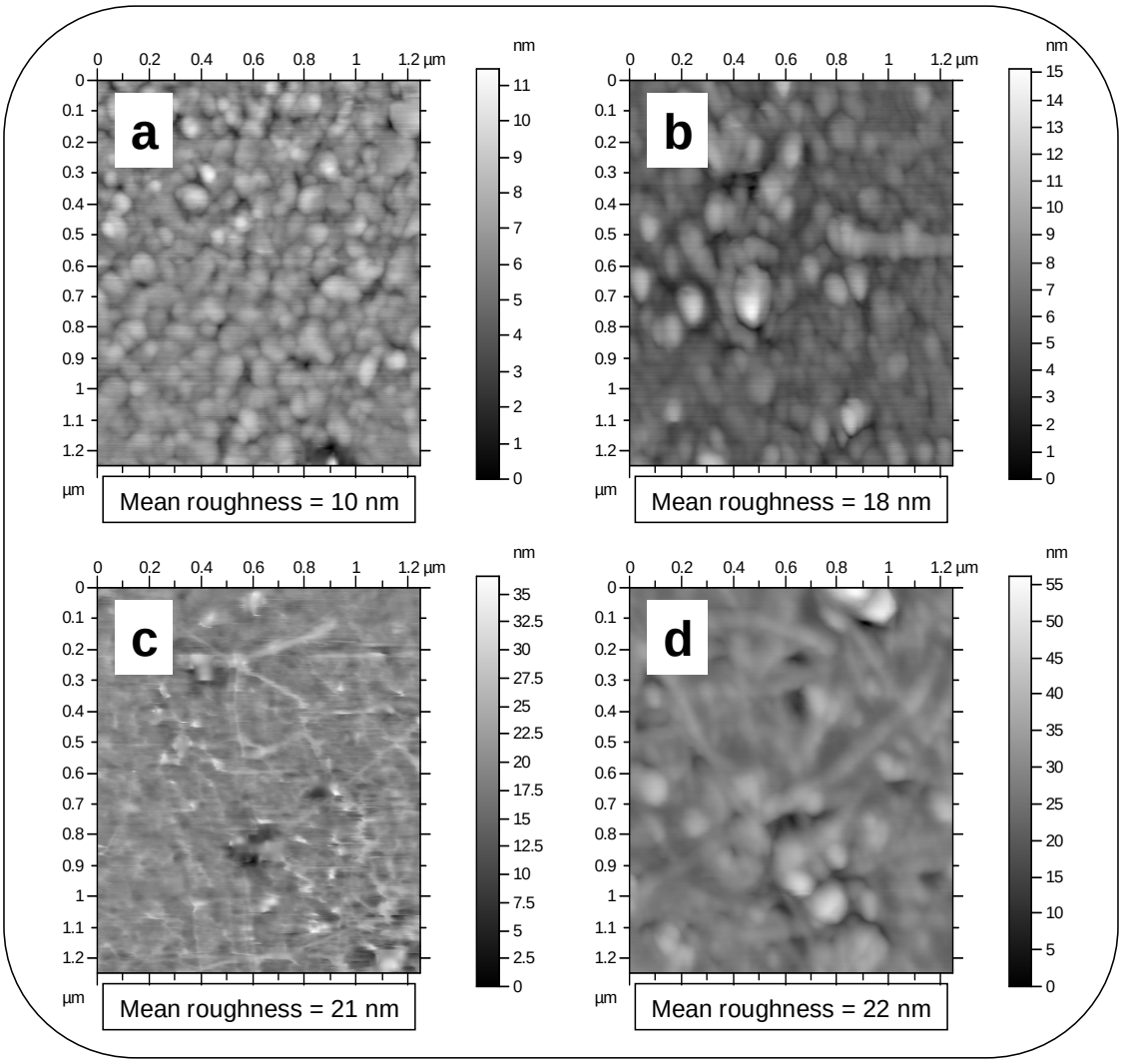

Figure 3.30: Topographic AFM images of (a) Au-DMAET, (b) Au-DMAET-FeTSPc, (c) Au-DMAET-SWCNT-PABS, (d) Au-DMAET-SWCNT-PABS/FeTSPc.

The presence of flat lying tubes is clearly visible in Figure 3.25 (c). Furthermore, there is an increase in root mean square (R_q) and height roughness (R_z) profiles compared to that of Au-DMAET. Upon

immobilization of Au-DMAET with FeTSPc, there is clear evidence of growth judging by (i) the bigger globular-like features on the image (Fig. 3.30b) which can be attributed to the FeTSPc aggregates, and (ii) increase in both R_q and R_z. The AFM features in Figure 3.30 clearly show the immobilization of both FeTSPc and SWCNT-PABS on Au-DMAET judging by mixed tubular and globular features of the images in an irregular arrangement. In addition, the R_q and R_z increased yet again.

3.4.2.2 Cyclic Voltammetry in Aqueous (pH 7.4) Conditions

Figure 3.31 compares the cyclic voltammograms of Au-DMAET, Au-DMAET-SWCNT-PABS, Au-DMAET-FeTSPc and Au-DMAET-SWCNT-PABS/FeTSPc in PBS (pH 7.4) recorded at 50 mV s^{-1}.

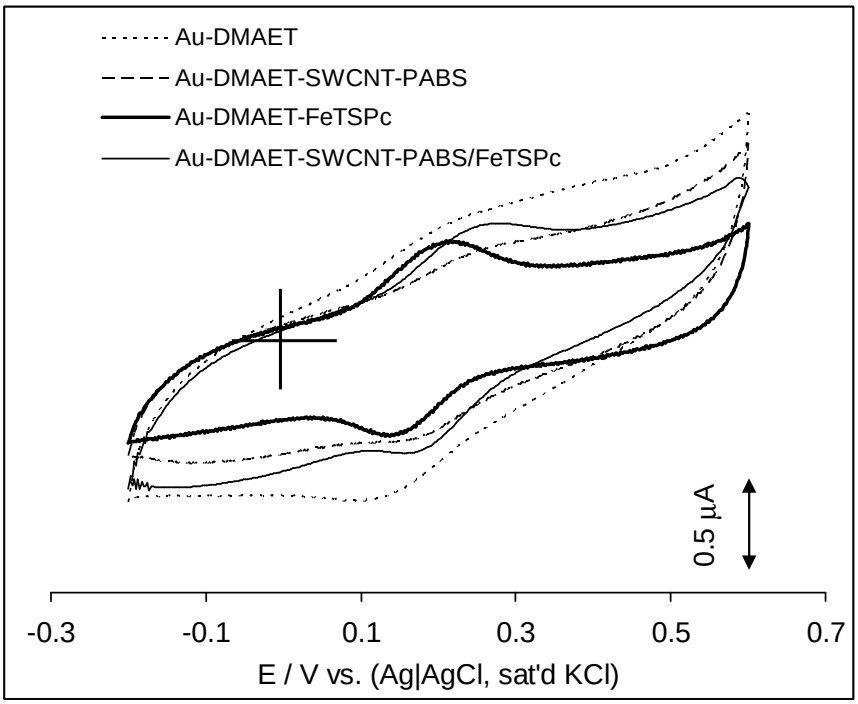

Figure 3.31: Comparative cyclic voltammograms in phosphate buffer pH 7.4 solutions obtained at Au-DMAET, Au-DMAET-SWCNT-PABS, Au-DMAET-FeTSPc and Au-DMAET- SWCNT-PABS/FeTSPc. Scan rate = 50 mV s^{-1}.

The weak reversible process shown by the Au-DMAET is attributed to the electric-field driven protonation/deprotonation process described earlier. It should be pointed out here that the CV of Au-DMAET is well-defined only when less deposition time (≤ 24 h) and/or slightly lower concentration of DMAET (< 5 mM) is used in the fabrication as observed earlier. Both Au-DMAET-FeTSPc and Au-DMAET-SWCNT-PABS/FeTSPc showed well-defined reversible peaks, attributed to the Fe^{2+}/Fe^{3+} redox processes [39]. The ratio of the anodic and cathodic

peak current densities (I_{pa}/I_{pc}) are approximately equal, indicating electrochemical reversibility.

Figure 3.32 (a) and (b) shows the cyclic voltammograms obtained at different scan rates (25 – 1000 $mV.s^{-1}$ range) in phosphate buffer pH 7.4 solution obtained at (a) Au-DMAET-FeTSPc and (b) Au-DMAET-SWCNT-PABS/FeTSPc respectively. The formal potentials ($E_{1/2} = [E_{pa} + E_{pc}]/2$) of Au-DMAET-FeTSPc and Au-DMAET-SWCNT-PABS/FeTSPc are 170 and 220 mV, respectively. Ideally, at small scan rates, the peak-to-peak potential separation ($\Delta E_p = |E_{pa} - E_{pc}|$) in a monolayer should be zero. However, the ΔE_p values for the Au-DMAET-FeTSPc and Au-DMAET-SWCNT-PABS/FeTSPc are 78 and 112 mV, respectively. The electron transport (signified by the magnitude ΔE_p) is fastest at the Au-DMAET-FeTSPc and Au-DMAET-SWCNT-PABS/FeTSPc. Also, the width at half the peak current (E_{fwhm} / mV) slightly deviates from the ideal value of 90.6/n mV for n = 1 [40-42], where, the Au-DMAET-FeTSPc and Au-DMAET-SWCNT-PABS/FeTSPc are 122 and 127 mV, respectively. The deviation of the ΔE_p and E_{fwhm} from their ideal values is typical of redox species being in located in different environments with different formal potentials [43-45]. Thus, it may be said that the FeTSPc molecules are located at different environments with different formal potentials. Simply stated, the FeTSPc species have different formal potentials when immobilized at the DMAET and/or SWCNT-

PABS, and thus the effective voltammetric wave consists of a superposition of distinct electrochemical responses, resulting in the observed non-ideal voltammograms. In all cases, the electrochemical parameters of the DMAET-FeTSPc are slightly better than those recorded for the SWCNT-PABS/FeTSPc, which can be attributed to the different environments and complexities of the SWCNT-PABS platform.

At higher scan rates where the voltammetry is controlled by the rate of electron transport, the ΔE_p increases with scan rates. The plots of the peak currents (I_p) against the scan rate (v) are shown in Figure 3.32 (c), where Figure 3.32 (c) i-iv are respectively the I_a for SWCNT-PABS/FeTSPc, I_a for DMAET-FeTSPc, I_c for DMAET-FeTSPc and I_c for SWCNT-PABS/FeTSPc versus scan rate (v). The plots are all linear which is characteristic of surface-confined redox species.

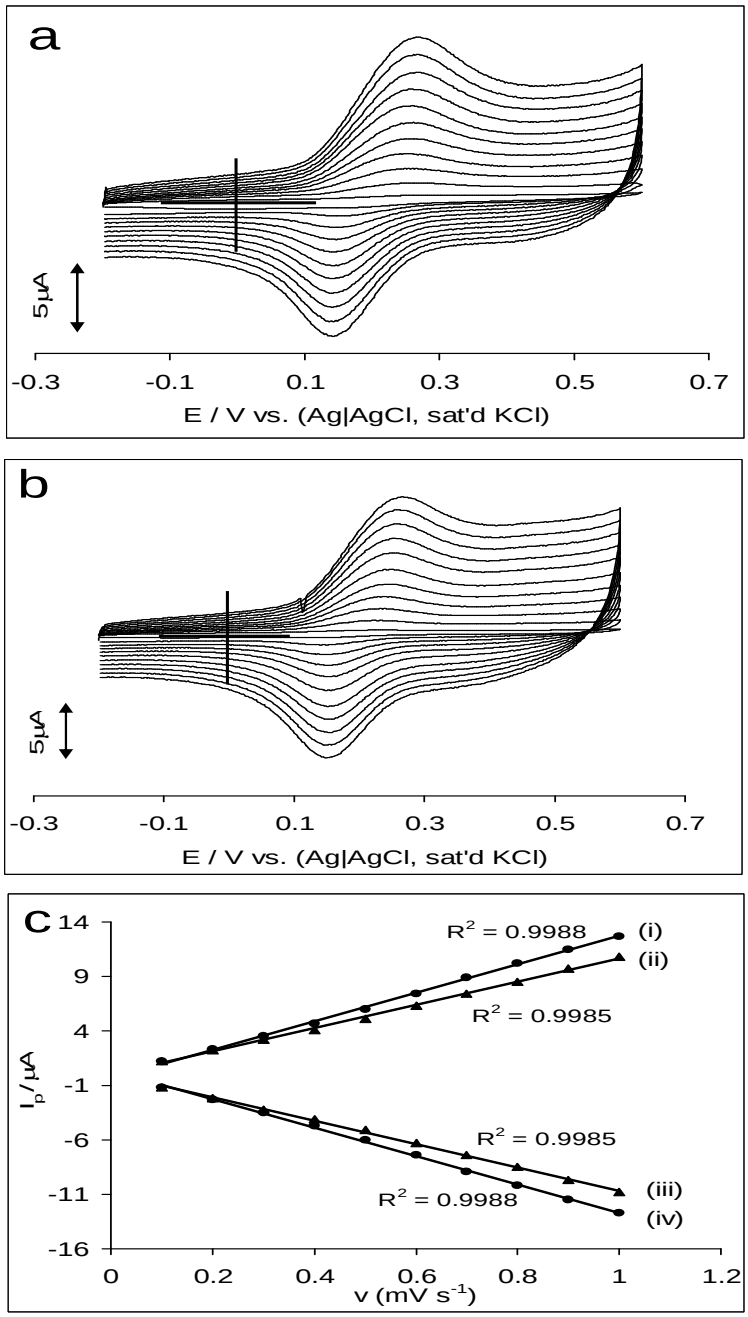

Figure 3.32: Cyclic voltammograms obtained at different scan rates (25 – 1000 mV s^{-1} range) in phosphate buffer pH 7.4 solution obtained at (a) Au-DMAET-FeTSPc; (b) Au-DMAET- SWCNT-PABS/FeTSPc and (c) Plots of I_p vs. v for I_a for (i) SWCNT-PABS/FeTSPc, (ii) I_a for DMAET-FeTSPc, (iii) I_c for DMAET-FeTSPc and (iv) I_c for SWCNT-PABS/FeTSPc.

3.4.2.3 Surface Coverage

The surface coverage (Γ/ mol cm^{-2}) of the FeTSPc at both (Au-DMAET and Au-DMAET-SWCNT-PABS) platforms were established from the slopes of the plots according to Equation 3.5 [39]:

$$I_p = \frac{n^2F^2A\Gamma\nu}{4RT} \qquad 3.5$$

where n = number of electrons involved in the redox process, F is the Faraday constant, and A is the area of the electrode, R is the ideal gas constant and T is the ideal temperature (K). The surface coverage was calculated to be (4.14 ± 0.21) x 10^{-8} mol cm^{-2} using the average slope values from both the I_a and I_c vs. ν plots for Au-DMAET-FeTSPc and (4.08 ± 0.28) x 10^{-8} mol cm^{-2} for Au-DMAET-SWCNT-PABS/FeTSPc. The estimated values indicate multilayer coverage rather than monolayers expected to be (for MPc molecules) in the ~ 10^{-10} mol cm^{-2} [46,47].

3.4.2.4 Stability Studies

The electrochemical stability of the Au-DMAET-FeTSPc and Au-DMAET-SWCNT-PABS/FeTSPc was conducted by repetitively scanning each electrode in PBS (pH 7.4). Figure 3.33 (a) shows the repetitive cycling of Au-DMAET-FeTSPc and Figure 3.33 (b) compares the CVs of the freshly prepared Au-DMAET-FeTSPc and Au-DMAET-FeTSPc after

one week of use in PBS. It can be seen from the repetitive cycling (Fig. 3.33a) as well as the comparative CVs (Fig. 3.33b) that in terms of I_p and E_p, there is so significant changes in CV patterns. The Au-DMAET-SWCNT-PABS/FeTSPc (not shown) showed a similar stability profile to that of the Au-DMAET-FeTSPc. Such remarkable stability is important for their electrochemical studies as well as their potential applications in aqueous conditions. This result is significant for the fact that FeTSPc is highly soluble in water but upon attachment to Au-DMAET film, there is a strong bond by electrostatic attraction between SO_3^- of FeTSPc and $NH^+(CH_3)_2$ of DMAET, and this bond is stable even when the electrode is used in aqueous media.

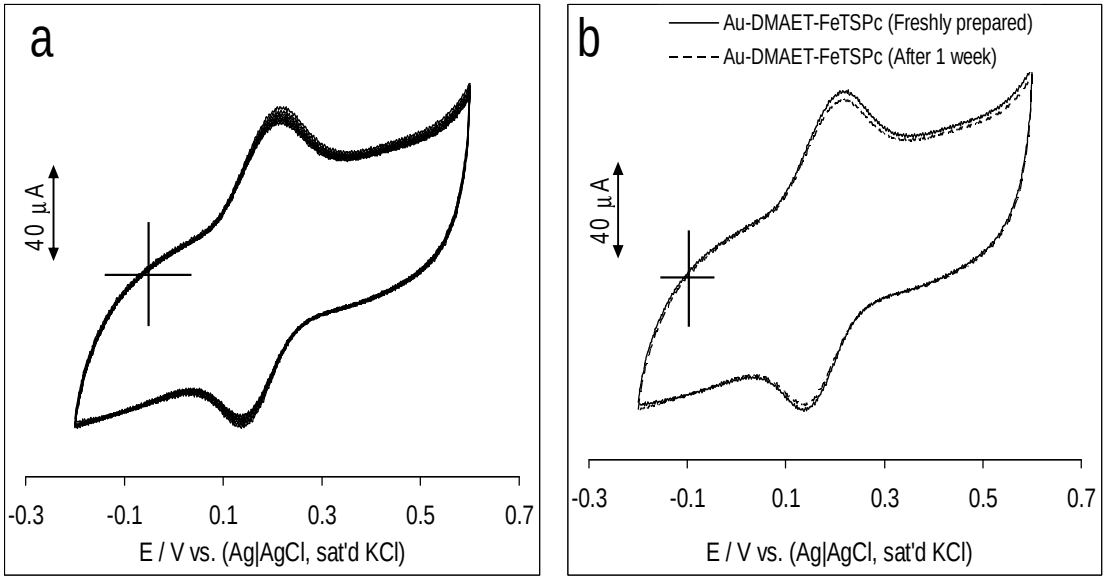

Figure 3.33: (a) Repetitive cyclic voltammograms obtained in PBS (pH 7.4) at Au-DMAET-FeTSPc and (b) CVs obtained at freshly prepared Au-DMAET-FeTSPc and a week later after use.

3.4.2.5 Cyclic Voltammetric Evolutions in $[Fe(CN)_6]^{3-/4-}$

Next, the extent to which the modifying species permit the electron transfer of the $[Fe(CN)_6]^{4-}/[Fe(CN)_6]^{3-}$ redox probe to the underlying gold electrode was investigated. From Figure 3.34 it can be seen that with the exception of the Au-DMAET-SWCNT-PABS/FeTSPc which showed the highest anodic and cathodic peak currents, the CV responses of the electrodes otherwise were essentially the same in terms of (i) peak-to-peak separation potential ($\Delta E_p \approx 70$ mV vs. Ag|AgCl, sat'd KCl), and (ii) the equilibrium potential ($E_{1/2} \approx 0.25$ V vs. Ag|AgCl, sat'd KCl).

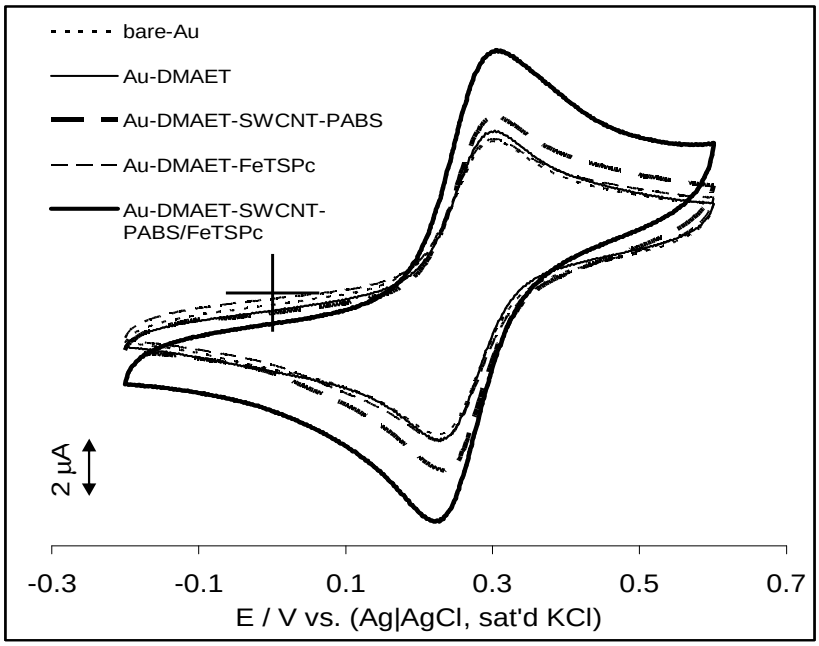

Figure 3.34: Cyclic voltammograms obtained in 1 mM $Fe(CN)_6^{3-/4-}$ in 0.1 M KCl at bare-Au, Au-DMAET, Au-DMAET-SWCNT-PABS, Au-DMAET-FeTSPc and Au-DMAET- SWCNT-PABS/FeTSPc.

3.4.2.6 Impedimetric Studies in $[Fe(CN)_6]^{3-/4-}$

For further understanding of the electronic behaviour of the electrodes, EIS studies were carried out in $[Fe(CN)_6]^{3-/4-}$ solution at the equilibrium potential of the redox couple ($E_{1/2} \approx 0.25$ V). Figure 3.35 (a) compares the nyquist plots of bare-Au, Au-DMAET, Au-DMAET-SWCNT-PABS, Au-DMAET-FeTSPc and Au-DMAET-SWCNT-PABS/ FeTSPc.

The bare gold electrode was satisfactorily fitted using the modified Randles' equivalent circuits (Fig. 1.8a). However, attempts to fit the modified electrodes with the ideal or modified Randles circuit or a simple one-reaction RC time constant circuit were unsuccessful as they led to very large fitting error values. The longer deposition times and slightly higher concentration of DMAET are believed to be reasons for the Au-DMAET and Au-DMAET-SWCNT-PABS not fitting the modified Randles' equivalent circuits as previously shown. The observed experimental data for Au-DMAET, Au-DMAET-SWCNT-PABS, Au-DMAET-FeTSPc and Au-DMAET-SWCNT-PABS/FeTSPc were satisfactorily fitted (judged by the low values of relative % errors in Table 3.3) with the electrical equivalent circuit two voigt RC element (Fig. 3.35b) involving solution resistance (R_s), double-layer capacitance (C_{dl}), electron-transfer resistance (R_{ct}) and CPE.

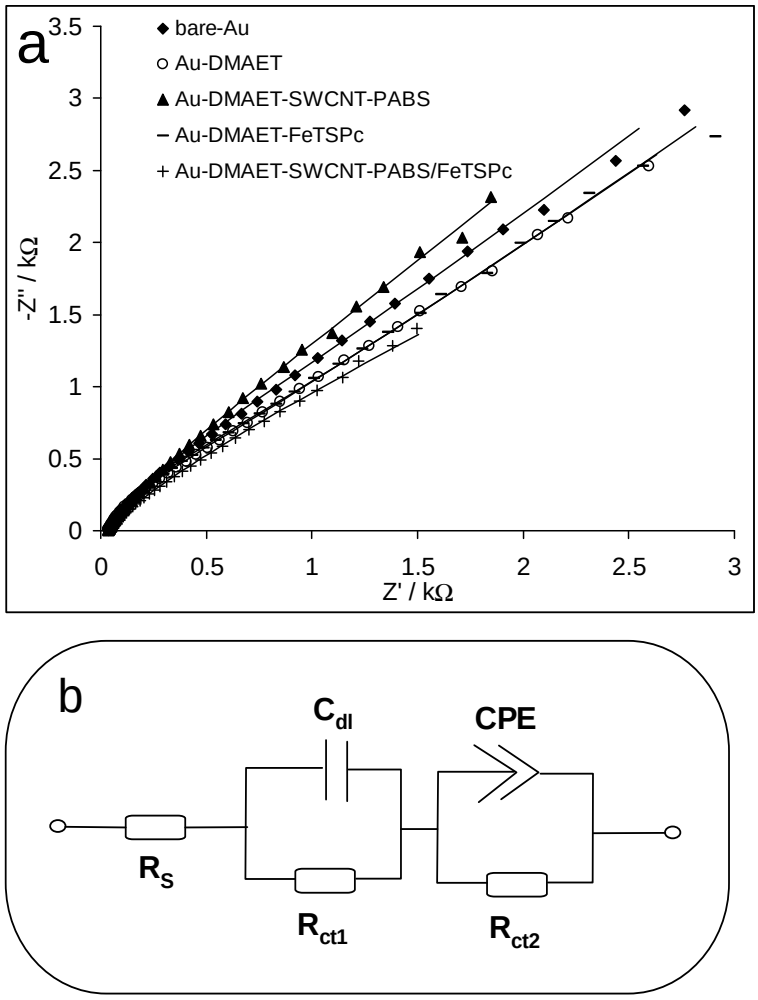

Figure 3.35: (a) Nyquist plots obtained in $Fe(CN)_6^{3-/4-}$ 0.1 M KCl at (i) bare-Au, (ii) Au-DMAET, (iii) Au-DMAET-SWCNT-PABS, (iv) Au-DMAET-FeTSPc and (v) Au-DMAET- SWCNT-PABS/FeTSPc and (b) the equivalent circuits used for fitting (ii) – (iv). Figure 1.8 (a) was used to fit (i).

The apparent electron transfer rate constant (k_{app}) values of the electrodes were obtained from the equation [48.49]:

$$k_{app} \approx k^o = \frac{RT}{n^2 F^2 A R_p C} \qquad 3.6$$

where n is the number of electron transferred (1), C is the concentration of the $[Fe(CN)_6]^{3-}$ (in mol cm^{-3}, the concentration of $[Fe(CN)_6]^{3-}$ and $[Fe(CN)_6]^{4-}$ are equal), A is the experimentally-determined area of the electrode, R_p is obtained by the series connection of the two charge-transfer resistances (i.e., $R_p = R_{ct1} + R_{ct2}$).

The following features shown by the impedimetric data of the modified electrodes should be emphasized. First, from data in Table 3.3, the Au-DMAET-SWCNT-PABS/FeTSPc gave the highest k_{app} value, indicating that charge-transfer processes between the $[Fe(CN)_6]^{3-/4-}$ and the underlying gold surface are made a lot easier by the synergistic combination of the FeTSPc and SWCNT-PABS. The reason for this is not fully understood but may be related to such factors as the high surface area of the SWCNT-PABS that permits diffusion of the redox probe as well as its ability to act as efficient electric conducting nanowires.

Second, equivalent circuit models suggesting physico-electrochemical phenomena involving more than one RC time constants, as seen from the circuit model (Fig. 3.35b), are mainly due to multiple or coupled reaction sequences, to roughening of the electrode, and to frequency-dependent ohmic resistances caused by non-uniform charging of the electrode/electrolyte double layer. The

impedance of CPE is defined by Equation 1.18. As mentioned above the capacitive nature of CPE can be deduced by the magnitude of n. Table 3.3 shows n ≥ 0.70, indicating pseudocapacitive behaviour. Also, from the bode plots (Fig. 3.36a) of log |Z| vs. log f the slopes are approximately similar (*ca*. –0.60) at the mid frequency region, indicative of pseudocapacitive behaviour.

Third, impedance spectra are known to contain features that could be directly related to microstructures, with the grain boundary phases of microstructures having a dominant blocking effect on the impedance spectra [50,51]. Since electron transport processes occurring via permeation of the redox probe through the spaces created by the assembled species is expected to be faster than that arising through the layers [52], the first Voigt element (R_{ct1}/C_{dl}) may be associated to the polarization phenomenon due to electron transfer occurring through the layers of the molecules and/or the grain boundaries, while the second voigt element (R_{ct2}/CPE) to processes that occur through the spaces amongst the self-assembled molecular layers.

Finally, an attempt to replace the ideal C_{dl} with a CPE (a real application situation) in the modelling circuit proved unsuccessful. The explanation of this observation may be found from the relationship between C_{dl} and CPE. It has been elegantly described by Orazem and Tribollet [51], that frequency dispersion leading to CPE behaviour occurs

as a result of distribution of time constants along either the area of the electrode surface (involving a 2-dimensional aspect of the electrode) or along the axis normal to the electrode surface (involving a 3-dimensional surface). A 2-D distribution presents itself as an ideal RC behaviour, meaning that impedance measurements are very useful in distinguishing whether the observed global CPE behaviour is due to a 2-D or 3-D distribution or both. Thus, the observed impedimetric behaviour seen at the modified electrodes likely involves 2-D and 3-D distributions. Also, note that despite the fitting of the spectra with ideal RC element (1st Voigt element), the phase angles seen on the Bode plots (i.e., –phase angle (θ) vs. log f, (Fig. 3.36b) are in the range of 48 - 56^{o}, which are less than the 90^{o} expected of an ideal capacitive behaviour, thus further confirming presence of the 2-D distribution arising from CPE behaviour and the pseudocapacitive nature of the modified electrodes.

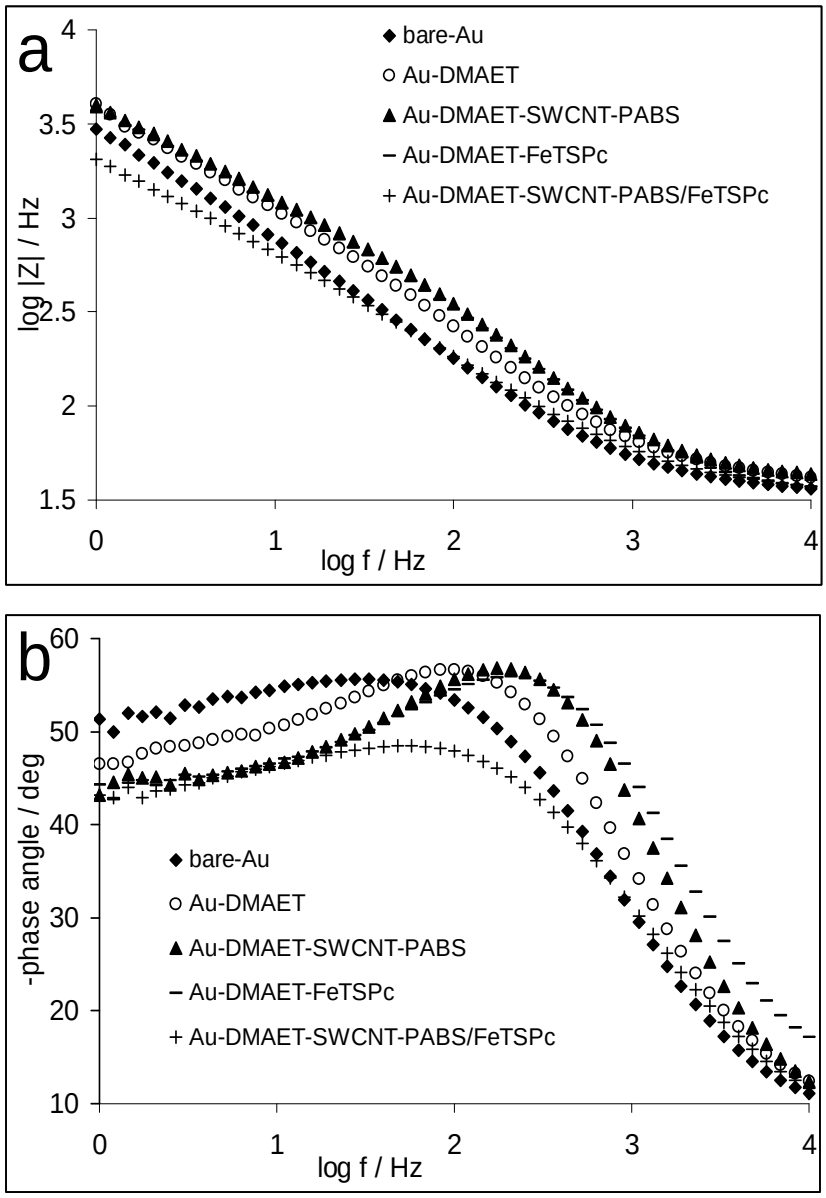

Figure 3.36: Bode plots of (a) log |Z| vs. log f and (b) -Phase angle vs. log f obtained in $Fe(CN)_6^{3-/4-}$ 0.1 M KCl at bare-Au, Au-DMAET, Au-DMAET-SWCNT-PABS, Au-DMAET-FeTSPc and Au-DMAET- SWCNT-PABS/FeTSPc.

Table 3.3: Comparative EIS paprameter data obtained for Au-DMAET, Au-DMAET-SWCNT-PABS, Au-DMAET-FeTSPc and Au-DMAET-SWCNT-PABS/FeTSPc.

Electrochemical impedance parameters[1]	**Electrode[2]**			
	Au-DMAET	**Au-DMAET-SWCNT-PABS**	**Au-DMAET-FeTSPc**	**Au-DMAET- SWCNT-PABS/FeTSPc**
R_s / Ω cm^2	0.98 (1.06)	0.99 (1.93)	0.78 (2.24)	0.81 (1.19)
R_{ct1} / kΩ cm^2	0.16 (4.62)	0.15 (5.77)	0.13 (5.93)	0.07 (8.22)
C_{dl} / µF cm^{-2}	1.22 (3.31)	1.05 (4.19)	1.17 (4.65)	3.36 (7.05)
R_{ct2} / kΩ cm^2	0.041 (4.38)	0.038 (4.89)	0.038 (5.42)	0.037 (7.09)
CPE / µF cm^{-2}	0.94 (3.02)	0.58 (5.40)	0.75 (5.18)	2.44 (3.05)
n	0.75 (0.60)	0.77 (0.99)	0.74 (0.97)	0.65 (0.71)
10^3 k_{app} / cm s^{-1}	1.32 ± 0.08	1.44 ± 0.10	1.54 ± 0.11	2.30 ± 0.22

1. Value in parenthesis is the estimated percent errors in fitting the experimental impedance spectra.

2. Bare gold electrode was fitted with the modified Randles equivalent circuit (Fig. 7b(i)) with estimated values of R_s ≈ 2.8 Ωcm^2, R_{ct} ≈ 15 Ω cm^2, Z_w ≈ 2 x 10^{-6} Ω cm^2, CPE ≈ 21 µF cm^{-2}, n ≈ 0.9 and k_{app} ≈ 18x10^{-3} cm s^{-1}. Estimated percent fitting errors ≤ 4%

3.4.3 Electrocatalytic Detection of Epinephrine

Electrocatalytic detection of EP was used to test the ability of the surface-confined FeTSPc to detect biologically significant analytes. Figure 3.37 compares cyclic voltammetric evolutions of 10^{-5} M EP in phosphate buffer solution (pH 7.4) at bare-Au, Au-DMAET-FeTSPc and Au-DMAET-SWCNT-PABS/FeTSPc.

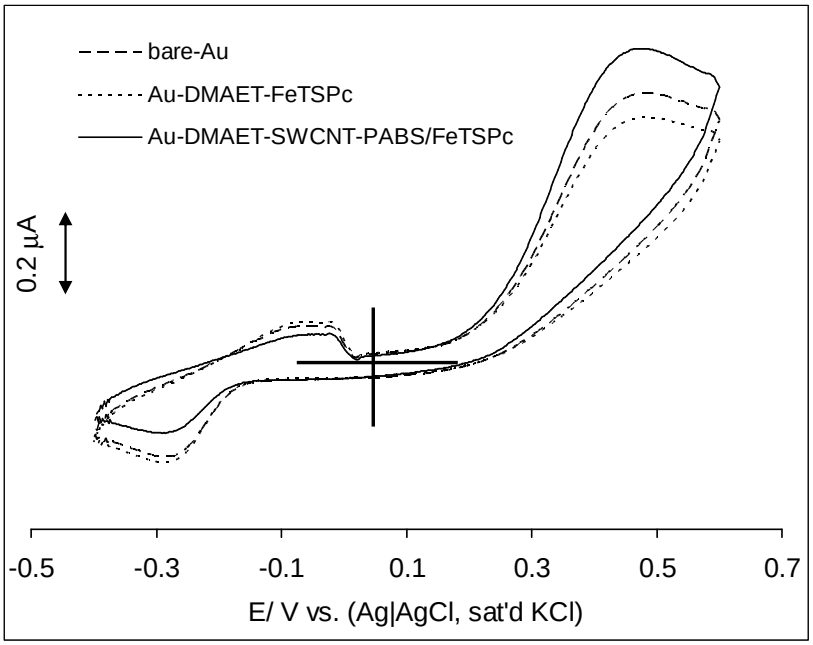

Figure 3.37: Cyclic voltammograms obtained at bare-Au, Au-DMAET-FeTSPc and Au-DMAET-SWCNT-PABS/FeTSPc in 10^{-4} M EP PBS (pH 7.4) Scan rate = 50 mV s^{-1}.

The relatively enhanced current response at the Au-DMAET-SWCNT-PABS/FeTSPc compared to Au-DMAET-FeTSPc is attributed to synergic properties arising from the co-existence of FeTSPc and

SWCNT-PABS. Hence, Au-DMAET-SWCNT-PABS/FeTSPc was further used for chronoamperometric detection of EP.

Double potential step chronoamperometric experiments were recorded at Au-DMAET-SWCNT-PABS/FeTSPc by polarizing the potentials to 0.35 V and 0.0 V. Figure 3.38 shows a well-resolved double-step chronoamperometric evolutions obtained in the absence (buffer alone) and presence of consecutive addition of 1 ml of 1 μM epinephrine in phosphate buffer solution (pH 7.4) to 20 ml phosphate buffer. Figure 3.38 (inset) clearly shows the corresponding plot of transient catalytic current (measured at 4 s) and epinephrine concentrations, a linear relationship (R^2 = 0.990) was obtained. The sensitivity of the plot of transient catalytic current (measured at 4 s) and epinephrine concentrations was found to be 2.45 AM^{-1}. The limit of detection was calculated to be 24 nM. From equations 1.12 and 1.13 the diffusion coefficient, D, and the catalytic rate constant, k, of 10 μM epinephrine in phosphate buffer (pH 7.4) were calculated to be 22.4 x 10^{-3} cm^2 s^{-1} and 5.49 x 10^6 M^{-1} s^{-1} respectively. For reasons previously mentioned n = 2 in the Cottrell equation.

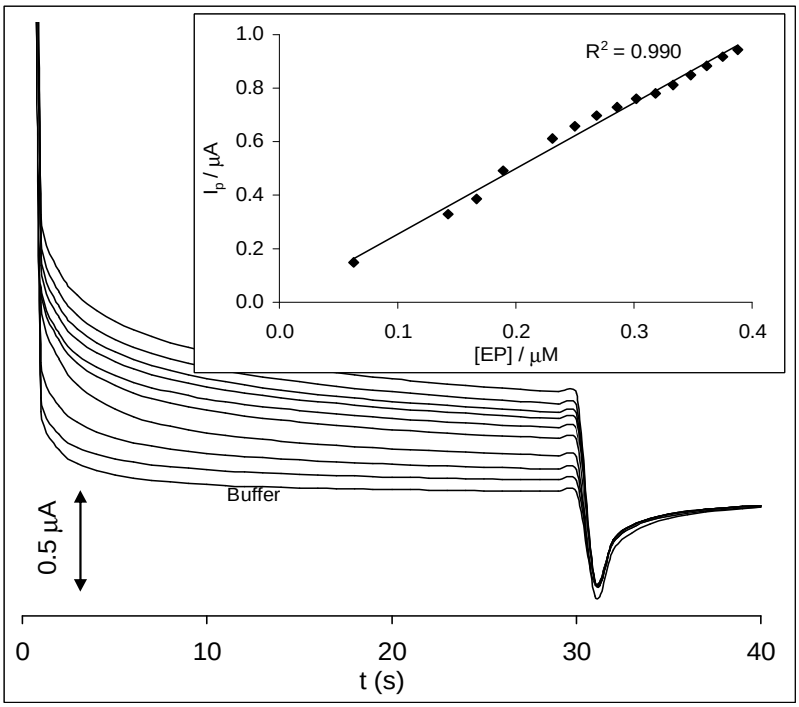

Figure 3.38: Typical double potential step chronoamperometric transients obtained for epinephrine electro-oxidation at Au-DMAET-SWCNT-PABS/FeTSPc. Inset: Plot of I_p vs. [EP] in phosphate buffer pH 7.4; 0.143, 0.167, 0.211, 0.231, 0.268, 0.302, 0.333, 0.362 and 0.388 µM are the concentrations from outer to inner. Inset shows the plot of chronoamperometric current at t = 1.6 s vs. [EP].

3.5 Monolayer-Protected Clusters of Gold Nanoparticles modified Gold Electrodes

The final part of this dissertation investigates the impact of different ratios of the protecting –OH and –COOH based monolayer ligands of redox-active gold nanoparticles on the dynamics of electron transport between solution species, in organic and aqueous media, and the electrode surface. The popular electrostatic self-assembly strategy technique was used for the immobilisation of MPCAuNPs onto the gold electrode. [53-59]. Considering the low concentration (~ 15 x 10^{-10} mol L^{-1}) of the MPCAuNPs, longer period adsorption (18 h) was adopted to allow for the electrostatic integration of the MPCAuNPs with the positively-charged DMAET SAM (Scheme 3.4). To my knowledge, this is the first time this type of architecture involving different ratios of carboxylated and hydroxyl containing ligands is fabricated and described.

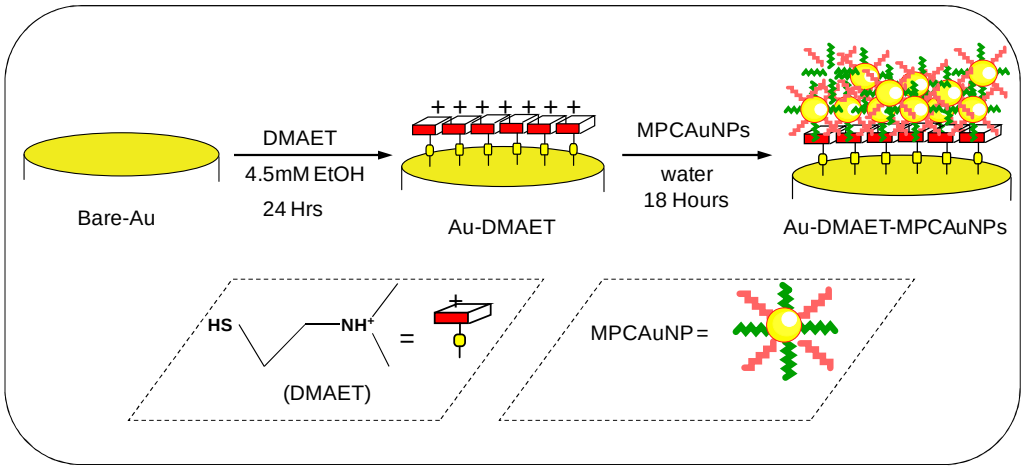

Scheme 3.4: Schematic of the self-assembly process via electrostatic interaction between the positively-charged DMAET monolayer and the negatively-charged monolayer-protected clusters of gold nanoparticles.

3.5.1 Spectroscopic and Microscopic Characterization

The preparation of the MPCAuNPs (summarized in Scheme 1.2) was adopted from the previous work by Tshikudo *et al.* [60]. The PEG-stabilized MPCAuNPs are extremely stable in the water. They can be centrifuged, dried and re-suspended in aqueous solution without any loss of materials. Unlike their citrate-stabilised counterpart that changed colour from red to colourless solution after about 2 months storage, the PEG-stabilised MPCAuNPs have not shown any detectable change in their ruby-red solutions even after 8 months. Also, unlike most other hydrosols, the PEG-stabilized MPCAuNPs do not show any detectable aggregation in 2 M NaCl solution. Their size is similar to their precursor citrate-stabilized gold nanoparticles (14±1 nm) as

confirmed by their TEM images, exemplified in Figure 3.39 with MPCAuNP-$COOH_{99\%}$.

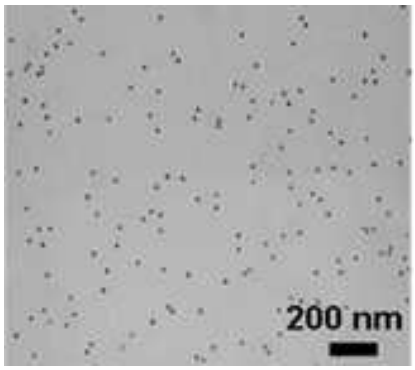

Figure 3.39: Typical TEM image of Au-DMAET-MPCAuNP-$COOH_{99\%}$.

Figure 3.40 shows the comparative 3-D AFM images of the bare-Au, Au-DMAET, Au-DMAET-MPCAuNP-$COOH_{50\%}$ and Au-DMAET-MPCAuNP-$COOH_{99\%}$.

As previously mentioned for an ultra thin film monolayer, there is very little difference between the thickness of bare-Au and Au-DMAET [1] which is also identified from the very small change in their roughness root mean square deviation (rms) values. However integration with the PEG-stabilized MPCAuNPs, the topographic heights increased to ~ 5 nm (with roughness factor of ~2.2 nm) for the Au-DMAET-MPCAuNP-$COOH_{1\%}$ (not shown), ~ 8 nm (with roughness factor of ~2.9 nm) for the Au-DMAET-MPCAuNP-$COOH_{50\%}$ and to about 10 nm (with roughness factor of ~3.2 nm) for the Au-DMAET-MPCAuNP-$COOH_{99\%}$. There is a slight increase in the topographic

height subsequent to adsorption of PEG-stabilized MPCAuNPs which may be attributed to the chain length of the ligands. The PEG-stabilized MPCAuNPs assembled as bundles with needle-like protrusions, presumably due to the strong van der Waal's attractive forces existing between carbon chains. In general, all the PEG-Stabilized MPCAuNPs show similar surface morphology.

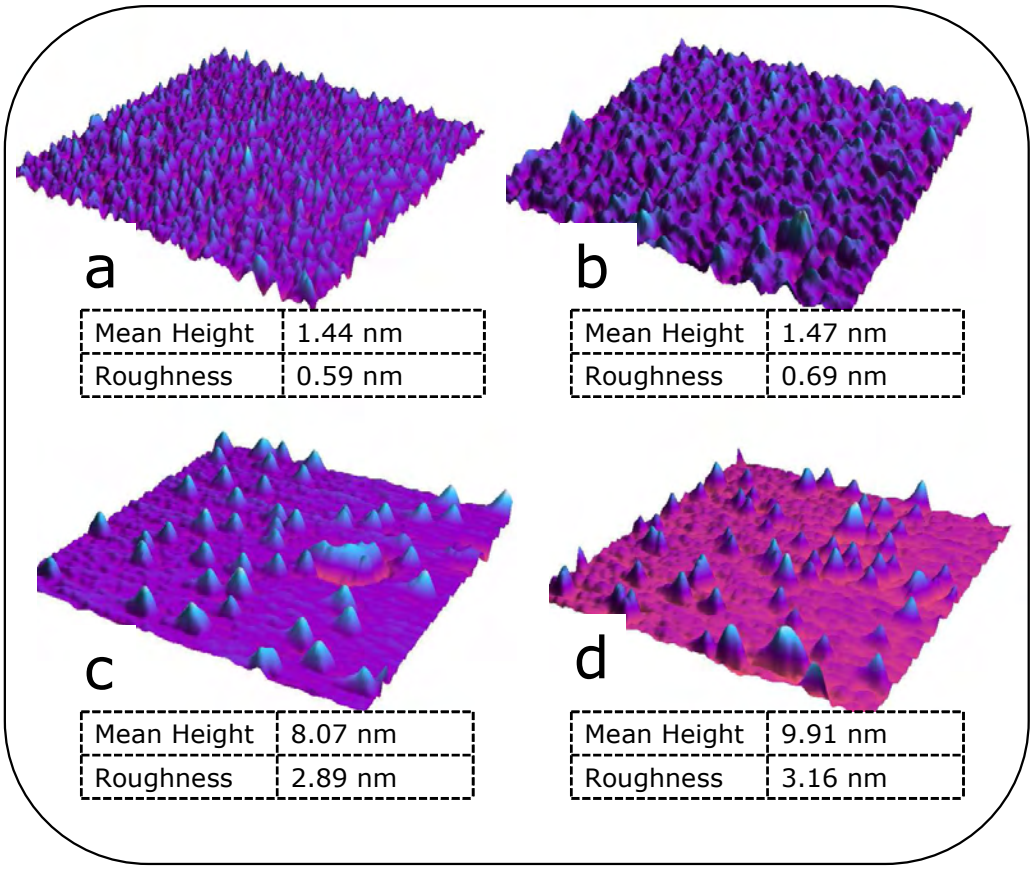

Figure 3.40: Typical 3-D AFM images of (a) bare-Au, (b) Au-DMAET, (c) Au-DMAET-MPCAuNP-$COOH_{50\%}$ and (d) Au-DMAET-MPCAuNP-$COOH_{99\%}$.

3.5.2 Cyclic Voltammetric Evolution and Electron Transfer in Non-Aqueous Solution

Figure 3.41 (a) shows the CV profiles of bare-Au, Au-DMAET, Au-DMAET-MPCAuNP-$COOH_{1\%}$, Au-DMAET-MPCAuNP-$COOH_{50\%}$ and Au-DMAET-MPCAuNP-$COOH_{99\%}$ in CH_2Cl_2 containing 0.1 M tetra-*n*-butylammonium perchlorate (TBAP). Some well-defined voltammetric peaks are observed in the potential range of –0.8 and +1.1 V (vs. AgCl). The activities in the negative potential region (0.0 to –0.8 V) may be attributed to the presence of the DMAET molecule since the bare gold electrode is the only electrode that shows no peak at -0.45 V. For clarity, the voltammetric evolutions in the positive potential region (0.0 to +1.1 V) are shown for the activities of the Au-DMAET-MPCAuNP-$COOH_{1\%}$ (Fig. 3.41b), Au-DMAET-MPCAuNP-$COOH_{50\%}$ (Fig. 3.41c) and Au-DMAET-MPCAuNP-$COOH_{99\%}$ (Fig. 3.41d).

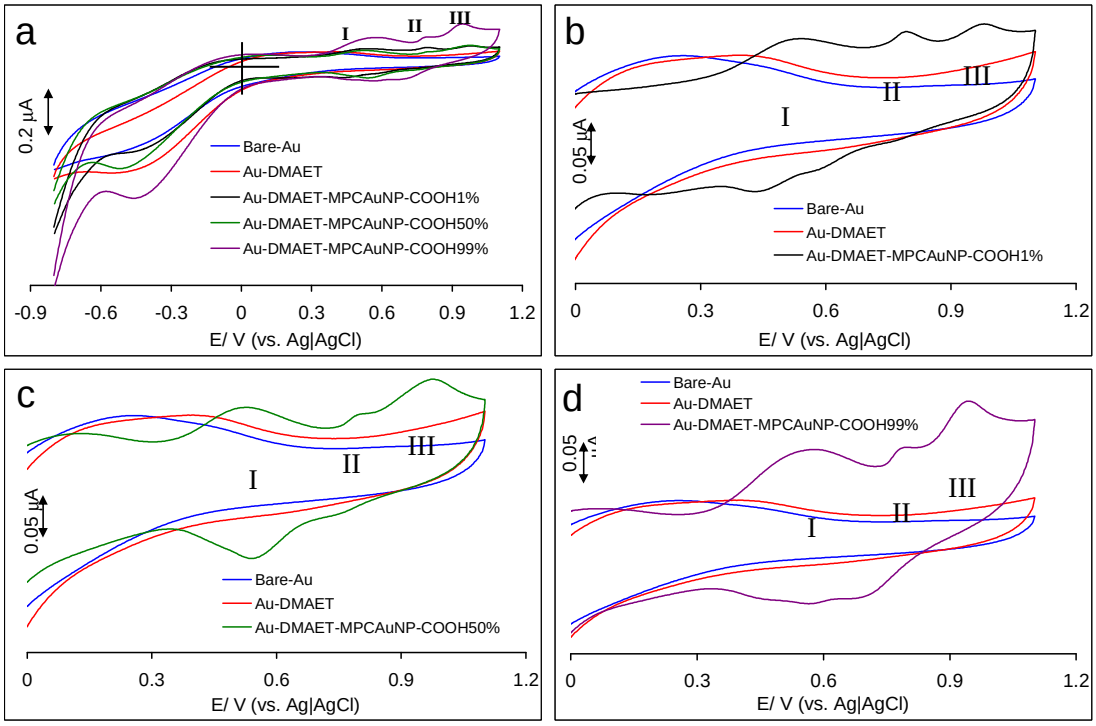

Figure 3.41: (a) Cyclic voltammograms of bare-Au, Au-DMAET, Au-DMAET-MPCAuNP-$COOH_{1\%}$, Au-DMAET-MPCAuNP-$COOH_{50\%}$ and Au-DMAET-MPCAuNP-$COOH_{99\%}$ in CH_2Cl_2 containing 0.1M TBAP at a scan rate of 25mV/s. The amplified area between 0 – 1.2 V (vs. Ag|AgCl) of Au-DMAET-MPCAuNP-$COOH_{1\%}$, Au-DMAET-MPCAuNP-$COOH_{50\%}$ and Au-DMAET-MPCAuNP-$COOH_{99\%}$ are exemplified in b, c and d respectively.

All the three PEG-stabilized MPCAuNP exhibit three well-defined redox processes at equilibrium potential ($E_{1/2} \approx 0.53$, 0.78 and 0.96 V vs. AgCl wire). From previous works on ligand-protected gold nanoparticles [61-63], these redox processes may be ascribed to the discrete charging of the adsorbed particle double layers [64,65]. The observation of the discretized double-layer charging is dependent on the nanoparticle potential change (ΔV) incurred upon a single electron

transfer to/from the working electrode or any other electron-donor/acceptor. ΔV is the space between any two neighbouring peak voltages. These nanoparticles are usually described as 'quantum capacitors', with their stored-charge potentials changing by values that are easily seen upon single-electron transfers. From Figure 3.41, it can be seen that the charging peak around 0.5 V (**I**) appeared broad for all three electrodes, suggesting the occurrence of a two-electron transfer process arising from two close ΔVs. In fact, a closer look at the scan rate studies, exemplified for the Au-DMAET-MPCAuNP-$COOH_{1\%}$ (Fig. 3.42a) and Au-DMAET-MPCAuNP-$COOH_{99\%}$ (Fig. 3.42b), clearly prove that the broad peak at the **I** is two peaks. Thus, the two close peaks are assigned to $MPC^{1+/0}$ and $MPC^{2+/1+}$, while processes **II** and **III** may be ascribed to the $MPC^{3+/2+}$ and $MPC^{4+/3+}$, respectively.

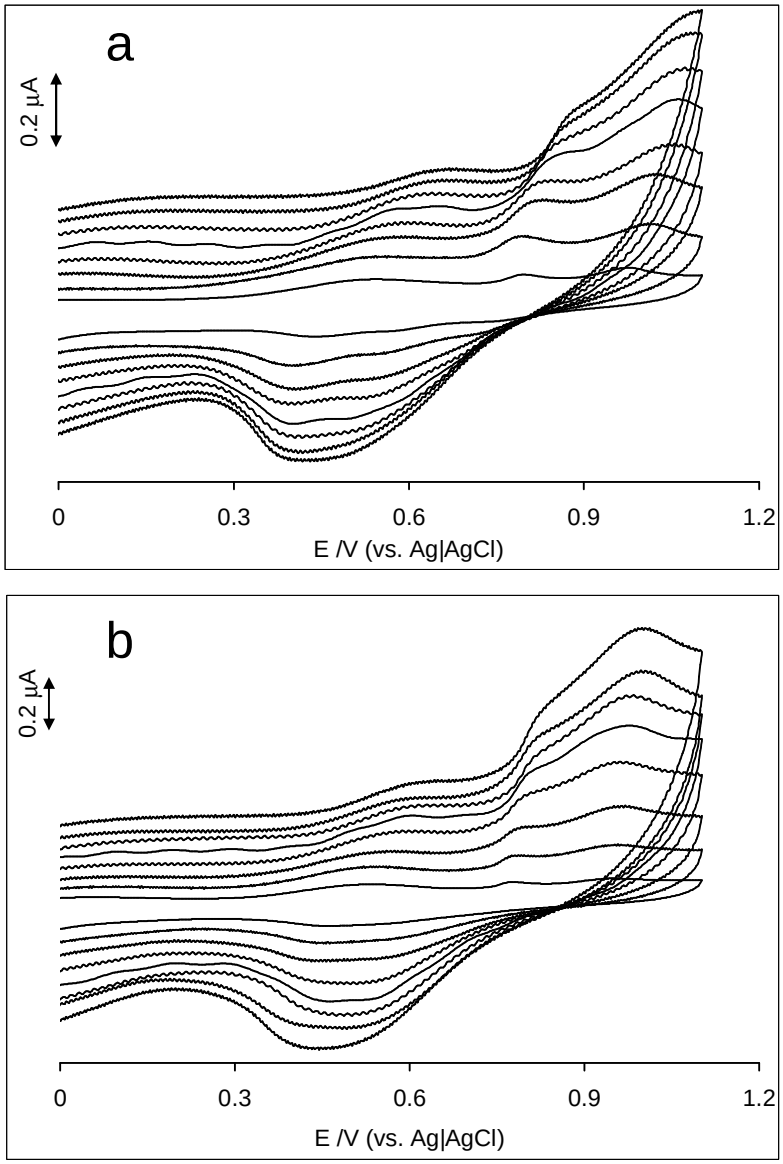

Figure 3.42: Scan rate studies at (a) Au-DMAET-MPCAuNP-$COOH_{1\%}$ (25 mV – 200 mV) and (b) Au-DMAET-MPCAuNP-$COOH_{99\%}$ (25 mV – 300 mV).

Electrochemical impedance spectroscopy represents a crucial technique for probing the heterogeneous electron transfer kinetics at gold electrodes modified with self-assembled MPCAuNPs. EIS

experiments were carried out for each of the modified electrodes. Figure 3.43 presents typical comparative Nyquist plots obtained for the three modified electrodes, based at different potentials (~0.53, 0.78 and 0.96 V vs. Ag|AgCl). The experimental data were satisfactorily fitted with the modified Randles electrical equivalent circuit (Fig. 3.39).

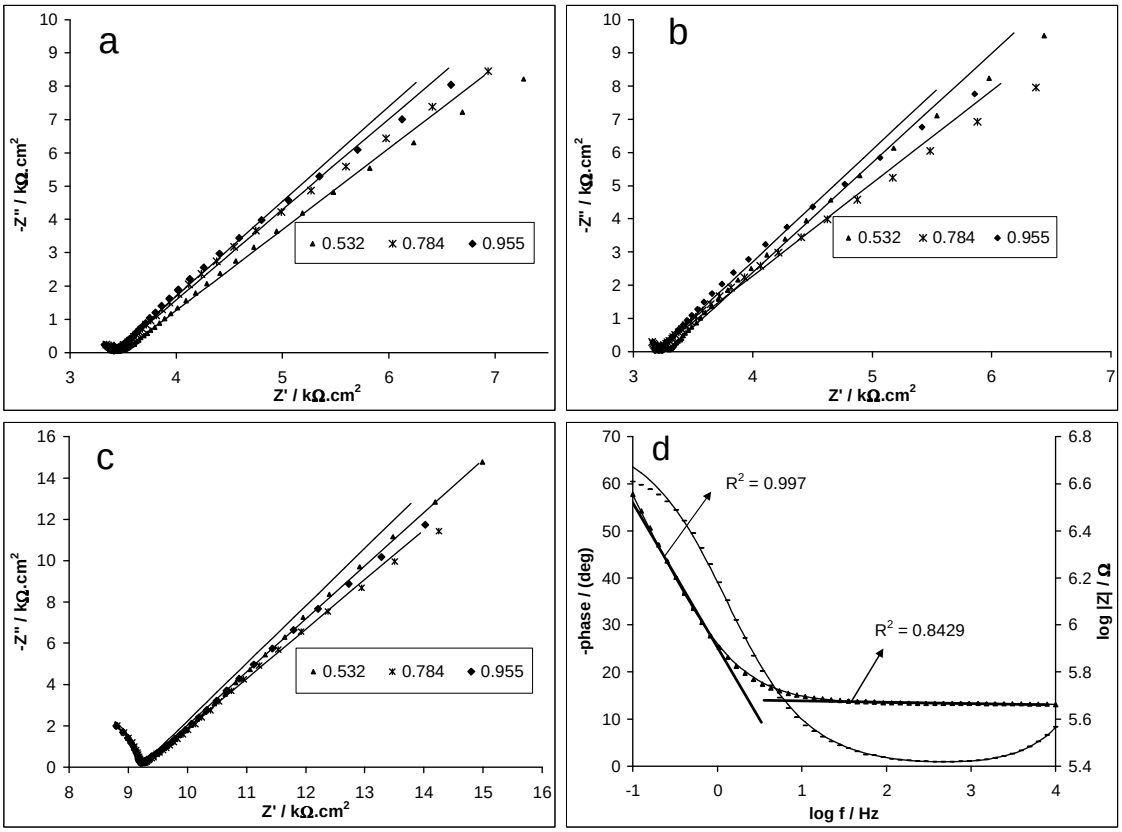

Figure 3.43: (a-c) Nyquist plots resulting from Au-DMAET-MPCAuNP-$COOH_{1\%}$, Au-DMAET-MPCAuNP-$COOH_{50\%}$ and Au-DMAET-MPCAuNP-$COOH_{99\%}$ respectively, in CH_2Cl_2 containing 0.1 M TBAP. (d) Typical bode plot of Au-DMAET-MPCAuNP-$COOH_{99\%}$ in the same solution.

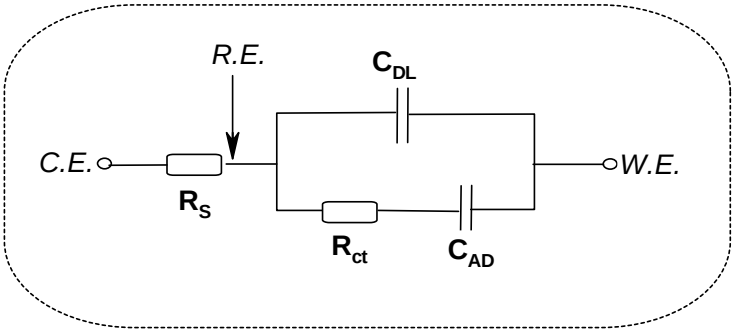

Figure 3.44: Modified Randles electrical equivalent circuit.

In the model, the R_s is the solution or electrolyte resistance, R_{ct} represents the electron-transfer resistance, C_{Au} is double-layer capacitance of the gold electrode, while C_{ads} is the capacitance of the adsorbed MPCAuNP species, defined as Equation 3.7:[66].

$$C_{ads} = \frac{F^2 A\Gamma}{4RT} \qquad 3.7$$

where F is the Faraday constant, A is the area of the electrode, Γ is the surface coverage, R is the gas constant, and T is the Kelvin temperature. From this equation, the values of surface coverage (determined using the one-electron processes **II** ($MPC^{3+/2+}$) and **III** ($MPC^{4+/3+}$) in Figure 3.42 are: Au-DMAET-MPCAuNP-$COOH_{1\%}$ (*ca.* 9.2 x 10^{-12} mol cm^{-2} or 5.54 x 10^{12} molecules cm^{-2}), Au-DMAET-MPCAuNP-$COOH_{50\%}$ (*ca.* 8.5 x 10^{-12} mol cm^{-2} or 5.12 x 10^{12} molecules cm^{-2}) and Au-DMAET-MPCAuNP-$COOH_{99\%}$ (*ca.* 10.7 x 10^{-12} mol cm^{-2} or 6.44 x 10^{12} molecules cm^{-2}).

Table 3.4: Comparative EIS data obtained for the electrodes in CH_2Cl_2 containing 0.1 M TBAP.

Electrodes	**Potentials (V)**	**R_s (kΩ cm^2)**	**C_{dl} (μF cm^{-2})**	**R_{ct} (kΩ cm^2)**	**C_{ads} (μF cm^{-2})**	**Γ (mol cm^{-2})**	**K_{et} (s^{-1})**
Au-DMAET-MPCAuNP-$COOH_{1\%}$	0.532	3.06 (0.870)	9.50 (4.164)	8.56 (8.964)	12.43 (7.839)	9.17 x 10^{-12}	4.69 ± 0.45
	0.784	3.01 (0.832)	9.93 (4.271)	7.38 (8.928)	13.05 (7.019)	9.63 x 10^{-12}	5.19 ± 0.47
	0.955	2.96 (0.760)	11.07 (3.644)	9.57 (9.370)	11.79 (8.010)	8.7 x 10^{-12}	4.43 ± 0.41
Au-DMAET-MPCAuNP-$COOH_{50\%}$	0.532	3.34 (0.640)	10.01 (3.114)	11.56 (9.425)	8.67 (6.763)	6.4 x 10^{-12}	4.98 ± 0.41
	0.784	3.25 (0.648)	10.98 (3.293)	9.49 (8.156)	12.05 (6.925)	8.89 x 10^{-12}	4.37 ± 0.42
	0.955	3.25 (0.584)	12.83 (3.022)	11.13 (9.320)	10.98 (7.746)	8.1 x 10^{-12}	4.09 ± 0.38
Au-DMAET-MPCAuNP-$COOH_{99\%}$	0.532	9.67 (1.106)	10.50 (3.684)	56.65 (8.605)	14.54 (7.665)	1.07 x 10^{-11}	0.61 ± 0.07
	0.784	9.61 (1.067)	11.02 (3.478)	63.08 (8.842)	13.94 (8.044)	1.03 x 10^{-11}	0.57 ± 0.06
	0.955	9.56 (1.075)	12.83 (3.678)	60.31 (9.767)	15.09 (8.776)	1.11 x 10^{-11}	0.55 ± 0.08

Assuming a closed-packed structure of the surface MPCAuNP assembly, this corresponds to a (centre-to-centre) inter-nanoparticle distance of approximately 4 nm. This value is smaller than the physical diameter of 14 nm (core + mixed ligand monolayers), and represents a surface coverage of about a magnitude higher than the expected monolayer for 14 nm (i.e., 8.47 x 10^{-12} mol cm^{-2} or 5.10 x 10^{11} molecules cm^{-2}). The reason for this higher coverage is possibly due to relatively higher assembling time used in this work. However, attempts at using short assembling time did not produce noticeable voltammeric response, necessitating the longer assembling period (18 h) used in this study.

For all the MPCAuNP-modified gold electrodes, the slopes of the Bode plots (log $|Z|$ vs. log f, Figure 3.43d) are approximately similar (*ca*. –0.62, r^2 = 0.992) at the mid frequency region, indicative of pseudocapacitive behaviour. At high frequency regions, the slopes are almost zero, indicative of resistive behaviour at these high frequency regions. The phase angles seen on the other Bode plots (i.e., –phase angle (ϕ) vs. log f, Figure 3.43d) are in the range of 49 - 60°, which are less than the 90° expected of an ideal capacitive behaviour. These results indicate that both C_{Au} and C_{ads} used in the fitting are constant phase elements (CPE), not true double-layer capacitances. CPE arises from such factors as (i) the nature of the electrode (e.g., roughness

and polycrystallinity), (ii) distribution of the relaxation times due to heterogeneities existing at the electrode/electrolyte interface, (iii) porosity and (iv) dynamic disorder associated with diffusion [67-69].

The electron transfer rate constant (k_{et} / s^{-1}) of each of the electrodes was obtained from [66]:

$$k_{et} = \frac{1}{2R_{ct}C_{ads}} \qquad 3.8$$

From Table 3.4, it is seen that the average k_{et} value decreases as the concentration of the surface-exposed –COOH group in the protecting monolayer ligand increases: Au-DMAET-MPCAuNP-$COOH_{1\%}$ (~ 5 s^{-1}) > Au-DMAET-MPCAuNP-$COOH_{50\%}$ (~ 4 s^{-1}) >> Au- DMAET-MPCAuNP-$COOH_{99\%}$ (~ 0.5 s^{-1}). Considering that the ionisation constant (pK_a) values of alkanols are inherently higher than their corresponding alkanoic acids [70]. Thus, this trend may be interpreted in terms of the hydrophobicity or affinity of the terminal functional groups (-COOH and –OH) with organic solvent such as CH_2Cl_2. Considering that the pK_a of –OH based monolayer ligands will be higher that their –COOH counterparts, the extent to which these MPCAuNPs will associate with the organic solvents will decrease as MPCAuNP-$COOH_{1\%}$ > MPCAuNP-$COOH_{50\%}$ > MPCAuNP-$COOH_{99\%}$.

Next, the same cyclic voltammetric experiment was carried out in 0.5 M H_2SO_4 for the three MPCAuNPs (Fig. 3.45) and made three

important findings. First, the quantized charging processes of the MPCAuNPs seen in the non-aqueous solution (Fig. 3.41) are not seen or clearly defined in aqueous solution (Fig. 3.45). This observation is in agreement with other workers who carried out similar experiments in aqueous PBS solution. The observation may be interpreted using the proposed equivalent circuit (Fig. 3.44). In organic solutions, the overall electrode double-layer capacitance is governed by the adsorbed MPCAuNPs (i.e., C_{ads} > C_{Au}, Table 3.4) [64,71] while the measured current response is the collective quantized charging of individual surface-confined MPCAuNP. In the aqueous solution, however, the inverse is the case (i.e., C_{ads} << C_{Au}) [64,71].

Second, from the comparative cyclic (Fig. 3.45a) and square wave voltammograms (SWV) (Fig. 3.45b), only the MPCPCAuNP-$COOH_{99\%}$ showed a weak redox peak at a formal potential ($E_{1/2}$) of about 0.22 V, attributed to the MPCAuNP redox process. Also, the three gold-modified MPCAuNPs, including the bare gold and Au-DMAET, showed a broad peak at ~0.45 V, which was ascribed in section 3.1.2 to surface reactions of the bare gold and/or the electric field-induced protonation/deprotonation redox processes of the DMAET SAM.

Third, it is clearly seen in Figure 3.45 that the Au-DMAET-MPCAuNP-$COOH_{99\%}$ showed slightly higher capacitive/background current than the Au-DMAET-MPCAuNP-$COOH_{1\%}$ or Au-DMAET-

MPCAuNP-COOH$_{50\%}$. This is also confirmed from the EIS experiment (Fig. 3.46, Table 3.5) where the C_{ad} value decreased as MPCAuNP-COOH$_{99\%}$ (0.51 µF) ≈ MPCAuNP-COOH$_{50\%}$ (0.51 µF) > MPCAuNP-COOH$_{1\%}$ (0.46 µF).

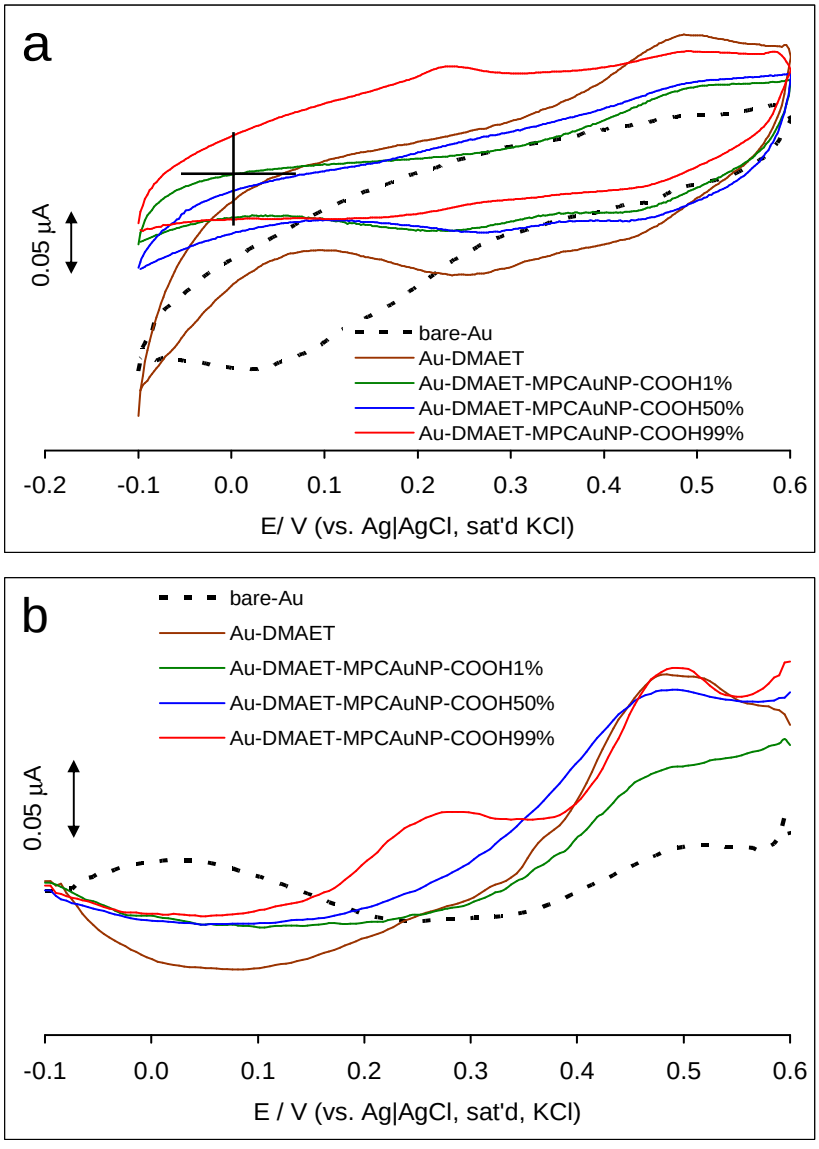

Figure 3.45: (a) CV and (b) SWV plots of bare-Au, Au-DMAET, Au-DMAET-MPCAuNP-COOH$_{1\%}$, Au-DMAET-MPCAuNP-COOH$_{50\%}$ and Au-DMAET-MPCAuNP-COOH$_{99\%}$ in 0.5 M H_2SO_4.

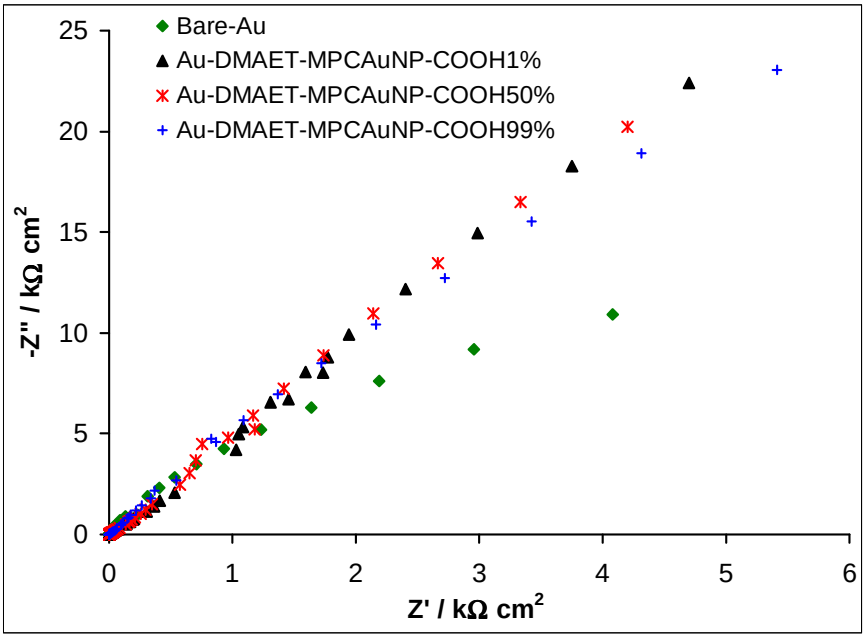

Figure 3.46: Nyquist plots resulting from bare-Au, Au-DMAET, Au-DMAET-MPCAuNP-$COOH_{1\%}$, Au-DMAET-MPCAuNP-$COOH_{50\%}$ and Au-DMAET-MPCAuNP-$COOH_{99\%}$ in 0.5 M H_2SO_4.

Table 3.5: Comparative EIS data obtained for the electrodes in H_2SO_4.

Electrodes	**R_s (Ω cm^2)**	**C_{dl} (μF cm^{-2})**	**R_{ct} (kΩ cm^2)**	**C_{ads} (μF cm^{-2})**	**K_{et} (s^{-1})**
Bare-Au	0.63 (9.524)	66.63 (3.425)	2.44 (23.488)	60.31 (13.616)	3.40
Au-DMAET-MPCAuNP-$COOH_{1\%}$	0.94 (33.465)	13.50 (6.134)	1.22 (24.429)	22.84 (12.471)	17.89
Au-DMAET-MPCAuNP-$COOH_{50\%}$	1.10 (20.416)	15.97 (5.144)	0.98 (20.125)	23.48 (10.46)	21.80
Au-DMAET-MPCAuNP-$COOH_{99\%}$	1.10 (16.168)	19.46 (4.654)	0.88 (21.889)	24.08 (7.665)	23.11

It is well established that the capacitance of any thiol-SAM is dependent on its terminal functional group, and increases as –COOH > -OH > -CH_3 [70]. In addition, the hydrophilic terminal groups are by nature quasi-liquids, while the hydrophobic groups are quasi-solids [70, 72-74], meaning that the SAMs of the –COOH terminal groups (in this case, the MPCAuNP-$COOH_{99\%}$) should be more permeable to solution ions than those of the –OH terminated MPCAuNPs (notably the Au-DMAET-MPCAuNP-$COOH_{1\%}$). The charge transfer constants, also estimated from Equation 3.8, decreased as follows: Au-DMAET-MPCAuNP-$COOH_{99\%}$ (23.11 s^{-1}) > Au-DMAET-MPCAuNP-$COOH_{50\%}$ (21.80 s^{-1}) > Au-DMAET-MPCAuNP-$COOH_{1\%}$ (17.89 s^{-1}). The higher k_{et} value of the MPCAuNP-$COOH_{99\%}$ may also be explained by the quasi-liquidity of these materials that allow the penetration of the solution species. Such penetration may be enhanced by (i) the electrostatic interactions between the negatively-charged carboxylic head group of the MPCAuNP-$COOH_{99\%}$ and the H_3O^+ of the electrolyte solution, and/or (ii) the repulsive interactions between the neighbouring ionised –COOH head groups that could create some interparticle voids or pinholes that permit the penetration of the solution ions [75]. As a contrast, the relatively lower k_{et} of the more hydrophobic MPCAuNP-$COOH_{1\%}$ is due to the unfavoured interaction of the solution ions with the unionised, quasi-solid terminal -OH groups.

3.5.3 Electron transfer Kinetics in an Aqueous Solution of $[Fe(CN)_6]^{3-/4-}$

Electron transport properties of the electrodes were studied in 0.1 M KCl containing equimolar (1 mM) mixture of $K_4Fe(CN)_6$ and $K_3Fe(CN)_6$. Typical comparative CVs are shown in Figure 3.47. The modified electrodes exhibited stable electrochemistry as the voltammograms recorded did not change after several repetitive cycling.

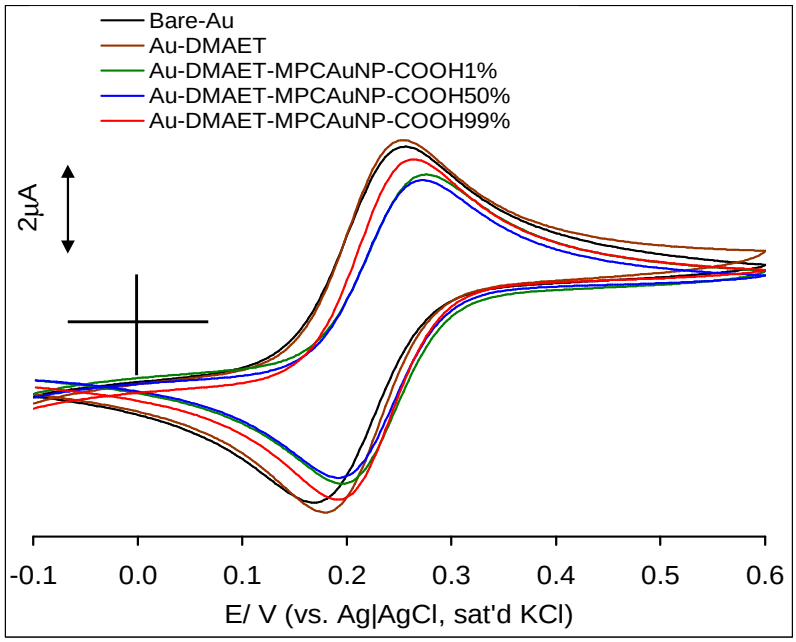

Figure 3.47: CV profiles showing bare-Au, Au-DMAET, Au-DMAET-MPCAuNP-$COOH_{1\%}$, Au-DMAET-MPCAuNP-$COOH_{50\%}$ and Au-DMAET-MPCAuNP-$COOH_{99\%}$ in 0.1 M KCl containing equimolar mixture of $K_4Fe(CN)_6$ and $K_3Fe(CN)_6$ at a scan rate of 25 mV s^{-1}.

From the CV, the current responses of the modified electrode are essentially the same as that of the bare gold electrode. This type of behaviour has been elegantly described by the theoretical framework of Davies [76-77] and Compton [76-78] as the type 4 behaviour (i.e., planar / linear diffusion, wherein the diffusion layer thickness, δ, is much larger than the insulating layer leading to a complete or heavily overlapping of the adjacent diffusion layers and a linear concentration profile).

Also, the cyclic voltammograms in Figure 3.47 shows that the peak-to-peak separation potential (ΔE_p) approximately follows this trend, MPCAuNP-$COOH_{1\%}$ (0.081 V) > MPCAuNP-$COOH_{50\%}$ (0.079 V) > MPCAuNP-$COOH_{99\%}$ (0.070 V), suggesting that the electron transport at the MPCAuNP-$COOH_{1\%}$ is slowest compared to the other electrodes. All the electrodes showed almost same formal potential ($E_{1/2} \approx 220$ mV).

Electrochemical impedance spectroscopy experiments were carried out for further insights into the electron transport properties. Figure 3.48 shows typical Nyquist plots obtained for the electrodes in 0.1 M KCl containing the $[Fe(CN)_6]^{4-}$/ $[Fe(CN)_6]^{3-}$ solution at the formal potential of the electrodes (0.22 V vs. Ag|AgCl sat'd KCl).

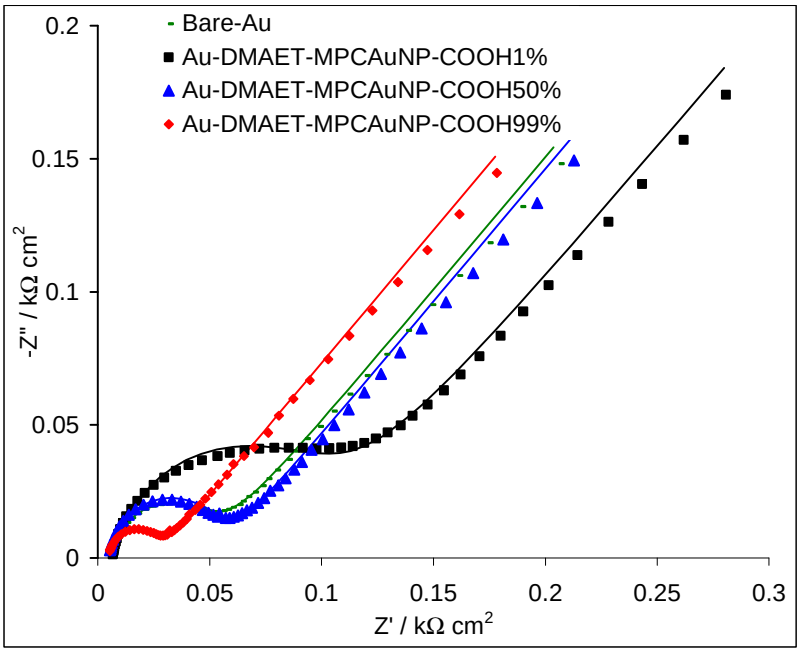

Figure 3.48: Nyquist plots resulting from bare-Au, Au-DMAET, Au-DMAET-MPCAuNP-$COOH_{1\%}$, Au-DMAET-MPCAuNP-$COOH_{50\%}$ and Au-DMAET-MPCAuNP-$COOH_{99\%}$ in 0.1 M KCl containing equimolar mixture of $K_4Fe(CN)_6$ and $K_3Fe(CN)_6$.

The EIS data were satisfactorily fitted with the modified Randles equivalent circuit model (Fig. 1.8a), wherein the true capacitance is replaced by the CPE. In this model the Z_w is the Warburg impedance, while other parameters retain their usual meaning. The apparent electron transfer rate constant (k_{app} / cm s^{-1}) of each of the electrodes was obtained from Equation 3.6 [49]. However, in this experiment R_p = R_{ct}.

$$k_{app} \approx k^o = \frac{RT}{n^2 F^2 A R_p C}$$

where the R_{ct} value is obtained from the fitted Nyquist plots and all other terms retain their usual meaning. From Table 3.6, the k_{app} value decreases as the concentration of the surface-exposed –COOH group in the protecting monolayer ligand decreases: Au-DMAET-MPCAuNP-$COOH_{99\%}$ (12.2×10^{-3} cm s^{-1}) > Au-DMAET-MPCAuNP-$COOH_{50\%}$ (5.3×10^{-3} cm s^{-1}) > Au-DMAET-MPCAuNP-$COOH_{1\%}$ (2.7×10^{-3} cm s^{-1}).

Table 3.6: Comparative EIS data obtained for the electrodes in 0.1 M KCl containing equimolar mixture of $K_4Fe(CN)_6$ and $K_3Fe(CN)_6$

Electrodes	**R_s (Ω cm^2)**	**CPE (μF cm^{-2})**	**n**	**R_{ct} (Ω cm^2)**	**$10^3 Z_w$ (μF cm^{-2})**	**$10^3 K_{app}$ (cm s^{-1})**
Bare-Au	4.96 (0.851)	47.26 (3.308)	0.86 (0.466)	46.50 (0.700)	0.12 (0.545)	(5.7±0.04)
Au-DMAET-MPCAuNP-$COOH_{1\%}$	6.17 (1.367)	84.89 (4.991)	0.83 (0.793)	96.67 (1.577)	0.10 (1.556)	(2.7±0.04)
Au-DMAET-MPCAuNP-$COOH_{50\%}$	4.76 (1.992)	18.91 (6.102)	0.89 (0.783)	50.0 (1.017)	0.11 (0.960)	(5.3±0.05)
Au-DMAET-MPCAuNP-$COOH_{99\%}$	4.44 (1.741)	20.24 (6.910)	0.89 (0.876)	23.11 (1.033)	0.12 (0.536)	(12.2±0.12)

Also from the bode plot (-Phase angle vs. log. f, Figure 3.49) the frequency synonymous with rate of reaction [78-79] at which the phase angles were observed decreased as follows: Au-DMAET-MPCAuNP-$COOH_{99\%}$ (2511.9 Hz) > Au-DMAET-MPCAuNP-$COOH_{50\%}$ (1513.6 Hz) > Au-DMAET-MPCAuNP-$COOH_{1\%}$ (316.2 Hz), corroborating the k_{app} trend.

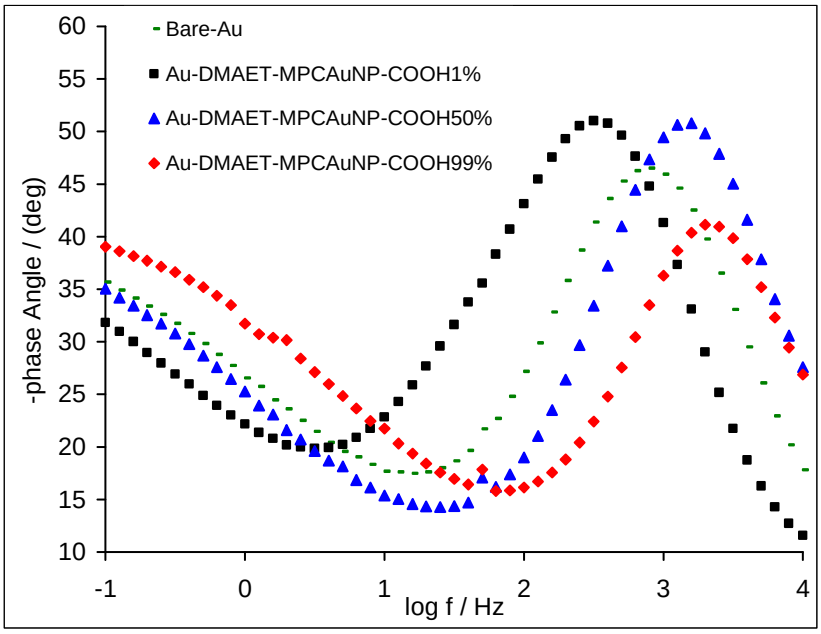

Figure 3.49: Bode plots showing the -phase angle vs. log. of frequency for the bare-Au, Au-DMAET, Au-DMAET-MPCAuNP-$COOH_{1\%}$, Au-DMAET-MPCAuNP-$COOH_{50\%}$ and Au-DMAET-MPCAuNP-$COOH_{99\%}$ in 0.1 M KCl containing equimolar mixture of $K_4Fe(CN)_6$ and $K_3Fe(CN)_6$.

The k_{app} for this outer-sphere redox probe in aqueous solution follows the same trend as in the 0.5 M H_2SO_4, but the reverse of the results obtained in the non-aqueous electrolyte already discussed. The high k_{app} value for the MPCAuNP-$COOH_{99\%}$ is interpreted as for the

experiment in the 0.5 M H_2SO_4, that is, in terms of its quasi-liquid nature as opposed to the quasi-solid nature of the MPCAuNP-$COOH_{1\%}$.

3.5.4 Surface pK_a of the MPCAuNPs

The pK_a of a surface-immobilized species is the value of the pH in contact with monolayer when half of the functional groups have been ionized [80]. Surface pK_a is easily determined with EIS strategy using solutions of $[Fe(CN)_6]^{4-}/[Fe(CN)_6]^{3-}$ of different pH values [81-83]. Figure 3.50 represent typical impedance spectral profiles of (a) MPCAuNP-$COOH_{1\%}$, (b) MPCAuNP-$COOH_{99\%}$ and Figure 3.51 shows (c) plots of the R_{ct} vs. pH for MPCAuNP-$COOH_{1\%}$ MPCAuNP-$COOH_{50\%}$ and MPCAuNP-$COOH_{99\%}$ obtained obtained in PBS solutions of $[Fe(CN)_6]^{4-}/[Fe(CN)_6]^{3-}$ (pH 1.91 – 10.0 range). There are four main findings in this experiment. First, at the pH < 8.0, the resistance to electron transport (R_{ct}) follows as MPCAuNP-$COOH_{1\%}$ > MPCAuNP-$COOH_{50\%}$ > MPCAuNP-$COOH_{99\%}$, which means that at low pH the redox species experiences more difficulty in penetrating the MPCAuNP monolayer as the concentration of the –COOH group decreases.

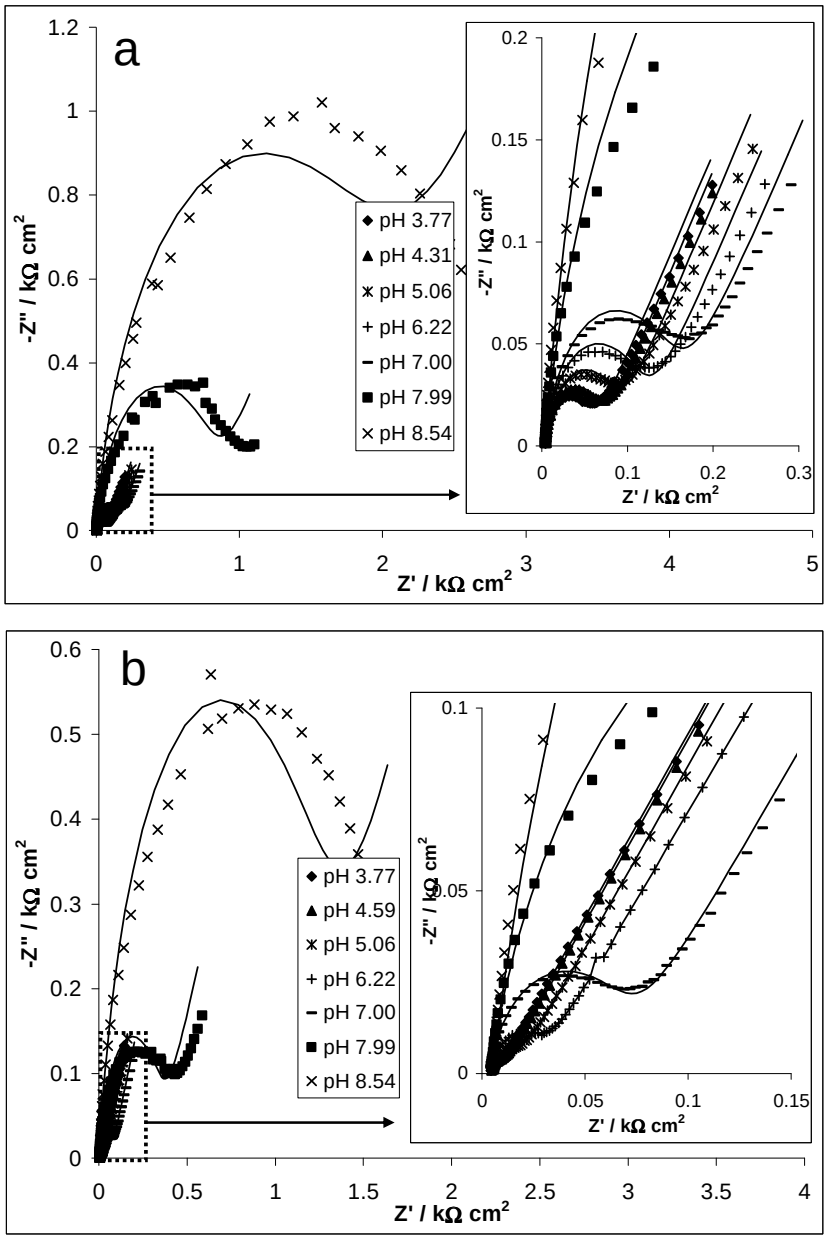

Figure 3.50: Typical impedance spectral profiles showing nyquist plots of (a) MPCAuNP-$COOH_{1\%}$, (b) MPCAuNP-$COOH_{99\%}$ obtained in PBS solutions of $[Fe(CN)_6]^{4-}/[Fe(CN)_6]^{3-}$.

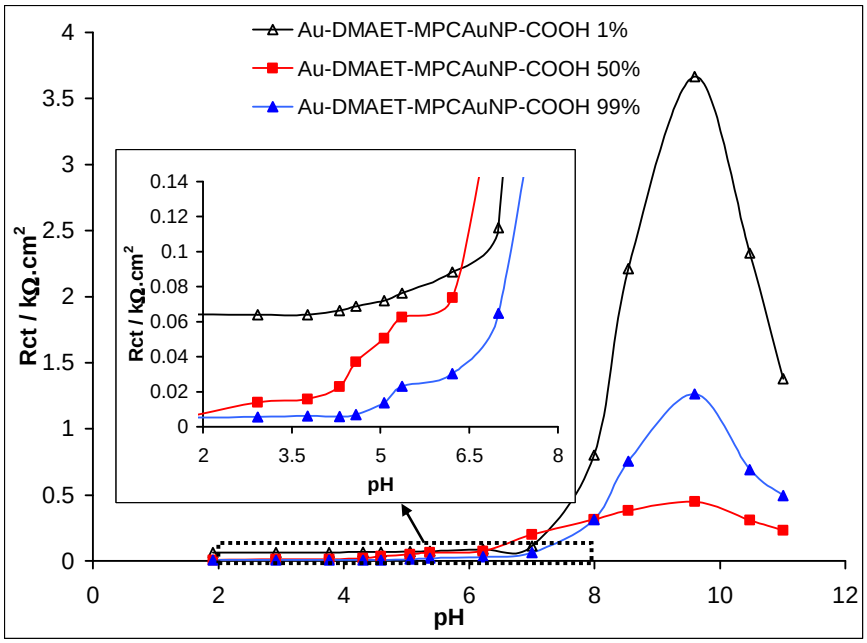

Figure 3.51: Plot of charge transfer resistance (R_{ct} / kΩ) against pH for MPCAuNP-$COOH_{1\%}$ MPCAuNP-$COOH_{50\%}$ and MPCAuNP-$COOH_{99\%}$ obtained in PBS solutions of $[Fe(CN)_6]^{4-}/[Fe(CN)_6]^{3-}$ (pH 1.91 – 10.0 range).

Second, the electron transport of the MPCAuNPs are much higher at pH > 8.0 than at pH < 8.0, indicating that the surface groups are more deprotonated at pH > 8.0, resulting in electrostatic repulsion between these negatively-charged head groups and the negatively-charged $[Fe(CN)_6]^{4-}/[Fe(CN)_6]^{3-}$. Note that at the pH > 8.0 the resistance to electron transport is more difficult at the MPCAuNP-$COOH_{1\%}$ compared to the MPCAuNP-$COOH_{50\%}$ and MPCAuNP-$COOH_{99\%}$, which means that the penetration of the redox probe at the terminal –OH group is more difficult compared to the –COOH groups. The

efficient electron transport observed for the MPCAuNP-$COOH_{50\%}$ and MPCAuNP-$COOH_{99\%}$ may be related to the enhanced repulsive interactions amongst the neighbouring deprotonated groups that create wider spaces (pinholes) for the penetration of the redox probe into the films. Third, unlike the MPCAuNP-$COOH_{1\%}$, both MPCAuNP-$COOH_{50\%}$ and MPCAuNP-$COOH_{99\%}$ exhibit a sigmoidal shape with a midpoint at ~ pH 5, signifying an initial pK_a of ~ 5. Fourth, at pH > 8, the three MPCAuNPs gave well defined sigmoidal curves; pK_a of ~8.2 for the MPCAuNP-$COOH_{1\%}$, while both MPCAuNP-$COOH_{50\%}$ and MPCAuNP-$COOH_{99\%}$ showed two pK_a values of ~5.0 and ~8.0. These two p*K*a's may be related to two possible locations of the –COOH groups, presumably the well surface-exposed –COOH groups that easily access the electrolyte, and the slightly 'buried' –COOH groups that are somewhat less easily accessible to the electrolyte solution.

In general, the electronic communication is strongly influenced by the hydrophobicity / hydrophilicity of the head groups (-OH and –COOH); in aqueous solution the electron transport of the –COOH based ligand is favoured, while in the non-aqueous medium the electron transport of the –OH based ligands is favoured. Unfortunately, there is no accessible literature for surface pK_a of MPCAuNP with which to compare the present data.

3.5.5 Voltammetric Detection of Ascorbic Acid and Epinephrine

Figure 3.52 shows comparative cyclic voltammetric evolutions at Au-DMAET-MPCAuNP-$COOH_{1\%}$, Au-DMAET-MPCAuNP-$COOH_{50\%}$ and Au-DMAET-MPCAuNP-$COOH_{99\%}$ in a PBS solution (pH 7.4) containing 10 µM ascorbic acid. Clearly, Au-DMAET-MPCAuNP-$COOH_{1\%}$ shows a significantly greater peak current response than the MPCAuNPs with higher carboxyl content. While the terminal –COOH group of the PEG-ligands and ascorbic acid are expected to be fully deprotonated at this pH 7.4 (pK_a of ascorbic acid = 4.17 [84]), the deprotonation of the terminal –OH group is highly unlikely considering the inherent high pK_a values of alkanolic compounds. Thus, the excellent suppression of the voltammetric response of the ascorbic acid by the Au-DMAET-MPCAuNP-$COOH_{99\%}$ may be attributed to the repulsive interaction between the negatively-charged ascorbic acid and the -COOH groups of the PEG-ligands.

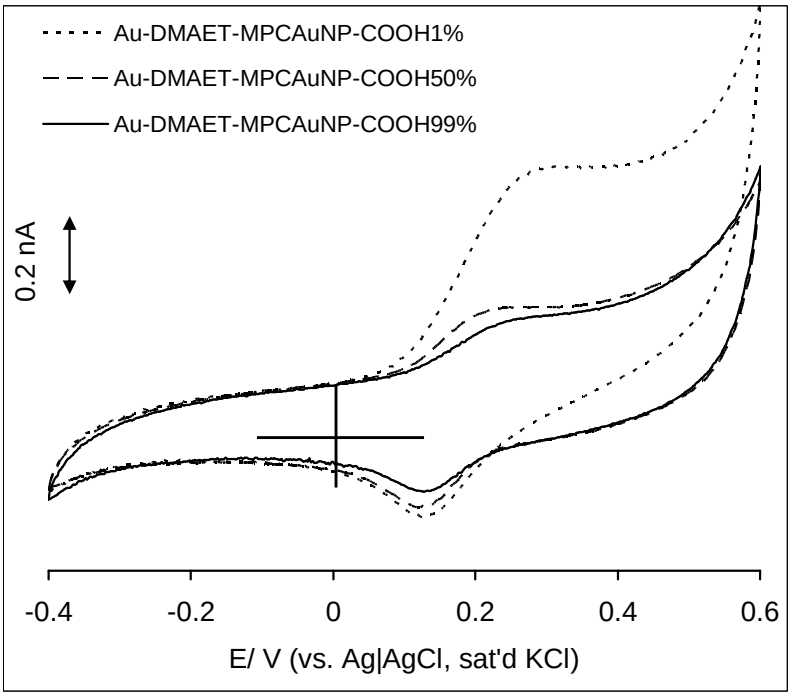

Figure 3.52: Cyclic voltammetric evolutions in 10 µM ascorbic acid at Au-DMAET-MPCAuNP-$COOH_{1\%}$, Au-DMAET-MPCAuNP-$COOH_{50\%}$ and Au-DMAET-MPCAuNP-$COOH_{99\%}$.

Figure 3.47 shows the voltammetric response of epinephrine in PBS solutions of different pH (pH 7.4 and 9.68) using the electrodes with two extreme mixtures (i.e., 1:99 and 99:1 ratios of PEG-COOH to PEG-OH ligands). Considering that epinephrine has different p*K*a's (8.7, 9.9 and 12.0 [85-87]), identical experiments in pH 7.4 and pH 9.68 were conducted. Figure 3.47 (a) and (c) shows comparative CV evolutions of Au-DMAET-MPCAuNP-$COOH_{1\%}$ and Au-DMAET-MPCAuNP-$COOH_{99\%}$ in 10 µM epinephrine pH7.4 and 9.68 respectively.

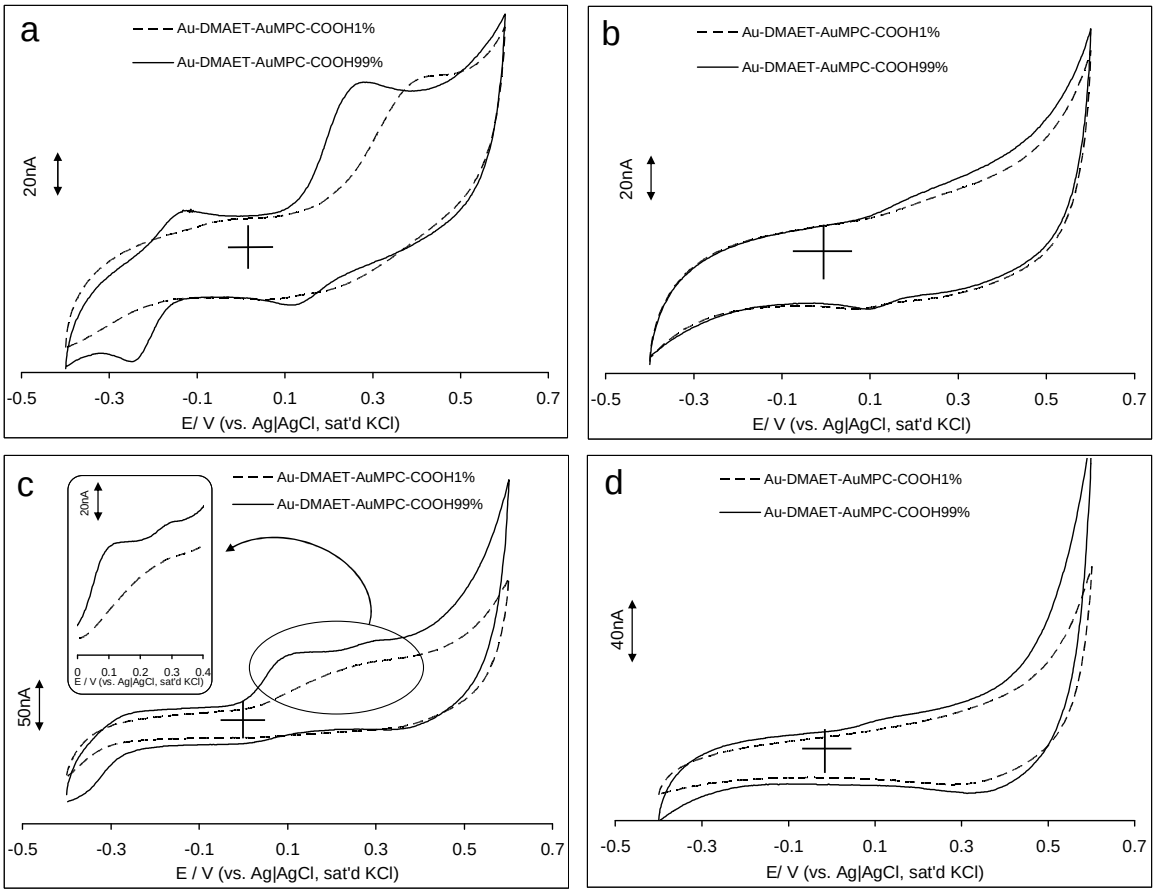

Figure 3.53: (a) and (c) shows comparative CV evolutions of Au-DMAET-MPCAuNP-$COOH_{1\%}$ and Au-DMAET-MPCAuNP-$COOH_{99\%}$ in 10 μM epinephrine pH7.4 and 9.68 respectively. (b) and (d) represent their corresponding CVs in their respective buffer solutions only.

Figure 3.40 (b) and (d) represents their corresponding CVs in their respective buffer solutions only. At pH 7.4, the onset potentials of the epinephrine were obtained at 0.10 and 0.15 V for the Au-DMAET-MPCAuNP-$COOH_{99\%}$ and Au-DMAET-MPCAuNP-$COOH_{1\%}$, respectively. The peak potential at the Au-DMAET-MPCAuNP-$COOH_{99\%}$ was at 0.3 V, while at the Au-DMAET-MPCAuNP-$COOH_{1\%}$ it was observed at a more

positive value (0.5 V). Also, in the alkaline medium (pH 9.68), Au-DMAET-MPCAuNP-$COOH_{99\%}$ and Au-DMAET-MPCAuNP-$COOH_{1\%}$ showed onset potential of 0.0 and 0.07 V, respectively. The current response at the Au-DMAET-MPCAuNP-$COOH_{99\%}$ is better defined than that at the Au-DMAET-MPCAuNP-$COOH_{1\%}$. These results clearly indicate that the Au-DMAET-MPCAuNP-$COOH_{99\%}$ exhibits more electrocatalytic activity towards the detection of epinephrine than the Au-DMAET-MPCAuNP-$COOH_{1\%}$. Also, unlike the Au-DMAET-MPCAuNP-$COOH_{1\%}$, the Au-DMAET-MPCAuNP-$COOH_{99\%}$ showed two oxidation peaks for epinephrine in pH 9.68 at 0.1 and 0.3 V (inset of Figure 3.47). The occurrence of these two oxidation peaks may be related to the oxidation of the different forms of the epinephrine in this pH conditions.

From the results in pH 7.4, considering peak current responses, it seems that for a simultaneous detection of the AA and EP in physiological pH medium, the Au-DMAET-MPCAuNP-$COOH_{1\%}$ may prove to be the best electrode. Further experiments are required to prove this concept, and will be the subject of future engagement. However, the key finding in this experiment is that one can possibly tune the ability of the gold nanoparticles to electrochemically recognize AA or EP in aqueous medium by smart manipulation of the ratios of their monolayer-protecting PEG-ligands.

Reference:

1. J. M. Campiña, A. Martins, F. Silva, *J. Phys. Chem. C.* 111 (2007) 5351.
2. H.S. White, J.D. Peterson, Q. Cui, K.J. Stevenson, *J. Phys. Chem. B* 102 (1998) 2930.
3. I. Burgess, B. Seivewright, R.B. Lennox, *Langmuir* 22 (2006) 4420.
4. S.M. Rosenthal, I.J. Burgess, *Electrochim. Acta* 53 (2008) 6759.
5. C.P. Smith, H.S. White, *Langmuir* 9 (1993) 1.
6. H. O. Finklea in Encyclopedia Chemistry, A. J. Bard and I. Rubinstein, Eds., Marcel Dekker: New York, 1996, Vol.19, pp109-335.
7. T.R. Lee, R.D. Carey, H.A. Biebuyck, G.M. Whitesides, *Langmuir* 10 (1994) 741.
8. D. Nkosi, K.I. Ozoemena, *Electrochim. Acta* 53 (2008) 2782.
9. B.O. Agboola, K.I. Ozoemena, *Phys.Chem.Chem.Phys* 10 (2008) 2399.
10. F. Caruso, E. Rodda, D.N. Furlong, V. Haring, *Sens. Actuators B* 41 (1997)189.
11. C. Saby, B. Ortiz, G.Y. Champagne, D. Bèlanger, *Langmuir* 13 (1997) 6805.

12. P. Abiman, A. Crossley, G.G. Wildgoose, J.H. Jones, R.G. Compton, *Langmuir* 23 (2007) 7847.

13. P. Abiman, G.G. Wildgoose, A. Crossley, J.H. Jones, R.G. Compton, *Chem. Eur. J.* 13 (2007) 9663.

14. J. Pillay, K. I. Ozoemena, *Electrochem. Commun*. 7 (2007) 1816.

15. K.I. Ozoemena, T. Nyokong, *Electrochim. Acta* 51 (2006) 2669.

16. B-Y. Chang, S-Y. Hong, J-S. Yoo, S-M. Park, *J. Phys.Chem. B.* 110 (2006) 19385.

17. L. Yang, Y. Li, *Biosens. Bioelectron*. 20 (2005) 1407.

18. G.D. Christian, Analytical Chemistry, sixth ed., John Wiley and Sons, New York, 2004.

19. S. Majdi, A. Jabbari, H. Heli, A. A. M-Movahedi, *Electrochimica Acta* 52 (2007) 4622.

20. Z. Yang, G. Hu, X. Chen, J. Zhao, G. Zhao, *Colloids Surf. B: Biointerf.* 54 (2007) 230.

21. L. Wang, J. Bai, P. Huang, H. Wang, L. Zhang, Y. Zhao, *Electrochem. Commun.* 8 (2006) 1035.

22. M.D. Hawley, S.V. Tatawawadi, S. Piekarski, R.N. Adams, *J.Am. Chem. Soc.* 89 (1967) 447.

23. S. H. Kim, J. W. Lee, I-H. Yeo, *Electrochim. Acta* 45 (200) 2889.

24. K. I. Ozoemena, D. Nkosi, J. Pillay, *Electrochim. Acta* 53 (2008) 2844.

25. N.B. Li, W. Ren, H.Q. Luo, *Anal. Chim. Acta* 378 (1999) 151.

26. J.H. Zagal, S. Lira, S. Ureta-Zanartu, *J. Electroanal. Chem.* 210 (1986) 95.

27. J.P. Collman, M. Kaplun, C.J. Sunderland, R. Boulatov, *J. Am. Chem. Soc.* 126 (2004) 11166.

28. A. Star, T.R. Han, J. Christophe, P. Gabriel, K. Bradley, G. Gruner *Nano. Lett.* 3 (2003) 403.

29. J. Zhang, M. Kambayashi, M. Oyama, *Electroanalysis* 17 (2005) 408.

30. B. O. Agboola, K. I. Ozoemena, *Electroanalysis* 20 (2008) 1696.

31. J.Y. Bai, L. Wang, H.J. Wang, P.F. Huang, Y.Q. Zhao, S.D.Fan, *Microchim. Acta* 156 (2007) 321.

32. L. Wang, J. Bai, P. Huang, H. Wang, L. Zhang, Y. Zhao, *Int. J.Electrochem. Sci.* 1 (2006) 238.

33. Y. B. He, H. Q. Luo, N. B. Li, *Instrum. Sci. Technol.* 35 (2007) 163.

34. B. Zeng, Y. Yang, F. Zhao, *Electroanalysis* 15 (2003) 1054.

35. B. Fang, X.-H. Deng, X.-W. Kan, H.-S. Tao,W.-Z. Zhang, M.-G. Li, *Anal. Lett.* 39 (2006) 697.

36. Y.-X. Sun, S.-F. Wang, X.-H. Zhang, Y.-F. Huang, *Sens.Actuators B* 113 (2006) 156.

37. A. Salimi, C. E. Banks, R. G. Compton, *Analyst* 129 (2004) 225.

38. [a] P. Liljeroth, D. Vanmaekelbergh, V. Ruiz, K. Kontturi, H. Jiang, E. Kauppinen, B.M. Quinn, *J. Am. Chem. Soc.* 126 (2004) 7126. [b] D. Bethell, M. Brust, D.J. Schiffrin, C. Kiely, *J. Electroanal. Chem.* 409 (1996) 137.

39. A.B.P. Lever, E.L. Milaeva, G. Speier, In Phthalocyanines: Properties and Applications; eds.; VCH Publishers: New York, 1993.

40. H.O. Finklea, In Encyclopaedia of Analytical Chemistry, Applications, Theory and Instrumentations; eds.; R.A. Meyers, Wiley: Chichester, 2000.

41. H.O. Finklea, *J. Am. Chem. Soc.* 114 (1992) 3173.

42. H.O. Finklea, M.S. Ravenscroft, D.A. Snider, *Langmuir* 9 (1993) 223.

43. J. Liu, M.N. Paddon-Row, J.J. Gooding, *J. Phys. Chem. B* 108 (2004) 8460.

44. J.J. Gooding, A. Chou, J. Liu, D. Losic, J.G. Shapter, D.B. Hibbert, *Electrochem. Commun.* 9 (2007) 1677.

45. B.S. Flavel, J. Yu, A.V. Ellis, J.G. Shapter, *Electrochim. Acta* 54 (2009) 3191.

46. K.M. Kadish, K.M. Smith, R. Guilard, The Porphyrin Handbook; eds.; Academic Press, Boston, 2003.

47. M.P. Somashekarappa, J. Keshavaya, S. Sampath, *Pure Appl. Chem.* 74 (2002) 1609.

48. E. Sabatini, I. Rubinstein, *J. Phys. Chem.* 91 (1987) 6663.

49. A.J. Bard and L.R. Faulkner, in *Electrochemical Methods: Fundamentals and Applications, 2nd ed*., John Wiley & Sons Inc., Hoboken, NJ, 2001.

50. E. Barsoukov, J.R. Macdonald, Impedance Spectroscopy: Theory Experiment, and Applications; 2nd ed.; Wiley: Hoboken, New Jersey, 2005.

51. M.E. Orazem, B. Tribollet, Electrochemical Impedance Spectroscopy; John Wiley & Sons Inc: Hoboken, NJ. 2008.

52. J-Y. Park, Y-S. Lee, B.H. Kim, S-M. Park, *Anal. Chem.* 80 (2008) 4986.

53. F. Caruso, E. Rodda, D. N. Furlong and V. Haring, *Sens. Actuators* B 41 (1997)189.

54. M. Aslam, N.K. Chaki, Jadab Sharma, K. Vijayamohanan, *Current Applied Physics* 3 (2003) 115.

55. K. Stolarczyk, R. Bilewics, *Electrochim. Acta* 51 (2006) 2358.

56. J. Tien, A. Terfort, G.M. Whitesides, *Langmuir* 13 (1997) 5349.

57. Y. Lui, Y. Wang, H. Lu, R.O. Claus, *J. Phys. Chem. B* 103 (1999) 2035.

58. H. Paloneimi, M. Lukkarinen, T. Aäritalo, S. Areva, J. Leiro, M. Heinonen, K. Haapakka, J. Lukkari, *Langmuir* 22 (2006) 74.

59. J. Shen, Y. Hu, C. Li, C. Qin, M. Shi, M. Ye, *Langmuir* 25 (2009) 6122.

60. T. R. Tshikhudo, D. Demuru, Z. Wang, M. Brust, A. Secchi, A. Arduini and A. Pochini, *Angew. Chem. Int. Ed.* 44 (2005) 2.

61. S. Chen, R.S. Ingram, M.J. Hostetler, J. J. Pietron, R.W. Murray, T.G. Schaaff, J.T. Khoury, M.M. Alvrez, R.L. Whetten, *Science* 280 (1998) 2098.

62. J.F. Hicks, F.P. Zamborini, R.W. Murray, *J. Phys. Chem. B* 106 (2002) 7751.

63. B. Su, H.H. Girault, *J. Phys. Chem. B* 109 (2005) 23925.

64. S. Chen, R.W. Murray, *J. Phys. Chem. B* 103 (1999) 9996.

65. S. Chen, R.W. Murray, *Langmuir* 15 (1999) 682.

66. S. E. Creager, T.T. Wooster, *Anal. Chem.* 70 (1998) 4257.

67. D.D. MacDonald, *Electrochim. Acta* 51 (2006) 1376.

68. M.E. Orazem, B. Tribollet, *Electrochemical Impedance Spectroscopy*. New Jersey: John Wiley & Sons; 2008.

69. E. Barsoukov, J.R. Macdonald (Eds), *Impedance spectroscopy: Theory, Experiment, and Applications*. 2nd ed. New Jersey: John Wiley & Sons; 2008.

70. P.Y. Bruice, *Organic Chemistry*, fiftth ed., Person Prentice Hall, NewJersey, 2007, pp. 1041–1045, chapter 22.

71. S. Chen, *J. Phys. Chem. B* 104 (2000) 663.

72. H.O. Finklea, in: R.A. Meyers (Ed.), Encyclopedia of Analytical Chemistry: Applications, Theory and Instrumentations, Vol.11, Wiley & Sons, Chichester, 2001.

73. C.E.D. Chidsey, D.N. Loiacono, *Langmuir* 6 (1990) 682.

74. K.I. Ozoemena, T. Nyokong and P. Westbroek, *Electroanalysis* 15 (2003) 1762.

75. Y.Y. Jun, K.S. Beng, *Electrochem. Commun*. 6 (2004) 87.

76. T.J. Davies, R.G. Compton, *J. Electroanal. Chem.* 585 (2005) 63.

77. T.J. Davies, C.E. Banks, R.G. Compton, *J. Solid. State Electrochem.* 9 (2005) 797.

78. X. Dai, G.G. Wildgoose, C. Salter, A. Crossley, R.G. Compton, *Anal. Chem*. 78 (2006) 102.

79. E. Sabatani, I. Rubinstein, *J. Phys. Chem.* 91 (1987) 6663.

80. T.R. Lee, R.D. Carey, H.A. Biebuyck, G.M. Whitesides, *Langmuir* 10 (1994) 741.

81. D. Nkosi, K.I. Ozoemena, *Electrochim. Acta* 53 (2008) 2782.

82. B O. Agboola, K.I. Ozoemena, *Phys. Chem. Chem. Phys.* 10 (2008) 2399.

83. R.Z. Shervedani, M. Bagherzadeh, S.A. Mozaffari, *Sens. Actuators B* 115 (2006) 614.

84. M.H. Pournaghi-Azar, R. Ojani, *Talanta* 42 (1995) 1839.

85. S. L. Jewett, S. Eggling, L. Geller, *J. Inorg. Biochem*. 66 (1997) 165.

86. C. E. Sanger-van de Griend, A. G. Ek, M. E. Widahl-Nasman, E. K. M. J. Andersson, *Pharm. Biomed. Anal.* 41 (2006) 77.

87. E. L. Ciolkowski, K. M. Maness, P. S. Cahlil, R. M. Wightman, *Anal. Chem.* 66 (1994) 3611.

CONCLUSION

AND

RECOMMENDATIONS

CONCLUSION

This dissertation essentially describes the electrocatalytic properties of MPCAuNP, SWCNT-PABS and MPCAuNP, SWCNT-PABS functionalized with ironphthalocyanine complexes on gold electrode electrode towards the detection of hydrogen peroxide and epinephrine. The following important results obtained in this work should be emphasised:

- The electrochemical properties of DMAET SAM, with and without integration with SWCNT-PABS were probed for the first time. SWCNT-PABS was found to be irreversibly attached to the DMAET.
    - Electric field-induced protonation/deprotonation of the DMAET head group ($-N(H)^{+}(CH_3)_2$) resulted in the well-defined reversible voltammetry observed for DMAET SAM.
    - The surface pK_a of DMAET was examined for the first time and its value of ~7.6 was found to be ~3 pK_a units less than its solution pK_a.
- The integration of SWCNT-PABS and nanoparticles of redox-active FePc complex via electrostatic layer-by-layer assembly on Au-DMAET were explored for the first time.
    - The electron transfer kinetics of the ferricyaninde/ferrocyanide redox probe decreased with added alternating layers of SWCNT-PABS and nanoparticles of FePc.

- The reduction rate of hydrogen peroxide increased with added alternating layers of SWCNT-PABS and nanoparticles of FePc.
- DMAET-SWCNT-PABS SAM proved to be more efficient in epinephrine detection than the layer-by-layer nano-architectural assembly.

- The combined integration of FeTSPc complex and SWCNT-PABS investigated for the first time.
  - The nano-thin films of the combined redox-active species exhibited excellent electrochemical stability and showed faster electron transport in $[Fe(CN)_6]^{4-}/[Fe(CN)_6]^{3-}$ redox probe compared to the individual FeTSPc and SWCNT-PABS.
  - The combined species also showed enhanced detection towards epinephrine.
- The solid films exhibited excellent electrochemical stability. The SWCNT-PABS acts as efficient conducting species in the mixed hybrids (Au-DMAET-SWCNT-PABS/FeTSPc) thus facilitating electron transport between the integrated FeTSPc and the underlying gold substrate.
- For the first time the electron transfer dynamics of surface-confined gold nanoparticles involving different ratios of carboxylated- and hydroxyl-containing ligands has been fabricated and described.

Conclusion.....

- In both aqueous and nonaqueous solutions, there is electronic communication between the immobilized MPCAuNPs and the gold electrode, possibly from electron tunneling between these protecting ligands and the gold electrode.
- the electronic communication is strongly influenced by the hydrophilicity of the head groups (-OH and -COOH); in aqueous solution the electron transport of the –COOH based ligand is favoured, while in the nonaqueous medium the electron transport of the -OH based ligands is favoured.
- Au-DMAET-MPCAuNP-$COOH_{99\%}$ showed an excellent suppression of the voltammetric response of the ascorbic acid and an enhanced electrocatalytic activity towards the detection of epinephrine compared to other MPCAuNPs studied.
- Simply put, this study has provided some useful physical insights into the impact of different ratios of the protecting –OH and –COOH based monolayer ligands of redox-active gold nanoparticles on the dynamics of electron transport between solution species, in organic and aqueous media, and the electrode surface.

RECOMMENDATIONS

- The amplification of the electrochemical response to H_2O_2 detection suggests that this type of electrode could provide an important nano-architectural sensing platform for biosensor development.
- The extent to which the ratios of protecting ligands in MPCAuNP influence electron transport is crucial for the potential applications of such platforms in many areas such as in molecular electronics as well as chemical and biological sensing.
- Integration of *nano*FePc and MPCAuNP for the detection of H_2O_2.
- The use of HRP and Cyt C instead of FePc complexes for MPCAuNP studies.
- Other analytes and neurotoxins can be investigated using the modified electrodes.
- Interchange the order of the attached species in the assembly strategy by using charges opposite to that used in this work.
- Use of a negatively charged base monolayer.

It is envisaged that the results shown in this dissertation should provide some thoughts on the factors that should be considered when designing molecular-scale electronics or electrocatalytic sensing devices that employ these materials, and possibly for some other redox-active metal nanoparticles.

APPENDIX A: PEER-REVIEWED ARTICLES RELATED:

(a) DIRECTLY TO THIS DISSERTATION:

1. **J. Pillay**, B. O. Agboola, K. I. Ozoemena, Layer-by-layer self-assembled nanostructured phthalocyaninatoiron(II) / SWCNT-*poly*(*m*-aminobenzene sulfonic acid) hybrid system on gold surface: Electron transfer dynamics and amplification of H_2O_2 response", *Electrochem. Commun.* 11 (2009) 1292.
2. **J. Pillay**, K.I. Ozoemena, Electrochemistry of 2-dimethylaminoethanethiol SAM on gold electrode: Interaction with SWCNT-poly(*m*-aminobenzene sulphonic acid), electric field-induced protonation-deprotonation, and surface pK_a", *Electrochim. Acta* 54 (2009) 5053.
3. **J. Pillay**, K.I. Ozoemena, T.R. Tshikhudo, "Monolayer-Protected Gold Nanoparticles: Impacts of Stabilizing Ligands on the Heterogeneous Electron Transfer Dynamics and Voltammetric Detection", *Langmuir* (2010) DOI: 10.1021/la904463g
4. B.O. Agboola, **J. Pillay**, K. Makgopa, K.I. Ozoemena, "Cyclic voltammetric and impedimetric properties of mixed self-assembled nanothin films of water-soluble SWCNT-*poly*(*m*-aminobenzene sulfonic acid) and iron (II) tetra-sulphophthalocyanine at gold electrode", Submitted to *Thin Solid Films*.

5. **J. Pillay**, K.I. Ozoemena, "Electron transport and voltammetric detection properties of gold nanoparticle-nanosized iron (II) phthalocyanine bilayer films", in preparation.

(b) INDIRECTLY TO THIS DISSERTATION:

1. A.S. Adekunle, **J. Pillay**, K. I. Ozoemena, "Electrocatalysis of 2-Diethylaminoethanethiol at Nickel Nanoparticle-Electrodecorated Single-Walled Carbon Nanotube Platform: An Adsorption-Controlled Electrode Process", *Electroanalysis* 20 (2008) 2587.
2. K. I. Ozoemena, D. Nkosi, **J. Pillay**, "Influence of solution pH on the electron transport of the self-assembled nanoarrays of single-walled carbon nanotube-cobalttetra-aminophthalocyanine on gold electrodes: Electrocatalytic detection of epinephrine", *Electrochimica Acta* 53 (2008) 2844.
3. B. O. Agboola, A. Mocheko, **J. Pillay** and K. I. Ozoemena, "Nanostructured cobalt phthalocyanine single-walled carbon nanotube platform: electron transport and electrocatalytic activity on epinephrine", *Journal of Porphyrins and Phthalocyanines* 12 (2008) 1289.
4. N.S. Mathebula, **J. Pillay**, G. Toschi, J.A. Verschoor, K.I. Ozoemena, "Recognition of anti-mycolic acid antibody at self-assembled mycolic acid antigens on a gold electrode: a potential

impedimetric immunosensing platform for active tuberculosis" *Chem. Comm.* 23 (2009) 3345.

5. A.S. Adekunle, **J. Pillay**, K.I. Ozoemena, "Probing the electrochemical behaviour of SWCNT-Cobalt nanoparticles and their electrocatalytic activities towards the detection of nitrite at acidic and physiological pH conditions", *Electrochimica Acta* (2008), doi:10.1016/j.electacta. 2009.02.102.
6. D. Nkosi, **J. Pillay**, K.I. Ozoemena, K, Nouneh, M. Oyamac, "Heterogeneous electron transfer kinetics and electrocatalytic behaviour of mixed self-assembled ferrocenes and SWCNTs layers", *Physical Chemistry Chemical Physics* (2009) DOI: 10.1039/b00000.
7. K.I. Ozoemena, N.S. Mathebula, **J. Pillay**, G. Toschi, J.A. Verschoor, "Electron transfer dynamics across self-assembled N-(2-mercaptoethyl) octadecanamide/ mycolic acid layers: impedimetric insights into the structural integrity and interaction with anti-mycolic acid antibodies", *Physical Chemistry Chemical Physics* (2009) DOI: 10.1039/b915930d.
8. A.S. Adekunle, B.O. Agboola, **J. Pillay**, K.I. Ozoemena, "Electrocatalytic detection of dopamine at SWCNT/Fe_2O_3 nanoparticle platform", submitted to *Sensors and Actuators B*.

APPENDIX B: LIST OF CONFERENCE PRESENTATIONS RELATED DIRECTLY TO THIS DISSERTATION:

1. "Monolayer-Protected Gold Nanoclusters as a Platform for the Development of High-Performance Electrochemical Biosensors", Jeseelan Pillay and Kenneth I. Ozoemena, International SA-UK Research Network on Electrochemistry for Nanotechnology, CSIR International Convention Centre, Pretoria, SOUTH AFRICA, April 9 – 10,2008 (**ORAL PRESENTATION BY J. PILLAY**).

2. Jeseelan Pillay, NRF South African PhD Project Conference, Emperor's Palace, Kemton Park, Guateng, SOUTH AFRICA, May 25 – 27, 2008. 1 of 300 Invited Delegates.

3. "Layer-by-Layer Self Assembled Nano-Architectural Platform of SWCNT-nanoFePc: Characterization and Electrocatalysis", Jeseelan Pillay and Kenneth I. Ozoemena, 1st International Symposium on Electrochemistry, ElectrochemSA, University of Western Cape, Cape Town, SOUTH AFRICA, July 9 – 11, 2008 (**ORAL PRESENTATION BY J. PILLAY**).

4. "Electrocatalytic and Sensing Platforms based on Molecular and Nanomaterials", Jeseelan Pillay and Kenneth I. Ozoemena, University of Pretoria Chemistry Department 2008 Research Day, University of Pretoria, Pretoria, SOUTH AFRICA, July 21, 2008 (**ORAL PRESENTATION BY J. PILLAY**).

5. "Biosensing Platform based on LBL Networks incorporating Enzyme and Nanomaterial", Jeseelan Pillay and Kenneth I.

Ozoemena, 39th National Convention of the South African Chemical Institute, Stellenbosch University, Stellenbosch, SOUTH AFRICA, November 30 – December 5, 2008 (**ORAL PRESENTATION BY J. PILLAY**).

6. "Self-Assembled Layer-by-Layer Networks Incorporating Single-Walled Carbon Nanotubes and Iron Phthalocyanine", Jeseelan Pillay and Kenneth I. Ozoemena, Nanomaterials Conference, Ocean Maya, Playa del Carmen, MEXICO, December 7 – 10, 2008 (**POSTER PRESENTATION BY J. PILLAY**).

7. "Electron Transfer and Electrocatalysis of Self- Assembled Films of Monolayer-Protected Clusters of Gold Nanoparticles", Jeseelan Pillay and Kenneth I. Ozoemena, International Conference on Nanoscience and Nanotechnology, CSIR International Convention Centre, South Africa, 1 – 4 February, 2009 (**ORAL PRESENTATION BY J. PILLAY**).

8. "Architecture of monolayer protected clusters of gold nanoparticles containing different ligand composition on gold electrodes", Jeseelan Pillay, Kenneth I. Ozoemena, T.R. Tshikhudo, DST/Mintek annual NIC "Nanotechnology for Development" Workshop, Council Chambers, Kingsway Campus, Auckland Park, University of Johannesburg, 24 – 25 September, 2009 (**ORAL PRESENTATION BY J. PILLAY**).